

**An Investigation Into The Use Of Real-Time Simulation And  
Hardware-In-The-Loop Techniques For Studying The Dynamic  
Performance Of Adjustable Speed Drives Under Fault Conditions**

by

**Chenal Palhad**

**Supervisor: Dr B S Rigby**

Submitted in fulfilment of the academic requirement for the degree of Master of Science in Engineering, College of Agriculture, Engineering and Science, University of KwaZulu-Natal, Durban, South Africa.

**Examiner's Copy**

April 2015

# COLLEGE OF AGRICULTURE, ENGINEERING AND SCIENCE

## DECLARATION 1 — PLAGIARISM

I, Chenal Palhad, declare that:

1. The research reported in this thesis, except where otherwise indicated, is my original research.
2. This thesis has not been submitted for any degree or examination at any other university.
3. This thesis does not contain other persons' data, pictures, graphs or other information, unless specifically acknowledged as being sourced from other persons.
4. This thesis does not contain other persons' writing, unless specifically acknowledged as being sourced from other researchers. Where other written sources have been quoted, then:
  - a. Their words have been re-written but the general information attributed to them has been referenced.
  - b. Where their exact words have been used, then their writing has been placed in italics and inside quotation marks, and referenced.
5. This thesis does not contain text, graphics or tables copied and pasted from the Internet, unless specifically acknowledged, and the source being detailed in the thesis and in the References sections.

**Chenal Palhad**

(BScEng)

\_\_\_\_\_  
Signature

\_\_\_\_\_  
Date

As the candidate's Supervisor I agree to the submission of this thesis.

**Supervisor: Bruce Rigby**

(BScEng, MScEng, PhD (Natal), MIEEEE)

\_\_\_\_\_  
Signature

\_\_\_\_\_  
Date

# COLLEGE OF AGRICULTURE, ENGINEERING AND SCIENCE

## DECLARATION 2 — PUBLICATIONS

The publications that include the findings presented in this thesis are listed as follows.

Publication 1:

Palhad C and Rigby B S: “A Laboratory Test System to Evaluate the Performance of Adjustable-Speed Drives Under Fault Conditions”, *Southern African Universities Power Engineering Conference, SAUPEC 2011*, Cape Town, South Africa, 13-15 July 2011.

Publication 2:

Palhad C and Rigby B S: “Real-Time Simulation and Laboratory Measurements of a System to Study Fault Tolerance of Adjustable Speed Drives”, *IEEE AFRICON 2011*, Livingstone, Zambia, pp. 1-6, 13-15 September 2011.

Publication 3:

Palhad C and Rigby B S: “An Investigation Into the Use of Hardware-In-Loop Testing Techniques for Assessing the Performance of Adjustable Speed Drives in Response to Power Quality Events”, *Protection, Automation and Control World Conference 2013*, Dublin, Ireland, 24-27 June 2013.

Publication 4:

Palhad C and Rigby B S: “Hardware-In-Loop Test to Assess the Performance of Adjustable Speed Drives in Response to Power Quality Events”, *Protection, Automation and Control World Africa Conference 2013*, Cape Town, South Africa, 30 July - 2 August 2013.

This thesis is dedicated

to

My Family.

## Abstract

Sophisticated adjustable speed drives (ASDs) have for decades been an ever-increasing part of industrial automation and control systems. The control schemes in the drives themselves have been continually developed to exploit improvements made in electrical machine, control system and power-electronic technologies to fulfil application requirements in industry. One particular trend is the emergence of active front-end type drives, in which advanced control techniques aim to allow ASDs to exhibit increased immunity to power quality problems, in particular voltage sags. The ability to test the impact of power quality events on such drives, as well as the interaction of the drives themselves with other protection and control equipment elsewhere in the system during such events, will be of obvious importance in future, in particular with the increased penetration of such technology in future into both industry and utility systems, and, very importantly, because of the unique characteristics of such controls in each drive manufacturer's proprietary implementations.

This thesis describes a study into the use of real-time digital simulators as a tool for hardware-in-loop (HIL) testing of commercial adjustable speed drive control hardware in order to evaluate the performance of these drives under realistic fault contingencies in an upstream utility power system supply network, rather than relying on limited and simplistic voltage sag tests that are currently often used in such testing.

The results of the investigations in the thesis show that, provided key components of the plant in the drive system are modelled in appropriate detail, very accurate results can be obtained from HIL testing of drive controls interfaced to a real-time simulation model of the electrical supply system and of the drive converters and motor plant.

The investigations in the thesis also show how different types of adjustable speed drive technology not only respond differently to the same power system disturbances, but also how they can interact differently with the power system, resulting in different degrees of harmonic distortion, fault currents, and depths of voltage sag within the utility power system itself during upstream fault conditions. These results further emphasize the value of being able to test the response of actual drive controller hardware using detailed and realistic real-time simulation models of the supply system when carrying out power quality studies.

This real-time simulation approach considered in the thesis constitutes a full, closed-loop test of the actual drive control hardware, but has the advantage of allowing the inclusion of far more detailed representations of the plant in the ASD system itself, and in the utility power supply system, as well as

the inclusion of representations of neighbouring plant fed off busbars in the vicinity of the drive, than is possible in a small-scale laboratory hardware test system such as that which has been used in this thesis for initial validation purposes. However, with the necessary confidence established in the method as a result of the investigations in this thesis, the HIL approach to testing adjustable speed drive controls has potential applications in future for studying the impact of power quality issues on various types of drive system equipment in much larger-scale representations of utility supply networks.

## Acknowledgements

The work presented in this thesis was carried out under the supervision of Dr B S Rigby. I wish to thank Dr Rigby for his invaluable guidance, advice, encouragement, constant support and kindness, as well as for the time and energy that he has willingly put into guiding and assisting me not only to complete the work of this thesis, but also to improve my technical and writing abilities as an engineer. Furthermore, I wish to thank Dr Rigby for his efforts in the production of papers which documented the findings of this thesis, and also for providing financial support which made it possible for me to present these papers at local and international conferences.

A special word of thanks is also due to:

my family for their constant support, patience, sacrifices and encouragement, and especially for everything that they have done in order to make it possible for me to complete this project;

Tyne Muller and her family for their great kindness, friendship, encouragement and support, as well as for the unforgettable times that we all shared;

Lance Benn and Bruce Burton for their valuable support, and for introducing me to the fields of industrial automation and field oriented control based ASD systems, and especially for showing me how to think 'outside the box';

Mr Tony Munnik for his valuable advice, friendship, encouragement and assistance;

the team at the Little Italian and especially Nicky for their great friendship and hospitality, with an extra special thank you to the 'missable' Trevlyn and Shana for their awesome kindness, encouragement and inspiration;

Yu-Ting Huang, Trevor Lorimer and Kerrylynn Pillay for their friendship, kindness and encouragement;

the University of KwaZulu-Natal (UKZN) for providing equipment, resources and support, and especially for allowing full-time access to their Machines Research Laboratory;

the technical staff at UKZN for their assistance, especially Johan Swanepoel and his team for their great support and encouragement;

the Durban University of Technology (DUT) for generously allowing unrestricted use of their RTDS™ Technologies real-time digital simulation equipment, and also for their valuable support;

the Eskom TESP Programme for providing financial support.

# Table Of Contents

<b>Abstract.....</b>	<b>i</b>
<b>Acknowledgements .....</b>	<b>iii</b>
<b>List of Figures.....</b>	<b>ix</b>
<b>List of Tables .....</b>	<b>xix</b>
<b>List of Abbreviations and Symbols .....</b>	<b>xxi</b>
<b>Chapter 1: Introduction .....</b>	<b>1</b>
1.1 General .....	1
1.2 Literature Review .....	3
1.2.1 Modern Industrial Motion Control Systems .....	3
1.2.2 Adjustable Speed Drive Testing Methods .....	6
1.2.3 Real-Time Simulation Technology .....	10
1.3 Research Objectives .....	13
1.4 Thesis Layout .....	15
1.5 Research Publications .....	16
1.6 Summary .....	16
<b>Chapter 2: An Introduction To Field Oriented Control.....</b>	<b>17</b>
2.1 General .....	17
2.2 Torque Production in a Squirrel Cage Induction Machine.....	19
2.3 A Mathematical Model of the Squirrel Cage Induction Machine.....	24
2.4 The Method of Operation of the Field Oriented Control Algorithm.....	33

2.5	Summary .....	40
<b>Chapter 3: The All-Hardware Laboratory-Scale Implementation Of The Study System</b>		
.....		<b>41</b>
3.1	Introduction .....	41
3.2	Overview of the Laboratory-Scale Study System.....	42
3.3	The Practical Implementation of the Motion Control System.....	43
3.3.1	Introduction .....	43
3.3.2	The Squirrel Cage Induction Machine and Load .....	43
3.3.3	The Frequency Converter System.....	46
3.4	Commissioning of the Frequency Converter Controllers.....	50
3.4.1	Introduction .....	50
3.4.2	Commissioning of the Controller within the VC Inverter Unit .....	50
3.4.3	Commissioning of the Controller within the AFE Converter Unit .....	52
3.5	The Practical Implementation of the Power System Network.....	54
3.6	Summary .....	58
<b>Chapter 4: Development And Parameterization Of The Real-Time Model For The</b>		
<b>Hardware-In-Loop Simulation Implementation Of The Study System.....</b>		<b>59</b>
4.1	Introduction .....	59
4.2	Overview of the Real-Time Models in the HIL Simulation Study System.....	60
4.3	The Distribution Network and Fault Application Circuit Component Models .....	61
4.3.1	Validation of the Real-Time Models.....	63
4.4	The 10 kVA Transformer Model.....	69
4.4.1	Validation of the Real-Time Model .....	73
4.5	The Line Reactor Model .....	83

4.5.1	Validation of the Real-Time Model .....	85
4.6	The Micro-Induction Machine and Dynamometer Models .....	94
4.6.1	Induction Machine Electrical Model .....	94
4.6.2	Induction Machine and Dynamometer Mechanical Model .....	95
4.6.3	Validation of the Real-Time Models .....	98
4.7	The AFE Converter, VC Inverter and Diode-Rectifier Models .....	106
4.7.1	The AFE Converter .....	106
4.7.2	The VC Inverter .....	108
4.7.3	The Diode Rectifier .....	110
4.8	Real-Time Model of the Complete Study System and its Decomposition into Large and Small Time Step Networks .....	111
4.9	Summary .....	113
 <b>Chapter 5: The Hardware-In-Loop Simulation Implementation Of The Study System And The Performance Of The Diode Rectifier Energised ASD Under Voltage Sag Conditions .....</b>		
<b>115</b>		
5.1	Introduction .....	115
5.2	The Hardware-In-Loop Simulation Implementation of the Study System .....	116
5.3	Comparisons of the Results from the All-Hardware and HIL Simulation Implementations of the Study System Under Voltage Sag Conditions for the Case of the Diode Rectifier Energised ASD System .....	121
5.3.1	Introduction .....	121
5.3.2	ASD Response to Single-Phase to Ground Faults .....	124
5.3.3	ASD Response to Double-Phase to Ground Faults .....	132
5.3.4	ASD Response to Three-Phase to Ground Faults .....	139
5.3.5	Summary of the ASD's Response to Upstream Faults .....	146
5.4	Summary .....	147

**Chapter 6: The Performance Of The AFE Converter Energised ASD System Under Voltage Sag Conditions.....148**

6.1 Introduction ..... 148

6.2 Comparisons of the Results from the All-Hardware and HIL Simulation Implementations of the Study System Under Voltage Sag Conditions for the Case of the Active Front End Converter Energised ASD System ..... 150

6.2.1 Introduction ..... 150

6.2.2 AFE Converter Energised ASD Response to Single-Phase to Ground Faults..... 153

6.2.3 AFE Converter Energised ASD Response to Double-Phase to Ground Faults ..... 162

6.2.4 AFE Converter Energised ASD Response to Three-Phase to Ground Faults..... 168

6.2.5 Summary of the AFE Converter Energised ASD Response to Upstream Faults..... 176

6.3 An Investigation into the Influence of Different ASD Front-End Converter Technologies on the Performance of a Power System Network During Network Faults ..... 177

6.3.1 Introduction ..... 177

6.3.2 Performance of the Power System Network Feeding AFE- and UDR-Type Drives During Asymmetric Fault Conditions ..... 181

6.3.3 Performance of the Power System Network Feeding AFE- and UDR-Type Drives During Symmetric Fault Conditions ..... 192

6.3.4 Summary of the Results of Tests into the Response of the Power System Network Feeding AFE- and UDR-Type Drives During Network Fault Conditions ..... 201

6.4 Summary ..... 203

**Chapter 7: Conclusion.....204**

7.1 Introduction ..... 204

7.2 An Introduction to Field Oriented Control ..... 205

7.3 The All-Hardware Laboratory-Scale Implementation of the Study System..... 205

7.4 Development and Parameterization of the Real-Time Model for the HIL Simulation Implementation of the Study System ..... 205

7.5	The HIL Simulation Implementation of the Study System and the Performance of the Diode Rectifier Energised ASD Under Voltage Sag Conditions .....	206
7.6	The Performance of the AFE Converter Energised ASD System Under Voltage Sag Conditions .....	207
7.7	Concluding Comments .....	208
7.8	Suggestions for Further Work .....	208
<b>Appendix A: Real-Time Simulation Model Of The Power-Level Plant In The Laboratory-Scale Study System Used For HIL Tests.....</b>		<b>210</b>
<b>References .....</b>		<b>213</b>

## List of Figures

Figure Title	Page No.
Figure 1-1: A general AC machine based motion control system.	3
Figure 1-2: All-hardware test implementation.	7
Figure 1-3: Hardware-in-loop connection of the ASD's controls to a real-time simulation model.	8
Figure 1-4: RTDS implementation of a hardware-in-loop simulation test system for protection devices.	11
Figure 1-5: Schematic diagram of the all-hardware study system.	13
Figure 1-6: Schematic diagram of the hardware-in-loop simulation implementation of the study system.	14
Figure 2-1: Partially dismantled, 370 W, three-phase, two-pole, squirrel cage induction machine [58].	19
Figure 2-2: Schematic diagram of a squirrel cage induction machine and the various reference frames.	25
Figure 2-3: Signal flow representation of the two-axis dynamic model of a squirrel cage induction machine.	31
Figure 2-4: A space vector diagram showing $\overline{\lambda}_r$ aligned to $i_{ds}$ .	33
Figure 2-5: Signal flow representation of a squirrel cage induction machine with signal paths of $\lambda_{qr}$ highlighted in blue, (adapted from [60]).	35
Figure 2-6: Signal flow representation of an induction machine with $\lambda_{qr} = 0$ ; the natural cross-coupling between $i_{ds}$ and $i_{qs}$ is highlighted in red and green, (adapted from [60]).	37
Figure 2-7: Signal flow diagram representation of the induction machine under field oriented control with closed-loop stator current and pre-compensation control applied (adapted from [60]).	38
Figure 2-8: Dynamic structure of the induction machine under field oriented control and constant rotor flux linkages (adapted from [60]).	39
Figure 3-1: Schematic diagram of the laboratory-scale study system.	42

Figure 3-2: Schematic diagram of the motion control system within the laboratory-scale study system.	43
Figure 3-3: The micro-induction machine used in the laboratory-scale study system, with a close-up view of its deep-bar rotor design shown on the right-hand side.	44
Figure 3-4: Induction machine, torque transducer and dynamometer.	45
Figure 3-5: Schematic diagram of the motion control system showing component ratings and the additional support components required in the practical commissioning of the system.	47
Figure 3-6: Rating information for the converter units, inverter unit and induction machine.	48
Figure 3-7: Photograph of the final, fully-commissioned, frequency-converter system hardware for the laboratory-scale system shown in Figure 3-5, housed in its special-purpose drive enclosure.	49
Figure 3-8: Schematic diagram of the all-hardware laboratory-scale study system.	54
Figure 3-9: Practical implementation of the all-hardware laboratory scale study system.	56
Figure 4-1: A schematic diagram of the all-hardware implementation of the study system.	60
Figure 4-2: Schematic diagram of the faulted distribution network in the laboratory-scale study system and its representation in RSCAD.	61
Figure 4-3: Sub-system of the laboratory-scale study system containing the 220 V source, distribution network, and fault application circuit.	63
Figure 4-4 — Validation of faulted distribution network model: (i) Phase A-ground fault with 70 % voltage sag at Bus 2.	65
Figure 4-5 — Validation of faulted distribution network model: (ii) Phase A-B-ground fault with 50 % voltage sag at Bus 2.	66
Figure 4-6 — Validation of faulted distribution network model: (iii) Phase A-B-C-ground fault with 70 % voltage sag at Bus 2.	68
Figure 4-7: The three-phase, three-limb, 10 kVA transformer used in the all-hardware implementation of the laboratory-scale study system.	69
Figure 4-8: The RSCAD real-time implementation of the UMEC model.	70

Figure 4-9: Measured magnetisation curve of the 10 kVA transformer.	72
Figure 4-10: Sub-system used to test the validity of the UMEC model of the 10 kVA transformer component.	73
Figure 4-11 (a) — Validation of drive transformer model: (i) Phase C-ground fault with 70 % voltage sag; Bus 2 voltages.	75
Figure 4-11 (b) — Validation of drive transformer model: (i) Phase C-ground fault with 70 % voltage sag; Bus 3 voltages and currents.	76
Figure 4-12 (a) — Validation of drive transformer model: (ii) Phase A-B-ground fault with 50 % voltage sag; Bus 2 voltages.	78
Figure 4-12 (b) — Validation of drive transformer model: (ii) Phase A-B-ground fault with 50 % voltage sag; Bus 3 voltages and currents.	79
Figure 4-13 (a) — Validation of drive transformer model: (iii) Phase A-B-C-ground fault with 70 % voltage sag; Bus 2 voltages.	80
Figure 4-13 (b) — Validation of drive transformer model: (iii) Phase A-B-C-ground fault with 70 % voltage sag; Bus 3 voltages and currents.	81
Figure 4-14: The three-phase, three-limb, line reactor used in the all-hardware implementation of the laboratory-scale study system.	83
Figure 4-15: Measured magnetisation curve of the line reactor.	84
Figure 4-16: Sub-system used to test the validity of the UMEC model of the line reactor component.	85
Figure 4-17 (a) — Validation of line reactor model: (i) Phase A-ground fault with 70 % voltage sag; Bus 2 voltages.	87
Figure 4-17 (b) — Validation of line reactor model: (i) Phase A-ground fault with 70 % voltage sag; Bus 3 voltages and currents.	88
Figure 4-18 (a) — Validation of line reactor model: (ii) Phase A-B-ground fault with 70 % voltage sag; Bus 2 voltages.	89
Figure 4-18 (b) — Validation of line reactor model: (ii) Phase A-B-ground fault with 70 % voltage sag; Bus 3 voltages and currents.	90

Figure 4-19 (a) — Validation of line reactor model: (iii) Phase A-B-C-ground fault with 70 % voltage sag; Bus 2 voltages.	91
Figure 4-19 (b) — Validation of line reactor model: (iii) Phase A-B-C-ground fault with 70 % voltage sag; Bus 3 voltages and currents.	92
Figure 4-20: Rotational mechanical system model for the induction machine and dynamometer set.	95
Figure 4-21: Measured torque-speed characteristic of the dynamometer.	97
Figure 4-22: Subsystem used to test the validity of the real-time models of the micro-induction machine and dynamometer test set.	98
Figure 4-23 (a) — Validation of induction machine-dynamometer set models: (i) Phase A-ground fault with 70 % voltage sag; Bus 2 voltages and currents.	100
Figure 4-23 (b) — Validation of induction machine-dynamometer set models: (i) Phase A-ground fault with 70 % voltage sag; shaft speed.	101
Figure 4-24 (a) — Validation of induction machine-dynamometer set models: (ii) Phase A-B-ground fault with 70 % voltage sag; Bus 2 voltages and currents.	102
Figure 4-24 (b) — Validation of induction machine-dynamometer set models: (ii) Phase A-B-ground fault with 70 % voltage sag; shaft speed.	103
Figure 4-25 (a) — Validation of induction machine-dynamometer set models: (iii) Phase A-B-C-ground fault with 70 % voltage sag; Bus 2 voltages and currents.	104
Figure 4-25 (b) — Validation of induction machine-dynamometer set models: (iii) Phase A-B-C-ground fault with 70 % voltage sag; shaft speed.	105
Figure 4-26: The two-level, three-phase AFE converter.	106
Figure 4-27: The model of a practical valve used in the RSCAD small-time step modelling environment.	107
Figure 4-28: The RSCAD model of the AFE converter.	107
Figure 4-29: The two-level, three-phase VC inverter.	108
Figure 4-30: The RSCAD model of the VC inverter.	109
Figure 4-31: The three-phase AC to DC diode-rectifier converter topology.	110

Figure 4-32: The RSCAD model of the diode rectifier.	110
Figure 4-33: Schematic diagram showing final decomposition of the real-time model of the laboratory study system into large and small time step networks.	112
Figure 5-1: Schematic diagram of the HIL simulation implementation of the study system.	117
Figure 5-2: Photograph showing hardware-in-loop connection of the ASD system to the real-time simulator.	118
Figure 5-3: The I/O connections made within the ASD hardware to allow exchange of variables with the real-time simulator for hardware-in-loop testing.	119
Figure 5-4: The I/O hardware used to interface the ASD's controls to the real-time simulator.	119
Figure 5-5: Schematic diagram of the laboratory-scale study system for the case in which the diode-rectifier unit was used to energise the machine-side inverter in the ASD system.	122
Figure 5-6 (a): Comparison of all-hardware versus HIL simulation implementations of study system — response of ASD system with diode-rectifier front end to phase A to ground fault causing sag of nominal depth 35 %, and duration 200 ms (Bus 3 variables).	125
Figure 5-6 (b): Comparison of all-hardware versus HIL simulation implementations of study system — response of ASD system with diode-rectifier front end to phase A to ground fault causing sag of nominal depth 35 %, and duration 200ms (ASD system variables).	126
Figure 5-7 (a): Comparison of all-hardware versus HIL simulation implementations of study system — response of ASD system with diode-rectifier front end to phase A to ground fault causing sag of nominal depth 50 %, and duration 100 ms (Bus 3 variables).	129
Figure 5-7 (b): Comparison of all-hardware versus HIL simulation implementations of study system — response of ASD system with diode-rectifier front end to phase A to ground fault causing sag of nominal depth 50 %, and duration 100 ms (ASD system variables).	130
Figure 5-8 (a): Comparison of all-hardware versus HIL simulation implementations of study system — response of ASD system with diode-rectifier front end to phase A to B to ground fault causing sag of nominal depth 35 %, and duration 100 ms (Bus 3 variables).	133

Figure 5-8 (b): Comparison of all-hardware versus HIL simulation implementations of study system — response of ASD system with diode-rectifier front end to phase A to B to ground fault causing sag of nominal depth 35 %, and duration 100 ms (ASD system variables).	134
Figure 5-9 (a): Comparison of all-hardware versus HIL simulation implementations of study system — response of ASD system with diode-rectifier front end to phase A to B to ground fault causing sag of nominal depth 50 %, and duration 100 ms (Bus 3 variables).	136
Figure 5-9 (b): Comparison of all-hardware versus HIL simulation implementations of study system — response of ASD system with diode-rectifier front end to phase A to B to ground fault causing sag of nominal depth 50 %, and duration 100 ms (ASD system variables).	137
Figure 5-10 (a): Comparison of all-hardware versus HIL simulation implementations of study system — response of ASD system with diode-rectifier front end to phase A to B to C to ground fault causing sag of nominal depth 50 %, and duration 100 ms (Bus 3 variables).	140
Figure 5-10 (b): Comparison of all-hardware versus HIL simulation implementations of study system — response of ASD system with diode-rectifier front end to phase A to B to C to ground fault causing sag of nominal depth 50 %, and duration 100 ms (ASD system variables).	141
Figure 5-11 (a): Comparison of all-hardware versus HIL simulation implementations of study system — response of ASD system with diode-rectifier front end to phase A to B to C to ground fault causing sag of nominal depth 70 %, and duration 100 ms (Bus 3 variables).	144
Figure 5-11 (b): Comparison of all-hardware versus HIL simulation implementations of study system — response of ASD system with diode-rectifier front end to phase A to B to C to ground fault causing sag of nominal depth 70 %, and duration 100 ms (ASD system variables).	145
Figure 6-1: Schematic diagram of the laboratory-scale study system for the case in which the AFE converter unit was used to energise the machine-side inverter in the ASD system.	151

Figure 6-2 (a): Comparison of all-hardware versus HIL simulation implementations of study system — response of ASD system with active front end converter to phase A to ground fault causing sag of nominal depth 35 %, and duration 200 ms (Bus 3 variables).	155
Figure 6-2 (b): Comparison of all-hardware versus HIL simulation implementations of study system — response of ASD system with active front end converter to phase A to ground fault causing sag of nominal depth 35 %, and duration 200 ms (ASD system variables).	156
Figure 6-3 (a): Comparison of all-hardware versus HIL simulation implementations of study system — response of ASD system with active front end converter to phase A to ground fault causing sag of nominal depth 50 %, and duration 100 ms (Bus 3 variables).	160
Figure 6-3 (b): Comparison of all-hardware versus HIL simulation implementations of study system — response of ASD system with active front end converter to phase A to ground fault causing sag of nominal depth 50 %, and duration 100 ms (ASD system variables).	161
Figure 6-4 (a): Comparison of all-hardware versus HIL simulation implementations of study system — response of ASD system with active front end converter to phase A to B to ground fault causing sag of nominal depth 35 %, and duration 100 ms (Bus 3 variables).	163
Figure 6-4 (b): Comparison of all-hardware versus HIL simulation implementations of study system — response of ASD system with active front end converter to phase A to B to ground fault causing sag of nominal depth 35 %, and duration 100 ms (ASD system variables).	164
Figure 6-5 (a): Comparison of all-hardware versus HIL simulation implementations of study system — response of ASD system with active front end converter to phase A to B to ground fault causing sag of nominal depth 50 %, and duration 100 ms (Bus 3 variables).	166

Figure 6-5 (b): Comparison of all-hardware versus HIL simulation implementations of study system — response of ASD system with active front end converter to phase A to B to ground fault causing sag of nominal depth 50 %, and duration 100 ms (ASD system variables).	167
Figure 6-6 (a): Comparison of all-hardware versus HIL simulation implementations of study system — response of ASD system with active front end converter to phase A to B to C to ground fault causing sag of nominal depth 50 %, and duration 100 ms (Bus 3 variables).	169
Figure 6-6 (b): Comparison of all-hardware versus HIL simulation implementations of study system — response of ASD system with active front end converter to phase A to B to C to ground fault causing sag of nominal depth 50 %, and duration 100 ms (ASD system variables).	170
Figure 6-7 (a): Comparison of all-hardware versus HIL simulation implementations of study system — response of ASD system with active front end converter to phase A to B to C to ground fault causing sag of nominal depth 70 %, and duration 100 ms (Bus 3 variables).	173
Figure 6-7 (b): Comparison of all-hardware versus HIL simulation implementations of study system — response of ASD system with active front end converter to phase A to B to C to ground fault causing sag of nominal depth 70 %, and duration 100 ms (ASD system variables).	174
Figure 6-8: Schematic diagram of the HIL real-time simulation implementation of the laboratory-scale study system used to investigate the influence of an ASD equipped with active front end converter technology on a power system network during fault conditions.	177
Figure 6-9: Schematic diagram of the HIL real-time simulation implementation of the laboratory-scale study system used to investigate the influence of an ASD equipped with uncontrolled diode rectifier front-end converter technology on a power system network during fault conditions.	178

Figure 6-10 (a): Comparison of power system performance when feeding an ASD equipped with AFE- versus UDR-type front-end technologies — response to phase-A to ground fault with $R_{\text{FAULT}} = 1.0 \Omega$ , and duration 100 ms (Bus 3 variables).	182
Figure 6-10 (b): Comparison of power system performance when feeding an ASD equipped with AFE- versus UDR-type front-end technologies — response to phase-A to ground fault with $R_{\text{FAULT}} = 1.0 \Omega$ , and duration 100 ms (220 V source currents and fault currents).	183
Figure 6-10 (c): Comparison of power system performance when feeding an ASD equipped with AFE- versus UDR-type front-end technologies — response to phase-A to ground fault with $R_{\text{FAULT}} = 1.0 \Omega$ , and duration 100 ms (ASD system variables).	184
Figure 6-11 (a): Comparison of power system performance when feeding an ASD equipped with AFE- versus UDR-type front-end technologies — response to phase A to B to ground fault with $R_{\text{FAULT}} = 3.5 \Omega$ , and duration 100 ms (Bus 3 variables).	189
Figure 6-11 (b): Comparison of power system performance when feeding an ASD equipped with AFE- versus UDR-type front-end technologies — response to phase A to B to ground fault with $R_{\text{FAULT}} = 3.5 \Omega$ , and duration 100 ms (220 V source currents and fault currents).	190
Figure 6-11 (c): Comparison of power system performance when feeding an ASD equipped with AFE- versus UDR-type front-end technologies — response to phase A to B to ground fault with $R_{\text{FAULT}} = 3.5 \Omega$ , and duration 100 ms (ASD system variables).	191
Figure 6-12 (a): Comparison of power system performance when feeding an ASD equipped with AFE- versus UDR-type front-end technologies — response to phase A to B to C to ground fault with $R_{\text{FAULT}} = 3.2 \Omega$ , and duration 100 ms (Bus 3 variables).	193
Figure 6-12 (b): Comparison of power system performance when feeding an ASD equipped with AFE- versus UDR-type front-end technologies — response to phase A to B to C to ground fault with $R_{\text{FAULT}} = 3.2 \Omega$ , and duration 100 ms (220 V source currents and fault currents).	194

Figure 6-12 (c): Comparison of power system performance when feeding an ASD equipped with AFE- versus UDR-type front-end technologies — response to phase A to B to C to ground fault with $R_{\text{FAULT}} = 3.2 \Omega$ , and duration 100 ms (ASD system variables).	195
Figure 6-13 (a): Comparison of power system performance when feeding an ASD equipped with AFE- versus UDR-type front-end technologies — response to phase A to B to C to ground fault with $R_{\text{FAULT}} = 0.5 \Omega$ , and duration 100 ms (Bus 3 variables).	198
Figure 6-13 (b): Comparison of power system performance when feeding an ASD equipped with AFE- versus UDR-type front-end technologies — response to phase A to B to C to ground fault with $R_{\text{FAULT}} = 0.5 \Omega$ , and duration 100 ms (220 V source currents and fault currents).	199
Figure 6-13 (c): Comparison of power system performance when feeding an ASD equipped with AFE- versus UDR-type front-end technologies — response to phase A to B to C to ground fault with $R_{\text{FAULT}} = 0.5 \Omega$ , and duration 100 ms (ASD system variables).	200
Figure A-1: Real-time model representation of the power-level plant in the laboratory-scale study system that was interfaced hardware-in-loop to the physical controllers of the industrial ASD system. The variables that were exchanged between the controllers and the model during testing are also shown.	210
Figure A-2: Detailed real-time model representation of the power system network in the laboratory-scale study system.	211
Figure A-3: Detailed real-time model representation of the ASD pre-charge circuit and line reactor in the laboratory-scale study system.	211
Figure A-4: Detailed real-time model representation of the ASD frequency converter and motor in the laboratory-scale study system.	211
Figure A-5: Detailed real-time model representation of the dynamometer load in the laboratory-scale study system.	212

## List of Tables

<b>Table Title</b>	<b>Page No.</b>
Table 3-1: Rating information for the deep-bar rotor micro-induction machine.	44
Table 3-2: Sag characteristics and nominal sag depths at the Bus 3 voltage for the six particular fault conditions considered during experimental tests on the laboratory-scale study system.	57
Table 4-1: Measured series resistance and inductance values of the distribution network impedances ( $Z_{TL1-ZX}$ ), $ZX$ , and $Z_{TL2}$ in the laboratory-scale system.	61
Table 4-2: Summary of the fault conditions applied to the test subsystem of Figure 4-3 together with the resulting voltage sag characteristics seen at Bus 2.	64
Table 4-3: Rating information of the 10 kVA transformer.	71
Table 4-4: Measured equivalent per-phase electrical parameters of the 10 kVA transformer.	71
Table 4-5: Normalised core aspect ratios measured from the 10 kVA transformer's 3-limb core.	71
Table 4-6: Summary of the fault conditions applied to the test subsystem of Figure 4-10 together with the resulting voltage sag characteristics seen at Bus 2.	74
Table 4-7: Rating information for the line reactor.	84
Table 4-8: Measured equivalent per-phase electrical parameters of the line reactor.	84
Table 4-9: Normalised core aspect ratios measured from the line reactor's 3-limb core.	84
Table 4-10: Summary of the fault conditions applied to the test subsystem of Figure 4-16 together with the resulting voltage sag characteristics seen at Bus 2.	86
Table 4-11: Per-phase equivalent double-cage model parameters derived from actual parameter measurements of the deep-bar rotor micro-induction machine.	95
Table 4-12: Measured values of the parameters of the mechanical dynamic model of the micro-induction machine and dynamometer test set.	96
Table 4-13: Summary of the fault conditions applied to the test subsystem of Figure 4-22 together with the resulting voltage sag characteristics seen at Bus 2.	99
Table 4-14: Calculated values of the parameters $R_{off}$ , $C_{off}$ , and $L_{on}$ for the valves in the RSCAD	108

model of the AFE converter.

Table 4-15: Calculated values of the parameters  $R_{off}$ ,  $C_{off}$ , and  $L_{on}$  for the valves in the RSCAD 109

model of the VC inverter.

Table 4-16: Calculated values of the parameters  $R_{off}$ ,  $C_{off}$ , and  $L_{on}$  for the valves in the RSCAD 110

model of the diode rectifier.

Table 5-1: Sag characteristics and nominal sag depths at the Bus 3 voltage for the six particular 123

fault conditions considered during experimental tests on the laboratory-scale study system.

Table 6-1: Sag characteristics and nominal sag depths at the Bus 3 voltage for the six particular 152

fault conditions considered during experimental tests on the laboratory-scale study system.

Table 6-2: Details of the conditions applied at the Fault Bus in the study system during HIL 179

simulation test comparisons of AFE-equipped and UDR-equipped ASD systems.

## List of Abbreviations and Symbols

The commonly used abbreviations and symbols that are adopted in this thesis are listed below. Other abbreviations and symbols used in the text are explained where they first occur.

### General Abbreviations

AFE	active front end
ASD	adjustable speed drive
FOC	field oriented control
HIL	hardware-in-loop
MMF	magnetomotive force
RTDS	real-time digital simulator
UDR	uncontrolled diode rectifier
UMEC	unified magnetic equivalent circuit
VC	vector control

### Induction Machine Symbols

$\bar{i}_s$	stator current space vector [A]
$i_{ds}$	direct-axis component of the stator current space vector [A]
$i_{qs}$	quadrature-axis component of the stator current space vector [A]
$\bar{v}_s$	stator voltage space vector [V]
$v_{ds}$	direct-axis component of the stator voltage space vector [V]
$v_{qs}$	quadrature-axis component of the stator voltage space vector [V]
$\bar{\lambda}_r$	rotor flux linkage space vector [Wb-t]
$\lambda_{dr}$	direct-axis component of the rotor flux linkage space vector [Wb-t]
$\lambda_{qr}$	quadrature-axis component of the rotor flux linkage space vector [Wb-t]
$\delta$	angle between the rotor flux linkage and stator current space vectors [rad]
$T_{em}$	instantaneous electromagnetic torque produced by the machine [Nm]
$L_1$	per phase leakage inductance of the stator winding [H]

$L_2$	per phase leakage inductance of the rotor circuit [H]
$L_m$	per phase mutual inductance [H]
$L_{11}$	per phase self inductance of the stator winding [H]
$L_{22}$	per phase self inductance of the rotor circuit [H]
$R_1$	per phase stator resistance [ $\Omega$ ]
$R_2$	per phase rotor resistance [ $\Omega$ ]
$\omega_s$	synchronous speed [rad/s]
$\omega_{re}$	angular speed of the rotor [rad/s]
$\omega_{slip}$	slip angular frequency [rad/s]
$\omega_{\lambda r}$	angular speed of the rotor flux linkage space vector [rad/s]

# Chapter 1: Introduction

## 1.1 General

The desire for accurate, reliable, efficient and robust motion control of an electrical machine to fulfil its designated automation task has always been present in industry applications. In order to achieve this desire, ever improving motion control techniques are continually being developed and implemented as fast as the latest technological advancements allow. The integration of these techniques into industrial hardware results in ever advancing motion control systems. A testing method to accurately predict the response of these sophisticated systems under nominal and faulted conditions would be of immense benefit to manufacturers, commissioning personnel and operators. Such a testing method could be used to analyze how the motion control system interacts with other systems and plant it has been interconnected with. The results of the analysis may reveal changes that could be made to the settings in the control hardware of the motion control system to further improve its performance, for example to improve its resilience to power system network disturbances. Furthermore, manufacturers of motion control systems could also use such testing methods during the design phase to quickly test, evaluate and enhance control algorithms for new products. The broad objective of the work in this thesis has been to investigate the feasibility of one possible approach to implementing such a test method in which the actual physical control hardware of the manufacturer's motion control system is connected in a hardware-in-loop arrangement with a real-time digital simulation of the industrial plant under control.

This chapter provides the context that lead to the interest in this thesis topic by presenting a review of the relevant literature. The review comprises three sections, the first of which begins by describing the components of a sophisticated modern-day industrial motion control system capable of serving high performance applications. The second section describes methods that are currently used to test the response of these systems, with the benefits and drawbacks of each method outlined in order to lay the basis for considering the particular approach investigated in this thesis in which a real-time simulation is interfaced in closed-loop with physical motion control hardware. An obvious requirement of this approach is a powerful, high-speed computing platform capable of solving mathematical models of the industrial plant and power system under control in real time. Hence, the third section of the review focuses on real-time simulation technology and the developments that have been made in this field that enable the proposed testing approach to be implemented practically on modern motion control drive systems.

Finally, this chapter also outlines the specific objectives of the research, and the procedures that were adopted in carrying out the studies presented in the thesis.

## 1.2 Literature Review

### 1.2.1 Modern Industrial Motion Control Systems

Continuous advances in the fields of microprocessors, semiconductor technology and electrical machines have allowed highly sophisticated motion control strategies to be successfully implemented within hardware. Since the 1990s these advances have led to AC machine based systems being the preferred option for all fields of motion control applications as expressed by Leonhard [1]. Such motion control systems possess significant features of high dynamic performance, efficient operation and increased reliability which may be suited to fulfil virtually any high-level industrial application. An AC machine based motion control system may be often implemented as shown in Figure 1-1: the heart of the system comprises a frequency converter and a machine, collectively termed an adjustable speed drive (ASD), which serves a mechanical load [2].

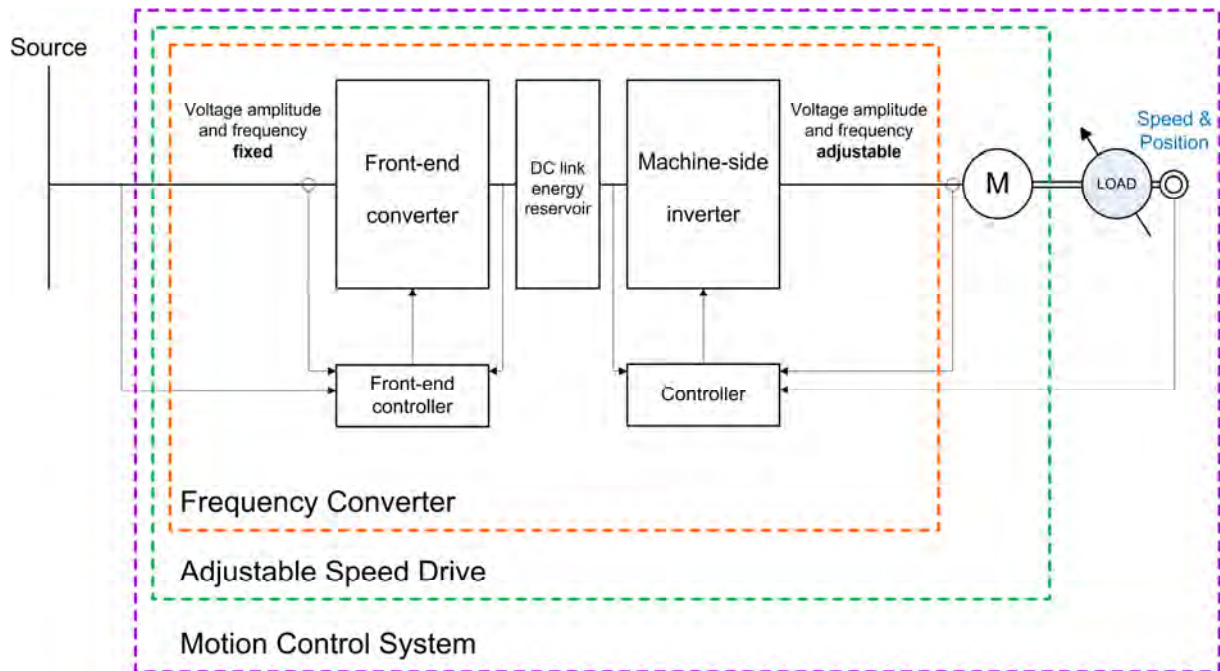


Figure 1-1: A general AC machine based motion control system.

Essentially, an ASD converts a supply of electrical energy (power) into an accurately regulated source of mechanical energy (power) that is available at the output of the machine. The first stage of the energy conversion process is achieved by the front-end converter, which changes the nominally-fixed amplitude and frequency of the source voltage into a rectified form which feeds an energy reservoir in the DC link. The front-end converter controller manages this initial energy-conversion process with assistance from its sensors. The second stage of the energy conversion process takes place through the machine-side inverter. For high dynamic motion control performance in industrial applications, a

voltage source converter [3, 4] has been one of the most commonly used power-electronic converter technologies for the machine-side inverter. This converter topology enables the machine-side inverter to synthesize, from the DC link voltage, a set of AC output voltage phasors of adjustable amplitude and frequency which can be used to regulate the transfer of energy to the machine. Typically, some form of sophisticated algorithm within the machine-side inverter controller detects the operating state of the motion control system via sensors and calculates a suitable response trajectory to fulfil the control objective with the aid of an on-line mathematical model of the controlled machine. The algorithm then transforms this calculated response into an equivalent set of voltage phasor commands that is sent to the machine-side inverter. The resulting set of AC output voltage phasors that is applied to the terminals of the machine then produces the required mechanical response at the shaft. Two types of high-performance AC machine control algorithms that may typically be executed within the machine-side inverter controller are field oriented control (FOC) [5, 6], also known as vector control (VC), and direct torque control (DTC) [7]. Vector control and direct torque control are both well-known, commercially-available, high-performance control algorithms [3] that may be used to serve virtually any industrial task. However, due to the different ways in which these algorithms are practically implemented, inherent advantages may be revealed that would favour one of these control algorithms over the other for a particular application.

With respect to their front-end converter technologies, industrial ASD systems have historically typically used either a diode rectifier or a four-quadrant line-commutated phase-controlled thyristor converter to energise the DC link [4, 8]. A significant aspect of both of these converter technologies is that they draw non-sinusoidal currents, and this may lead to high levels of harmonic distortion being visible on the supply voltages [4, 8] that can negatively impact on other interconnected systems. This disadvantage coupled with strict power quality requirements denoted in IEEE Standard 519 [9] and the NRS 048-2:2003 Standard [10] may initiate a movement toward the use of self-commutated, active front end (AFE) voltage source converters [4, 11] for AC to DC conversion within industrial ASD systems. This innovative class of AFE converters possesses the benefits of: being able to draw near-sinusoidal currents from the supply (thus minimizing the injected harmonic content); the capability for full regenerative operation without the need for an additional converter coupled to an autotransformer as required in a four-quadrant line-commutated thyristor converter installation [12]; the facility to operate with an adjustable power factor, potentially providing reactive power support at the ASD front end [13]; and the capability to isolate the motion control system from certain types of utility disturbance [4, 11]. These benefits of AFE converter technology are made possible by the

implementation of a vector control algorithm within the AFE controller [4, 11]. The type of power-electronic converter that is required to implement an active front end in a drive system is well-established and commercially-available technology [11]. However, in order to derive the full benefit from active front end (AFE) technology, the AFE controller has to be specifically commissioned and tuned for the steady state and dynamic operating conditions associated with the particular ASD system in question, as well as to be able to manage the transient power quality characteristics of the utility supply system that this ASD will be interconnected with. These custom tuning requirements are crucial for the successful operation of an AFE converter because of the high level of interaction it has with its interconnected systems.

Overall, an adjustable speed drive system that has been specified, designed and commissioned to serve a particular application may comprise any suitable combination of front-end converter, machine-side inverter and motor. For example, a state of the art, high-performance ASD system may consist of an active front end converter coupled to a vector controlled inverter feeding a custom-designed motor. The result is a highly sophisticated motion control system in its own right, which may then react in various ways in response to the transient behaviour of the utility power system, and other equipment in that system, under nominal and faulted conditions. In particular, the interaction of an AFE converter with the utility power system network may intensify during supply voltage sag conditions as a result of the fast-acting AFE controller attempting to draw more current from the stressed network in order to satisfy its power requirements, which could potentially make the voltage sag conditions more severe. Therefore, a testing method to precisely predict the response of these complex motion control systems under different scenarios would be a powerful tool for both the manufacturers of the ASD systems and field personnel to possess.

### **1.2.2 Adjustable Speed Drive Testing Methods**

Between 1999 and 2005, work by several researchers was presented [14-17] to test the performance of ASDs in response to voltage sags caused by utility disturbances using the technique of supplying the drive system under test via a programmable source. To create a scenario representing a particular utility disturbance, pre-defined synthesized voltage sag input waveforms indicative of the fault conditions were fed to the ASD using the programmable source. This technique was successfully used to assess the sensitivity of ASD equipment to voltage sags expressed in terms of voltage-tolerance curves [17], where the curves represent the maximum voltage sag depth and duration an ASD system can tolerate before a malfunction results. The work in [17] also included a critical review of standards [18-20] and previously published papers in the area of ASD testing. A significant finding of the review in [17], as well as the research work presented in [17] itself, was that the practical response of ASD equipment to disturbances has a complex nature that is both drive and application specific, with even different ASD models made by the same manufacturer often responding differently to given voltage sags. Furthermore, the authors of the work in [17] proposed extensions to the reviewed standards related to ASD testing, with a great emphasis placed on the need for the test voltages applied to the drive to emulate sags with a full, clear representation of the sag type, depth and duration for all phases as a minimum to be able to precisely assess the sensitivity of ASDs.

In summary, the results presented in [17] highlighted the importance of using the actual physical ASD control hardware for testing the response of a drive to voltage sags and the need for an accurate representation of the sag characteristics themselves during such testing. Although the extensive tests performed in [14-17] provide valuable information on the sensitivity of ASDs to disturbances, a limitation of the method that was used to test drives in these studies is that it does not represent the interaction between a drive system and the upstream utility supply network, since the supply voltages provided when testing a drive using this method are pre-defined, synthesized waveforms. This lack of interaction restricts the ability of this testing technique to predict how the response of the ASD controller (and the resulting currents drawn by the ASD during a utility fault causing a sag in its supply voltages) would themselves affect the depth and asymmetry of the sag in these supply voltages. One way to overcome this limitation of the technique used in [17] is to test the full ASD hardware associated with the motion control system using a laboratory representation of the actual power system network that would subsequently be used to supply it in the field as illustrated in Figure 1-2.

In the test approach illustrated in Figure 1-2, the voltage sags at the input to the drive would be created by means of actual faults in the upstream network, rather than using synthesized voltage inputs to the drive.

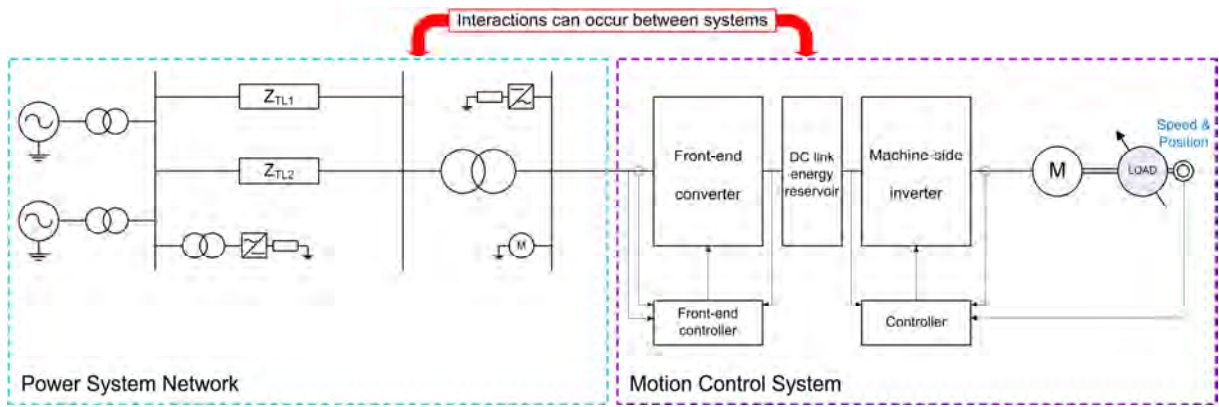


Figure 1-2: All-hardware test implementation.

The key advantage of this approach is that it provides a full, closed-loop test of the motion control system that includes its response to, and interactions with, the upstream utility power system. However, implementing such an all-hardware testing method may prove to be difficult in a laboratory if the actual utility power system feeding the motion control system of interest has a complex, multi-layered topology that is interconnected to other systems and plant, or if the equipment associated with the motion control system itself has a power rating too large for laboratory-type testing. Alternatively, these practical difficulties associated with using laboratory equipment to represent a utility supply system in more detail may be avoided by relying entirely on mathematical models to represent both the power supply system and the motion control system in an all-simulation test approach as carried out in [21, 22]. The disadvantage (and limitation) of this all-simulation test approach is that it requires information on all modelled components to be fully defined and freely available. In practice this is not normally possible because the high-performance control algorithms within the ASD industrial hardware are the intellectual property of the manufacturer. The objective in this thesis is to consider a hybrid approach for testing ASDs that combines the advantages of each of the approaches discussed above. In this hybrid approach, the full ASD industrial controller hardware to be used in the motion control system is interfaced to detailed real-time simulation models of both the utility power supply system, and the power-electronic converters, energy reservoirs, AC motor and mechanical load that comprise the plant of the motion control system itself. This approach is illustrated in Figure 1-3.

Figure 1-3 shows that in this hybrid approach, the control hardware of the ASD system under test is interfaced to the real-time simulation models at signal level in a full closed-loop arrangement. By interfacing the controls within the ASD system to a detailed simulation model of the test plant at signal level it becomes possible, in principle, to carry out detailed testing of ASD systems of any power rating, and not just those with power ratings that lend themselves to laboratory tests.

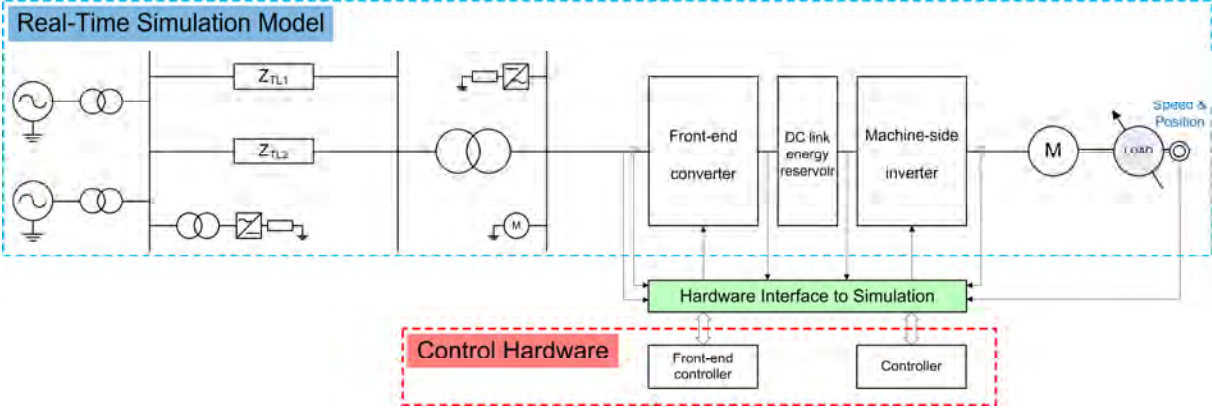


Figure 1-3: Hardware-in-loop connection of the ASD's controls to a real-time simulation model.

As is the case with the all-hardware testing approach discussed earlier, this hybrid (simulation with hardware in the loop) test approach also allows the practical ASD controllers to be tested under different scenarios in a full, closed-loop manner in response to voltage sags created realistically by means of faults in the upstream utility network. However, the use of real-time simulation models of the plant provides the flexibility to be able to represent far more complex power system networks with additional interconnected plant, various ASD power electronic converter / inverter topologies, and more types of machines and mechanical drive applications than would be the case using laboratory hardware to represent the test plant. Furthermore, by interfacing the actual industrial ASD control hardware to the real-time simulation model, the proprietary algorithms within the controllers can be tested without having to request disclosure of any intellectual property from the ASD manufacturer. Hence this hybrid approach combines the benefits of, and overcomes the disadvantages associated with, the all-hardware and all-simulation test approaches, as well as allowing drive-specific and application-specific case studies to be tested using far more realistic representations of the utility power system supply network during nominal and fault conditions.

Hardware-in-loop testing approaches have been considered by others in the area of power electronics and drive systems. A signal-level hardware-in-loop testing approach has been used in 2005 by Liu et. al. [23] and as recently as 2012 by Seung et. al. [24] to successfully test and analyse the performance of power electronic control hardware. A variation of the signal-level interfaced hardware-in-loop

testing approach described above has been implemented by Steurer et. al. [25] that relies on interfacing ASD equipment to a real-time simulation model of the power system network at the power-level via high-precision amplifiers. Although this approach used by Steurer et. al. is also a full, closed-loop testing technique, the use of large power amplifiers in the interface between the simulation and the hardware introduces time delays and non-linearities into the loop [25] that can significantly reduce the accuracy of the test results and furthermore, it may even lead to simulations becoming unstable [26]. Additionally, if the power rating of the ASD to be tested is extremely high, it may be difficult to acquire a high-precision amplifier with sufficient power rating to supply the ASD during nominal and faulted conditions, although advances in the high-precision, high-power amplifiers required for such power hardware in the loop tests continue to be made [27].

### 1.2.3 Real-Time Simulation Technology

From as early as the 1920s power systems were beginning to expand into networks that were sufficiently complex to promote interest in more powerful solution methods [28]. Analysing the steady state and transient behaviour of the networks of that era was still possible using mathematical representations solved on paper. However, this method of analysis began to become too time consuming and impractical as the systems under study grew in complexity [29]. Hence, to reduce the calculation time, computing devices such as analogue simulators [28, 30] and transient network analyzers [29, 31] were developed. An analogue computing device possesses a major advantage of being able to operate in real-time because essentially it is an electrically scaled-down version of the power system under study. This implies that actual network protection and control hardware can be interfaced to, and tested on, an analogue simulator representation of a power system. However, large-scale, intricate power systems may become potentially difficult to represent using an analogue simulator since the number of electrical devices making up the simulator increases as the network being represented grows larger [32]. Furthermore, the electrically scaled down devices used in such simulators may not accurately replicate the parameters, non-linearities and dynamic performance of the actual power system components they were intended to represent [32].

To overcome the difficulties encountered in using analogue simulators, one possible approach developed by Dommel, in the 1960s, was a general solution method to determine the responses of electromagnetic transients in multiphase power system networks using a digital computer [33]. In this method, the electrical components of the power system under study are represented by mathematical models designed to be solved at discrete time intervals within a program. According to electrical conditions applied to the modelled power system, a digital computer is then used to calculate the responses of the models at every discrete time step, essentially creating a digitally-simulated power system. In the 1970s [34], the Dommel method was utilised to develop a power system simulation software package called the electromagnetic transient program (EMTP), and later developments to study AC and DC networks [35] resulted in the creation of another digital simulation program termed electromagnetic transients including DC (EMTDC<sup>TM</sup>). In contrast to using analogue simulation, digital simulation possesses an advantage of being able to solve large power system networks with the capability to accurately model the non-linearities and dynamic performance of the power system components in great detail [32]. However, unlike analogue simulators, a major limitation of digital simulation software such as EMTP and EMTDC is that it does not operate in real-time which prevents physical hardware from being tested in closed-loop together with the simulated power system [36, 37].

During the 1990s, a powerful high speed computing platform known as a real-time digital simulator (RTDS™) [37, 38] was developed to digitally simulate power system networks in real-time with the capability to rapidly exchange variables between the simulation and external hardware interfaced to it for closed-loop testing. The RTDS system combined the advantages of both analogue and digital power system simulation methods with the realisation of the concept being made possible by advances in digital signal processor technology [38] that allowed Dommel’s general solution method [33] to be solved in real-time. The RTDS platform has been used extensively for hardware-in-loop testing of power system controllers for static var compensators [39], high voltage DC transmission systems [40], thyristor controlled series capacitors [41] and a range of other utility applications as described in [42, 43]. Furthermore, several successful implementations of closed-loop testing of utility protection devices with the RTDS system have been reported in [38, 44-46]. A schematic diagram illustrating the approach used to carry out closed-loop testing of power system protection schemes on an RTDS simulator is shown in Figure 1-4.

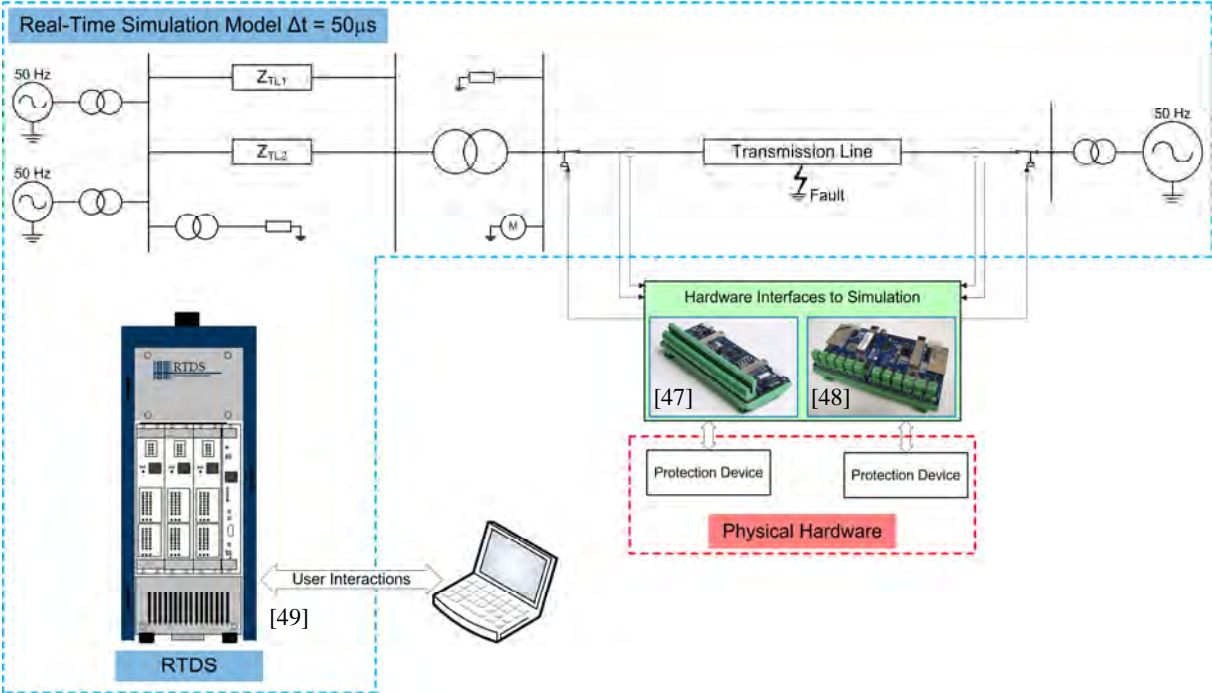


Figure 1-4: RTDS implementation of a hardware-in-loop simulation test system for protection devices.

During testing of the protection scheme, the primary plant of interest, including alternators, transformers, transmission lines and loads is simulated in real-time by the RTDS. The physical protection hardware is connected to the real-time simulation model via high speed analogue and digital input / output interfaces, hence completing the closed-loop arrangement. While the simulation is running, a user may interact with the modelled environment via a personal computer to test the

response of the protection devices to changes in operating conditions or fault scenarios. If the response is not as desired, the settings of the protection devices may be altered and re-tested using the real-time simulation. Once the required responses have been obtained from the protection scheme, a high level of confidence can be placed in its ability to operate as desired when installed in the field.

A real-time simulation model running on an RTDS is typically solved with a 50  $\mu$ s time step [38]. This level of resolution in the solution of the models representing the power system is suitable when testing interfaced utility protection and control hardware operating at conventional 50 to 60 Hz system frequencies such as in the example shown in Figure 1-4. Depending on the size and complexity of the network, the processor cards of the RTDS system are easily able to carry out the solution of the mathematical models in the power system and exchange variables in real-time between the interfaced devices and the simulated environment within 50  $\mu$ s. On the other hand, high performance motion control systems have power electronic converters with valves switched in the kilohertz frequency range by their high speed controllers. For an RTDS system to correctly simulate these fast switching valves in real-time for closed-loop controller testing, it has to be able to solve the mathematical valve models with sufficient resolution in time between changes in the converter firing pulses in order to be able to correctly simulate the response of the converters for the interfaced control hardware. Recent developments have been made [51] that enable the RTDS power electronic converter valve models to be solved at much smaller time steps (of about 2  $\mu$ s) which provides the required resolution for real-time closed-loop testing of controllers for power electronic converters switching in the kilohertz frequency range.

These recent developments that have been made for the RTDS platform have therefore expanded its potential scope into the domain of high-performance motion control systems, which in turn has inspired the research undertaken in this thesis, namely an investigation into using a real-time simulation, interfaced in closed-loop to physical ASD control hardware, as a method for studying the performance of motion control systems under dynamic conditions. The specific objectives of the research, and the procedure adopted in order to evaluate the integrity of the proposed testing method are outlined in the following section.

### 1.3 Research Objectives

The main objectives of this project are to evaluate the suitability and accuracy of the proposed testing method of interfacing real-time simulation models in closed-loop with physical ASD controllers to study the dynamic performance of motion control systems. To achieve these objectives, a structured, procedural approach was developed, which can be described as follows. Firstly, a representative study system example was devised that consists of a simple power system network supplying a high performance motion control system running at nominal load as illustrated in Figure 1-5. This study system was then implemented practically in a laboratory environment using hardware components in order to serve as a benchmark. The topology of the power system network in this study system was designed to allow a range of pre-selected controlled faults to be applied under laboratory conditions, which would in turn then produce disturbances at the supply voltage inputs to the motion control system in order to be able to test its dynamic performance.

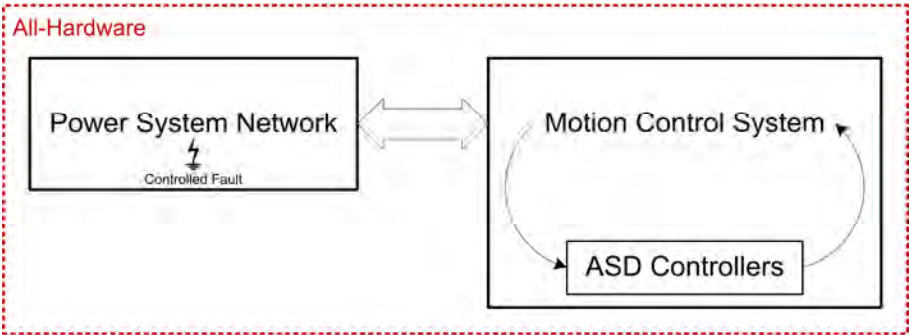
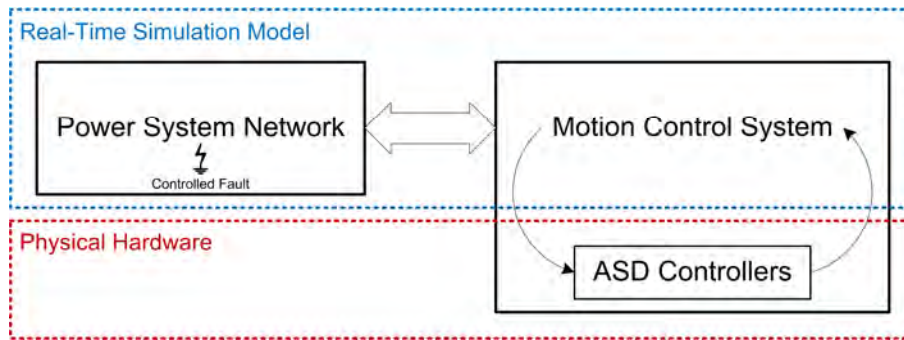


Figure 1-5: Schematic diagram of the all-hardware study system.

The pre-selected range of faults was then applied to the all-hardware implementation of the test system in the laboratory and the measured performance of the motion control system in response to these disturbances was captured. Thereafter, a second implementation of the same study system example was developed in the form of a detailed real-time simulation model of the plant in the system, and this real-time model was interfaced to the same ASD control hardware used in the first stage of the tests as illustrated in Figure 1-6.



*Figure 1-6: Schematic diagram of the hardware-in-loop simulation implementation of the study system.*

In this second implementation of the study system, all of the plant in the power system supply network and in the motion control system (with the exception of the ASD controllers) was represented using a real-time simulation model. Considerable effort was invested to ensure that each component in this real-time model of the study system was accurately modelled and contained carefully-measured parameters from the actual laboratory equipment used in the all-hardware, laboratory implementation of this study system during the first stage of the tests. The same ASD hardware controls with the controller design settings used in the first stage of the tests were then connected to this real-time model in a complete, closed-loop arrangement in the same manner as they had previously been connected to the components of the all-hardware implementation of the study system. This hardware-in-loop real-time simulation model of the study system was then subjected to the same range of pre-selected faults that were applied to the all-hardware implementation of the same system, and the performance of the hardware-in-loop simulated motion control system was captured and compared to the benchmark performance measured on the all-hardware implementation of the system. The level of agreement between the performance of the hardware-in-loop simulated system and the all-hardware benchmark system then served as the basis to evaluate the suitability and accuracy of the proposed testing method.

As an additional dimension to the research in the thesis, the comparative procedure described above was utilised to evaluate the proposed testing method for two different types of front-end converter technology that are currently used within motion control systems. The two front-end converter technologies considered are a diode rectifier, which was chosen to represent a conventional ASD, and a self-commutated active front end (AFE) converter chosen to represent a state of the art, high performance ASD.

## 1.4 Thesis Layout

The work in the main body of the thesis is arranged by chapter as outlined below.

Chapter 2 presents an introduction to the field oriented control algorithm and describes its sophisticated method of operation that enables the torque produced by a squirrel cage induction machine to be accurately dynamically controlled to achieve high-performance industrial motion control tasks.

Chapter 3 describes the design and commissioning of the all-hardware laboratory scale study system used for practical testing of the motion control system under fault conditions in subsequent investigations in the thesis.

Chapter 4 describes the development and parameterization of the real-time digital simulator model of the small-scale study system plant presented in Chapter 3. Furthermore, this chapter also includes a comparison of the measured and simulated responses of key constituent sub-sections of the laboratory-scale study system in order to verify the correctness and accuracy of each sub-model within the real-time simulator model of the study system plant as a whole.

Chapter 5 presents detailed comparisons of the results of the hardware-in-loop real-time simulator testing approach against the measured results obtained from the all-hardware implementation of the study system for the case of an ASD with a diode-rectifier front end when subjected to faults in the utility supply network.

Chapter 6 then presents similarly detailed comparisons of the results obtained from hardware-in-loop real-time simulator testing versus measured results from the all-hardware implementation of the study system for the case of an ASD with an active front end converter when subjected to utility supply network faults.

Chapter 7 discusses the main findings and technical contributions of the work, and examines, in particular, what conclusions can be reached from the evaluation of the proposed hardware-in-loop real-time simulation testing method for ASDs. The potential applications of the testing method for investigating the dynamic interactions between motion control systems, utility networks and other interconnected systems are also discussed.

## **1.5 Research Publications**

The findings of this thesis have also been presented at a number of local and international conferences [52-55].

## **1.6 Summary**

This chapter has highlighted the development of modern motion control schemes into sophisticated high performance systems engineered to achieve demanding industrial applications. This development has been possible as a result of advances in technology that have allowed complex control algorithms to be executed within the controllers of today's adjustable speed drive systems. A test method to accurately predict the performance of these complex motion control systems and their interactions with the utility network under dynamic conditions would be of immense benefit. One possible approach has been described that could realise such a test method using recent developments made in real-time simulation technology. This approach is based on simulating the power-level plant associated with the motion control system in real-time and interfacing the physical ASD control hardware at signal-level in a closed-loop arrangement with the simulated plant. Finally, the chapter has outlined the procedures to be used in the thesis to evaluate the suitability and accuracy of the proposed testing method on a practical laboratory-scale benchmark study system.

The industrial ASD control hardware procured for this project that was firstly used in the benchmark all-hardware implementation of the study system, and then later connected hardware-in-loop to the real-time simulation model of the same study system makes use of the manufacturer's own proprietary implementation of the field oriented control algorithm, the details of which are not publicly available. Therefore, to provide a sense of the sophisticated nature of a high-performance motion control algorithm of this type, the general principles of the field oriented control algorithm, which are well known, and which were initially developed by Hasse [5] and Blaschke [6], and later presented by Leonhard [56], are described in the following chapter.

## Chapter 2: An Introduction To Field Oriented Control

### 2.1 General

A high-performance adjustable speed drive system has to accurately control the torque produced by its rotating machine to match the dynamic and steady state torque requirements of the motion control task at hand. With the use of suitable energy conversion and control hardware, a separately-excited DC machine can be easily operated to produce a controlled torque using a technique that controls the currents supplied to its armature and field windings. The dynamic and steady state torque requirements of many high-performance industrial motion control tasks could be accurately matched by the torque produced by separately-excited DC machine based adjustable speed drives, hence ASDs of this type were predominantly used in industry in the past. However, an inherent disadvantage of a DC machine is the limited ability of its mechanical commutator and brushes to transfer power to its rotating conductors. This power transfer limitation of DC machines, together with their need for expensive maintenance, initiated a change toward using AC machines without commutators and brushes in adjustable speed drives [2, 57].

A squirrel cage induction machine is a superior alternative to a DC machine since it uses electromagnetic induction to transfer power to its rotating conductors, and not a separate power source connected to the rotating conductors via brushgear. Relative to the DC machine, the squirrel cage induction machine is a cost-effective, low-maintenance and robust option for adjustable speed drives provided that the torque produced by the squirrel cage induction machine can, as in the case of the separately-excited DC machine, be accurately dynamically controlled to meet the torque requirements of high-performance motion control tasks. In comparison to a DC machine, a squirrel cage induction machine with an equivalent power rating generally has a higher maximum torque, a higher maximum speed, a lower total mass and a smaller rotational inertia. Therefore, if the torque produced by a squirrel cage induction machine can be accurately dynamically controlled, the resulting adjustable speed drive would obviously outperform an adjustable speed drive based on a DC machine with an equivalent power rating.

Field oriented control [5, 6] is one possible algorithm that enables the torque produced by a squirrel cage induction machine to be accurately dynamically controlled to achieve high-performance motion control tasks. To understand the method of operation of the field oriented control algorithm when applied to a squirrel cage induction machine, it is imperative to firstly understand the manner in which a squirrel cage induction machine operates to produce torque. Therefore, the next section discusses the

construction and method of operation of a squirrel cage induction machine in general. Thereafter, subsequent sections of the chapter then present a mathematical model of a squirrel cage induction machine and describe the method of operation of the field oriented control algorithm.

## 2.2 Torque Production in a Squirrel Cage Induction Machine

Figure 2-1 shows a three-phase, two-pole, squirrel cage induction machine that has been partially dismantled to show the internal components and construction of this type of machine.

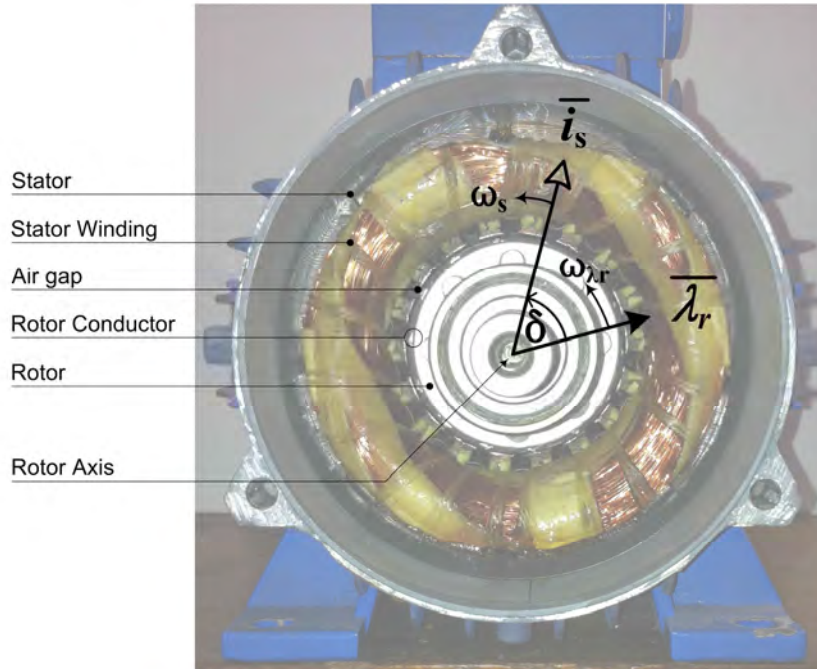


Figure 2-1: Partially dismantled, 370 W, three-phase, two-pole, squirrel cage induction machine [58].

A three-phase, squirrel cage induction machine contains a stator winding and a set of rotor conductors which are both involved in the production of torque. The stator of a squirrel cage induction machine is generally made up of a magnetic core structure with a cylindrical inner surface that has slots. The slots within the stator magnetic core are evenly spaced around the inner circumference of the stator, and they span the complete length of the stator core. The stator winding is made up of a set of three individual phase windings that are physically and electrically identical to each other. The stator phase windings are symmetrically distributed within the slotted stator magnetic core in such a way that the axis of symmetry of each phase winding is displaced by  $120^\circ$  in space from the other two phase windings. The rotor of a squirrel cage induction machine is generally made up of a shaft that is rigidly attached to a cylindrical magnetic core structure which houses the rotor conductors. The cylindrical rotor magnetic core has slots that are evenly spaced around its outer circumference, and the slots span the complete length of the rotor core. The conductors within the rotor are generally made up of a number of aluminium bars and two aluminium end rings. The rotor bars are symmetrically distributed within the slotted rotor core and they are short-circuited at both ends by the end rings to form a three-phase rotor circuit. The rotor of the induction machine is mechanically suspended on bearings inside

the stator so that the outer surface of the cylindrical rotor core is evenly spaced from the inner cylindrical stator surface. The tubular-shaped clearance between the stator and rotor cores is typically termed the air gap of the induction machine. Furthermore, the axis of rotation of the rotor is termed the rotor axis as shown in Figure 2-1.

When a balanced, three-phase voltage source with a frequency  $\omega_o$  is connected to the stator winding of a squirrel cage induction machine, balanced, three-phase currents are drawn by the stator winding. The resulting current distribution in the stator winding around the periphery of the air gap of the induction machine produces an approximately sinusoidal magnetomotive force (MMF) distribution in the air gap. Consequently, the maximum and minimum points of this stator MMF distribution are spatially displaced by  $180^\circ$  from each other around the circumference of the air gap. Due to the displacement in *space* of  $120^\circ$  between the stator phase windings and the displacement in *time* of  $120^\circ$  between the three-phase stator voltages and winding currents, the sinusoidal stator MMF distribution rotates around the air gap of the induction machine about its rotor axis at an angular frequency  $\omega_s$  which is equal to the frequency  $\omega_o$  of the three-phase source voltages. The frequency of rotation  $\omega_s$  of the stator MMF is referred to as the synchronous frequency (or synchronous speed) of the machine.

In order to represent the stator MMF distribution in the air gap of an induction machine diagrammatically, a space-vector termed the stator current space vector  $\bar{i}_s$  [59] can be used as shown on the picture of the induction machine in Figure 2-1. In the space-vector diagram superimposed on the picture of the machine windings shown in Figure 2-1, the length of the stator current space vector  $\bar{i}_s$  represents the amplitude of the currents flowing in all three phases of the stator winding, and the angle of the stator current space vector represents the spatial position of the maximum in the stator MMF wave in the air gap of the induction machine. Furthermore, the stator current space vector has an angular speed of rotation  $\omega_s$  corresponding to the angular speed of rotation of the stator MMF distribution.

As a result of the MMF distribution created by the stator winding currents, a magnetic flux distribution is created by the stator that links with other elements of the machine. Some of the magnetic flux created by the stator leaks around the turns of the stator windings, but most of this flux passes through the air gap and links with the conductors of the rotor circuit, and is therefore referred to as the mutual flux. Since this magnetic flux is produced by the stator MMF distribution that rotates around the air gap at synchronous speed, this flux also rotates around the air gap at synchronous speed about the rotor axis. If a load torque is applied to the shaft of the rotor such that the angular speed of the rotor

$\omega_{re}$  becomes less than synchronous speed ( $\omega_{re} < \omega_s$ ), the short-circuited bars on the rotor then move relative to the synchronously-rotating mutual flux which results in currents being induced in them. The speed of the relative motion between the rotor bars and the stator MMF wave is referred to as the slip speed, and results in the induced currents in the rotor circuit being at slip frequency  $\omega_{slip} = \omega_s - \omega_{re}$ .

The resulting slip-frequency currents in the rotor set up sinusoidal rotor MMF and flux distributions that rotate at slip frequency relative to the rotor conductors in which they are established. As with the stator flux, some of the flux established in the rotor by its own currents leaks around the rotor conductors but most of this flux contributes to the mutual flux passing through the air gap that then links both the stator and rotor conductors. The rotor flux wave rotates in space about the rotor axis at a frequency  $\omega_{\lambda r}$  given by the sum of the slip frequency  $\omega_{slip}$  of the currents in the rotor conductors and the angular speed of rotation of the conductors  $\omega_{re}$ , such that  $\omega_{\lambda r} = \omega_{slip} + \omega_{re}$ .

The total magnetic flux linking the rotor conductors of the induction machine can be represented diagrammatically by a rotating space vector referred to as the rotor flux linkage space vector  $\overline{\lambda}_r$  [59] as shown in Figure 2-1. The length of the rotor flux linkage space vector in Figure 2-1 represents the amplitude of the magnetic flux wave linking the three-phase rotor circuit, and the angle of this space vector represents the spatial orientation of the magnetic flux wave linking the rotor circuit. Furthermore, the rotor flux linkage space vector has an angular speed of rotation  $\omega_{\lambda r}$  corresponding to the angular speed of rotation of the rotor flux wave.

As previously mentioned, when a load torque is applied to a squirrel cage induction machine, the rotor has to slow down relative to the stator current space vector  $\overline{i}_s$  and the associated MMF wave it produces in order to allow currents to be induced in the rotor conductors and thus to enable the required electromagnetic counter torque to be produced within the machine as a result of the interaction between the stator current and rotor flux linkage space vectors. As the load torque applied to the shaft of the machine increases, the rotor slows down further and currents are induced in the rotor in such a manner that the magnitude of the rotor flux linkage space vector becomes larger, and its angular orientation is further displaced relative to the axis of the stator current space vector  $\overline{i}_s$  and its associated MMF wave.

The angle between the rotor flux linkage space vector  $\overline{\lambda}_r$  and the stator current space vector  $\overline{i}_s$  (and hence stator MMF) is referred to as the torque angle  $\delta$  as seen in Figure 2-1.

The instantaneous electromagnetic torque produced by the induction machine can be expressed mathematically in terms of the stator current and rotor flux linkage space vectors as [59]:

$$T_{em} = k \frac{L_m}{L_{22}} (\overline{\lambda_r} \times \overline{i_s}) \quad (2-1a)$$

$$T_{em} = k \frac{L_m}{L_{22}} |\overline{\lambda_r}| |\overline{i_s}| \sin \delta \quad (2-1b)$$

where:

$T_{em}$  is the instantaneous electromagnetic torque produced by the induction machine [Nm]

$k$  is a constant dependent on the design parameters of the machine

$L_m$  is the per phase mutual inductance of the machine [H]

$L_{22}$  is the per phase self inductance of the rotor circuit of the machine [H],

where  $L_{22} = L_m + L_2$

$L_2$  is the per phase leakage inductance of the rotor circuit of the machine [H]

$\overline{\lambda_r}$  is the rotor flux linkage space vector [Wb-t]

$\overline{i_s}$  is the stator current space vector [A]

$\delta$  is the angle between the rotor flux linkage and stator current space vectors [rad].

The value of  $k$  for a squirrel cage induction machine is constant and, typically, when the machine is operated within its nominal ratings, its inductances  $L_m$  and  $L_{22}$  are also constant. Therefore, according to Equation (2-1b) in order to be able to control the torque produced by a squirrel cage induction machine, it is necessary to be able to influence its torque angle  $\delta$  and the magnitudes of its rotor flux linkage and stator current space vectors. When some constant value of load torque is applied to the shaft of an induction machine, the magnitudes of its rotor flux linkage and stator current space vectors, and the torque angle between them adjust naturally according to the characteristics of the machine to produce a constant amount of electromagnetic counter torque to match the load torque. Under steady state conditions the magnitudes of the stator current space vector  $\overline{i_s}$  and rotor flux linkage space vector  $\overline{\lambda_r}$ , and the angle  $\delta$  between them are all constant, implying that  $\overline{i_s}$  and  $\overline{\lambda_r}$  rotate at the same speed ( $\omega_s = \omega_{\lambda_r}$ ). However, under non steady-state conditions, the magnitudes of the space vectors  $\overline{i_s}$  and  $\overline{\lambda_r}$  are no longer constant and their natural response exhibits under-damped oscillatory dynamics. Likewise, under transient conditions, the angular speed of the rotor flux linkage space vector exhibits

under-damped natural oscillations about the synchronous speed  $\omega_s$ , which results in under-damped oscillations in the torque angle. Hence, according to Equation (2-1b), these under-damped oscillations in  $|\overline{\lambda}_r|$ ,  $|\overline{i}_s|$  and  $\delta$  under dynamic conditions result in the torque produced by the induction machine likewise naturally exhibiting under-damped oscillatory dynamics. An induction machine could not be used to achieve high-performance motion control tasks if the oscillatory dynamics in its torque were to vary substantially from the value of torque demanded. However, if the induction machine is operated under the field oriented control algorithm, its torque angle and the magnitudes of its rotor flux linkage and stator current space vectors are directly or indirectly regulated in such a way as to make the machine produce torque, in a controlled manner, without any unintended oscillations, to match dynamic variations in a demanded torque profile. Hence, an induction machine operating under the field oriented control algorithm can be used to achieve high-performance motion control tasks.

The following section presents a mathematical model of a squirrel cage induction machine that represents its dynamic behaviour in sufficient detail for high performance motion control studies. This dynamic model is then used in a subsequent section to discuss the method of operation of the field oriented control algorithm.

### 2.3 A Mathematical Model of the Squirrel Cage Induction Machine

This section presents a space vector model of a squirrel cage induction machine [59] that can suitably represent the dynamic and steady-state behaviour of the machine. The following simplifying assumptions were made in deriving the model. Firstly, the magnetic materials used within the induction machine are assumed to have an infinite permeability. Secondly, the tubular-shaped air gap between the inner cylindrical surface of the stator magnetic core and the outer cylindrical surface of the rotor magnetic core is assumed to have a uniform thickness. Thirdly, the distributed three-phase stator windings and rotor circuits in the induction machine are assumed to be perfectly symmetrical and balanced. Finally, the magnetomotive force distributions produced in the air gap by each of the three stator phase windings and the three rotor phase circuits (as a result of the currents flowing in the stator phase windings and rotor phase circuits) are assumed to be sinusoidal.

Generally, a set of complex coordinate axes, fixed to a frame of reference, is required to express the space vectors of a rotating machine. In the case of an induction machine, these complex axes may be fixed to one of the following frames of reference: the rotor reference frame; the synchronous reference frame; the stationary reference frame. As implied by the names, the rotor reference frame rotates at the angular speed of the rotor, the synchronous reference frame rotates at the angular speed  $\omega_s$  of the stator MMF distribution, and the stationary reference frame is fixed in space and does not rotate. In the case of the model presented in this section, the set of complex axes chosen to represent the space vectors is fixed to the synchronous reference frame because the resulting space vector model of the induction machine is then better suited to the task of explaining the field oriented control algorithm in the next section.

The electrical circuits on the stator and rotor of a squirrel cage induction machine may be represented as concentrated coils which are shown in the schematic diagram of the machine in Figure 2-2.

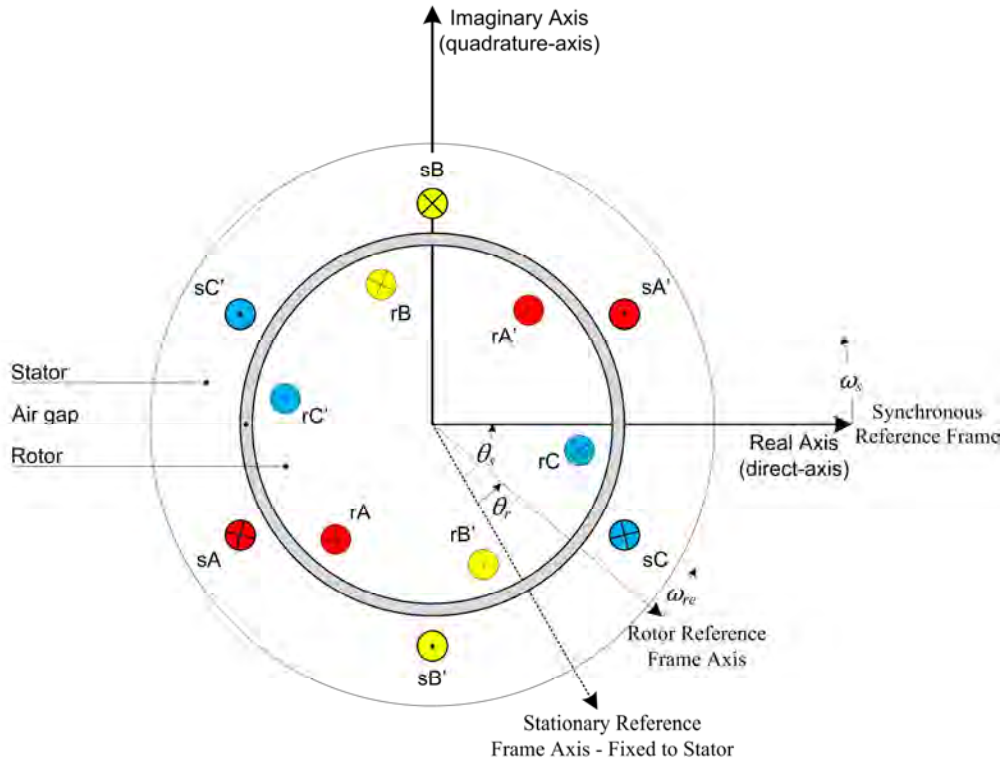


Figure 2-2: Schematic diagram of a squirrel cage induction machine and the various reference frames.

In the diagram in Figure 2-2:

sA to sA' is the concentrated coil representing the phase A stator winding

sB to sB' is the concentrated coil representing the phase B stator winding

sC to sC' is the concentrated coil representing the phase C stator winding

rA to rA' is the concentrated coil representing the phase A rotor circuit

rB to rB' is the concentrated coil representing the phase B rotor circuit

rC to rC' is the concentrated coil representing the phase C rotor circuit

$\theta_s$  is the angle between the stationary reference frame axis and the direct-axis of the space vector reference frame [rad]

$\theta_r$  is the angle between the stationary reference frame axis and the rotor reference frame axis [rad]

$\omega_s$  is the synchronous speed [rad/s]

$\omega_{re}$  is the angular speed of the rotor [rad/s].

The stator voltage space vector  $\bar{v}_s$  of a squirrel cage induction machine can be expressed in terms of the instantaneous phase voltages applied to its stator winding as follows:

$$\bar{v}_s = \sqrt{\frac{2}{3}} (v_{sA}(t) + av_{sB}(t) + a^2v_{sC}(t)) \quad (2-2)$$

where:

$\bar{v}_s$  is the stator voltage space vector [V]

$v_{sA}(t)$ ,  $v_{sB}(t)$ , and  $v_{sC}(t)$  are the instantaneous phase A, B, and C voltages of the stator winding respectively [V]

$a$  is the complex operator,  $e^{j2\pi/3}$ .

Furthermore, the stator current space vector  $\bar{i}_s$  can be expressed in terms of the instantaneous phase currents in the stator as follows:

$$\bar{i}_s = \sqrt{\frac{2}{3}} (i_{sA}(t) + ai_{sB}(t) + a^2i_{sC}(t)) \quad (2-3)$$

where:

$\bar{i}_s$  is the stator current space vector [A]

$i_{sA}(t)$ ,  $i_{sB}(t)$ , and  $i_{sC}(t)$  are the instantaneous phase A, B, and C stator currents respectively [A].

With respect to the short-circuited rotor conductors of a squirrel cage induction machine, the rotor voltage space vector  $\bar{v}_r$ , and the rotor current space vector  $\bar{i}_r$  can be expressed as:

$$\bar{v}_r = \sqrt{\frac{2}{3}} (v_{rA}(t) + av_{rB}(t) + a^2v_{rC}(t)) = 0 \quad (2-4)$$

$$\bar{i}_r = \sqrt{\frac{2}{3}} (i_{rA}(t) + ai_{rB}(t) + a^2i_{rC}(t)) \quad (2-5)$$

where:

$\bar{v}_r$  is the rotor voltage space vector [V]

$v_{rA}(t)$ ,  $v_{rB}(t)$ , and  $v_{rC}(t)$  are the instantaneous phase A, B, and C rotor voltages respectively [V]

$\bar{i}_r$  is the rotor current space vector [A]

$i_{rA}(t)$ ,  $i_{rB}(t)$ , and  $i_{rC}(t)$  are the instantaneous phase A, B, and C rotor currents respectively [A].

The stator flux linkage and rotor flux linkage space vectors of the machine can be expressed as:

$$\bar{\lambda}_s = L_{11}\bar{i}_s + L_m\bar{i}_r \quad (2-6)$$

$$\bar{\lambda}_r = L_{22}\bar{i}_r + L_m\bar{i}_s \quad (2-7)$$

where:

$\bar{\lambda}_s$  is the stator flux linkage space vector [Wb-t]

$L_{11}$  is the per phase self inductance of the stator winding [H], where  $L_{11} = L_m + L_1$

$L_m$  is the per phase mutual inductance of the machine [H]

$L_1$  is the per phase leakage inductance of the stator winding [H]

$\bar{\lambda}_r$  is the rotor flux linkage space vector [Wb-t]

$L_{22}$  is the per phase self inductance of the rotor circuit [H], where  $L_{22} = L_m + L_2$

$L_2$  is the per phase leakage inductance of the rotor circuit [H].

The space vector model of the machine can then be expressed by the following stator and rotor voltage equations in the synchronous frame of reference:

$$\bar{v}_s = R_1\bar{i}_s + \frac{d}{dt}(\bar{\lambda}_s) + j\omega_s\bar{\lambda}_s \quad (2-8)$$

$$\bar{v}_r = R_2\bar{i}_r + \frac{d}{dt}(\bar{\lambda}_r) + j(\omega_s - \omega_{re})\bar{\lambda}_r = 0 \quad (2-9)$$

where:

$R_1$  and  $R_2$  are the per phase stator and rotor resistances of the machine respectively [ $\Omega$ ]

$\omega_s$  is the synchronous speed [rad/s]

$\omega_{re}$  is the angular speed of the rotor [rad/s].

An expression for the instantaneous electromagnetic torque produced by the machine, which was presented previously in Equation (2-1a), is repeated here for completeness:

$$T_{em} = k \frac{L_m}{L_{22}} (\bar{\lambda}_r \times \bar{i}_s) \quad (2-10)$$

where:

$T_{em}$  is the instantaneous electromagnetic torque [Nm]

$k$  is a constant dependent on the machine design.

The space vectors used to represent the machine's variables may also be resolved into their respective real (direct-axis) and imaginary (quadrature-axis) components as follows:

$$\bar{v}_s = v_{ds} + jv_{qs} \quad (2-11)$$

$$\bar{i}_s = i_{ds} + ji_{qs} \quad (2-12)$$

$$\bar{\lambda}_s = \lambda_{ds} + j\lambda_{qs} \quad (2-13)$$

$$\bar{v}_r = v_{dr} + jv_{qr} \quad (2-14)$$

$$\bar{i}_r = i_{dr} + ji_{qr} \quad (2-15)$$

$$\bar{\lambda}_r = \lambda_{dr} + j\lambda_{qr} \quad (2-16)$$

where:

$v_{ds}$  and  $v_{qs}$  are the direct-axis and quadrature-axis components of the stator voltage space vector respectively [V]

$i_{ds}$  and  $i_{qs}$  are the direct-axis and quadrature-axis components of the stator current space vector respectively [A]

$\lambda_{ds}$  and  $\lambda_{qs}$  are the direct-axis and quadrature-axis components of the stator flux linkage space vector respectively [Wb-t]

$v_{dr}$  and  $v_{qr}$  are the direct-axis and quadrature-axis components of the rotor voltage space vector respectively [V]

$i_{dr}$  and  $i_{qr}$  are the direct-axis and quadrature-axis components of the rotor current space vector respectively [A]

$\lambda_{dr}$  and  $\lambda_{qr}$  are the direct-axis and quadrature-axis components of the rotor flux linkage space vector respectively [Wb-t]

By substituting Equations (2-11) to (2-13) into Equation (2-8), and resolving the resultant complex equation for the stator voltage space vector into its real (direct-axis) and imaginary (quadrature-axis) components, the following equations are obtained:

$$v_{ds} = R_1 i_{ds} + p\lambda_{ds} - \omega_s \lambda_{qs} \quad (2-17)$$

$$v_{qs} = R_1 i_{qs} + p\lambda_{qs} + \omega_s \lambda_{ds} \quad (2-18)$$

where:

$p$  is the differential operator  $\frac{d}{dt}$ .

Furthermore, by substituting Equations (2-14) to (2-16) into Equation (2-9), and resolving the resultant complex equation for the rotor voltage space vector into its real (direct-axis) and imaginary (quadrature-axis) components, the following equations are obtained:

$$v_{dr} = R_2 i_{dr} + p\lambda_{dr} - (\omega_s - \omega_{re})\lambda_{qr} = 0 \quad (2-19)$$

$$v_{qr} = R_2 i_{qr} + p\lambda_{qr} + (\omega_s - \omega_{re})\lambda_{dr} = 0 \quad (2-20)$$

By substituting Equations (2-12), (2-13) and (2-15) into Equation (2-6), and resolving the resultant complex equation for the stator flux linkage space vector into its real (direct-axis) and imaginary (quadrature-axis) components, the following equations are obtained:

$$\lambda_{ds} = L_{11} i_{ds} + L_m i_{dr} \quad (2-21)$$

$$\lambda_{qs} = L_{11} i_{qs} + L_m i_{qr} \quad (2-22)$$

Furthermore, by substituting Equations (2-12), (2-15) and (2-16) into Equation (2-7), and resolving the resultant complex equation for the rotor flux linkage space vector into its real (direct-axis) and imaginary (quadrature-axis) components, the following equations are obtained:

$$\lambda_{dr} = L_{22}i_{dr} + L_m i_{ds} \quad (2-23)$$

$$\lambda_{qr} = L_{22}i_{qr} + L_m i_{qs} \quad (2-24)$$

Finally, by substituting Equations (2-12) and (2-16) into Equation (2-10), the instantaneous electromagnetic torque produced by the machine can be expressed in terms of the direct- and quadrature-axis components of the relevant space vectors as:

$$T_{em} = k \frac{L_m}{L_{22}} (i_{qs}\lambda_{dr} - i_{ds}\lambda_{qr}) \quad (2-25)$$

Equations (2-17) to (2-25) are a direct- and quadrature-axis component representation of the space vector model of a squirrel cage induction machine, and this representation of the space vector model is also known as the two-axis model of the machine.

This two-axis model of the induction machine can be represented in the form of a signal flow diagram as shown in Figure 2-3.

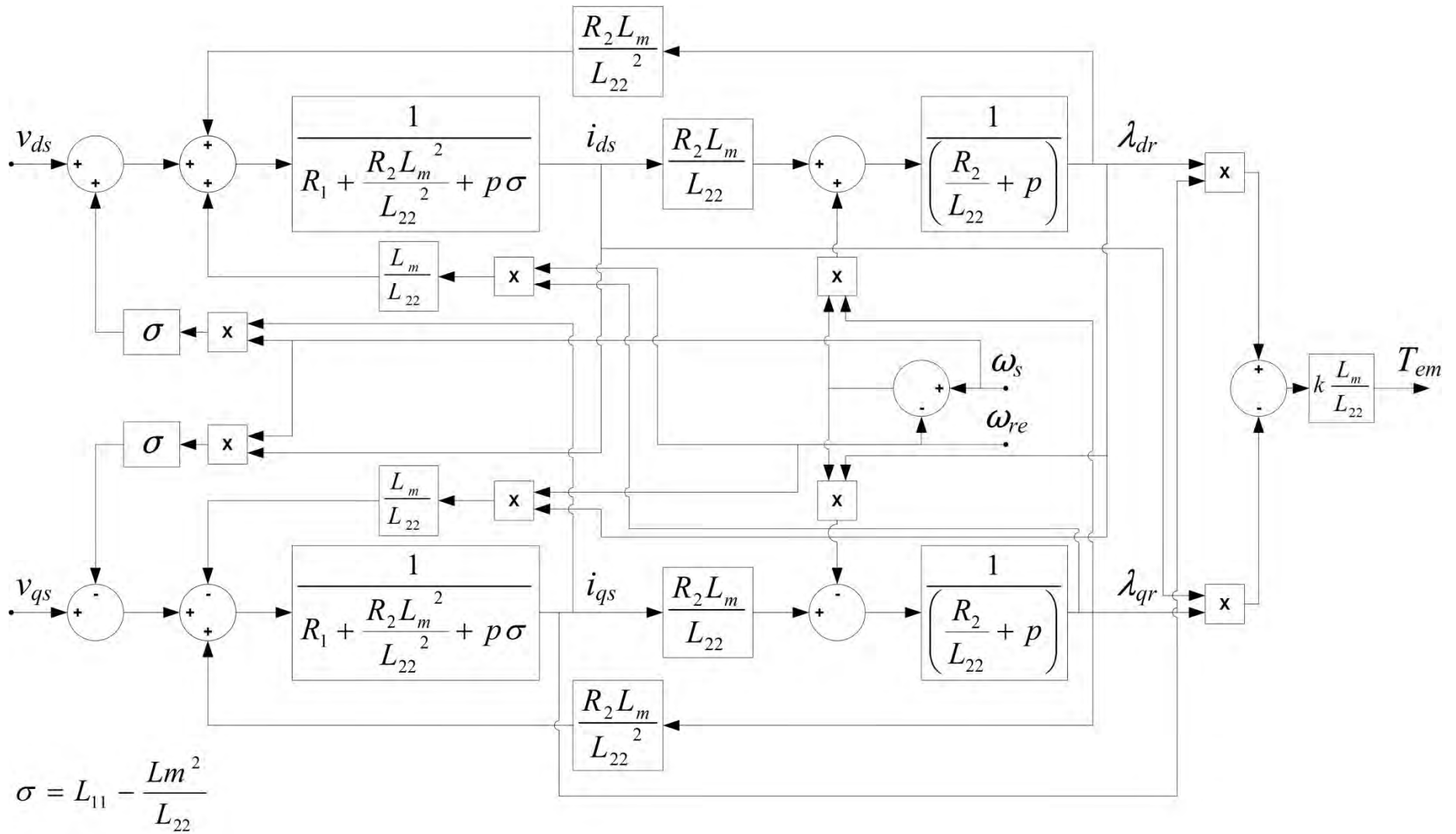


Figure 2-3: Signal flow representation of the two-axis dynamic model of a squirrel cage induction machine.

The representation of the dynamic model of the induction machine in signal flow format shown in Figure 2-3 has the advantage of demonstrating the mechanism of electromagnetic torque production in the machine in terms of the direct- and quadrature-axis components  $v_{ds}$  and  $v_{qs}$  of its stator voltage space vector, the angular speed  $\omega_{re}$  of its rotor, and the synchronous speed  $\omega_s$ . Choosing to express the torque of the machine in terms of these particular variables is done intentionally in order to allow this signal flow diagram representation of the machine to be adapted in order to explain the principles of, and method of operation of field oriented control in the next section.

## 2.4 The Method of Operation of the Field Oriented Control Algorithm

As discussed previously, under transient conditions, the torque produced by an uncontrolled induction machine is characterised by under-damped oscillatory dynamic components because of the presence of similar such components in its rotor flux linkage and stator current space vectors, and hence in its torque angle, under transient conditions. However, the expression for the electromagnetic torque of the induction machine shown in Equation (2-1b) suggests that one possible approach through which these torque oscillations could be controlled is to regulate, directly or indirectly, the magnitude of the machine's rotor flux linkage space vector  $|\overline{\lambda}_r|$ , and the product  $|\overline{i}_s| \sin \delta$  of its stator current space vector magnitude and the sine of its torque angle. Indeed, the principle underlying the method of field oriented control of the induction machine is to achieve dynamic control of the machine's torque by influencing (regulating) these two components  $|\overline{\lambda}_r|$  and  $|\overline{i}_s| \sin \delta$  [56]. In order to explain the method of field oriented control, an approach developed in [60] can be used as follows.

The first step of the field oriented control algorithm is to dynamically regulate the slip frequency  $\omega_{\text{slip}}$  of the induction machine in such a way that the machine's rotor flux linkage space vector becomes aligned to the direct-axis component of its stator current space vector, as illustrated in Figure 2-4.

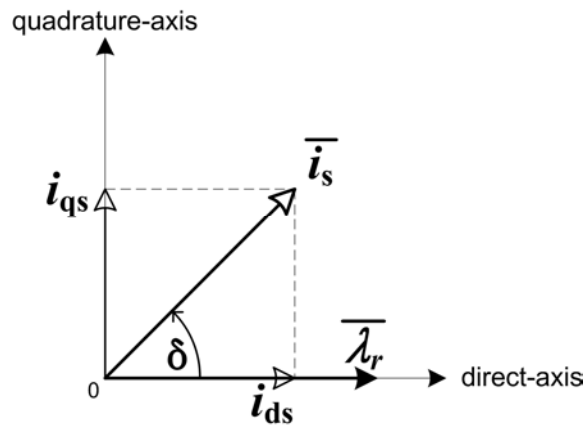


Figure 2-4: A space vector diagram showing  $\overline{\lambda}_r$  aligned to  $i_{ds}$ .

The consequence of achieving this particular orientation of the machine's rotor flux linkage space vector is that the angle of the stator current space vector with respect to the direct-axis of the coordinate frame used to measure and control the machine variables now corresponds directly to the torque angle  $\delta$  of the machine; this in turn means that the expression for the quadrature-axis component of the stator current space vector  $i_{qs}$  reduces to:

$$i_{qs} = \bar{i}_s \sin \delta \quad (2-26a)$$

$$\Rightarrow |i_{qs}| = |\bar{i}_s| \sin \delta \quad (2-26b)$$

Equation (2-26b) shows that under these conditions a regulator designed simply to control the magnitude of the quadrature-axis component of the stator current space vector would, in effect, be achieving the control of the term  $|\bar{i}_s| \sin \delta$  required as one of the two conditions for successful field oriented control.

A further consequence of achieving the particular orientation of the machine's rotor flux shown in Figure 2-4 is that the rotor flux linkage space vector  $\bar{\lambda}_r$  lies entirely along the direct-axis of the coordinate frame being used, such that  $\bar{\lambda}_r$  then has no component along the quadrature-axis, that is:

$$\bar{\lambda}_r = \lambda_{dr} \text{ and } \lambda_{qr} = 0 \quad (2-27a)$$

$$\Rightarrow |\bar{\lambda}_r| = |\lambda_{dr}| \quad (2-27b)$$

Figure 2-5 shows a diagram of the two-axis dynamic model of the induction machine in signal flow form annotated in such a way as to highlight in blue the impact on the machine's dynamics of achieving the required orientation of  $\bar{\lambda}_r$  such that  $\lambda_{qr} = 0$ .

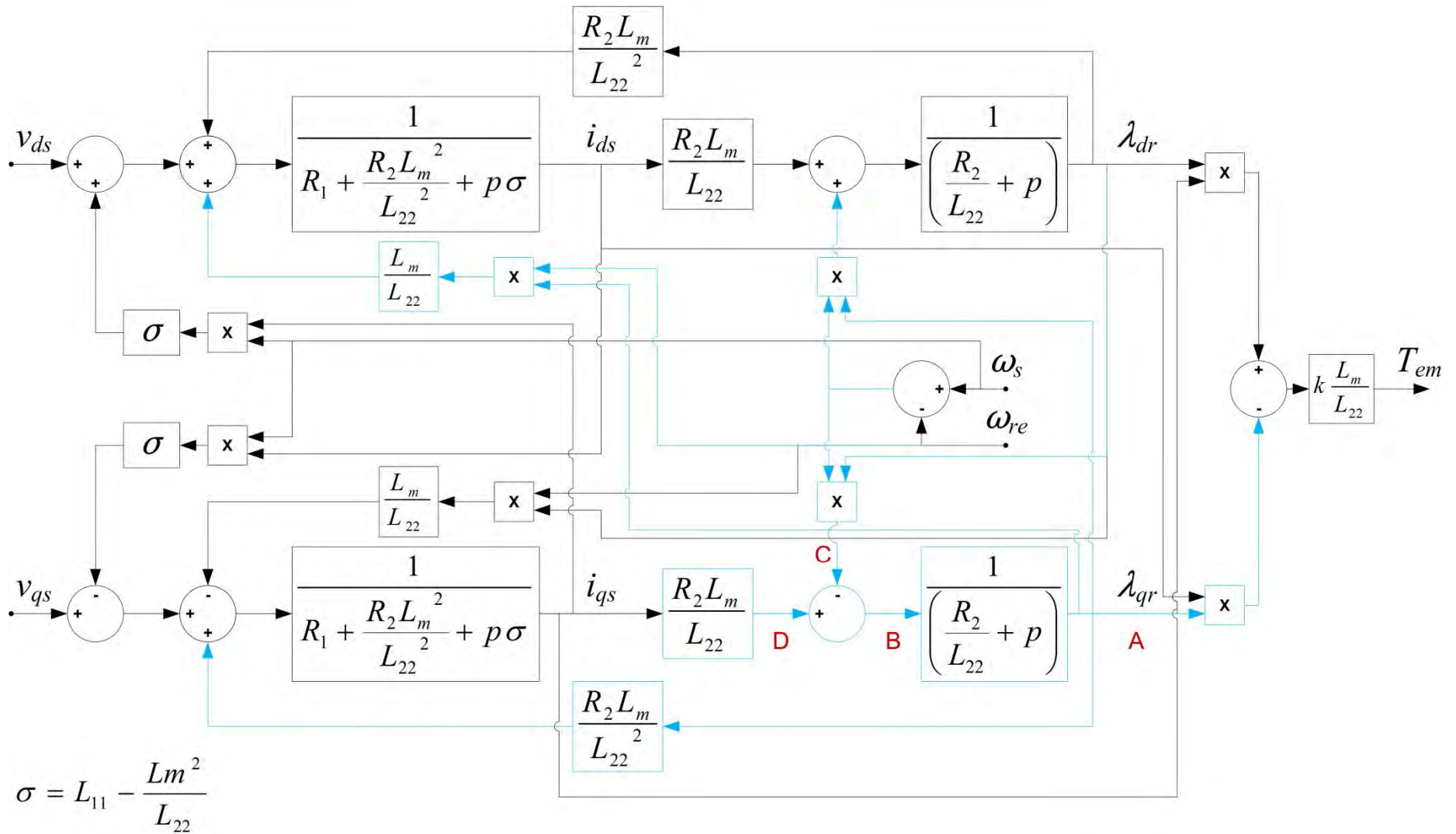


Figure 2-5: Signal flow representation of a squirrel cage induction machine with signal paths of  $\lambda_{qr}$  highlighted in blue, (adapted from [60]).

Figure 2-5 illustrates that by orienting  $\overline{\lambda}_r$  in such a way that  $\lambda_{qr} = 0$ , the signals at point A and B in the dynamic model of the machine become zero; this in turn requires that the inputs C and D to the preceding summer must remain equal. By equating the expressions for the signals at these points C and D in the signal flow representation of the machine's dynamic model, it is possible to gain insight into the conditions needed to achieve this orientation of the rotor flux linkages as follows:

$$C = D \quad (2-28a)$$

$$\Rightarrow (\omega_s - \omega_{re})\lambda_{dr} = i_{qs} \frac{R_2 L_m}{L_{22}} \quad (2-28b)$$

$$\Rightarrow \omega_{slip} = (\omega_s - \omega_{re}) = \frac{i_{qs} R_2 L_m}{\lambda_{dr} L_{22}} \quad (2-28c)$$

The Equation (2-28c) above that results from this analysis is an expression for the value of the slip frequency required in order to achieve the desired alignment of  $\overline{\lambda}_r$  to  $i_{ds}$ . If the condition shown in Equation (2-28c) can be maintained under dynamic conditions by an external controller, then  $\lambda_{qr}$  can be assumed to be zero. The diagram in Figure 2-6 then shows how the dynamics of the induction machine are simplified if this condition of  $\lambda_{qr} = 0$  in the machine is maintained by a suitable external controller, which then effectively removes all the dynamic paths that were highlighted in blue in the previous diagram in Figure 2-5.



The diagram in Figure 2-6 illustrates the simplification of the induction machine's dynamic characteristics that arises by maintaining the orientation of the machine's rotor flux so as to meet the first part of the requirements of the field oriented control algorithm. However, the diagram also illustrates that the direct- and quadrature-axis variables of the machine are still cross coupled (that is the behaviour of the direct-axis stator current is affected by the behaviour of the quadrature-axis stator current, and vice versa). The second objective of the field oriented control algorithm is to decouple the internal dynamics between the direct- and quadrature-axis variables of the induction machine so that the machine effectively appears as, and can be controlled in a manner similar to, a DC machine.

In practice the decoupling of the direct-axis and quadrature-axis dynamics of the induction machine is achieved by means of sufficiently high-bandwidth closed-loop control of the stator currents of the machine, in conjunction with pre-compensating controllers, such that the currents  $i_{ds}$  and  $i_{qs}$  on the direct and quadrature axes in the diagrammatic representation of the machine's dynamics in Figure 2-6 appear as independently-regulated current source inputs. Under these assumptions, the dynamics of the machine associated with its stator voltage equations (highlighted in red and green in Figure 2-6) fall away and the dynamic model of the machine then appears as shown in Figure 2-7.

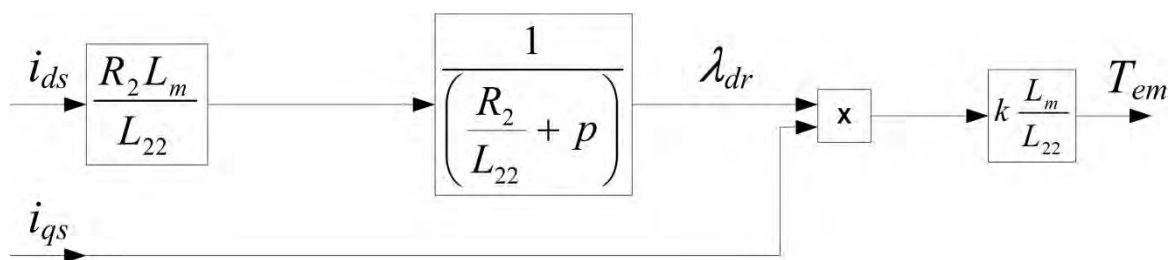


Figure 2-7: Signal flow diagram representation of the induction machine under field oriented control with closed-loop stator current and pre-compensation control applied (adapted from [60]).

Figure 2-7 shows that the dynamic characteristics of an induction machine under field oriented control resemble those of a separately-excited DC machine. The approach typically used to achieve high dynamic torque control in separately-excited DC machines is to maintain a constant value of field flux, and to control the machine's torque by means of closed-loop armature current control. With respect to an induction machine under field oriented control, the aforementioned approach used to control the torque of separately-excited DC machines is analogous to maintaining a constant magnitude of the rotor flux linkage space vector  $\overline{\lambda_r}$  of the induction machine (and hence of  $\lambda_{dr}$ , since  $\overline{\lambda_r}$  is controlled to lie along the direct-axis) by maintaining a constant value of direct-axis stator

current  $i_{ds}$ ; the torque produced by the induction machine is then controlled by means of controlling the quadrature-axis component of the stator current  $i_{qs}$ .

Equation (2-29) and Figure 2-8 below show how the dynamic characteristics of the induction machine under field oriented control are further simplified when the aforementioned approach to torque control, analogous to that used in separately-excited DC machines, is then applied.

$$\overline{\lambda_r} = \lambda_{dr} = L_m i_{ds} \quad (2-29a)$$

$$\Rightarrow |\overline{\lambda_r}| = |\lambda_{dr}| = L_m |i_{ds}| \quad (2-29b)$$

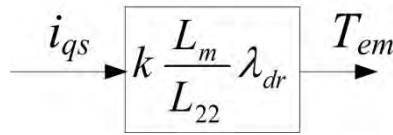


Figure 2-8: Dynamic structure of the induction machine under field oriented control and constant rotor flux linkages (adapted from [60]).

Figure 2-8 shows that under field oriented control the electromagnetic torque of the machine can be controlled in a linear fashion, directly by means of controlling the quadrature-axis component of the stator current  $i_{qs}$  (or in the full space-vector notation of Equation (2-1b), directly by means of  $|\overline{i_s}| \sin \delta$ ) for a given amplitude of rotor flux linkages  $|\overline{\lambda_r}| = |\lambda_{dr}|$  (set by means of some constant, controlled value of the direct-axis component of the stator current  $i_{ds}$ ).

## **2.5 Summary**

This chapter has described the manner in which torque is produced in a squirrel cage induction machine. Furthermore, with the use of the two-axis dynamic model of the induction machine, the method of operation of the field oriented control algorithm has been shown. A general understanding of the field oriented control algorithm is important because the industrial ASD system whose performance is being studied in this thesis makes use of its manufacturer's own proprietary implementation of the field oriented control algorithm.

The following chapter presents a description of this industrial ASD system and describes the design and commissioning of its hardware components and controllers to suit the specific laboratory-scale study system developed for the tests in this thesis. The chapter then reviews the layout and hardware components used to make up the rest of the plant in this study system, in particular the upstream power system supply network needed to be able to apply faults, and hence create voltage disturbances at the front end of the ASD, under controlled and repeatable conditions.

## **Chapter 3: The All-Hardware Laboratory-Scale Implementation Of The Study System**

### **3.1 Introduction**

Chapter 1 has explained that the main objectives of this thesis are to evaluate a particular approach to testing the dynamic performance of adjustable speed drives (ASDs) using hardware-in-loop (HIL) connection of the drive controls to a real-time simulator model of the drive plant and of the upstream power system supplying it. Chapter 1 also explained that, in order to evaluate this HIL testing approach, identical tests are to be carried out on an all-hardware laboratory-scale implementation of the same study system for direct comparison.

This chapter now describes the detailed characteristics of the practical components used to develop this all-hardware implementation of the study system in a machines research laboratory, as well as describing the design and commissioning of the industrial ASD hardware itself to suit the particular characteristics and ratings of the all-hardware laboratory-scale study system in which the ASD is to be tested.

### 3.2 Overview of the Laboratory-Scale Study System

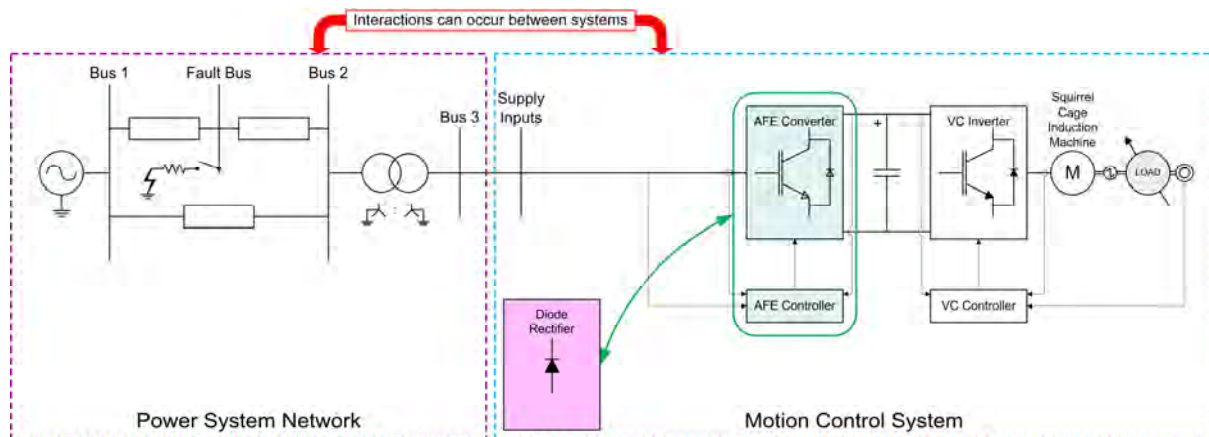


Figure 3-1: Schematic diagram of the laboratory-scale study system.

Figure 3-1 shows a single-line diagram representation of the laboratory-scale study system that was developed in order to test the dynamic response of ASDs to disturbances in this thesis. Figure 3-1 shows that the study system is made up of a small, realistic representation of a power system network that supplies the motion control system under study. The motion control system was commissioned to be able to regulate the shaft speed of a squirrel cage induction machine under closed-loop control for two cases in which distinct types of front-end converter technology were used to energise its machine-side inverter: firstly by means of a diode rectifier, and secondly by means of an active front end converter. The upstream power system supply network was included in the study system to allow sags in the voltages supplied to the front end of the motion control system to be applied in the most realistic manner possible so as to be able to test the dynamic performance of the motion control system and its interaction with the supply system in detail during voltage sag conditions. The voltage sags at the front end of the motion control system were produced by the application of carefully-controlled and repeatable short-circuit faults at the Fault Bus in the upstream power system network. The resulting characteristics of the voltage sags at the drive's front end under such conditions are, as in practical industrial systems, the result of the combined response of both the power system and the motion control system to the particular short-circuit fault being considered.

The following section describes the practical hardware that was used to construct the motion control system itself within this laboratory-scale study system.

### 3.3 The Practical Implementation of the Motion Control System

#### 3.3.1 Introduction

The diagram in Figure 3-2 below shows the motion control system that was introduced as part of the full laboratory-scale study system shown in Figure 3-1. The motion control system is made up of the following hardware components: a squirrel cage induction machine; a load; a frequency converter system (which could alternatively operate with a diode rectifier or an AFE converter at its front end). The subsections that follow describe each of these hardware components in more detail, beginning with the squirrel cage induction machine and load.

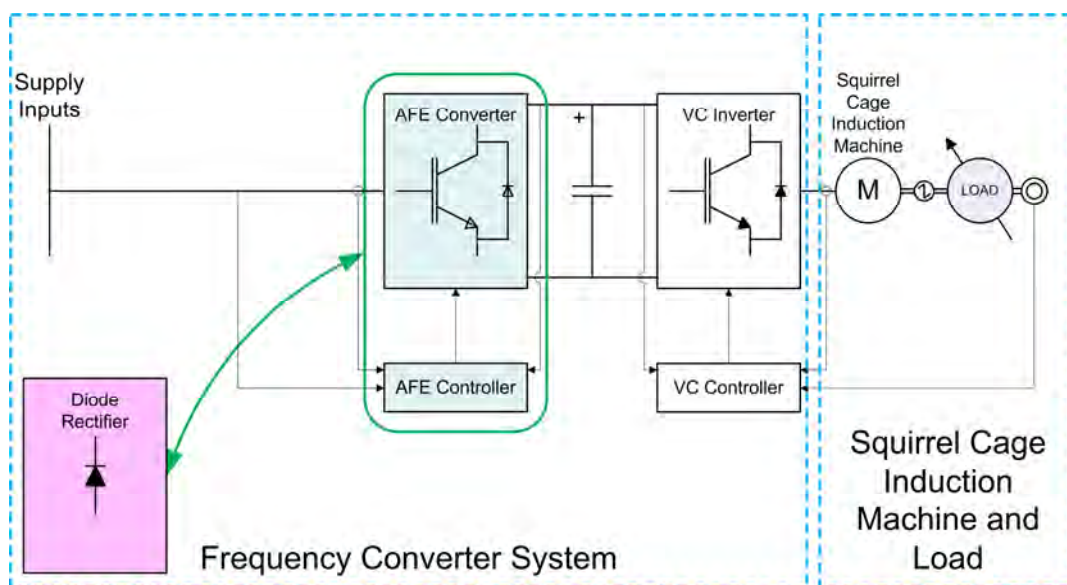


Figure 3-2: Schematic diagram of the motion control system within the laboratory-scale study system.

#### 3.3.2 The Squirrel Cage Induction Machine and Load

The machine that was used as the motor in the motion control system is a three-phase, 2.6 kW, squirrel cage micro-induction machine. The micro-induction machine was manufactured by Mawdsley's Limited and it is shown in Figure 3-3.

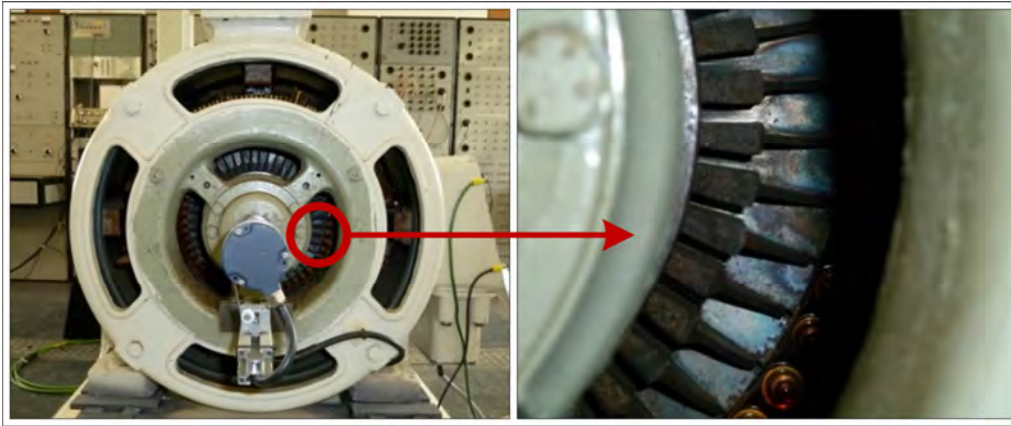


Figure 3-3: The micro-induction machine used in the laboratory-scale study system, with a close-up view of its deep-bar rotor design shown on the right-hand side.

A micro-induction machine is a machine of relatively-small size and rating, as suited to laboratory tests, but which is nevertheless specifically designed to have per-unit electrical and mechanical parameters that are representative of megawatt-sized induction machines typically found in much larger-scale industrial plant. Furthermore, the particular micro-induction machine used in these studies has a deep-bar rotor construction (as shown in Figure 3-3) that is likewise representative of the type of rotor construction common in induction machines of large power rating. The rating information for the micro-induction machine is shown in Table 3-1.

Table 3-1: Rating information for the deep-bar rotor micro-induction machine.

<i>Manufacturer; Origin; Year</i>	Mawdsley's Ltd; Dursley, England; 1974
<i>Machine Type</i>	3-phase AC induction machine
<i>Duty type</i>	Continuous
<i>Frequency [Hz]</i>	50
<i>Winding Connection</i>	Star
<i>Voltage [<math>V_{line-line}</math>]</i>	220
<i>Current [A]</i>	8.36
<i>Power at shaft [kW]</i>	2.6
<i>Power factor (<math>\cos \phi</math>)</i>	0.88
<i>Speed [rpm]</i>	1491
<i>Torque [Nm]</i>	16.6
<i>Efficiency [%]</i>	92

In the laboratory, the micro-induction machine was coupled to a dynamometer via an in-line torque transducer to form an induction machine and dynamometer test set as shown in Figure 3-4.

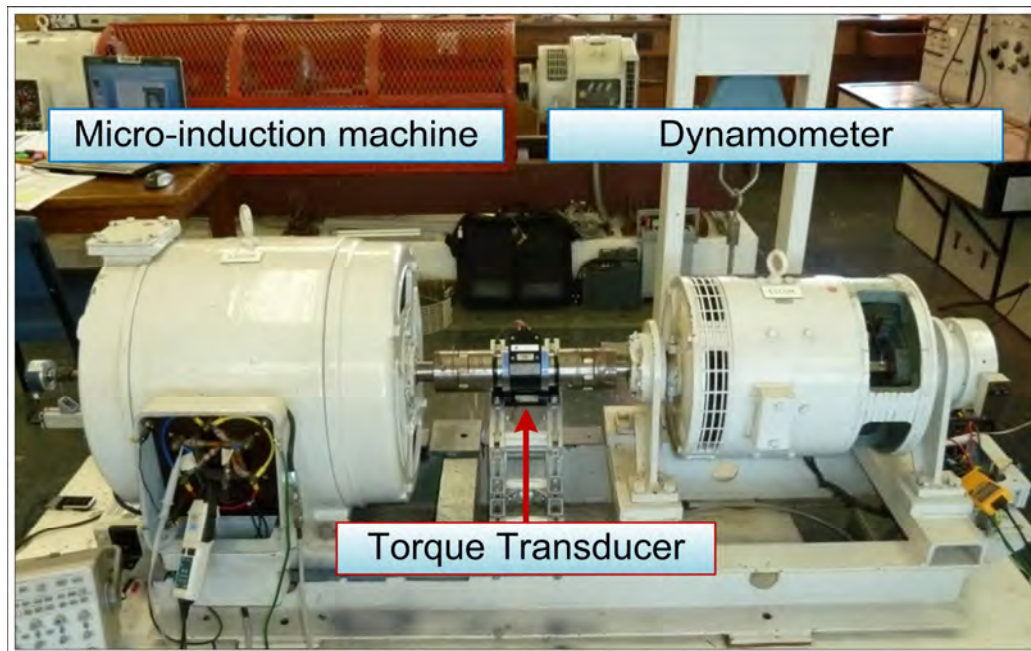


*Figure 3-4: Induction machine, torque transducer and dynamometer.*

The dynamometer shown in Figure 3-4 was used to exert a desired load torque characteristic on the shaft of the induction machine during the laboratory tests in which the machine was being fed by the different ASD configurations, and the in-line torque transducer was used to provide an online measurement of the differential torque between the machine and the dynamometer. The torque exerted by the dynamometer on the induction machine is linearly proportional to the shaft speed of the dynamometer; the gradient of the dynamometer's linear torque-speed characteristic is adjustable, and the maximum value to which the gradient of this torque-speed characteristic could be set was 20 Nm per 1500 rpm.

The frequency converter system at the heart of the ASD to be tested was specifically designed and commissioned to suit the electrical and mechanical ratings of the micro-induction machine that are shown in Table 3-1. The details of the design and commissioning of this frequency converter system, including the facility for changing its front-end converter technology between a diode-rectifier and an active front end converter, are described in the following subsection.

### 3.3.3 The Frequency Converter System

In the commercial market, there are several manufacturers of high-performance adjustable speed drive systems. Each manufacturer typically produces several types of power-electronic based frequency converter modules and drive system controllers that can be used to construct an adjustable speed drive system for a particular motion control application. For the purposes of the work in this thesis, industrial frequency converter modules and controllers from the Siemens Simovert<sup>®</sup> Masterdrives series [12] were selected to make up the frequency converter system for the all-hardware laboratory-scale study system. These particular frequency converter modules and controllers were chosen in part because, after carefully studying the technical information provided by the manufacturer [11, 12, 61, 62], it was confirmed that a frequency converter system made up of these modules and controllers would be suitable to operate the deep-bar type of micro-induction machine for high-performance motion control applications; however an additional aspect that was critical in their selection was that it was also confirmed that the input and output signals on the Simovert Masterdrives controllers could be accessed by the user, which was a key requirement for these controllers to be connected in closed-loop with a real-time simulation model of the drive plant during parts of the investigations.

The modules available in the Siemens Simovert Masterdrives series include front-end AC to DC converter units and machine-side DC to AC inverter units. Furthermore, each converter / inverter unit is generally equipped with a digital controller. The particular hardware components that were selected and procured to form the frequency converter system for the laboratory-scale study system include a Simovert Masterdrives AFE converter unit, a Simovert Masterdrives vector control (VC) inverter unit, a diode-rectifier unit, and various supporting components, in particular a pre-charge circuit, a three-phase line reactor, a voltage sensing board (VSB), and an incremental shaft encoder. Figure 3-5 is a schematic diagram of the resulting frequency converter system that was implemented for the work in the thesis, showing the functional arrangement of the aforementioned components together with the induction machine and load. Figure 3-5 also illustrates that the frequency converter system and machine are collectively referred to as the adjustable speed drive system, and that the ASD system together with the load are collectively referred to as the motion control system.

The pertinent practical details of the various components which make up the AFE converter unit, VC inverter unit, and the diode-rectifier unit in the laboratory-scale ASD system are described as follows. The AFE converter unit is made up of an insulated gate bipolar transistor (IGBT) based three-phase AC to DC voltage source converter, a bank of capacitors (which is connected across the DC output of the converter), a firing pulse circuit for the IGBTs, power- and signal-level protection circuits, an array of voltage and current sensors with signal conditioning circuitry, and a control card. The VC inverter unit is made up of an IGBT based DC to three-phase AC voltage source inverter, a bank of capacitors (which is connected across the DC input of the inverter), a firing pulse circuit for the IGBTs, power- and signal-level protection circuits, an array of voltage and current sensors with signal conditioning circuitry, and a control card. The diode-rectifier unit (used as an alternative form of front-end converter to the AFE unit) is made up of a three-phase AC to DC diode converter, a bank of capacitors (which is connected across the DC output of the diode converter), and a power-level protection circuit.

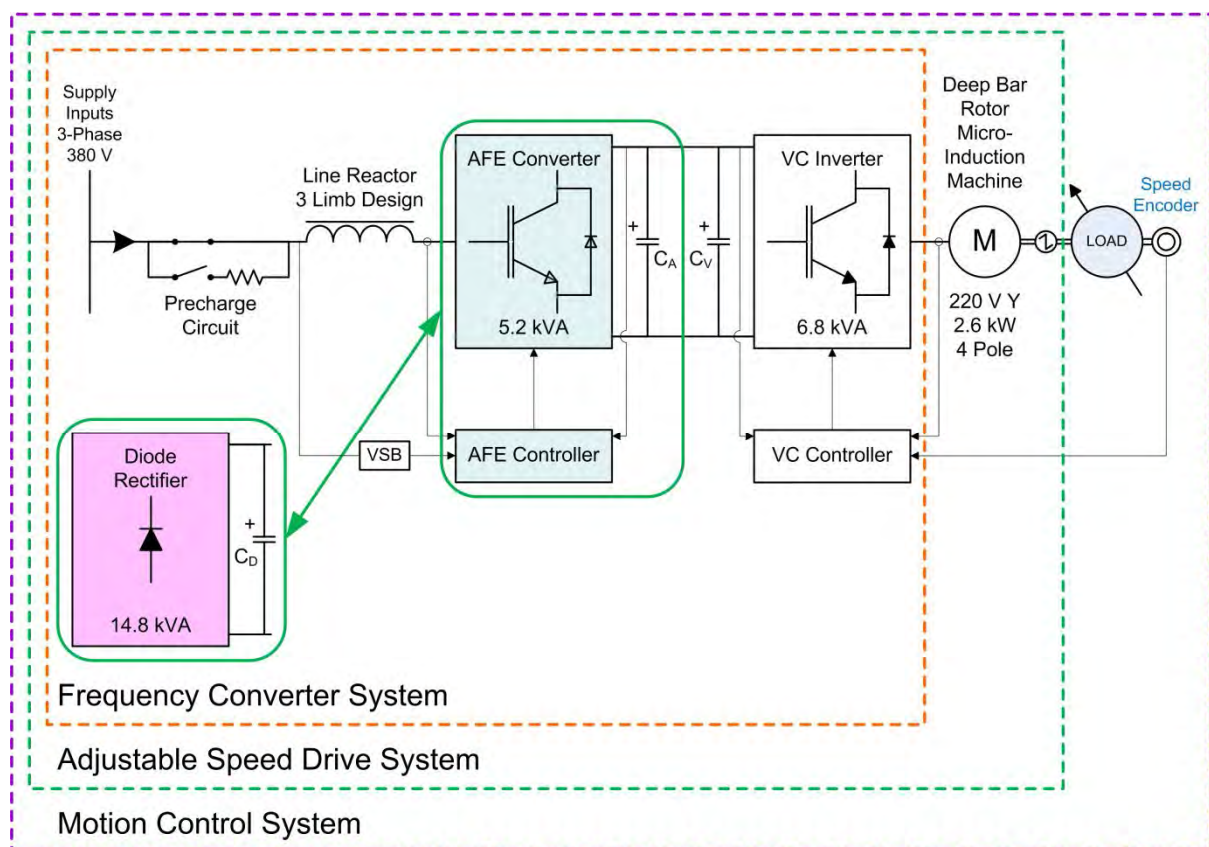


Figure 3-5: Schematic diagram of the motion control system showing component ratings and the additional support components required in the practical commissioning of the system.

The purpose of the supporting components for the frequency converter system in a practical ASD system such as that shown in Figure 3-5 can be explained as follows. The pre-charge circuit is

required to smoothly energise the capacitors in the DC link between the VC inverter and front-end converter units during the initial start-up of the frequency converter system. The line reactor is needed to filter out the effects of commutation that are produced by the front-end converters. The voltage sensing board is required to synchronize the operation of the AFE converter's firing controls with the three-phase source voltages that supply the front-end converter. The incremental shaft encoder provides the feedback measurement of the induction machine's rotor speed that is required for the closed-loop speed control implemented on the VC controller as part of the ASD's field-oriented control algorithm.

The diagram in Figure 3-6 provides further details regarding the equipment characteristics and ratings of the front-end converter and inverter units [11, 61, 63] and the induction machine that were used to make up the laboratory-scale study system. The converter and inverter units of the laboratory-scale ASD system were selected with specific ratings, as shown in Figure 3-5, to enable them to function well within their operating limits when the front-end converter is fed with 380 V and the induction machine is run at full load.

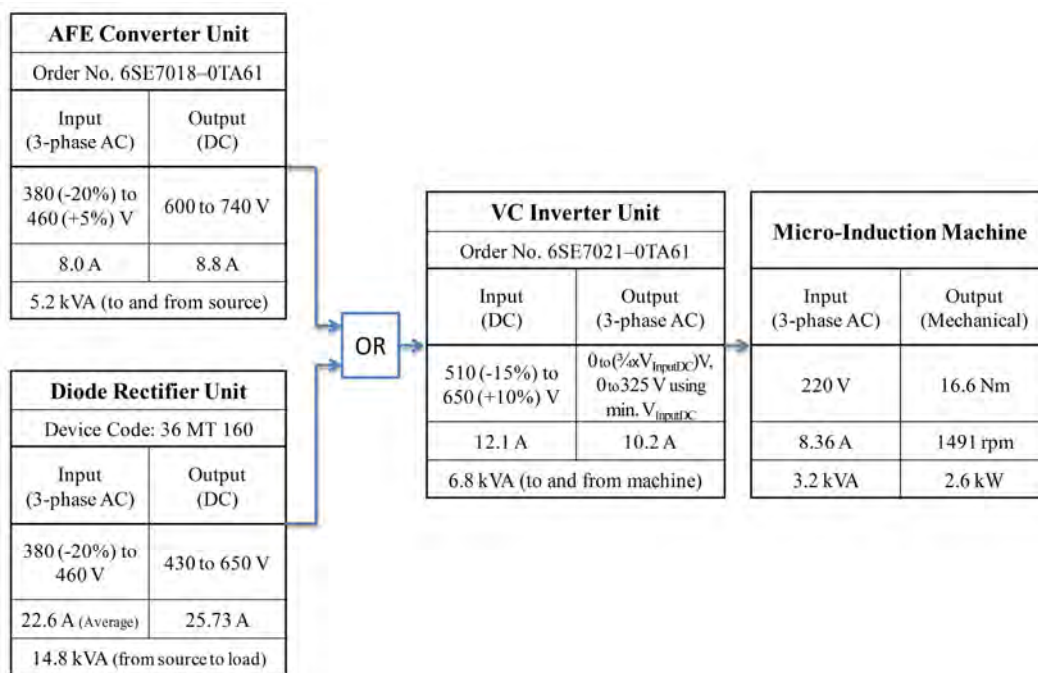
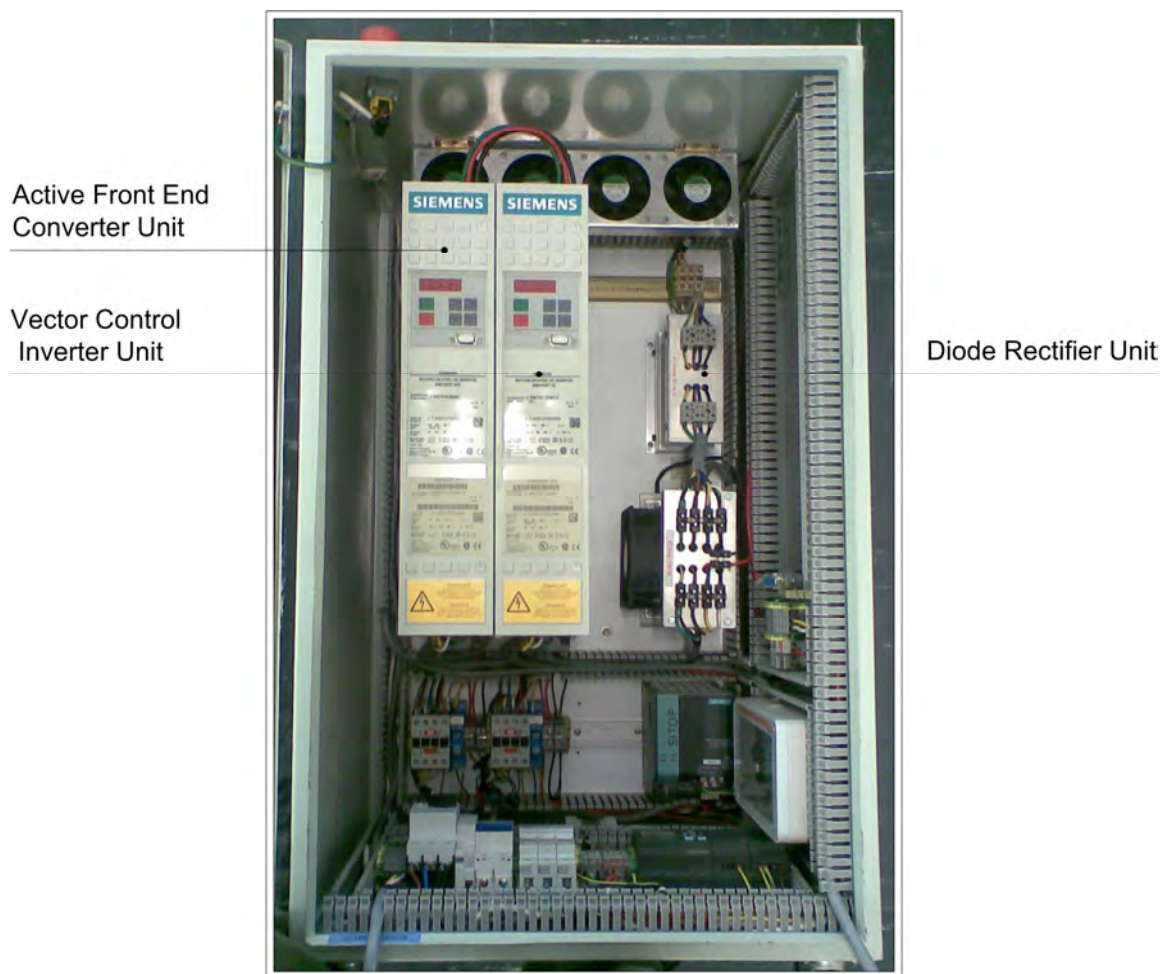


Figure 3-6: Rating information for the converter units, inverter unit and induction machine.

In order to gain a detailed understanding of the motion control system, all of the construction, commissioning and testing of the motion control system used in the laboratory-scale study system in the thesis was carried out by the author. These tasks included: the mechanical installation and alignment of the in-line torque transducer between the induction machine and dynamometer

(as shown in Figure 3-4); the mechanical installation of the Simovert Masterdrives units and their supporting components inside a special-purpose drive enclosure; the connection of the power and control wiring for the complete frequency converter system carried out according to the technical information supplied by the manufacturer [11, 61]; the commissioning of the frequency converter system to drive the induction machine under closed-loop rotor speed control; finally, the installation of sensors and data capturing equipment to record the performance of the motion control system during laboratory testing. Figure 3-7 shows the Simovert Masterdrives units and their supporting components that together make up the frequency converter system of the laboratory-scale ASD system, mounted in the special-purpose drive enclosure designed by the author.



*Figure 3-7: Photograph of the final, fully-commissioned, frequency-converter system hardware for the laboratory-scale system shown in Figure 3-5, housed in its special-purpose drive enclosure.*

The next section describes the commissioning of the individual controllers in the frequency converter system in order to manage their respective converter / inverter units to implement the closed-loop control of the induction machine's rotor speed.

## **3.4 Commissioning of the Frequency Converter Controllers**

### **3.4.1 Introduction**

In the adjustable speed drive system shown in Figure 3-5, the principal function of the front-end converter unit, be it the diode-rectifier unit or the AFE converter unit, is to convert the three-phase AC, 380 V supply at its input terminals into a suitable DC voltage at its output terminals. This DC voltage is then filtered by two banks of capacitors that are connected in parallel at the output of the converter unit and at the input of the inverter unit as shown in Figure 3-5. The principal function of the VC inverter unit is to convert the filtered DC link voltage into a three-phase AC voltage of adjustable magnitude and frequency that is applied to the terminals of the induction machine in order to control the torque produced by the machine so that the rotor speed of the machine can then be controlled in a closed-loop fashion.

The next subsection describes the commissioning of the controller within the VC inverter unit to implement closed-loop rotor speed control of the induction machine. The subsection that follows it describes the commissioning of the controller within the AFE converter unit to manage the three-phase AC to DC voltage conversion process for those cases in which the AFE converter unit was selected as the front-end converter technology of interest in the ASD system tests.

### **3.4.2 Commissioning of the Controller within the VC Inverter Unit**

The digital controller hardware for the VC inverter unit used in this thesis is referred to by the manufacturer as a CUVC control unit. The CUVC control unit has parameters within its memory that can be set by the user so as to commission it to implement a particular task. A personal computer installed with a software program called DriveMonitor<sup>®</sup> [64] was used to commission the CUVC control unit.

In order to implement closed-loop control of the induction machine's rotor speed, the CUVC control unit was commissioned in steps according to the technical manual provided by the manufacturer [62]. The significant steps in the commissioning process are described as follows. The first step was to store the ratings of the laboratory micro-induction machine into the memory of the CUVC unit so that it had the required information about the particular machine that it was to be used to control. The second step was to program the CUVC unit so as to select the particular type of motion control task that it was required to implement on the specified machine with the use of its inverter. In this instance, the programmed task was closed-loop speed control of the induction machine. Furthermore, the

CUVC unit was also programmed to select that the particular form of closed-loop speed control to be implemented on the machine would be the manufacturer's implementation of the field oriented control algorithm. The third step was to program the CUVC unit with the specific characteristics of the mechanical load that was coupled to the induction machine in the laboratory study system. The fourth step was to input practical maximum operational limit settings for the machine's stator currents, torque and speed into the CUVC unit. The final step was to command the CUVC unit to execute what is referred to by the manufacturer as its "Complete Motor Identification" function [62]. During the execution of this function the inverter is energised with DC voltage and a series of practical tests are automatically carried out on the induction machine by the inverter under the command of the CUVC unit. During these tests, measurements are recorded by the CUVC unit from the incremental shaft encoder attached to the rotor of the machine, and also from various sensors that are integrated into the power circuit of the inverter. The results obtained from these practical tests are first used by the CUVC unit to determine specific electrical and mechanical parameters of the machine. Thereafter, the CUVC unit then automatically calculates values for the gains of its closed-loop motion control algorithms and stores these gains in its memory. In this application the CUVC unit automatically determines gains for its field oriented control based torque control loops, and its closed-loop rotor speed control loops. These automatically-tuned gains for the torque and speed control loops of the selected motion control algorithms are typically calculated with conservative margins so as to ensure the reliability and stability of the resulting speed-controlled system under dynamic conditions. Once the values of these automatically-tuned motion controller gains are calculated and stored into the memory of the CUVC unit, the "Complete Motor Identification" function is concluded.

The technical manual for the VC inverter unit [62] suggests that the automatically-tuned values of the controller gains determined by its "Complete Motor Identification" function for a speed-controlled system can, if required, be further refined manually by the commissioning engineer in order to enable the system to produce a desired set of responses under particular dynamic conditions. In the case of the speed controls for the laboratory-scale drive system designed for this study, some of the automatically-tuned values for the control loops were fine tuned by the author in order to improve the response of the rotor speed controller to disturbance inputs in the DC link voltage.

### 3.4.3 Commissioning of the Controller within the AFE Converter Unit

The digital controller hardware for the AFE converter unit used in this thesis is referred to by its manufacturer as a CUSA control unit. Similarly to the CUVC control unit, the CUSA control unit has parameters within its memory that can be set by the user, by means of the DriveMonitor program, so as to commission the CUSA unit to implement a particular task.

In the case of the laboratory-scale ASD system in this work, the CUSA unit was commissioned to maintain a constant voltage at the DC terminals of the AFE converter unit by controlling the three-phase currents at the AC terminals of the AFE converter. When it is programmed to operate in this mode, the CUSA unit controls both the DC voltage and three-phase AC currents of the front-end converter in a closed-loop manner, with the closed-loop control for the currents implemented using a technique that is based on the field oriented control algorithm [11].

The CUSA unit was commissioned in steps according to the technical manual provided by the manufacturer [11]. The significant steps in the commissioning process are described as follows. The first step was to program the CUSA unit with the rated voltage and frequency of the three-phase AC source that was to be connected at the front-end converter's AC terminals (these being, in this case, 380 V and 50 Hz respectively). The second step was to select the operating mode for the AFE converter unit, which was set to "cos (phi)": this selection instructs the CUSA unit to control the AFE converter in such a way that the three-phase currents at the front-end converter's AC terminals are kept at a specified power factor under steady-state conditions. The value selected for the specified power factor was unity and it was chosen to make the resulting motion control system (shown in Figure 3-5) seem like a resistive load to the three-phase supply network when the micro-induction machine runs at steady state in motoring mode. The third step was to set the reference value of the DC link voltage to be maintained by the AFE converter's closed-loop voltage controller. The final step was to manually tune the gains within the CUSA unit for the field oriented control based current control loops, and the closed-loop DC link voltage control loops. By contrast with the CUVC unit, which is able automatically to tune the gains of its closed-loop motion control algorithms to suit a particular induction machine and load, the CUSA unit does not possess an equivalent function to determine the gains for its closed-loop current and voltage control loops; these gains therefore have to be tuned manually by the commissioning engineer in order to enable the AFE converter unit to be able to regulate the DC link voltage. In the case of the AFE converter unit for the laboratory-scale ASD system, the gains for the closed-loop current and voltage control loops were manually tuned by the

author to enable the resulting voltage controlled system to operate successfully, and to ensure the reliability and stability of the system, for the case when disturbance inputs are applied at the three-phase AC supply voltages of the AFE converter.

Thus far this chapter has described the practical details and commissioning of those components that were used to make up the motion control system within the laboratory-scale study system to be used in the thesis. The next section of the chapter describes the relevant details of those practical components that were used to make up the upstream power system supply network in the laboratory-scale study system.

### 3.5 The Practical Implementation of the Power System Network

The left-hand side of the schematic diagram in Figure 3-8 shows the upstream power system network that was used to supply the motion control system in the laboratory-scale study system used in the thesis. In the full, all-hardware implementation of this study system the power system network and its supply were built up using existing components in a machines research laboratory. The topology of the network was chosen to be detailed enough to represent the impact on the motion control system of upstream faults realistically, yet simple enough to be constructed with the equipment available in the research laboratory.

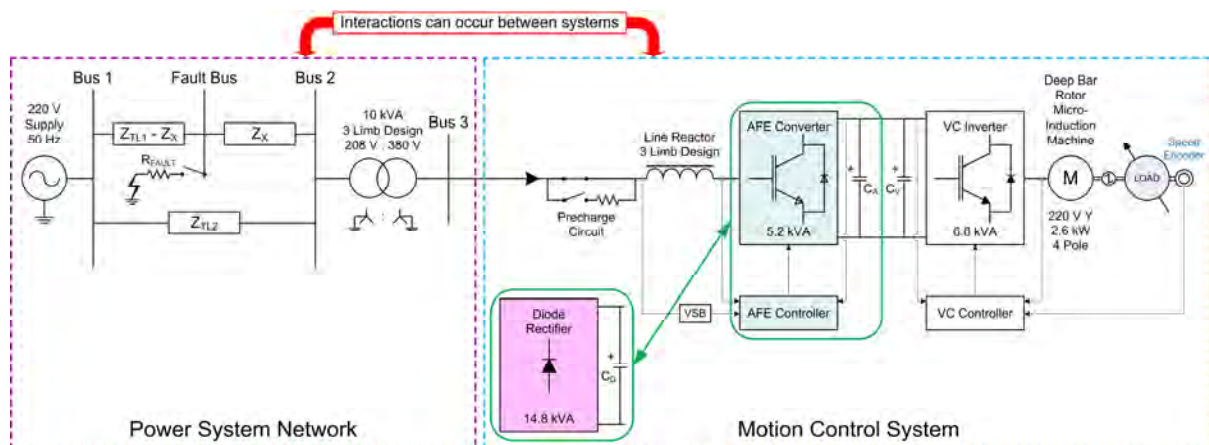


Figure 3-8: Schematic diagram of the all-hardware laboratory-scale study system.

In the full, all-hardware implementation of the study system, Bus 1 of the upstream network was fed from a three-phase, 220 V source. The distribution network between Buses 1 and 2 comprised two parallel paths such that during an upstream short-circuit fault, power could still be transferred to the motion control system to some extent (albeit influenced by the short-circuit fault) as would be the case in a practical distribution network. A transformer between Buses 2 and 3 was used to step up the incoming voltage at Bus 2 so that the front-end converter used by the motion control system was supplied with its rated voltage of 380 V at Bus 3. Controlled faults were applied at the Fault Bus within the distribution network in order to produce a range of sags of different characteristics in the voltages of the downstream Bus 3 feeding the motion control system.

Figure 3-9 shows a photograph of the equipment used to implement the faulted power system network in the laboratory. The distribution network between Buses 1 and 2 shown in the schematic diagram of Figure 3-8 was constructed using the lumped series resistances and inductances of the transmission line simulator panels in the laboratory seen in the rear of the photograph. The transformer used in the

laboratory-scale study system was a three-phase, three-limb 10 kVA device. The primary and secondary windings of the transformer were both connected in star, with both star points earthed.

The short circuits at the Fault Bus in the study system of Figure 3-8 were applied by means of timed closing of a three-phase vacuum contactor that was connected to ground at the corresponding point in the laboratory transmission line simulator panel through user-selectable resistance values  $R_{\text{FAULT}}$  inserted in each phase of the fault branch. This approach ensured that the short-circuit faults in the upstream network of the study system could be applied in a repeatable manner, with independent control of three distinct characteristics of the fault possible for each experimental test, namely:

- the resistance of the fault (by selecting the value of  $R_{\text{FAULT}}$  used);

- the type of fault (single-, double-, or three-phase to ground short circuits selected by controlling which poles of the vacuum contactor were allowed to close;

- the duration of the fault (by controlling the time for which the vacuum contactor was kept closed).

These three independently-controllable characteristics of the upstream fault could then be chosen for each experimental test in such a way as to influence, respectively, the following three important characteristics of interest in the voltage sags created at the input to the motion control system:

- sag depth;

- sag type;

- sag duration.

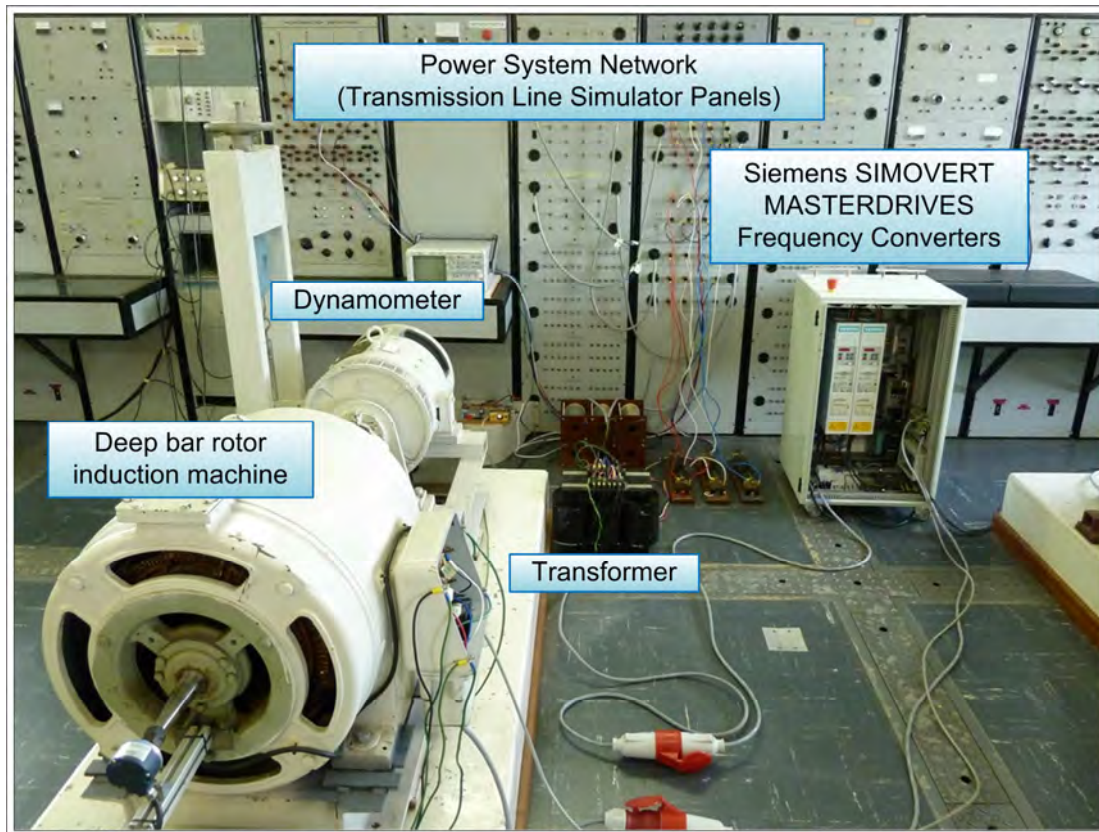


Figure 3-9: Practical implementation of the all-hardware laboratory scale study system.

The particular parameter values of the line impedances in the power system supply network of the laboratory-scale study system (i.e.  $Z_{TL1}$ ,  $Z_{TL2}$  and  $Z_X$  in Figure 3-8) were chosen to allow a practical compromise between the ability of the laboratory-scale network to transfer sufficient power to operate the ASD system at a realistic loading level relative to its rating without excessive voltage regulation at Bus 3 under steady-state conditions, and at the same time to be able to create significant depressions in the Bus 3 voltages under fault conditions so as to test the ASD's response to a representative range of dynamic input voltage sags.

Specifically, the impedances  $Z_{TL1}$ ,  $Z_{TL2}$  and  $Z_X$  were kept fixed during all the experimental tests at values chosen to allow the line-to-line voltage of Bus 3 to remain at a nominal voltage of 380 V while the micro-induction machine was driving a fixed-load torque of approximately 8 Nm at a controlled rotor speed of 1500 rpm (i.e. with the machine delivering approximately 50 % of its rated torque value of 16.6 Nm shown in Table 3-1).

The electrical location of the Fault Bus (determined by the relative sizes of the impedances ( $Z_{TLI}-Z_X$ ) and  $Z_X$  that make up the total impedance of the faulted line in the laboratory-scale system) likewise remained fixed during all experimental tests, with the value of the fault resistance  $R_{FAULT}$  being used to vary the depth of the voltage sag created at Bus 3 during short-circuit faults. In this manner it was possible to ensure a representative range of voltage sags at Bus 3 could be obtained while keeping the fault currents in the system within the short-term withstand capability of the laboratory components. Specifically, the parameters of the laboratory-scale system then allowed a set of six different experimental fault conditions to be chosen in order to create a representative range of sag types and nominal sag depths at the Bus 3 voltage that were considered suitable for thoroughly testing the ASD's dynamic performance.

Table 3-2 summarises the sag characteristics and nominal sag depths of the Bus 3 voltage associated with each of these six fault conditions to be considered in the studies in subsequent chapters. It should be noted that the sag depths shown in Table 3-2 are nominal values because the specific degree of voltage sag that occurs at the front end of the ASD system depends, in practice, on the type of front-end converter technology employed in the drive, which is itself a variable to be considered in the experimental tests to be presented in subsequent chapters of the work in the thesis.

*Table 3-2: Sag characteristics and nominal sag depths at the Bus 3 voltage for the six particular fault conditions considered during experimental tests on the laboratory-scale study system.*

Fault Condition	Sagged Phase/s	Duration [ms]	Voltage Sag Depth [%]	Remaining Voltage During Fault [%]
(i)	A	200	35	65
(ii)	A	100	50	50
(iii)	A, B	100	35	65
(iv)	A, B	100	50	50
(v)	A, B, C	100	50	50
(vi)	A, B, C	100	70	30

### **3.6 Summary**

This chapter has outlined the topology of the laboratory-scale study system used in the work of this thesis, and described the practical details of the key components that were used to implement both the power system supply network and the motion control system in this study system within a machines research laboratory. The chapter also described the modes of operation and the commissioning procedures adopted for the control hardware, both for the front-end converter and drive inverter units that combine to make up the industrial ASD system to be tested in subsequent chapters of the thesis. Finally, the chapter described how the study system was designed to allow a practical range of voltage sag conditions to be created in a controllable manner at the front end of the drive as a result of realistic upstream short-circuit faults applied in the supply network. As explained in Chapter 1 of the thesis, the measured performance of the ASD system in this full hardware implementation of the laboratory-scale study system is to be compared against a testing approach in which the study system plant is modelled entirely on a real-time digital simulator, and the ASD's drive controller modules are connected hardware-in-loop with this real-time model of the plant. The next chapter therefore describes how this same laboratory-scale study system was modelled on a real-time simulator for the purposes of this comparative evaluation.

# **Chapter 4: Development And Parameterization Of The Real-Time Model For The Hardware-In-Loop Simulation Implementation Of The Study System**

## **4.1 Introduction**

As explained in Chapter 1, one of the main objectives of this thesis is to evaluate a proposed method of testing an advanced motion control system in which the signal-level ASD controls of the motion control system are interfaced hardware-in-loop with a real-time simulation model of all of the power-level plant in the system, including the upstream power system supply network. Chapter 3 has described the machines, ASD controllers and other practical components that, together, were used to make up the motion control system and faulted power system network in the all-hardware implementation of a laboratory-scale study system that was chosen as the benchmark for these evaluations.

This chapter now describes the development and parameterization of the real-time simulation model of all of the practical components that constitute the power-level plant within this laboratory-scale study system. The real-time studies were carried out on an RTDS Technologies system, and the simulation model was developed using a software suite that is known as RSCAD [65]. The real-time model was built using elements from RSCAD's pre-defined user library of fundamental component models which were parameterized to suitably represent the individual practical power-level components in the laboratory-scale system. The next section presents an overview of the practical components in the study system plant that were represented with such RSCAD models.

## 4.2 Overview of the Real-Time Models in the HIL Simulation Study System

Figure 4-1 shows a schematic diagram of the all-hardware implementation of the laboratory-scale study system used for the purposes of this thesis.

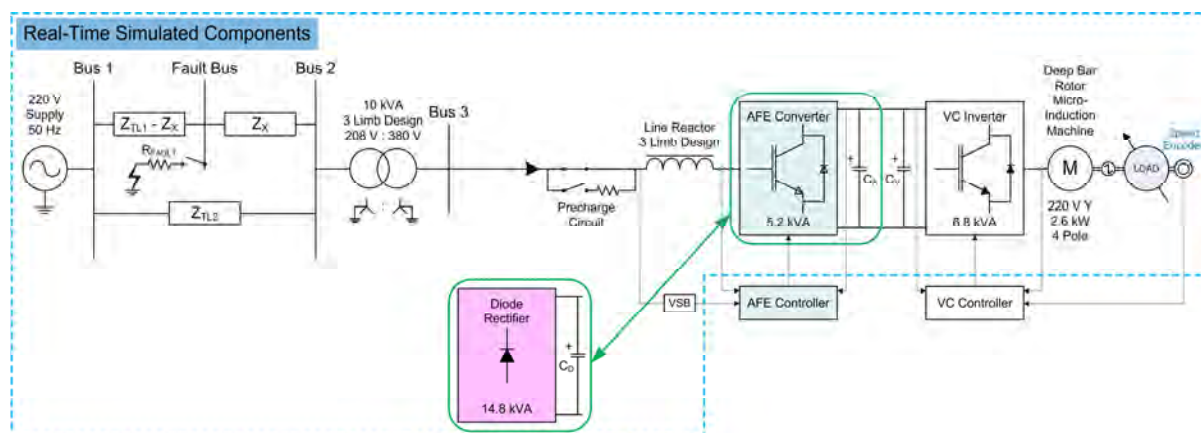


Figure 4-1: A schematic diagram of the all-hardware implementation of the study system.

The dotted blue line in the diagram of Figure 4-1 identifies all those parts of the laboratory study system that were represented using real-time simulation models during the hardware-in-loop tests, and the specific components in this real-time model are listed as follows: the 220 V source at Bus 1; the distribution network between Buses 1 and 2; the fault application circuit within the distribution network; the 10 kVA transformer; the ASD's pre-charge circuit and line reactor; the power-electronic circuits of the AFE converter, diode rectifier and VC inverter; the capacitor banks across the DC terminals of the inverter and each front-end converter; the deep-bar rotor micro-induction machine; the dynamometer. The sections that follow in the chapter describe the RSCAD models and the particular parameters that were used to represent each of the aforementioned components of the study system. In addition, as part of the process of validating the real-time model of the power-level plant in the study system, key sub-sets of the plant within the study system as a whole were tested under dynamic conditions in the laboratory and compared against their parameterized real-time models to verify the correctness and accuracy of the models.

The next section begins by describing the real-time model that was used to represent the part of the laboratory-scale study system that comprises the 220 V source, distribution network, and fault application circuit.

### 4.3 The Distribution Network and Fault Application Circuit Component Models

Figure 4-2 shows a schematic diagram of the faulted distribution network within the laboratory-scale study system and the real-time models that were used to represent this section of the laboratory-scale system in RSCAD.

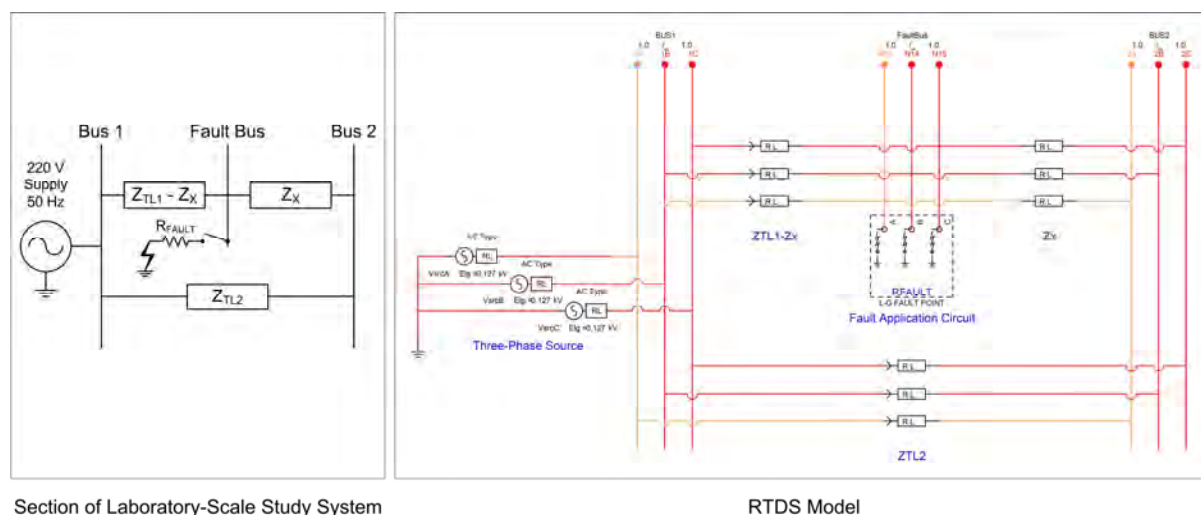


Figure 4-2: Schematic diagram of the faulted distribution network in the laboratory-scale study system and its representation in RSCAD.

Figure 4-2 shows that the three-phase source in the laboratory system was represented in the real-time model with three single-phase source components connected in star, with the star point earthed. Furthermore, the three-phase, lumped series resistances and inductances within the transmission line simulator panels that were used to make up the impedances ( $Z_{TL1-Z_X}$ ),  $Z_X$ , and  $Z_{TL2}$  of the distribution network in the laboratory system were represented with lumped series resistance and inductance components in the real-time model. The parameters of these lumped resistance and inductance components in the real-time model were obtained by direct measurements of the values of ( $Z_{TL1-Z_X}$ ),  $Z_X$ , and  $Z_{TL2}$  that were actually used in the transmission line simulator panels in the machines research laboratory, and these are shown in Table 4-1.

Table 4-1: Measured series resistance and inductance values of the distribution network impedances ( $Z_{TL1-Z_X}$ ),  $Z_X$ , and  $Z_{TL2}$  in the laboratory-scale system.

	$(Z_{TL1-Z_X})$	$Z_X$	$Z_{TL2}$
Resistance [ $\Omega$ ]	0.51	0.28	0.33
Inductance [mH]	38.12	2.63	9.45

Figure 4-2 shows that the fault application circuit in the laboratory-scale system was represented in the real-time model using a three-phase line-to-ground (L-G) fault component. As explained in Chapter 3, in the all-hardware implementation of the study system in the laboratory, various line-ground faults were applied using controlled closing of selected phases of a vacuum contactor connected in shunt at the Fault Bus through carefully-selected values of fault resistance  $R_{\text{FAULT}}$ . Similarly, RSCAD's three-phase L-G fault component model shown in Figure 4-2 allows selected phases to be included in the fault for a user-specified duration, and with the resistance of the fault branch available as an internally-selectable parameter. The L-G fault component in RSCAD was therefore configured to simulate the functionality of the laboratory implementation of faults at the Fault Bus by allowing: the resistances  $R_{\text{FAULT}}$  to be set; the type of fault to be chosen (i.e. single-, double-, or three-phase to ground short circuits); the duration of the fault to be chosen.

When carrying out measurements on the all-hardware implementation of the study system in the laboratory it was not possible to control the vacuum contactor so as to be able to apply short-circuit faults at a predetermined point on wave. However, with careful measurement, it was possible to establish, after the fact, what the point-on-wave of inception of the fault had actually been during each such laboratory measurement. The approach taken when comparing laboratory measurements against real-time simulations was to set up the control of the L-G fault component within the real-time simulation model so as to recreate the same duration and point-on-wave of inception of fault that had actually occurred during the laboratory measurement of the fault test under consideration.

The next section presents the validation of the real-time models of the laboratory source, distribution network and fault application circuit.

### 4.3.1 Validation of the Real-Time Models

In order to determine whether the practical source, distribution network, and fault application circuits used in the laboratory implementation of the study system were accurately represented by their parameterized real-time models, the following approach was adopted. The all-hardware implementation of the laboratory-scale study system was firstly configured to operate with only the abovementioned components by disconnecting all of the plant downstream from Bus 2. The resulting truncated configuration of the laboratory-scale system is shown in Figure 4-3, and this sub-section of the system was practically tested as follows.

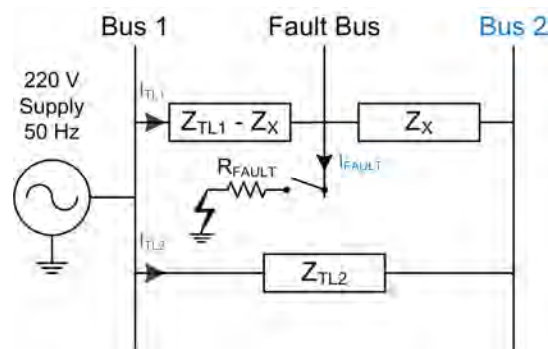


Figure 4-3: Sub-system of the laboratory-scale study system containing the 220 V source, distribution network, and fault application circuit.

The source at Bus 1 in the laboratory implementation of the test sub-system shown in Figure 4-3 was energised and thereafter, a specific set of short-circuit faults was applied at the Fault Bus which respectively produced a particular set of voltage sags at Bus 2. During each such test, measurements were made of the instantaneous currents at each of the locations  $I_{TL1}$ ,  $I_{TL2}$ , and  $I_{FAULT}$  defined in Figure 4-3, as well as of the instantaneous voltages at Bus 2. Thereafter, the same short-circuit faults were applied to the real-time simulation model of this test sub-system and recordings were made of the simulated responses of the currents  $I_{TL1}$ ,  $I_{TL2}$ , and  $I_{FAULT}$ , and of the simulated responses of the instantaneous voltages at Bus 2. These simulation results were then compared against the laboratory measurements as a means to validate the suitability and accuracy of the parameterized real-time models of the 220 V source, distribution network, and fault application circuit components.

Table 4-2 shows a summary of the particular fault conditions that were applied at the Fault Bus during the laboratory test measurements and simulation studies carried out on this sub-section of the laboratory-scale system. Table 4-2 shows that three different types of fault were applied at the Fault Bus for 200 ms, and each fault involved specific phases that were connected to ground via the corresponding phases of the three-phase resistance  $R_{FAULT}$ . During the application of a fault involving

particular phases at the Fault Bus, the voltages in the corresponding phases at Bus 2 were then caused to sag with a depth dependent on the value of  $R_{\text{FAULT}}$  used. The voltage sag depth caused by each of the faults is shown in Table 4-2 in the form of a percentage where 100 % corresponds to the nominal phase to neutral voltage at Bus 2.

*Table 4-2: Summary of the fault conditions applied to the test subsystem of Figure 4-3 together with the resulting voltage sag characteristics seen at Bus 2.*

	Fault type at Fault Bus [Phases to ground]	Duration [ms]	Voltage sag depth at Bus 2 [%]	Remaining voltage at Bus 2 during fault [%]
(i)	A-ground	200	70	30
(ii)	A-B-ground	200	50	50
(iii)	A-B-C-ground	200	70	30

In the graphical results that follow, measured and simulated results are compared for the case when each of the fault conditions shown in Table 4-2 was applied to the test subsystem of Figure 4-3. For each short-circuit fault, the corresponding variables obtained from the measured and simulated results are plotted on the same set of axes to allow direct comparison, with the measured variables shown in red, and the simulated variables shown in blue. The pink shaded area in each plot indicates the time period during which the short-circuit fault was applied.

Figure 4-4 below compares the results obtained from the practical and simulated implementations of the test sub-system in response to the phase A to ground fault described in Table 4-2. The comparison in Figure 4-4 shows that there is excellent agreement between the simulated and measured values of the currents in the upper and lower transmission paths of the distribution network connecting Bus 1 to Bus 2, and between the simulated and measured currents in the fault branch. The simulated and measured results show close agreement not only in respect of the final (steady) values of these currents prior to removal of the fault, but also in respect of the dynamic characteristics of the currents immediately following the fault inception. Also, importantly, the real-time simulation of the faulted test sub-system agrees closely with the laboratory measurements in respect of the impact of the fault on the Bus 2 voltage, both in terms of the depression in the amplitude of the voltage once the fault current has settled to its final value, as well as the dynamic characteristics of the voltage immediately following the application and removal of the fault.

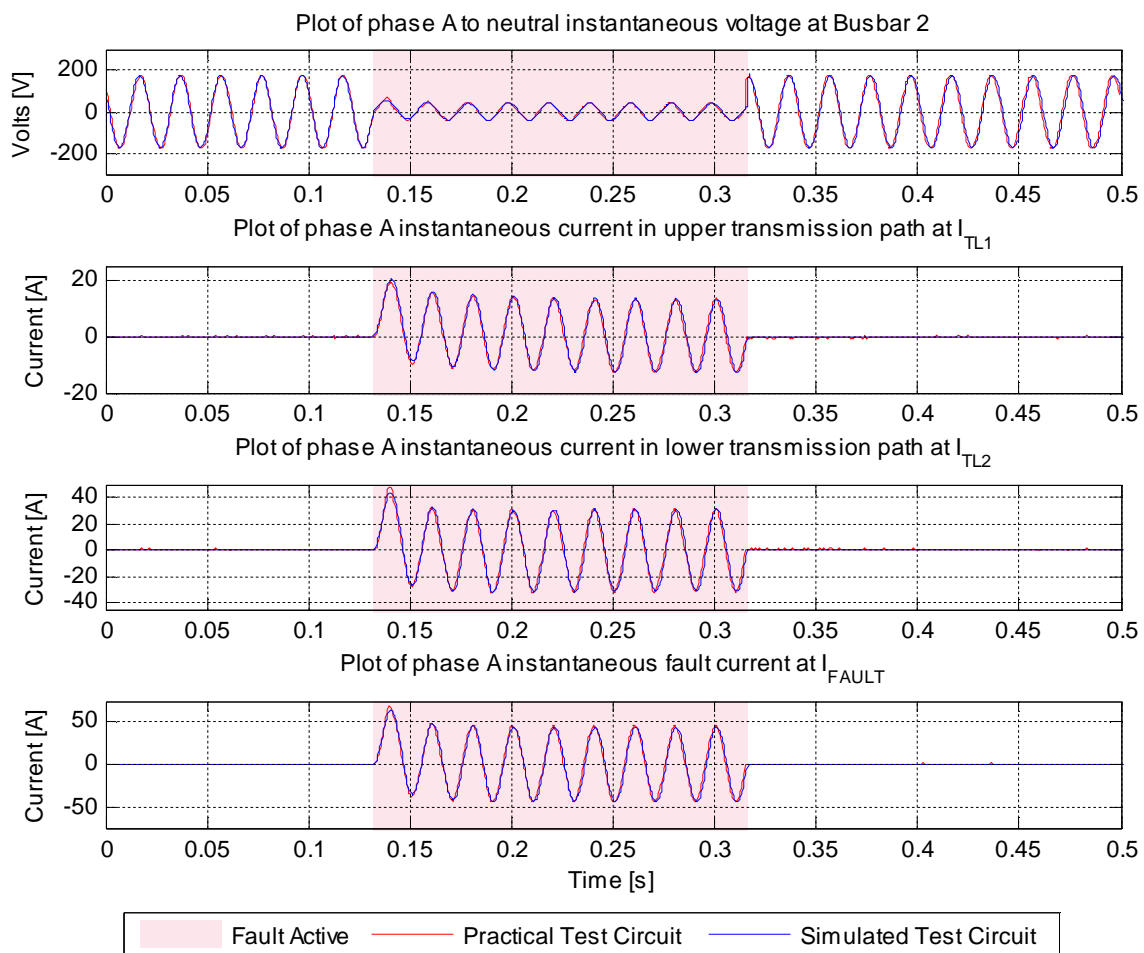


Figure 4-4 — Validation of faulted distribution network model: (i) Phase A-ground fault with 70 % voltage sag at Bus 2.

Figure 4-5 compares the results obtained from the laboratory and real-time simulation implementations of the test sub-system during the application of the phase A to B to ground fault described in Table 4-2 which caused a decrease of 50 % in the voltages of the respective phases at Bus 2.

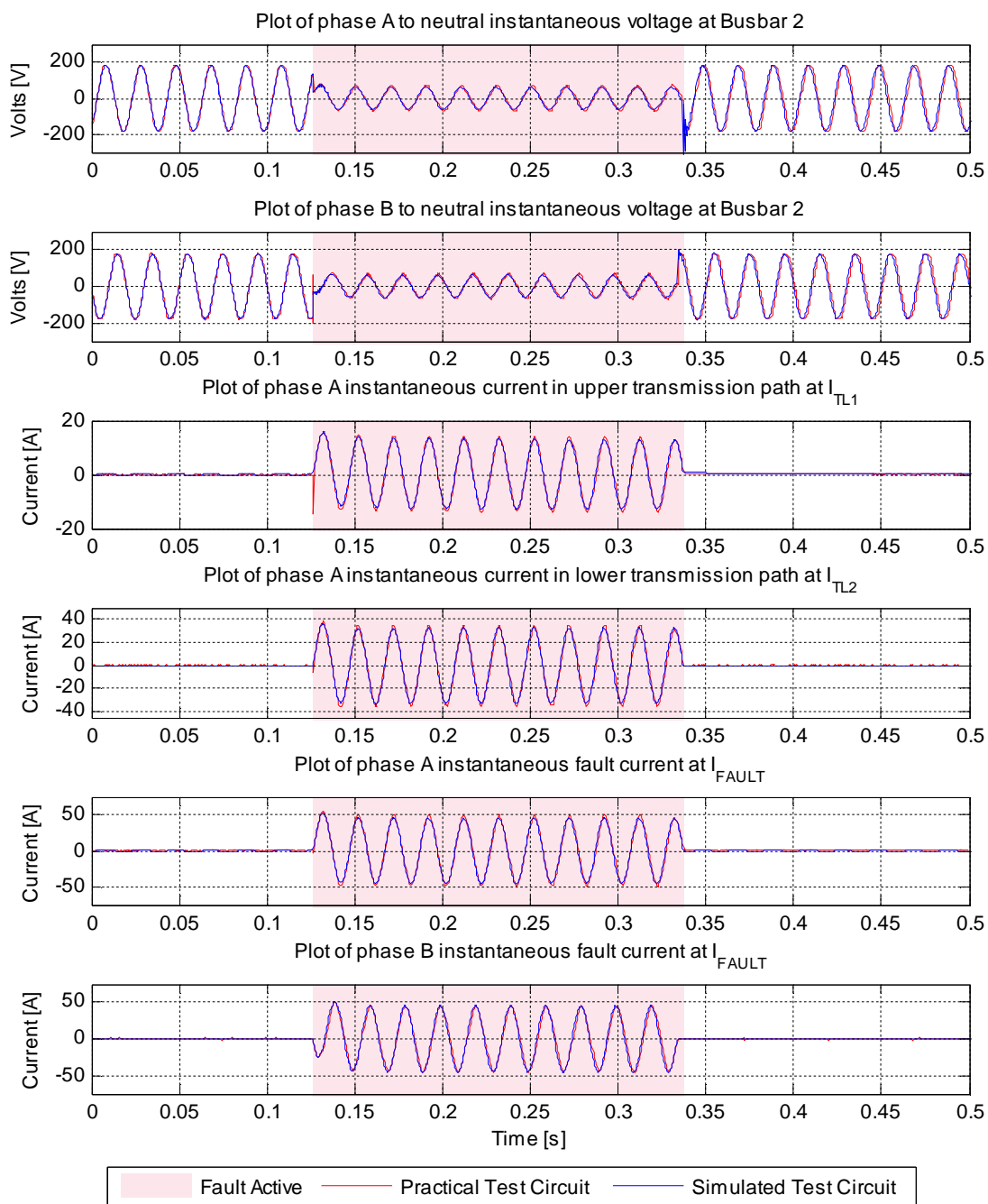


Figure 4-5 — Validation of faulted distribution network model: (ii) Phase A-B-ground fault with 50 % voltage sag at Bus 2.

The comparison in Figure 4-5 shows excellent agreement between the simulated and measured A- and B-phase voltages at Bus 2, particularly with respect to the dynamic characteristics at the inception and

removal of the fault. Furthermore, the amplitudes of the voltages in phases A and B during the fault obtained from the real-time simulation model agree closely with the amplitudes of these voltages in the measured results. Likewise, the simulated results agree closely with the laboratory measurements in respect of the currents flowing in the upper and lower transmission paths and in respect of the currents in the fault branch, both in terms of the amplitudes of the currents during the fault, as well as their dynamic characteristics at the inception and removal of the fault.

Finally, Figure 4-6 compares the measured and simulated responses of the test sub-system during the application of the three-phase to ground fault. The comparison in Figure 4-6 shows excellent agreement between the measured and simulated results for all three phases of the voltages at Bus 2, for the fault currents at the Fault Bus, as well as for the currents in the upper and lower transmission paths in the distribution network (of which only the phase A current is shown in Figure 4-6).

In summary, the close agreement between the measured and simulated results shown in Figures 4-4 to 4-6 therefore provides confidence that the real-time simulation models of the three-phase source, distribution network, and fault application circuit components in the small-scale study system accurately describe the actual characteristics of the equipment used to represent this plant in the all-hardware implementation of the study system in the laboratory.

The following section describes the real-time model that was used to represent the 10 kVA transformer in the laboratory-scale study system.

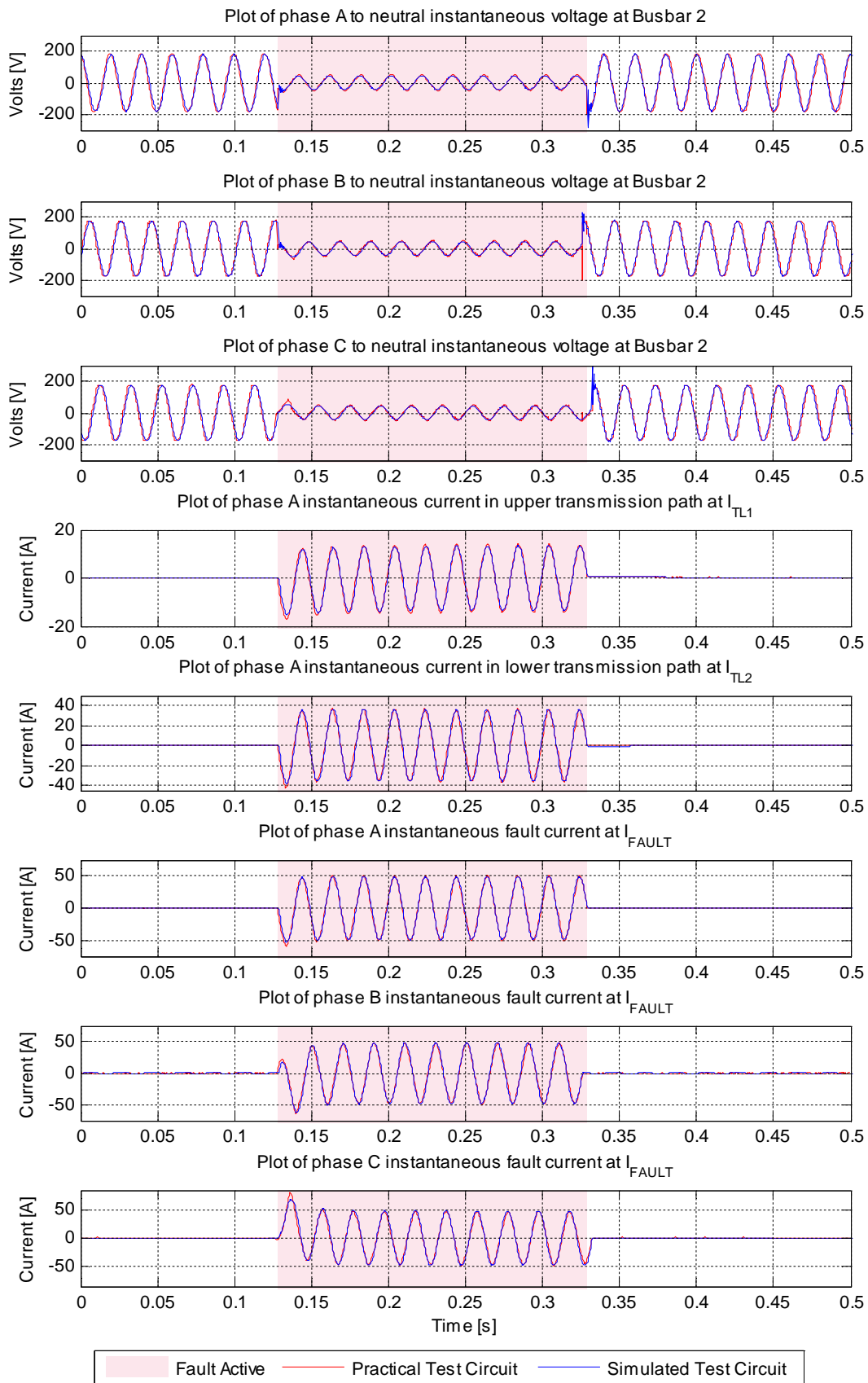


Figure 4-6 — Validation of faulted distribution network model: (iii) Phase A-B-C-ground fault with 70 % voltage sag at Bus 2.

#### 4.4 The 10 kVA Transformer Model

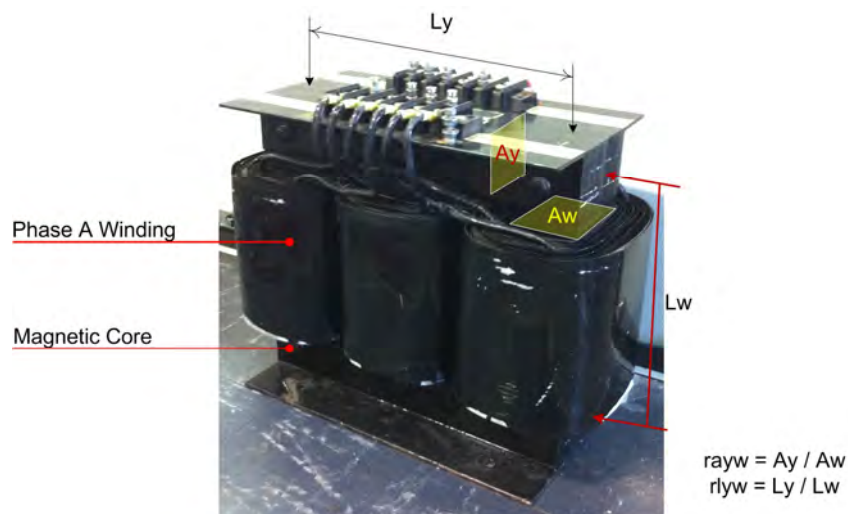


Figure 4-7: The three-phase, three-limb, 10 kVA transformer used in the all-hardware implementation of the laboratory-scale study system.

Figure 4-7 shows a photograph of the 10 kVA transformer that was used to supply the front end of the motion control system in the all-hardware implementation of the laboratory-scale study system. As shown in Figure 4-7, the windings of the transformer are situated on an inter-connected three-limb magnetic core structure as is commonly the case in three-phase power transformers. Initially, a regular RSCAD model of a three-phase transformer was used to represent this transformer within the real-time simulation. However, when attempts were made to validate this model against measured results during practical upstream fault tests on the laboratory-scale system similar to those described in the previous section, it was found that the regular RSCAD transformer model was not sufficiently detailed to represent the actual behaviour observed on the laboratory transformer during asymmetrical fault conditions as described below.

In practical measurements on the laboratory-scale study system it was found that a fault on any single phase in the upstream distribution network resulted in a sag in the transformer secondary voltage not only in the faulted phase, but also to a lesser, but still significant extent, in the un-faulted phases, despite the fact that the transformer primary and secondary windings were both connected in star and solidly earthed (Yyn). By contrast, when the regular RSCAD transformer model was used to represent this Yyn transformer connection being used in the laboratory-scale system, the simulation results incorrectly predicted that a single-phase fault in the upstream network would have a negligible effect on the secondary voltages and currents of the transformer in the un-faulted phases.

These observations in the laboratory tests suggested firstly that there is sufficient interaction between the phases of a standard, 3-limb, three-phase transformer due to mutual magnetic coupling that these effects need to be represented properly in the simulation model of the transformer used for asymmetric fault studies in this case; secondly, that the regular RSCAD model of a three-phase transformer does not represent these mutual coupling effects between the different phases of the transformer's magnetic circuit as is necessary for these studies.

In order to be able to properly represent the actual inter-phase magnetic coupling within the 10 kVA transformer during the simulation studies, a more-advanced transformer model that is available in RSCAD, known as a unified magnetic equivalent circuit (UMEC) model [66], was used. Figure 4-8 shows the appearance of the RSCAD implementation of the UMEC model [65] that was used to represent the 10 kVA laboratory transformer in these studies.

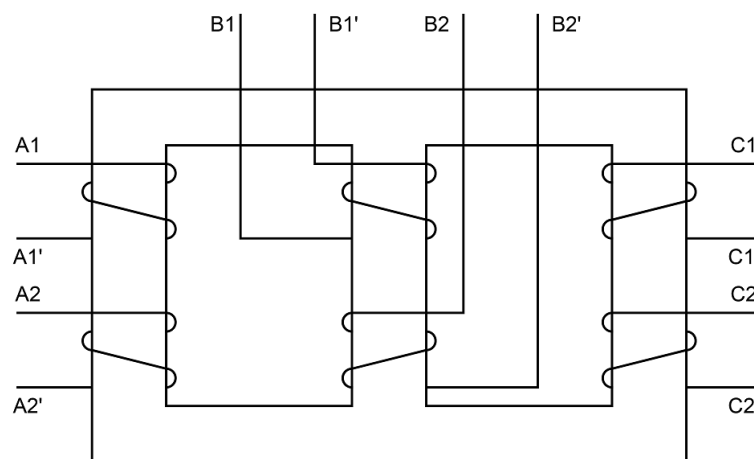


Figure 4-8: The RSCAD real-time implementation of the UMEC model.

In a similar manner to a regular transformer model, the UMEC model in RSCAD requires the rating information and saturation curve of the practical transformer being represented in the study, together with its electrical parameters as derived from standardised no-load and short-circuit tests. However, the UMEC model requires additional information in order to be able to correctly represent the mutual coupling characteristics between the different phases of the transformer's magnetic circuit by means of some simple normalised aspect ratios associated with the actual design characteristics of its three-limb core structure. The normalised aspect ratios that are required by the UMEC model from the practical transformer have been defined in [66] and they are the ratio of the transformer's core yoke to winding limb cross-sectional areas, as well as the ratio of the transformer's core yoke to winding limb lengths; these ratios are referred to as  $rayw$  and  $rlyw$  respectively in RSCAD. Figure 4-7 illustrates how the ratios  $rayw$  and  $rlyw$  required to complete the parameterization of the RSCAD UMEC model

were obtained from measurements of the actual core structure of the three-limb, 10 kVA transformer used in the all-hardware implementation of the laboratory study system. The rating information, electrical parameters, magnetisation curve and normalised core aspect ratios that were used to parameterize the RSCAD UMEC model of the 10 kVA laboratory transformer are shown in Tables 4-3 to 4-5.

*Table 4-3: Rating information of the 10 kVA transformer.*

<i>Manufacturer; Origin</i>	Abacus Controls Inc.; Somerville, NJ, USA
<i>Power rating [kVA]</i>	10
<i>Frequency [Hz]</i>	50
<i>Winding connection [Primary : secondary]</i>	Star : star, with both star points earthed
<i>Primary voltage [<math>V_{line-line}</math>]</i>	208
<i>Primary current [A]</i>	27.8
<i>Secondary voltage [<math>V_{line-line}</math>]</i>	380
<i>Secondary current [A]</i>	15.2

*Table 4-4: Measured equivalent per-phase electrical parameters of the 10 kVA transformer.*

<i>Primary winding resistance [<math>\Omega</math>]</i>	0.05
<i>Secondary winding resistance [<math>\Omega</math>]</i>	0.04
<i>Combined leakage reactance of windings [<math>\Omega</math>]</i>	0.08
<i>Core loss resistance [<math>\Omega</math>]</i>	1575.6
<i>Magnetising reactance [<math>\Omega</math>]</i>	124.7

*Table 4-5: Normalised core aspect ratios measured from the 10 kVA transformer's 3-limb core.*

<i>rayw = ratio of core yoke to winding limb cross-sectional areas</i>	1.048
<i>rlyw = ratio of core yoke to winding limb lengths</i>	1.157

Figure 4-9 shows the measured magnetisation curve of the laboratory 10 kVA transformer which was obtained during a magnetisation test. The curve is presented in per-unit voltage and percentage current. The base values that were used for the per-unit and percentage calculations are 120 V and 27.8 A which are the rated phase-to-neutral voltage and current of the transformer's primary windings respectively.

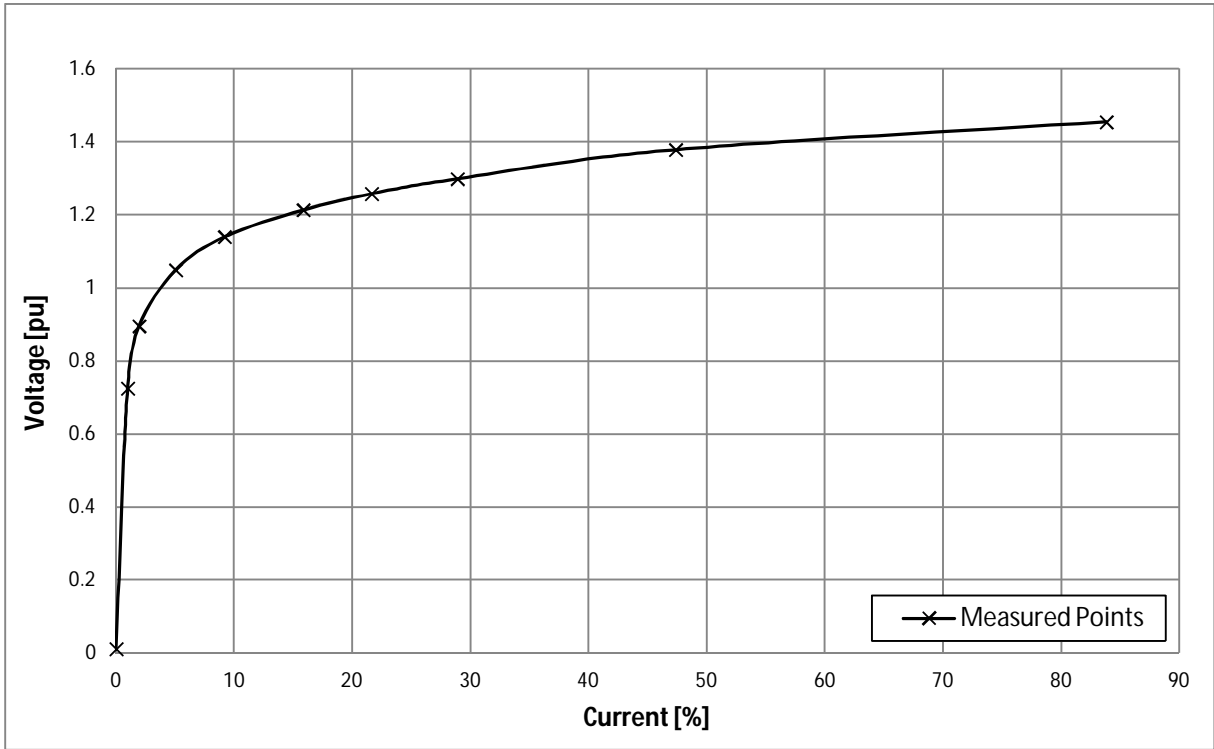


*Figure 4-9: Measured magnetisation curve of the 10 kVA transformer.*

The next section presents the validation of the UMEC model used to represent the 10 kVA transformer within the real-time simulation model of the laboratory-scale study system.

#### 4.4.1 Validation of the Real-Time Model

The approach used to validate the accuracy and suitability of the UMEC model of the 10 kVA transformer is an extension of that used already to validate the real-time simulation model of the faulted distribution network in the previous section. Furthermore, this approach is also used in subsequent sections to validate the real-time models of other key components of the plant within the laboratory-scale study system.

Figure 4-10 below shows the sub-section of the full laboratory-scale study system that was implemented in the laboratory and then simulated with real-time models in order to allow a comparison to be made between the performance of the practical 10 kVA transformer and its UMEC model under fault conditions.

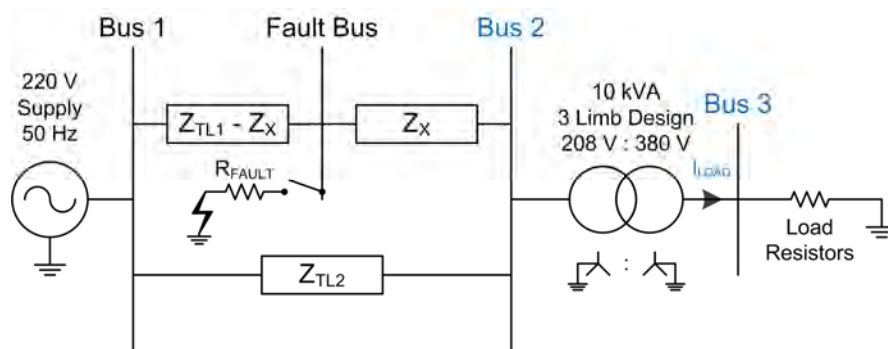


Figure 4-10: Sub-system used to test the validity of the UMEC model of the 10 kVA transformer component.

The test subsystem in Figure 4-10 is made up of the previously-validated part of the laboratory-scale study system (the faulted distribution network to the left of Bus 2), the 10 kVA transformer component situated between Buses 2 and 3, and a resistive load component connected at Bus 3. The test subsystem was operated as follows. Firstly, the source at Bus 1 was energised to supply the transformer at Bus 2 with nominal voltage via the two parallel paths of the distribution network situated between Buses 1 and 2. The transformer then stepped up the incoming voltage at Bus 2 so that the three-phase resistive load at Bus 3 was supplied with power at a nominal voltage of 380 V. A set of short-circuit faults was applied in particular phases at the Fault Bus so as to create voltage sags of desired depths in the corresponding phases of the transformer's Bus 2 input voltages. The value of the three-phase load resistance at Bus 3 was fixed in order to make the current in the 380 V windings of the transformer representative of the current that would later be supplied by these windings when the transformer was used to supply the motion control system in the full implementation of the laboratory-scale study system.

Table 4-6 shows a summary of the set of fault conditions that was applied at the Fault Bus and the characteristics of the resulting voltage sags that were created at Bus 2 during these model validation tests.

*Table 4-6: Summary of the fault conditions applied to the test subsystem of Figure 4-10 together with the resulting voltage sag characteristics seen at Bus 2.*

	Fault type at Fault Bus [Phases to ground]	Duration [ms]	Voltage sag depth at Bus 2 [%]	Remaining voltage at Bus 2 during fault [%]
(i)	C-ground	100	70	30
(ii)	A-B-ground	100	50	50
(iii)	A-B-C-ground	100	70	30

During each fault test, measurements were made of the primary and secondary winding voltages of the transformer in the laboratory system at Buses 2 and 3 respectively, and of the current  $I_{LOAD}$  flowing in the secondary winding of the transformer (as defined in Figure 4-10). Thereafter, these same fault tests were applied to the real-time simulation model of the test subsystem and recordings made of the simulated responses of the corresponding transformer variables. In the graphical results that follow the measured values of these transformer variables are compared against the values predicted by the real-time model for each of the three faults shown in Table 4-6.

Figures 4-11 (a) and (b) compare the results obtained from the practical and simulated implementations of the test subsystem in response to the phase C to ground fault described in Table 4-6. The comparison in Figure 4-11 shows that there is excellent agreement between the simulated and measured variables for all three phases of the Bus 2 voltages [Figure 4-11 (a)] and the Bus 3 voltages and currents [Figure 4-11 (b)], particularly in respect of the dynamic characteristics at the inception and removal of the fault. A close examination of the voltages at Bus 2 and Bus 3 during the active period of the fault reveals that sags are present in both the measured and simulated voltages of the un-faulted A and B phases and furthermore, the magnitudes of the currents supplied to the resistive load from the un-faulted phases during this period also decrease with respect to their pre-fault values. These results illustrate not only the important impact on voltage sags during asymmetric faults of the mutual coupling between the different phases in the magnetic circuit of a 3-limb transformer, but also that by means of a carefully-parameterized UMEC model it is possible to represent the influence of these inter-phase coupling effects on the voltage sags accurately within the real-time simulation model of the plant.

In particular, the close agreement between the actual voltage sags and load-currents measured on the secondary side of the transformer and those predicted by the UMEC model for both the faulted and un-faulted phases confirms both the accuracy and validity of the real-time model of the drive transformer to be used in the studies in this thesis.

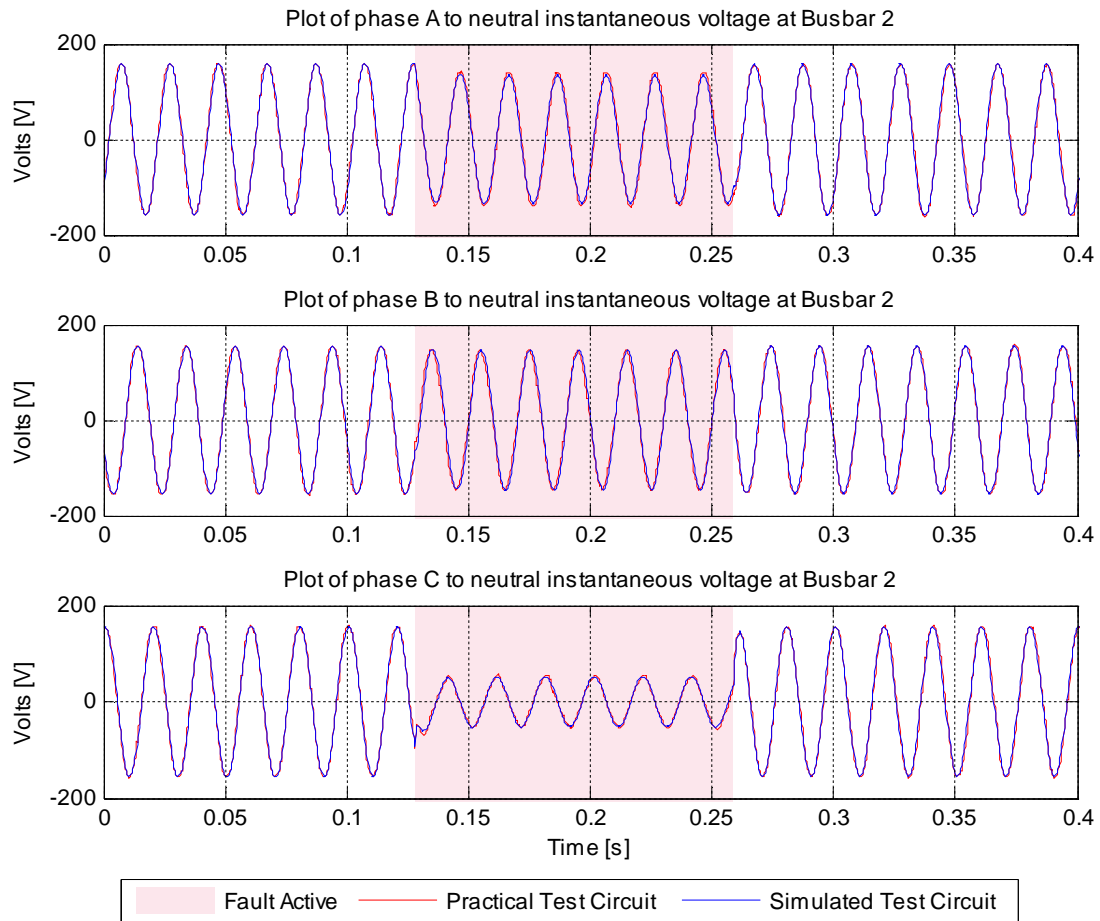


Figure 4-11 (a) — Validation of drive transformer model: (i) Phase C-ground fault with 70 % voltage sag; Bus 2 voltages.

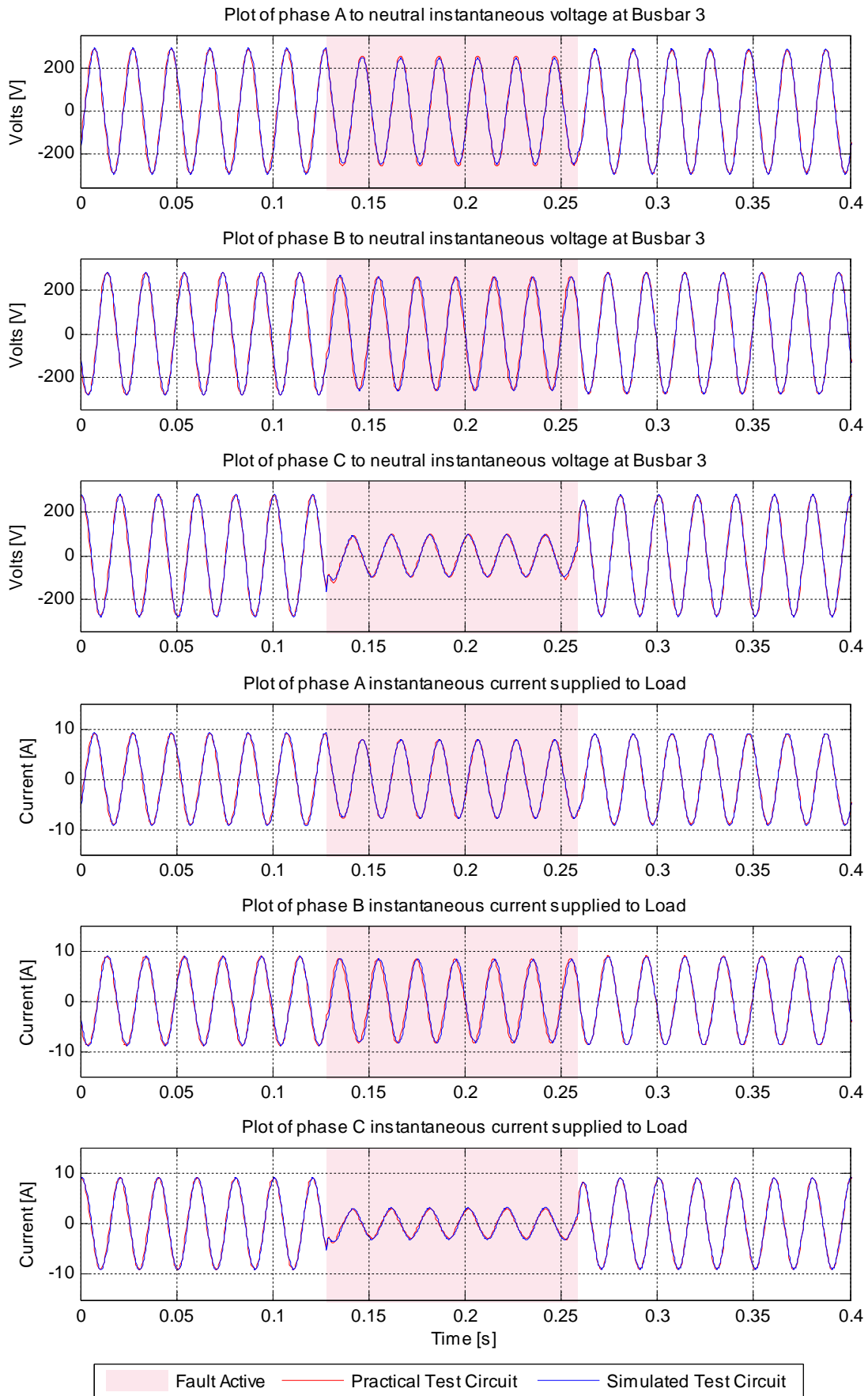


Figure 4-11 (b) — Validation of drive transformer model: (i) Phase C-ground fault with 70 % voltage sag; Bus 3 voltages and currents.

Figures 4-12 (a) and (b) compare the results obtained from the practical and simulated implementations of the test subsystem during the application of the phase A to B to ground fault described in Table 4-6. The comparisons in Figure 4-12 show that there is excellent agreement between the simulated and measured variables for all three phases of the Bus 2 voltages [Figure 4-12 (a)] and the Bus 3 voltages and currents [Figure 4-12 (b)], both in terms of the dynamic characteristics during the inception and removal of the fault, and also in respect of the depression in the magnitudes of the voltages and currents during the active period of the fault. A close examination of phase C of the Bus 2 voltages, and of phase C of the Bus 3 voltages and currents during the fault, reveals that significant depressions occur in the magnitudes of these variables despite the fact that no fault was applied to phase C at the Fault Bus.

Once again, the behaviour of the variables in the un-faulted phase during this test clearly illustrates the importance in voltage sag studies of properly representing the actual coupling that occurs between the magnetic fluxes in each phase of the transformer as a result of its interconnected multi-limb core structure. The results also clearly indicate the validity of the UMEC model for such studies and its ability to accurately represent these phenomena when correctly parameterized.

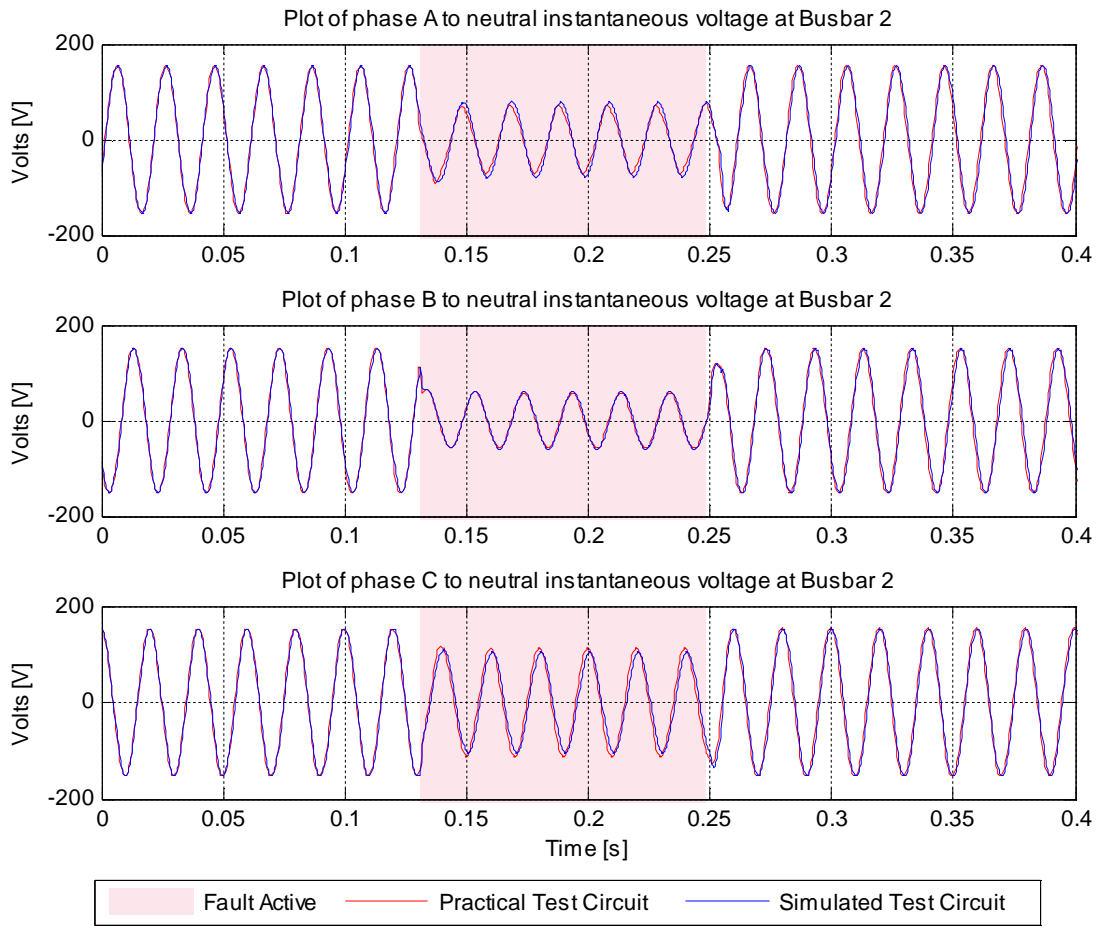


Figure 4-12 (a) — Validation of drive transformer model: (ii) Phase A-B-ground fault with 50 % voltage sag; Bus 2 voltages.

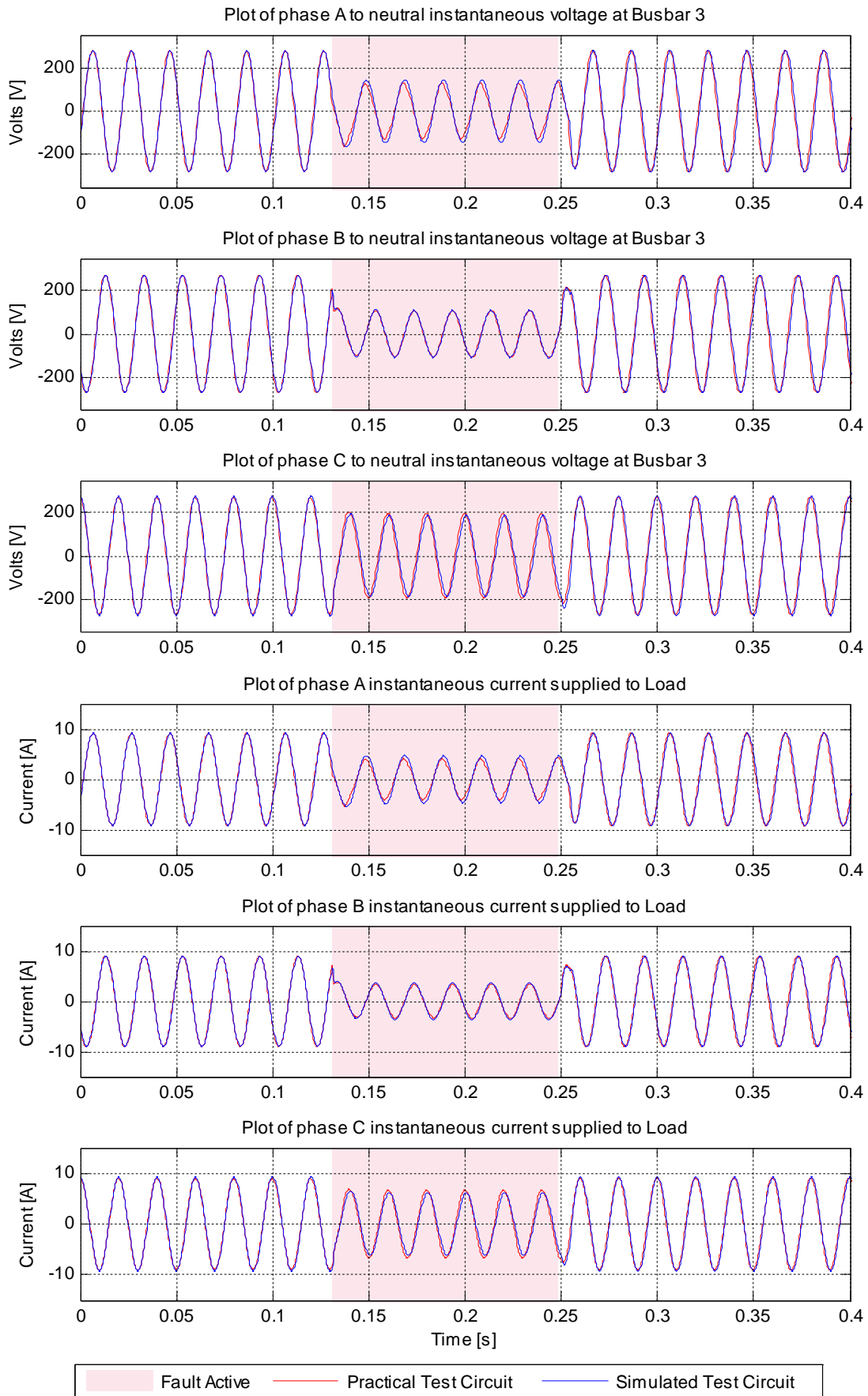


Figure 4-12 (b) — Validation of drive transformer model: (ii) Phase A-B-ground fault with 50 % voltage sag; Bus 3 voltages and currents.

Finally, Figures 4-13 (a) and (b) compare the results obtained from the practical and simulated implementations of the test subsystem during the application of the three-phase to ground fault at the Fault Bus. The comparisons in Figure 4-13 once again show that there is excellent agreement between the simulated and measured variables for all three phases of the Bus 2 voltages [Figure 4-13 (a)] and the Bus 3 voltages and currents [Figure 4-13 (b)] both in terms of the dynamic characteristics during the inception and removal of the fault, and also in terms of the depression in the magnitudes of these variables prior to the removal of the fault.

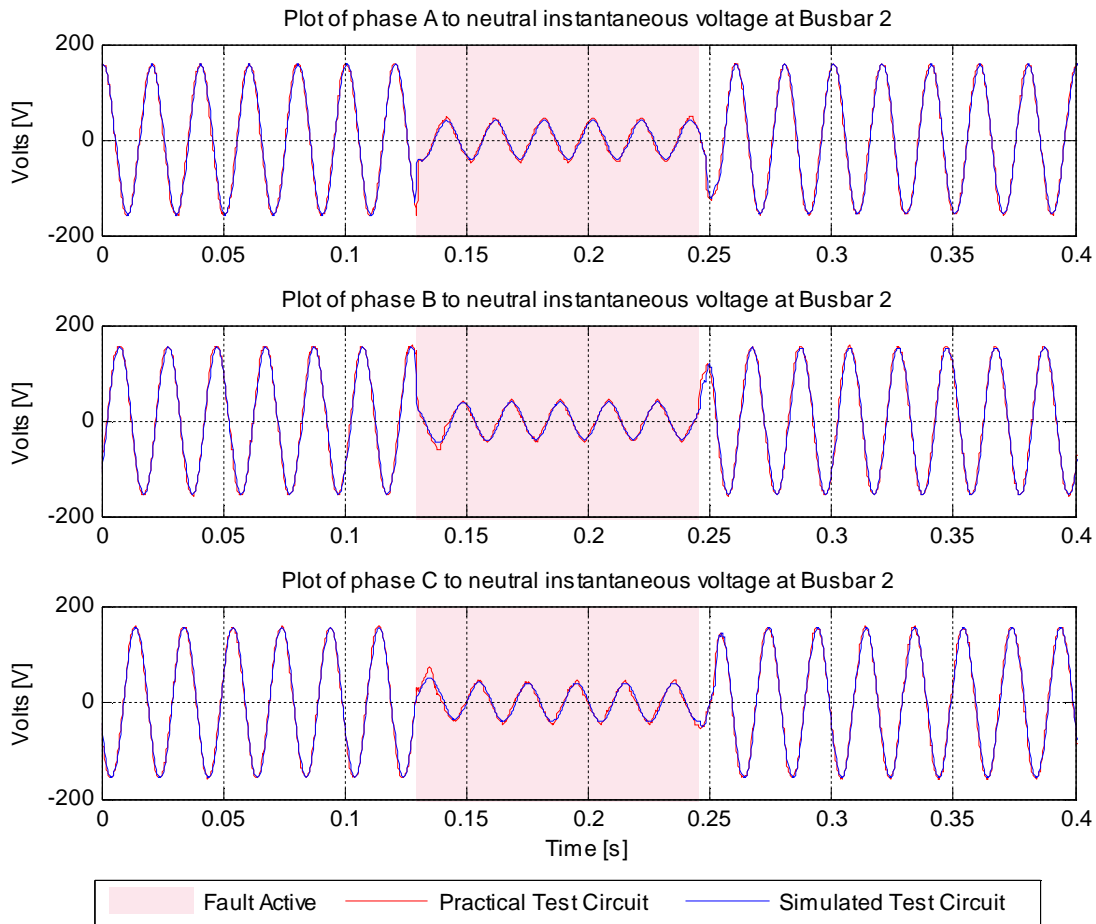


Figure 4-13 (a) — Validation of drive transformer model: (iii) Phase A-B-C-ground fault with 70 % voltage sag; Bus 2 voltages.

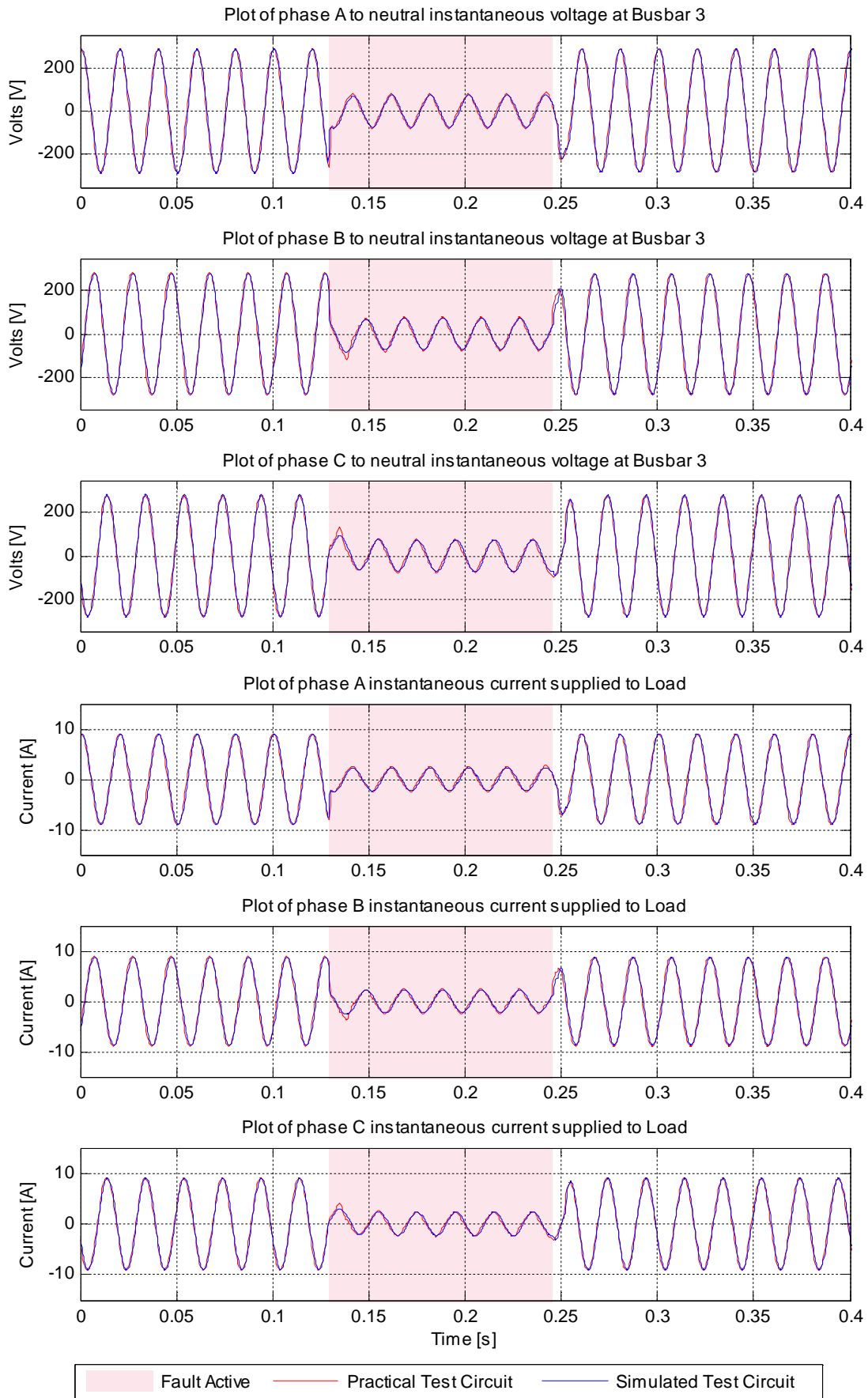


Figure 4-13 (b) — Validation of drive transformer model: (iii) Phase A-B-C-ground fault with 70 % voltage sag; Bus 3 voltages and currents.

It is interesting to note that in the results of the test shown in Figure 4-13, all three phases of the transformer secondary voltages and currents are depressed to the same extent due to the symmetrical nature of the upstream fault in this particular case. If the tests that the motion control system were to be subjected to in the thesis were limited to voltage sags caused by simple symmetrical faults, important interactions and influences on the performance of the system, such as mutual coupling between the phases of the drive transformer, would not be revealed in the analysis. These results therefore not only support the conclusions reached in [17] regarding the importance of testing ASDs using a full range of sag types, rather than simply using symmetrical three-phase sags, but further support the value of including detailed representations of the upstream supply system during such tests (as proposed in this thesis) in order to properly understand the likelihood of, causes, and extent of any inter-phase and inter-plant interactions.

The following section describes the real-time model that was used to represent the line reactor in the laboratory-scale study system.

## 4.5 The Line Reactor Model

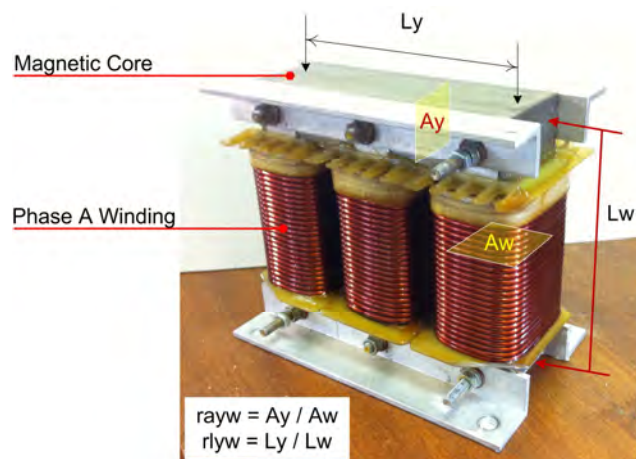


Figure 4-14: The three-phase, three-limb, line reactor used in the all-hardware implementation of the laboratory-scale study system.

Figure 4-14 shows a photograph of the line reactor that was used at the front end of the motion control system in the all-hardware implementation of the laboratory-scale study system. The photograph shows that the individual phase windings of the reactor are each wound on one limb of a single, coupled three-limb magnetic core structure in a similar manner to the windings of a three-phase transformer. This type of three-limb magnetic core structure is representative of the type of line reactor designs actually used in practice on active front-end converter installations in industrial drive systems. The results shown in the previous section have clearly demonstrated the importance of modelling the inter-phase magnetic coupling that arises as a result of the three-limb core structure of the drive transformer in studies such as this. Hence, as a result of these insights gained when modelling the inter-phase magnetic coupling of the drive transformer, a UMEC-type model was also chosen to represent the line reactor in the real-time simulation model of the laboratory-scale study system.

The line reactor's rating information, electrical parameters, normalised core aspect ratios (as defined in Figure 4-14), and magnetisation curve were used to parameterize its UMEC model; these parameter details are shown in Tables 4-7 to 4-9 and Figure 4-15 which follow.

Table 4-7: Rating information for the line reactor.

Nominal voltage [V]	400
Nominal current [A]	22.1

Table 4-8: Measured equivalent per-phase electrical parameters of the line reactor.

Winding resistance [ $\Omega$ ]	0.03
Leakage inductance [mH]	2.77

Table 4-9: Normalised core aspect ratios measured from the line reactor's 3-limb core.

$r_{yw}$ = ratio of core yoke to winding limb cross-sectional areas	0.912
$r_{lyw}$ = ratio of core yoke to winding limb lengths	0.980

Figure 4-15 shows the measured magnetisation curve of the practical line reactor which was obtained during a magnetisation test.

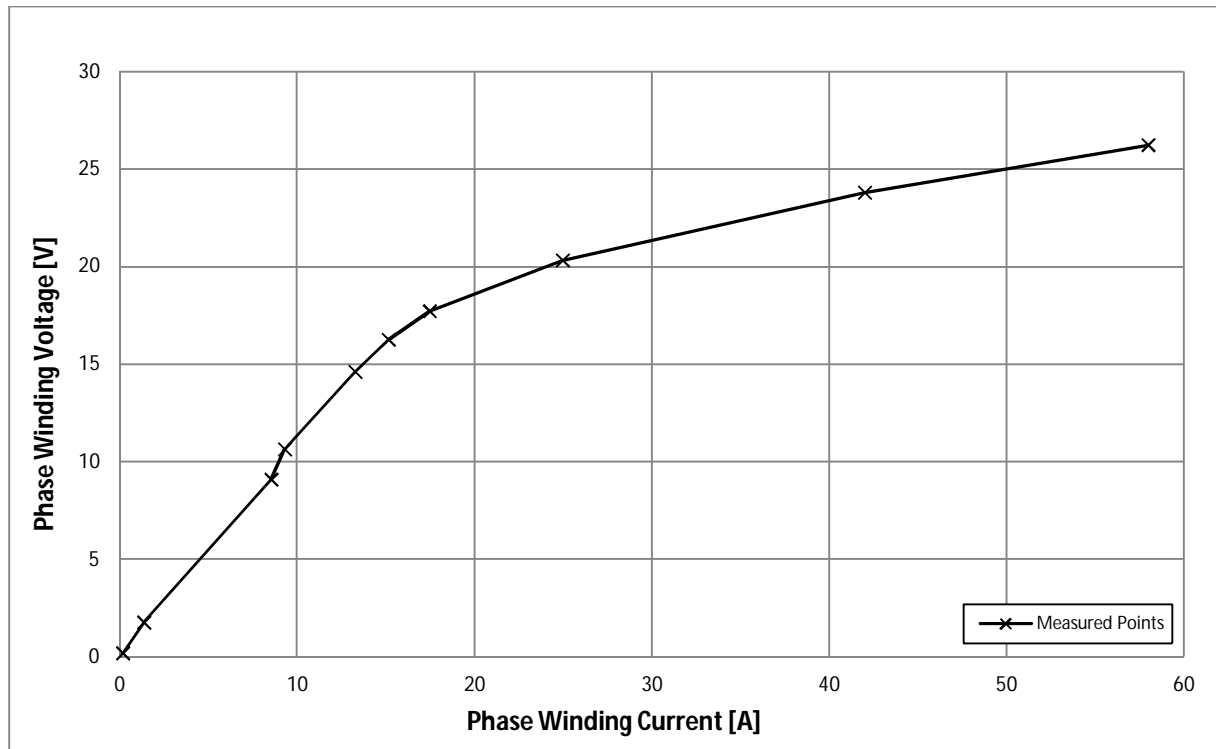


Figure 4-15: Measured magnetisation curve of the line reactor.

The following section presents the validation of the UMEC model used to represent the practical line reactor within the real-time simulation model of the laboratory-scale study system.

#### 4.5.1 Validation of the Real-Time Model

The approach used to validate the accuracy and suitability of the UMEC model of the line reactor is once again an extension of that used already to validate the model of the drive transformer in the previous section. Figure 4-16 below shows the sub-section of the full laboratory-scale study system that was implemented in the laboratory and then simulated with real-time models in order to allow a comparison to be made between the performance of the practical line reactor and its UMEC model under fault conditions.

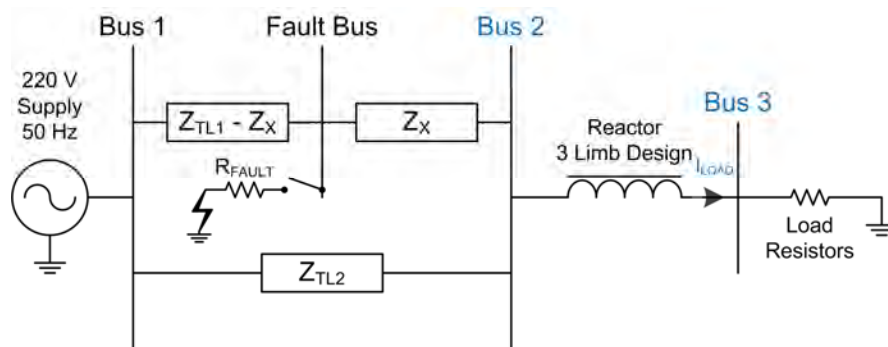


Figure 4-16: Sub-system used to test the validity of the UMEC model of the line reactor component.

The test subsystem in Figure 4-16 is made up of the previously-validated part of the laboratory-scale study system (the faulted distribution network to the left of Bus 2), the line reactor component situated between Buses 2 and 3, and a resistive load component connected at Bus 3. The test subsystem was operated as follows. Firstly, the source at Bus 1 was energised so that Bus 2 received nominal voltage via the two parallel paths of the distribution network situated between Buses 1 and 2. The reactor was then used to transfer energy from Bus 2 to the resistive load at Bus 3. A set of short-circuit faults was applied in particular phases at the Fault Bus so as to create voltage sags of desired depths in the corresponding phases at Bus 2. The value of the three-phase load resistance at Bus 3 was once again fixed to make the current in the line reactor's windings representative of the current that would later be supplied through these windings when the line reactor was used to feed the actual motion control system in the full implementation of the laboratory-scale study system.

Table 4-10 shows a summary of the set of fault conditions that were applied at the Fault Bus and the characteristics of the resulting voltage sags that were created at Bus 2 during these model validation tests.

*Table 4-10: Summary of the fault conditions applied to the test subsystem of Figure 4-16 together with the resulting voltage sag characteristics seen at Bus 2.*

	Fault type at Fault Bus [Phases to ground]	Duration [ms]	Voltage sag depth at Bus 2 [%]	Remaining voltage at Bus 2 during fault [%]
(i)	A-ground	100	70	30
(ii)	A-B-ground	100	70	30
(iii)	A-B-C-ground	100	70	30

During each fault test, measurements were made of the Bus 2 and Bus 3 voltages on either side of the reactor and of the current  $I_{LOAD}$  flowing through the line reactor's windings (as defined in Figure 4-16). Thereafter, these same fault tests were applied to the real-time simulation model of the test subsystem and recordings made of the simulated responses of the corresponding line reactor variables.

Figures 4-17 (a) and (b) compare the results obtained from the practical and simulated implementations of the test subsystem in response to the phase A to ground fault described in Table 4-10. The comparison in Figure 4-17 shows that there is excellent agreement between the simulated and measured variables for all three phases of the Bus 2 voltages [Figure 4-17 (a)] and the Bus 3 voltages and currents [Figure 4-17 (b)].

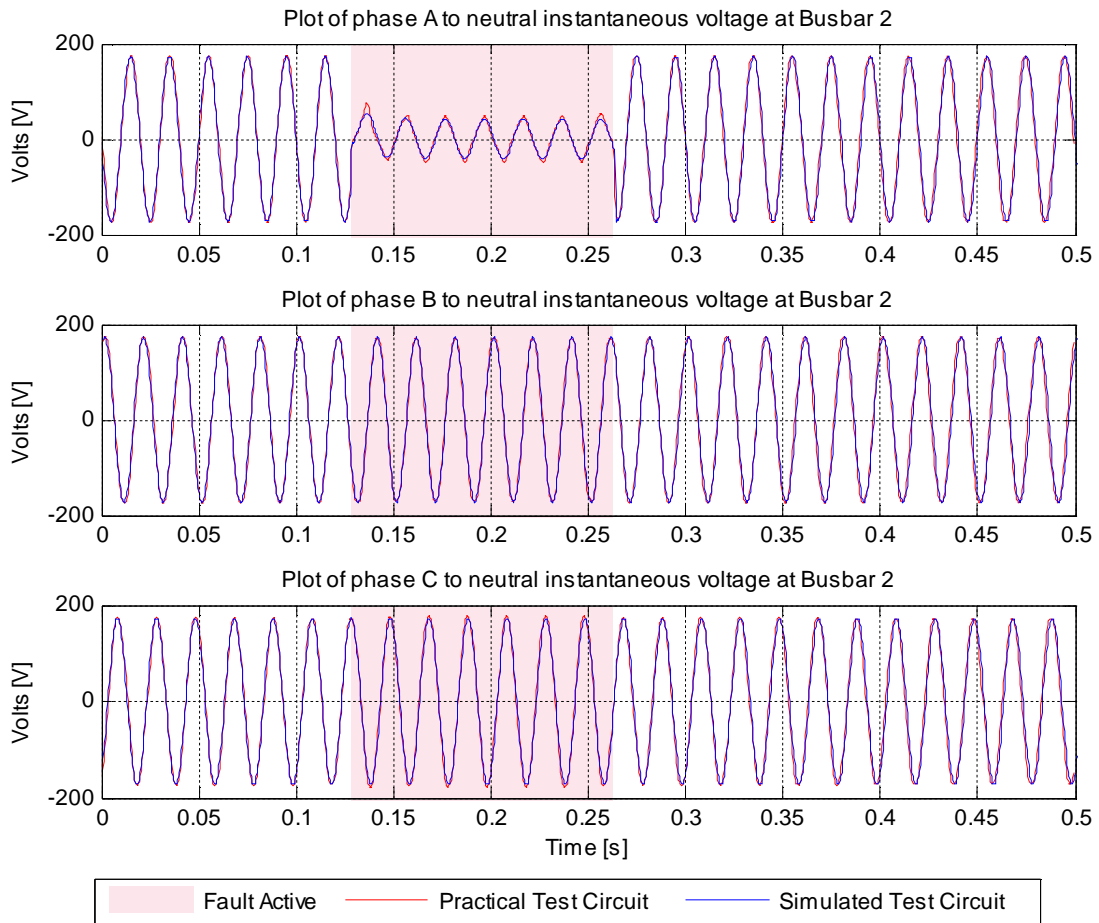


Figure 4-17 (a) — Validation of line reactor model: (i) Phase A-ground fault with 70 % voltage sag; Bus 2 voltages.

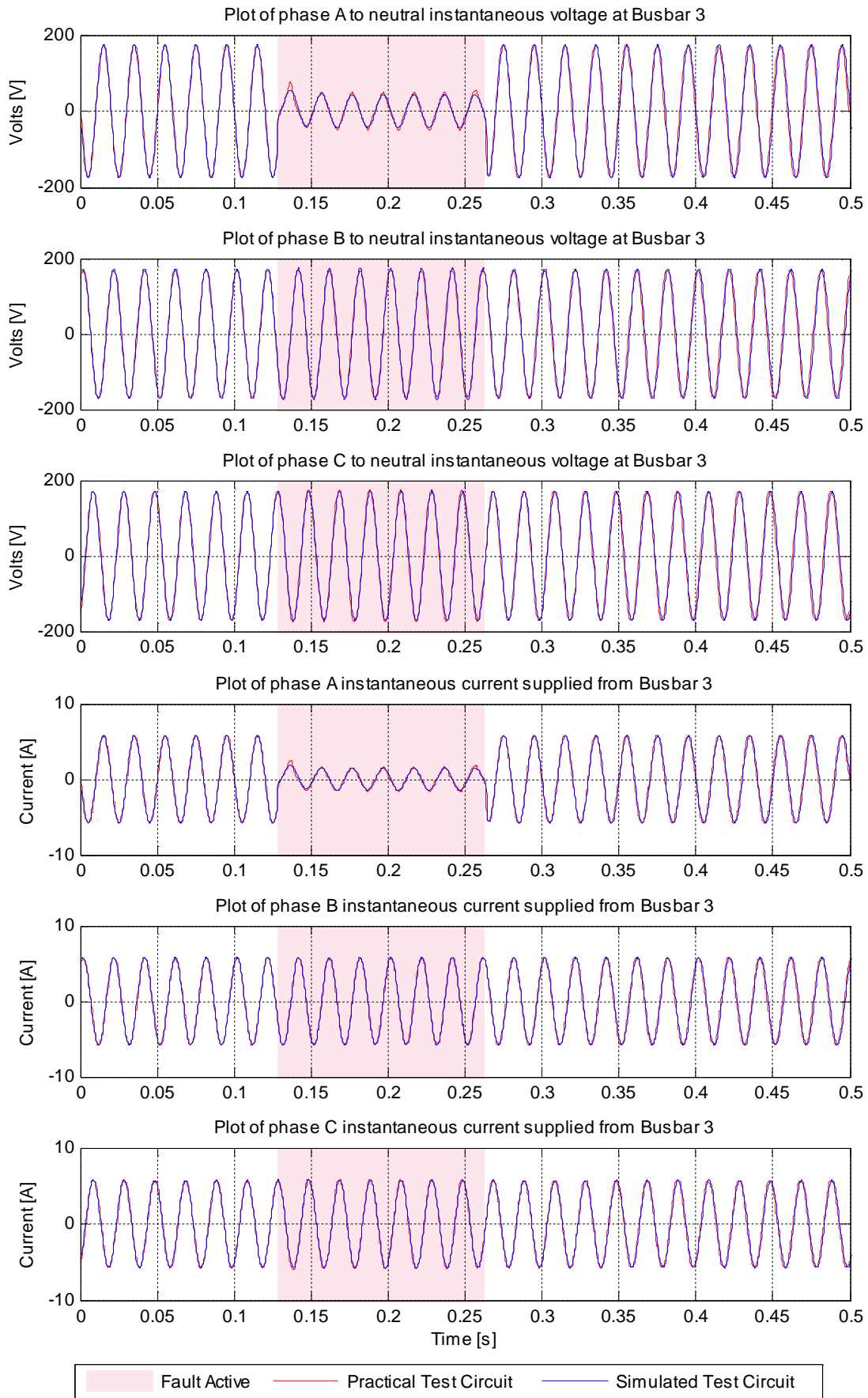


Figure 4-17 (b) — Validation of line reactor model: (i) Phase A-ground fault with 70 % voltage sag; Bus 3 voltages and currents.

Figures 4-18 (a) and (b) compare the results obtained from the practical and simulated implementations of the test subsystem in response to the double-phase to ground fault described in Table 4-10. The comparisons of the Bus 2 voltages [Figure 4-18 (a)] and of the Bus 3 voltages and currents [Figure 4-18 (b)] show that there is once again excellent agreement between the simulated and measured variables, in all three phases.

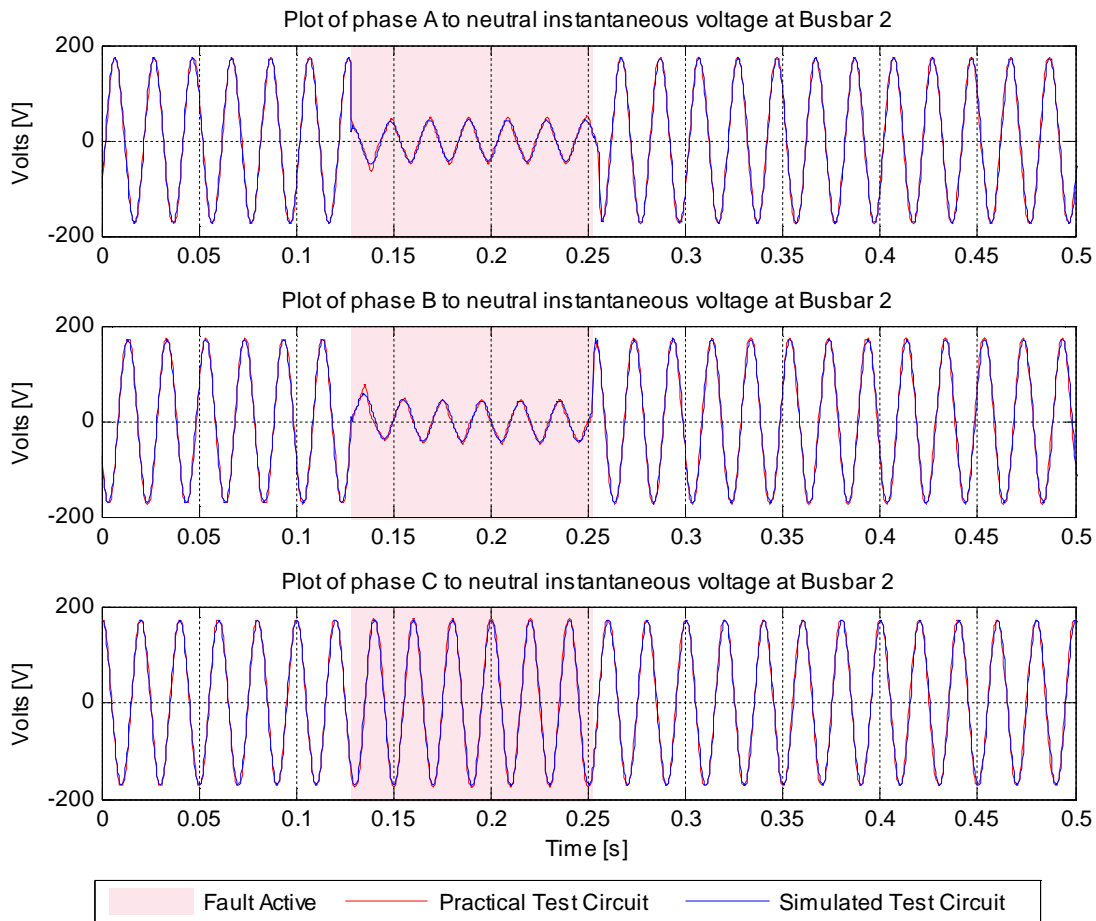


Figure 4-18 (a) — Validation of line reactor model: (ii) Phase A-B-ground fault with 70 % voltage sag; Bus 2 voltages.

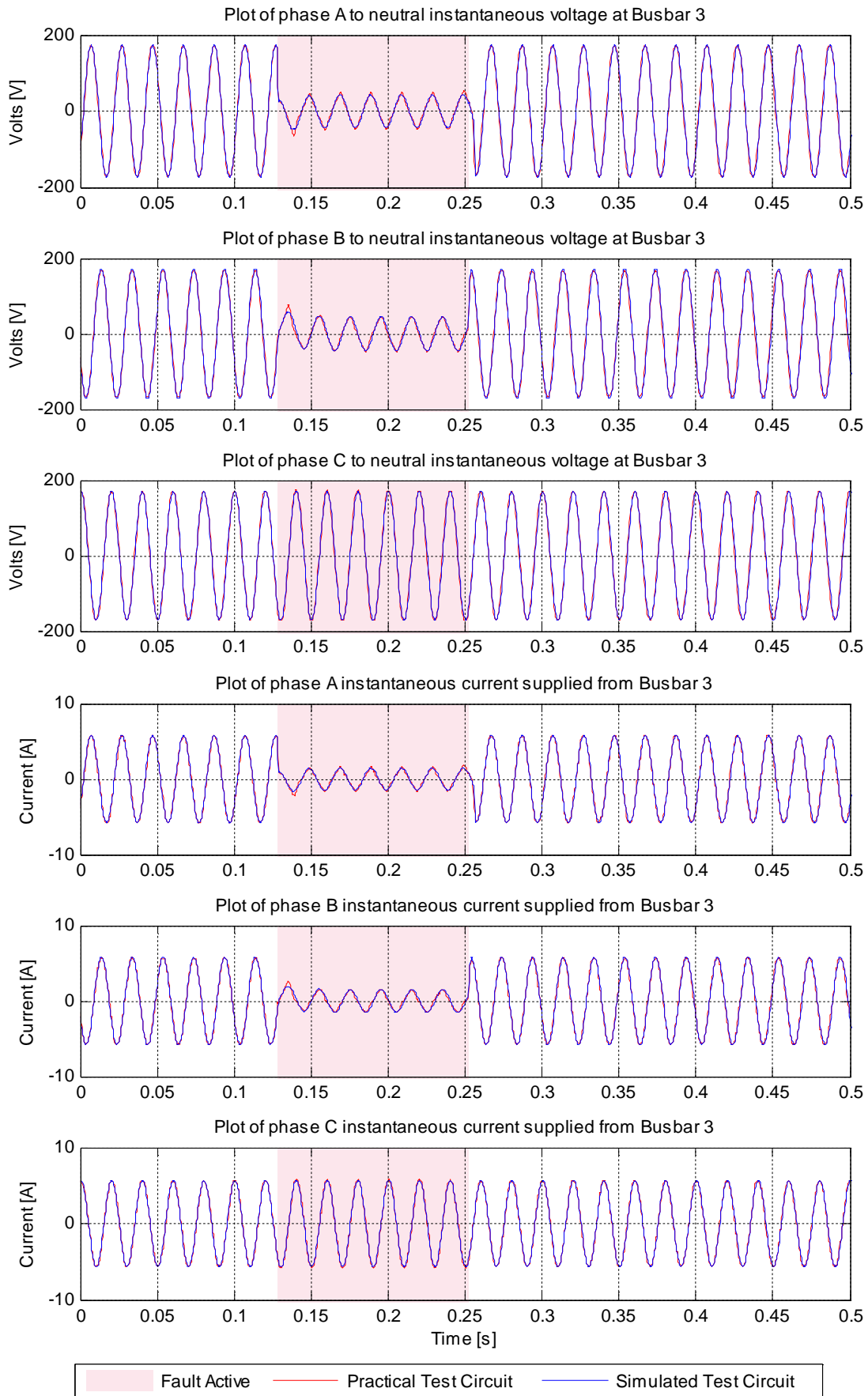


Figure 4-18 (b) — Validation of line reactor model: (ii) Phase A-B-ground fault with 70 % voltage sag; Bus 3 voltages and currents.

Finally, Figures 4-19 (a) and (b) compare the results obtained from the practical and simulated implementations of the test subsystem during the application of the three-phase to ground fault at the Fault Bus. The comparisons in Figure 4-19 once again show that there is excellent agreement between the simulated and measured variables for all three phases of the Bus 2 voltages [Figure 4-19 (a)] and the Bus 3 voltages and currents [Figure 4-19 (b)].

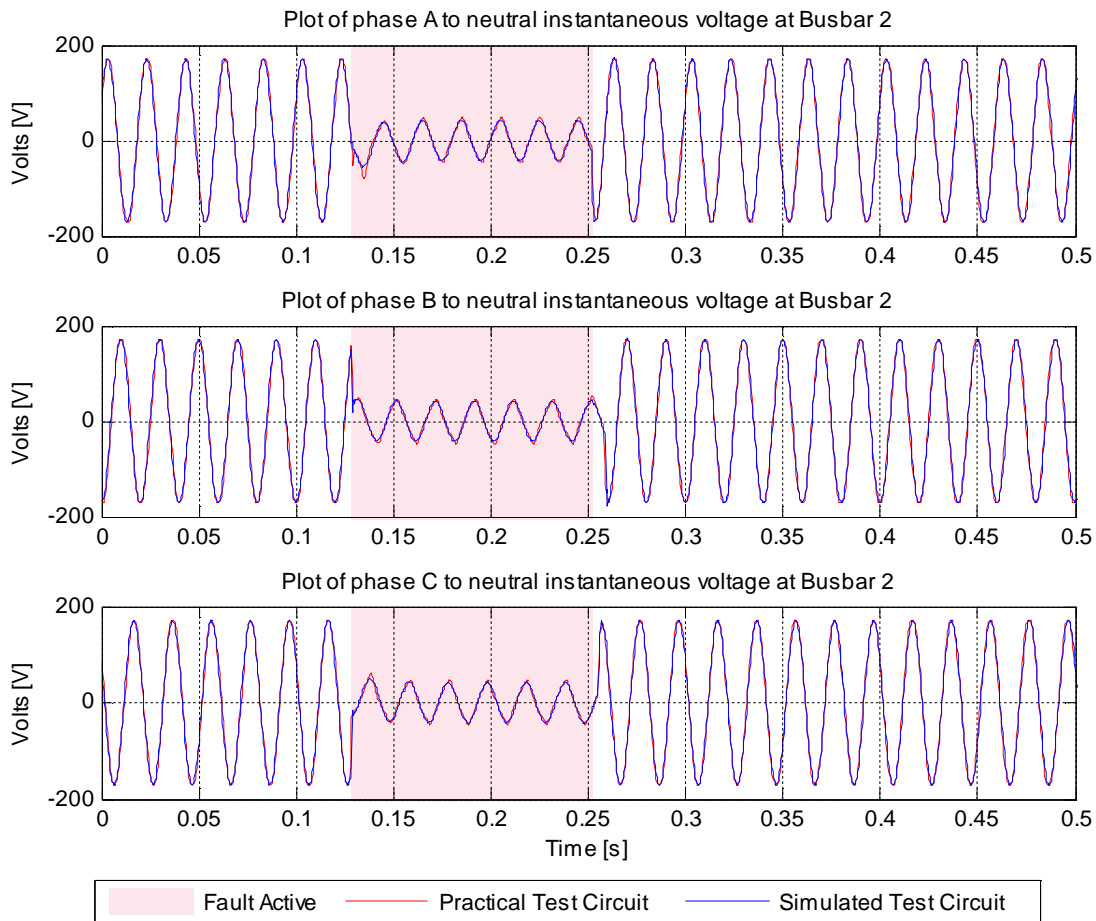


Figure 4-19 (a) — Validation of line reactor model: (iii) Phase A-B-C-ground fault with 70 % voltage sag; Bus 2 voltages.

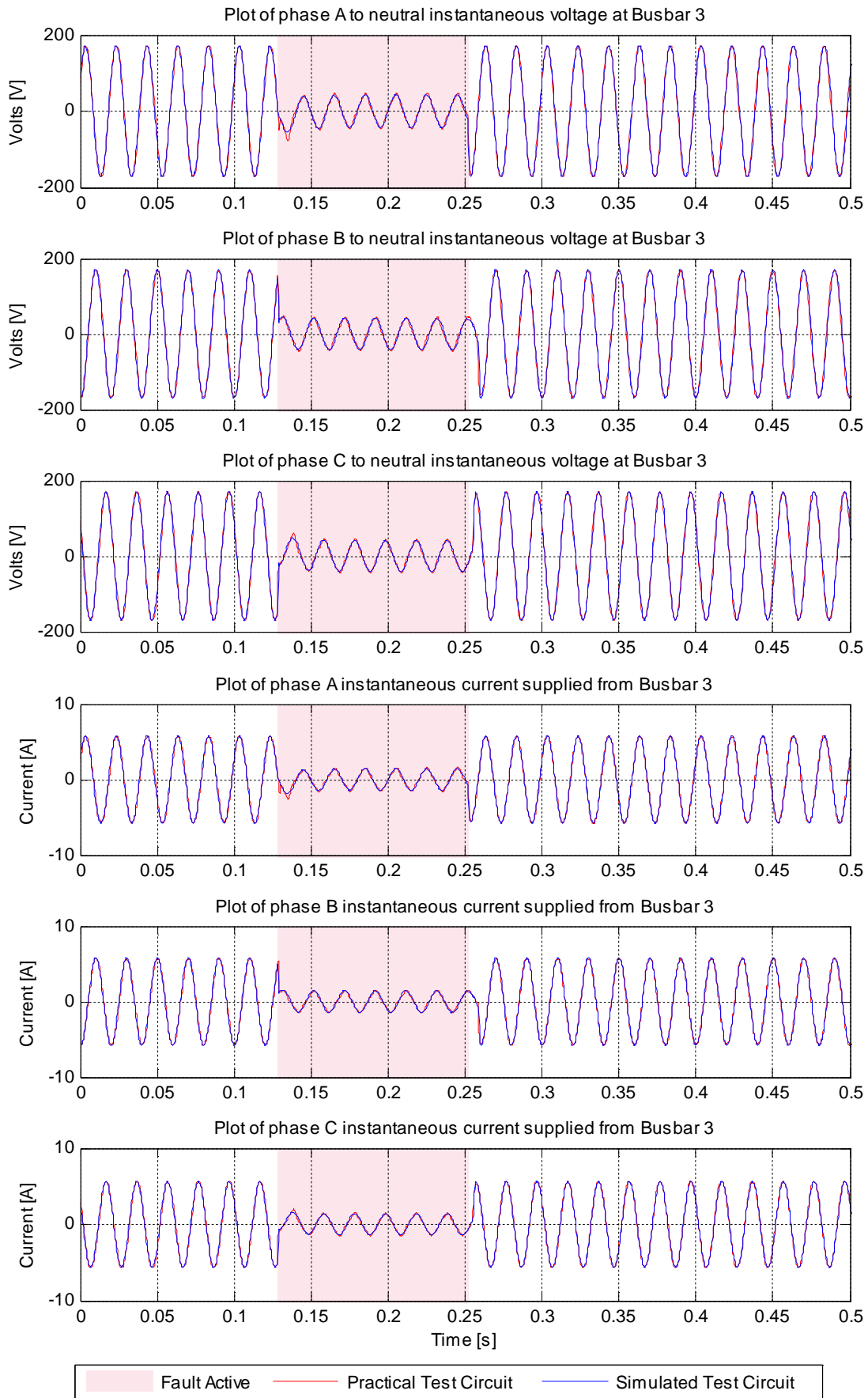


Figure 4-19 (b) — Validation of line reactor model: (iii) Phase A-B-C-ground fault with 70 % voltage sag; Bus 3 voltages and currents.

The results in all three sets of model validation tests presented in this section (Figures 4-17 to 4-19) indicate that at least in the case of the series line reactor component, its three-limb core structure does not appear to contribute to a significant extent to the inter-phase coupling effect that causes faults in one phase of the system to influence the voltages and currents of other phases that was observed for the three-limb drive transformer. As such, it may have been possible to use a simpler mathematical model to represent the drive reactor than the UMEC modelling approach adopted here. Nevertheless, these results confirm that the mathematical representation of the line reactor used in the real-time simulation models in these studies is sufficiently accurate and valid to correctly represent the characteristics of the actual drive reactor hardware used in the laboratory-scale study system.

The following section describes the real-time models that were used to represent the micro-induction machine and dynamometer in the laboratory-scale study system.

## **4.6 The Micro-Induction Machine and Dynamometer Models**

### **4.6.1 Induction Machine Electrical Model**

As previously mentioned in Chapter 3, the micro-induction machine that was used as the drive motor in the laboratory-scale study system has a deep-bar rotor construction. The RSCAD library used to develop the real-time simulation models in these studies does not provide a mathematical model of a deep-bar rotor induction machine but it does provide a model of a double-cage rotor induction machine. However, according to Vas [59], a deep-bar rotor induction machine can be suitably represented using the mathematical model of a double-cage rotor machine, and hence this latter type of induction machine model was chosen to represent the drive motor in the real-time model of the laboratory-scale study system. In order to determine a set of double-cage model parameters suitable for describing the characteristics of the deep-bar induction machine used in the laboratory system, a parameter fitting algorithm was specifically developed by the author. The algorithm required, as inputs, measurements of the stator resistance and particular operational inductances and time constants of the actual laboratory machine. To this end, a detailed standstill frequency response test, using a variable-frequency AC source connected to the stator of the laboratory machine, was used to measure the particular operational inductances and time constants of the deep-bar machine that were required by the parameter fitting algorithm. These measured frequency-response parameters of the actual deep-bar machine in the laboratory were then used by the algorithm to calculate a set of equivalent double-cage machine model parameters to suit the type of model available in RSCAD.

Table 4-11 shows the final parameters for the RSCAD double-cage model representation of the laboratory deep-bar rotor induction machine used in these studies, obtained using the measurement and parameter fitting algorithm approach described above.

Table 4-11: Per-phase equivalent double-cage model parameters derived from actual parameter measurements of the deep-bar rotor micro-induction machine.

Parameter	Value in per unit	Value in ohms
<i>Stator winding resistance</i>	0.0055	0.08
<i>Stator leakage reactance</i>	0.1493	2.27
<i>Magnetising reactance</i>	3.5234	53.53
<i>Inner cage rotor resistance</i>	0.0087	0.13
<i>Inner cage rotor leakage reactance</i>	0.0896	1.36
<i>Outer cage rotor resistance</i>	0.0577	0.877
<i>Outer cage rotor leakage reactance</i>	0.0395	0.6
<i>Mutual leakage reactance between rotor cages</i>	0.0597	0.91

Note: The base values used for the per-unit machine model parameters are 127 V and 8.36 A which are the rated line to neutral voltage and the rated current of the machine.

#### 4.6.2 Induction Machine and Dynamometer Mechanical Model

Chapter 3 explained that in the all-hardware implementation of the laboratory-scale study system the micro-induction machine that served as the drive motor was coupled to a dynamometer via an in-line torque transducer. In order to properly represent the dynamic characteristics of this induction machine and dynamometer test set in the real-time simulation model of the laboratory-scale system plant, a model had to be developed to describe the dynamics of each machine's rotating inertia and of the shaft system coupling them together. A diagrammatic representation of this coupled rotational mechanical system is shown in Figure 4-20.

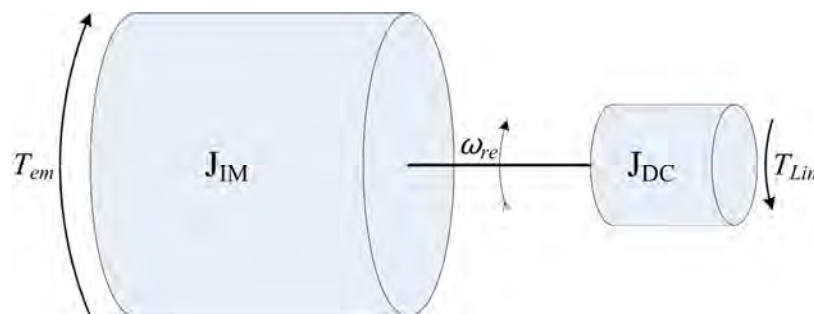


Figure 4-20: Rotational mechanical system model for the induction machine and dynamometer set.

Figure 4-20 shows that the rotating parts of the machine including its shaft, rotor, and coupling together with the in-line torque transducer were represented as a lumped inertia  $J_{IM}$ . This inertia was assumed to be rigidly connected to another lumped inertia  $J_{DC}$  used to represent the coupling, shaft and armature of the dynamometer. The frictional damping coefficients of the machine and dynamometer were also represented in the model. Finally, the load exerted on the shaft of the induction machine by the dynamometer was represented by the torque  $T_{Lin}$ .

The diagram in Figure 4-20 can be used to derive a differential equation describing the dynamics of this system as shown in Equation (4-1) below.

$$T_{em} = J_{IM} \frac{d\omega_{re}}{dt} + \beta_{IM} \omega_{re} + J_{DC} \frac{d\omega_{re}}{dt} + \beta_{DC} \omega_{re} + T_{Lin} \quad (4-1)$$

where:

$T_{em}$  is the instantaneous electromagnetic torque produced by the induction machine [Nm]

$J_{IM}$  is the total moment of inertia of the induction machine's shaft, rotor and coupling, lumped together with the moment of inertia of the torque transducer [kg.m<sup>2</sup>]

$\omega_{re}$  is the angular speed of the rotor [rad/s]

$\beta_{IM}$  is the coefficient of frictional damping of the induction machine [Nm/(rad/s)]

$J_{DC}$  is the total moment of inertia of the dynamometer's shaft, armature and coupling [kg.m<sup>2</sup>]

$\beta_{DC}$  is the coefficient of frictional damping of the dynamometer [Nm/(rad/s)]

$T_{Lin}$  is the load torque exerted by the dynamometer [Nm].

Measurements were carried out on the practical induction machine and dynamometer test set in the laboratory to determine the rotational inertia and frictional damping coefficient parameters for this dynamic model of the mechanical system; these measured parameters are shown in Table 4-12.

*Table 4-12: Measured values of the parameters of the mechanical dynamic model of the micro-induction machine and dynamometer test set.*

Parameter	Value
$\beta_{IM}$	0.003 Nm/(rad/s)
$\beta_{DC}$	0.0041 Nm/(rad/s)
$J_{IM}$	0.37 kg.m <sup>2</sup>
$J_{DC}$	0.042 kg.m <sup>2</sup>

As explained in Chapter 3, the dynamometer used in the laboratory-scale study system has a linear torque-speed characteristic, the gradient of which can be set by the user. The actual torque-speed characteristic of the dynamometer was measured for the particular setting to be used during the practical measurements on the laboratory-scale study system, and this characteristic is shown in Figure 4-21.

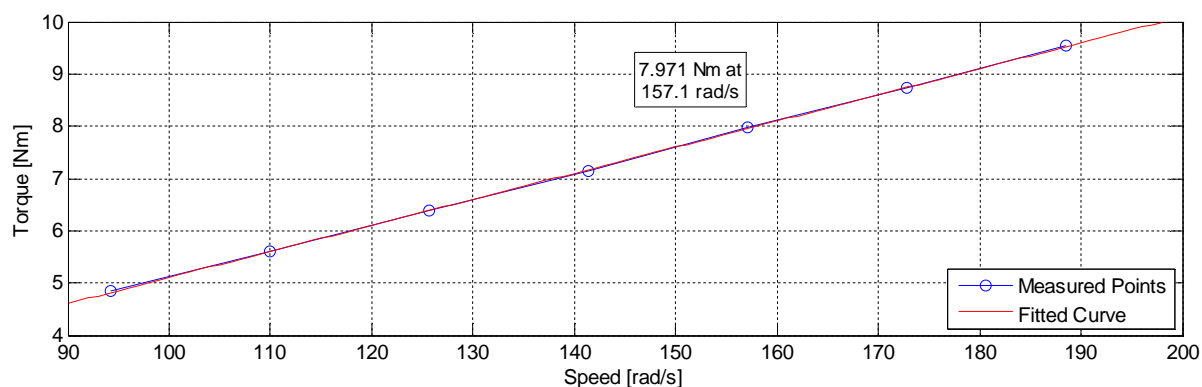


Figure 4-21: Measured torque-speed characteristic of the dynamometer.

An analysis of the measured torque-speed characteristic in Figure 4-21 was used to derive an equation describing the load torque  $T_{Lin}$  output by the dynamometer as a function of shaft speed as shown in Equation (4-2).

$$T_{Lin} = 0.05\omega_{re} + 0.116 \quad (4-2)$$

Equation (4-2) was then substituted into Equation (4-1) to form the complete differential equation model describing the rotational mechanical dynamics of the induction machine and dynamometer test set with the dynamometer settings actually used during tests on the all-hardware implementation of the laboratory-scale study system. This complete differential equation model was implemented using standard dynamic modelling functions from the RSCAD component model library in order to represent these rotational mechanical dynamics in the real-time simulation model of the study system.

The equivalent double-cage machine model used to represent the laboratory micro-induction machine and the mathematical model developed to describe the machine-dynamometer set's mechanical dynamics are validated in the next section.



*Table 4-13: Summary of the fault conditions applied to the test subsystem of Figure 4-22 together with the resulting voltage sag characteristics seen at Bus 2.*

	Fault type at Fault Bus [Phases to ground]	Duration [ms]	Voltage sag depth at Bus 2 [%]	Remaining voltage at Bus 2 during fault [%]
(i)	A-ground	100	70	30
(ii)	A-B-ground	100	70	30
(iii)	A-B-C-ground	100	70	30

During each fault test, measurements were made of the voltages supplied to the stator of the induction machine at Bus 2, the current  $I_{\text{MOTOR}}$  in the machine's stator windings (as defined in Figure 4-22), and the shaft speed of the machine-dynamometer set. The graphical results that now follow compare the measured behaviour of the induction machine during these tests with the response predicted by the real-time simulation model for each of the three faults shown in Table 4-13.

Figures 4-23 (a) and (b) compare the results obtained from the practical and simulated implementations of the test subsystem during the application of the upstream phase A to ground fault that caused a 70 % sag in the corresponding phase of the input voltage to the machine at Bus 2. The comparison in Figure 4-23 (a) shows excellent agreement between the measured and simulated values of the voltages and currents in the stator of the induction machine, both in respect of the dynamic characteristics of these variables during the inception and removal of the fault, as well as during the active period of the fault, when the transient behaviour of the asymmetric stator currents that was measured in the actual machine is accurately predicted by the double-cage dynamic model of the machine used in the real-time simulation model.

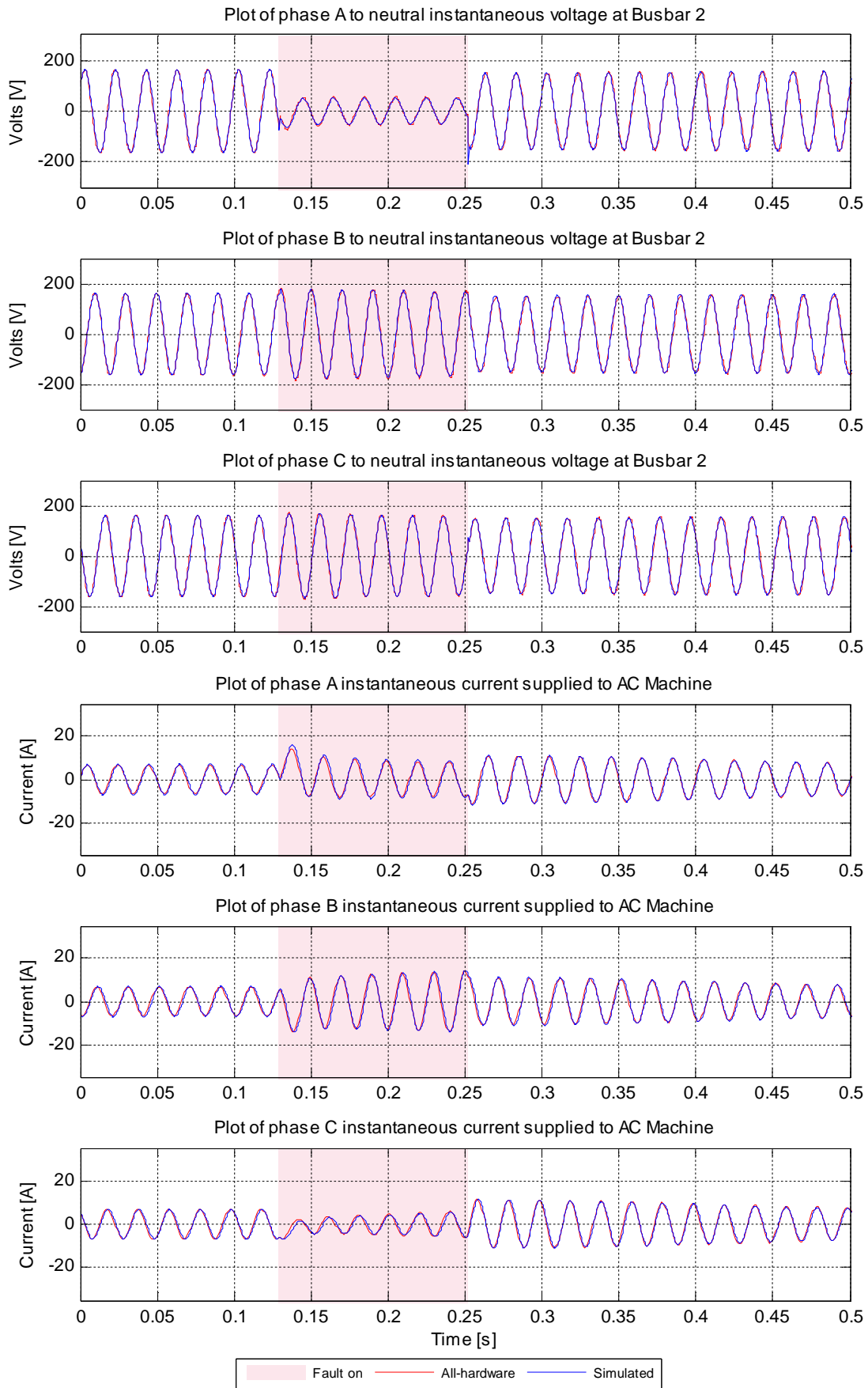


Figure 4-23 (a) — Validation of induction machine-dynamometer set models: (i) Phase A-ground fault with 70 % voltage sag; Bus 2 voltages and currents.

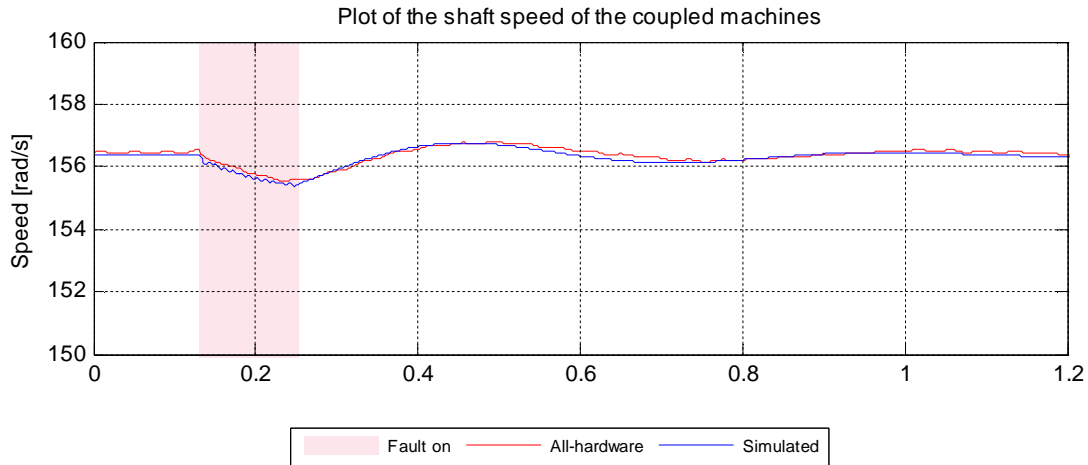


Figure 4-23 (b) — Validation of induction machine-dynamometer set models: (i) Phase A-ground fault with 70 % voltage sag; shaft speed.

Figure 4-23 (b) compares the simulated and measured behaviour of the shaft speed of the coupled induction machine-dynamometer test set during this phase A to ground fault test. The comparison in Figure 4-23 (b) shows that there is very good agreement between the simulated and measured behaviour of the rotational speed of the induction machine, both under steady state conditions and under dynamic conditions following the application of an asymmetric fault in the upstream supply network.

Figures 4-24 (a) and (b) compare the simulated and measured responses of the test subsystem during the application of the phase A to B to ground fault that caused a 70 % sag in the corresponding phases of the input voltage to the machine. The comparison in Figure 4-24 (a) shows excellent agreement between the measured and simulated values of the voltages and currents in the stator of the induction machine. Once again, the results show that the real-time simulation model of the induction machine is able to accurately predict the dynamic characteristics of the machine's voltages and currents at the inception and removal of the fault, as well as the transient behaviour of the machine's asymmetric stator currents during the upstream short-circuit fault.

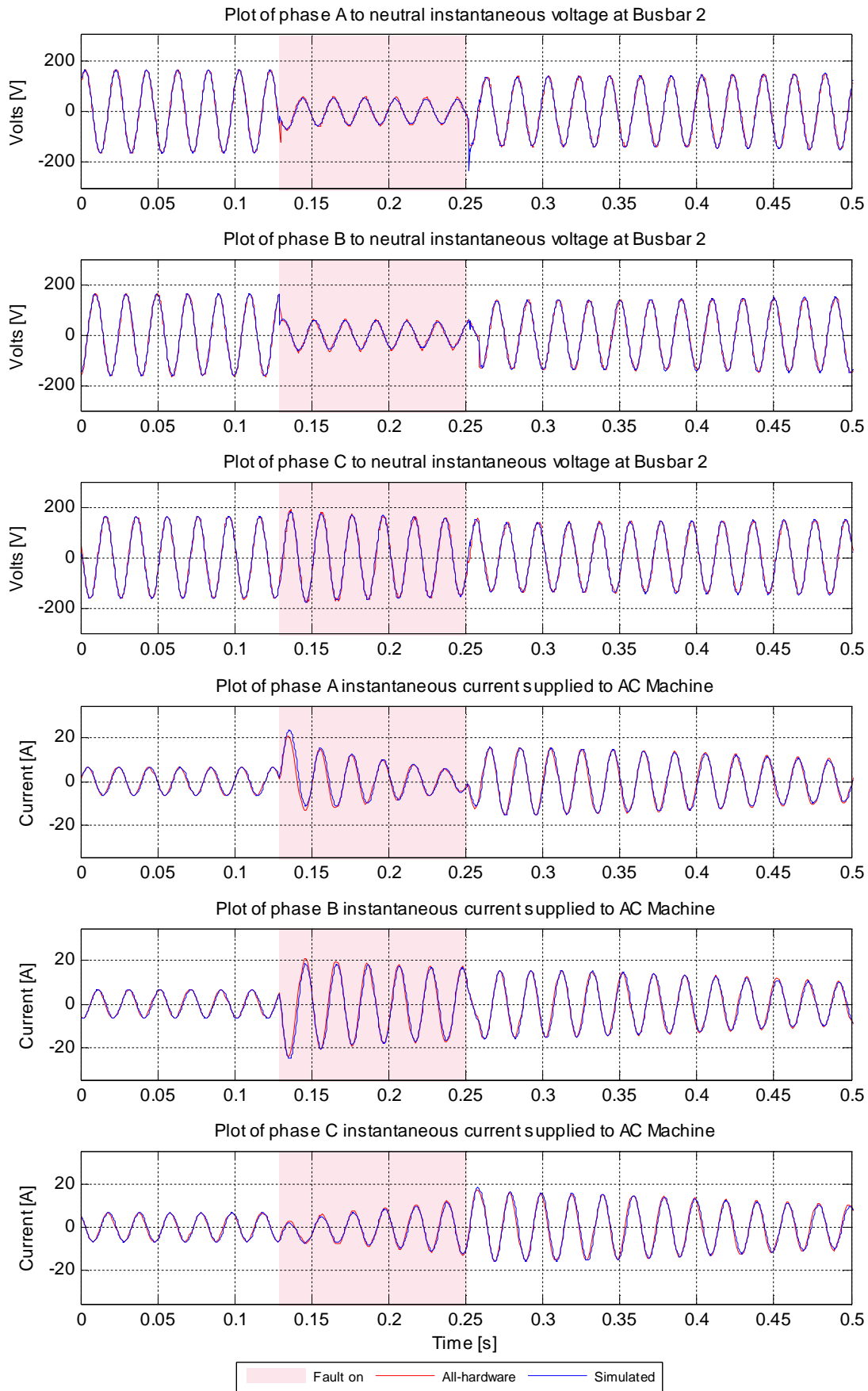


Figure 4-24 (a) — Validation of induction machine-dynamometer set models: (ii) Phase A-B-ground fault with 70 % voltage sag; Bus 2 voltages and currents.

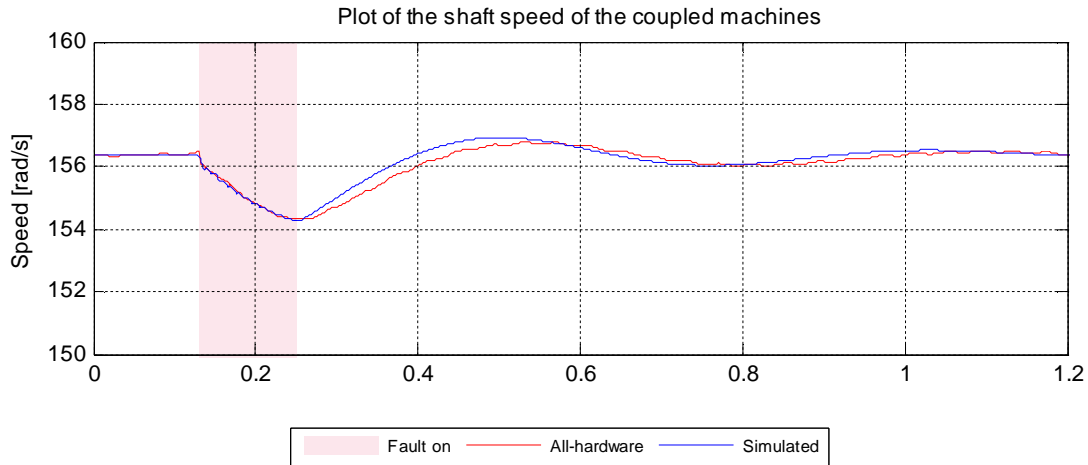


Figure 4-24 (b) — Validation of induction machine-dynamometer set models: (ii) Phase A-B-ground fault with 70 % voltage sag; shaft speed.

Figure 4-24 (b) shows a comparison of the simulated and measured behaviour of the shaft speed of the coupled induction machine-dynamometer set during this phase A to B to ground fault. The comparison in Figure 4-24 (b) shows that there is very good agreement between the simulated and measured behaviour of the machine speed especially in respect of the magnitude of the dip in speed that occurs during this fault; however, in the period immediately after the fault is removed, a slight difference can be seen between the transient behaviour of the machine speed measured on the laboratory system and that predicted by the simulation model. This difference may be due to the fairly simple model being used to describe the mechanical dynamics of the coupled dynamometer not being sufficiently detailed to represent its response for this particular fault, which is more severe than the single-phase to ground fault considered in the previous test. Nevertheless, the agreement between the simulated and measured behaviour of the machine speed is still sufficiently good, even in the case of this more severe fault condition.

Figures 4-25 (a) and (b) compare the simulated and measured responses of the test subsystem during the application of the three-phase to ground fault described in Table 4-13, which caused the voltages in all three phases at Bus 2 to sag by 70 %. The comparison in Figure 4-25 (a) shows that there is once again excellent agreement between the simulated and measured values of the voltages and currents in the stator of the induction machine, both at the points of inception and removal of the fault, as well as during the active period of the fault, when the simulation model is able to accurately represent the transient characteristics of the stator currents in the laboratory machine.

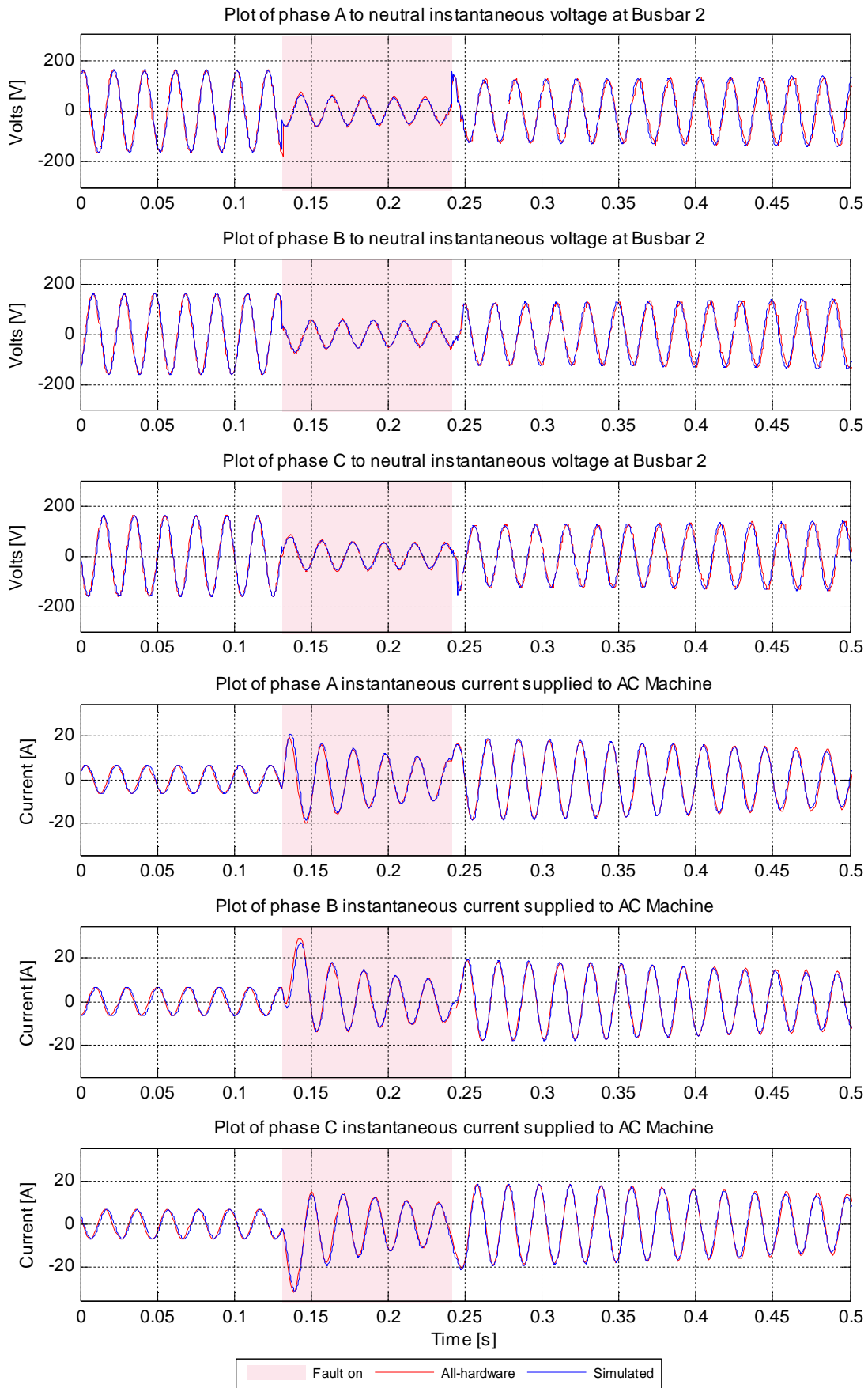


Figure 4-25 (a) — Validation of induction machine-dynamometer set models: (iii) Phase A-B-C-ground fault with 70 % voltage sag; Bus 2 voltages and currents.

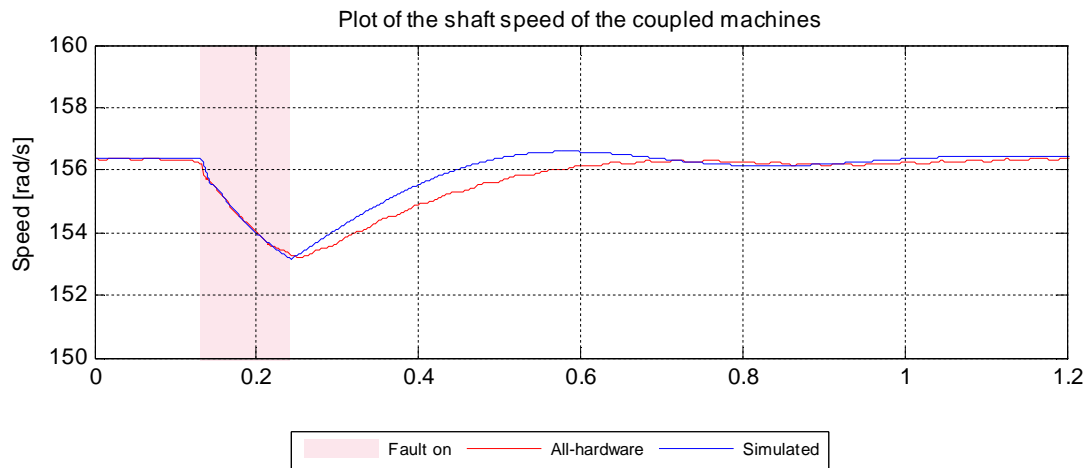


Figure 4-25 (b) — Validation of induction machine-dynamometer set models: (iii) Phase A-B-C-ground fault with 70 % voltage sag; shaft speed.

Figure 4-25 (b) shows a comparison of the simulated and measured behaviour of the shaft speed of the machine-dynamometer set during this three-phase to ground fault. The comparison in Figure 4-25 (b) shows that there is excellent agreement between the simulated and measured behaviour of the machine speed prior to and during the application of the fault; however, immediately after the fault is removed, a difference can be seen between the transient characteristics of the speed measured on the laboratory system and that predicted by the simulation model. Once again, this difference may be due to the model being used to represent the mechanical dynamics of the dynamometer being insufficiently detailed to represent its practical behaviour in detail for large disturbances, since this three-phase to ground fault is more severe than the double-phase to ground fault considered in the previous test. Nevertheless, there is still fairly good agreement between the simulated and measured behaviour of the machine's speed response for this most-severe fault test being considered in these studies.

In summary, the comparative results shown in Figures 4-23 to 4-25 therefore provide confidence that the double-cage machine model being used to represent the deep-bar rotor micro-induction machine and the mathematical model developed to describe the machine-dynamometer set's mechanical dynamics in the real-time simulation model are able to represent the measured behaviour of these parts of the plant in the laboratory-scale study system with sufficient accuracy and detail for the dynamic fault tests to be conducted in the thesis.

The following section describes the real-time models that were used to represent both the machine-side inverter and each of the two types of front-end converter being considered within the ASD system itself in the laboratory-scale study system.

## 4.7 The AFE Converter, VC Inverter and Diode-Rectifier Models

This section describes the models that were used to represent the AFE converter, VC inverter and diode-rectifier modules of the ASD system in the real-time simulation model of the laboratory-scale study system. The section is structured so that for each of these three modules, the topology of the power-electronic converter itself is first described, and thereafter the approach used within the real-time simulation environment to model the converter is discussed. The first subsection begins by describing the power-electronic topology of the AFE converter module.

### 4.7.1 The AFE Converter

Figure 4-26 shows the topology of the AFE converter actually employed within the industrial ASD system hardware to be tested in this thesis.

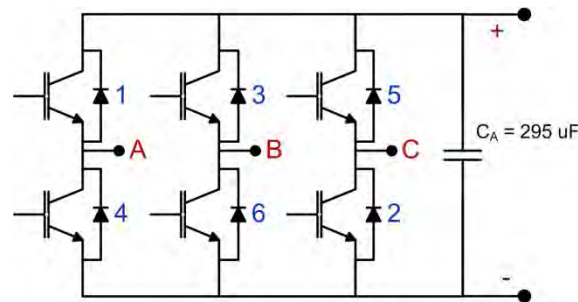


Figure 4-26: The two-level, three-phase AFE converter.

Figure 4-26 shows that the AFE module of the ASD system being tested comprises an IGBT-based, two-level, three-phase AC to DC voltage source converter, with a capacitance of 295  $\mu\text{F}$  connected across its DC terminals. The IGBTs within the particular AFE converter hardware considered in this thesis are switched at a frequency of 6 kHz. In order to simulate a fast-switching converter of this type in real-time with adequate resolution for closed-loop testing of physical drive controller hardware, the approach used on an RTDS Technologies real-time simulator is to represent each valve within the converter as an inductor when the valve is in the on state, and as a series-connected resistor and capacitor when the valve is in the off state [51] within a so-called small time step sub-network of the real-time simulation model. Figure 4-27 shows a pictorial representation of this modelling approach for a single valve within a larger converter model on an RTDS Technologies real-time simulator.

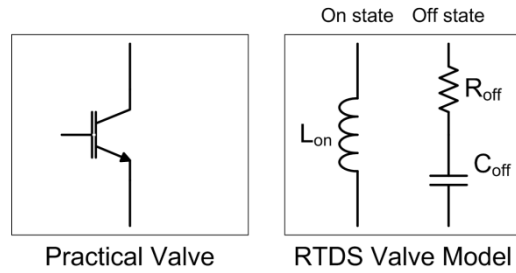


Figure 4-27: The model of a practical valve used in the RSCAD small-time step modelling environment.

The actual values of the resistance, capacitance, and inductance parameters  $R_{off}$ ,  $C_{off}$ , and  $L_{on}$  used to represent the valves within a small time step converter model in a real-time simulation are automatically calculated by the RSCAD simulation software according to a set of equations [51] based on information provided by the user regarding the values of voltage and current that will be switched in practice by the converter valves in the system to be simulated. The aim of this set of equations is to determine a suitable set of values for the parameters  $R_{off}$ ,  $C_{off}$ , and  $L_{on}$  that will allow the processors on the RTDS system to simulate all of the valves in the converter model in real-time with a time-step of approximately  $2 \mu s$ . However, a possible limitation of representing valves using this approach is that the values of  $R_{off}$ ,  $C_{off}$ , and  $L_{on}$  that are determined in order to satisfy the real-time modelling constraints using the equations described in [51] may lead to a higher level of switching loss in the simulated valves than is the case in the valves in the practical converter hardware [67].

Figure 4-28 shows the RSCAD model that was used to represent the AFE converter in the real-time simulation model of the laboratory-scale study system.

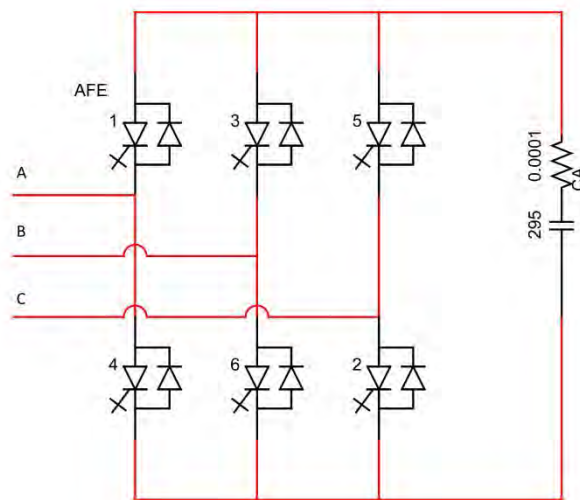


Figure 4-28: The RSCAD model of the AFE converter.

The actual values of  $R_{off}$ ,  $C_{off}$ , and  $L_{on}$  that were calculated by the RSCAD simulation software for each valve in the model of the AFE converter are shown in Table 4-14 below.

*Table 4-14: Calculated values of the parameters  $R_{off}$ ,  $C_{off}$ , and  $L_{on}$  for the valves in the RSCAD model of the AFE converter.*

$R_{off}$	$C_{off}$	$L_{on}$
63.36 $\Omega$	50.52 nF	0.11 mH

#### 4.7.2 The VC Inverter

Figure 4-29 shows the topology of the VC inverter actually employed within the industrial ASD system hardware to be tested in this thesis.

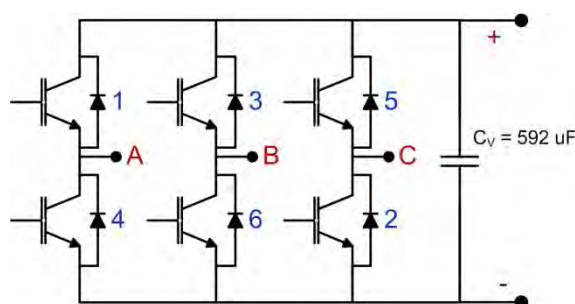


*Figure 4-29: The two-level, three-phase VC inverter.*

Figure 4-29 shows that the VC inverter module of the ASD system being tested comprises an IGBT-based, two-level, DC to three-phase AC voltage source inverter, with a capacitance of 592  $\mu$ F connected across its DC terminals. The IGBTs within the particular VC inverter hardware considered in this thesis are switched at a frequency of 1.8 kHz. The RSCAD model that was used to represent the VC inverter in the real-time simulation model of the laboratory-scale study system is shown in Figure 4-30.

The individual valves in the RSCAD converter model (Figure 4-30) that was used to represent the VC inverter module are represented using the same small time step modelling approach described in the previous subsection. The actual values of the parameters  $R_{off}$ ,  $C_{off}$ , and  $L_{on}$  that were calculated by the RSCAD simulation software to represent the valves in the VC inverter model are shown in Table 4-15.

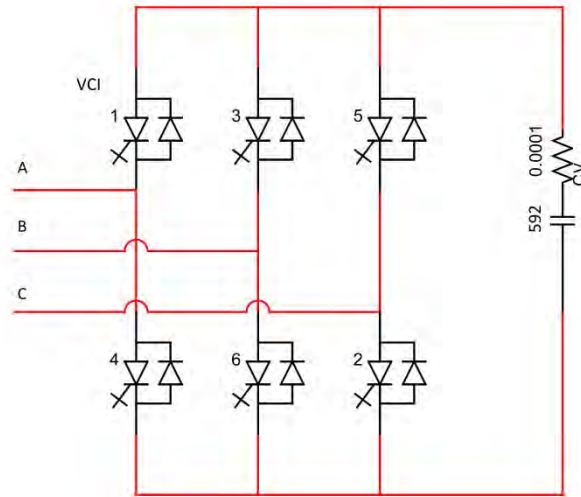


Figure 4-30: The RSCAD model of the VC inverter.

Table 4-15: Calculated values of the parameters  $R_{off}$ ,  $C_{off}$ , and  $L_{on}$  for the valves in the RSCAD model of the VC inverter.

$R_{off}$	$C_{off}$	$L_{on}$
126.71 $\Omega$	25.26 nF	0.21 mH

### 4.7.3 The Diode Rectifier

Figure 4-31 shows the topology of the diode rectifier actually used in the industrial ASD system hardware for those test cases in the thesis when the performance of an ASD system with non-active front-end converter technology was to be studied.

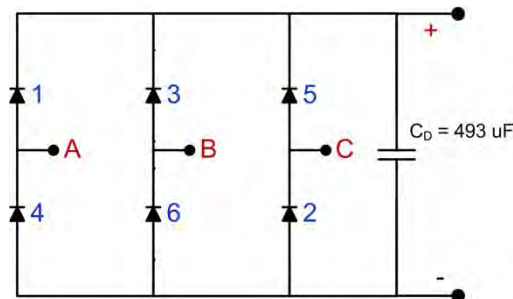


Figure 4-31: The three-phase AC to DC diode-rectifier converter topology.

Figure 4-31 shows that the diode-rectifier module of the ASD comprises a three-phase AC to DC converter, with a capacitance of 493  $\mu\text{F}$  connected across its DC terminals. The RSCAD model that was used to represent the diode rectifier in the real-time simulation model is shown in Figure 4-32, and the actual values of the parameters  $R_{\text{off}}$ ,  $C_{\text{off}}$ , and  $L_{\text{on}}$  that were calculated by the RSCAD simulation software to represent the valves in the diode-rectifier model are shown in Table 4-16.

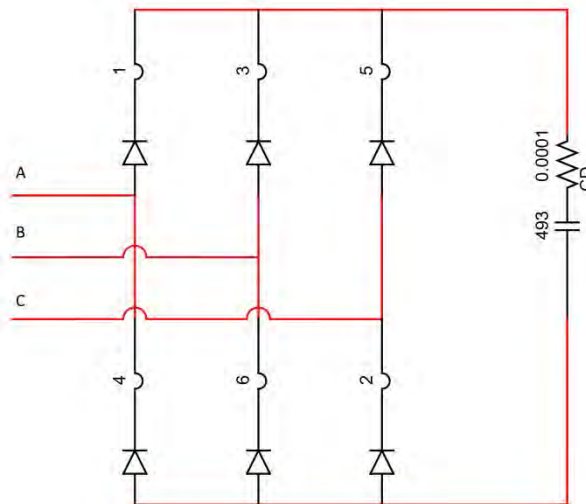


Figure 4-32: The RSCAD model of the diode rectifier.

Table 4-16: Calculated values of the parameters  $R_{\text{off}}$ ,  $C_{\text{off}}$ , and  $L_{\text{on}}$  for the valves in the RSCAD model of the diode rectifier.

$R_{\text{off}}$	$C_{\text{off}}$	$L_{\text{on}}$
126.71 $\Omega$	25.26 nF	0.21 mH

As mentioned in this section, the approach used on an RTDS Technologies simulator to represent fast-switching converters in a real-time simulation is to solve the mathematical models of such converters at small time-step intervals (on the order of  $2 \mu\text{s}$ ) in a sub-network of the real-time model, whilst the models of other parts of the plant are solved at a relatively large time-step interval of  $50 \mu\text{s}$  in the main network solution. In order to allow this multi-rate solution of different sub-networks of the real-time model to be carried out in a mathematically-valid manner, an appropriate means of interfacing the two sub-networks of the system model is required. The following section explains briefly how this interfacing was achieved in the case of the real-time model of the laboratory-scale study system developed for this thesis.

#### **4.8 Real-Time Model of the Complete Study System and its Decomposition into Large and Small Time Step Networks**

The RSCAD software suite provides a range of pre-defined models of power plant components that can (if desired) be included within a small time step sub-network along with the models of any power-electronic converters that must, by necessity, be solved within the small time step sub-network because of their high switching frequencies. The method of then connecting any electrical plant being modelled within the small time step sub-network to the electrical plant modelled in the main network solution is by means of a special purpose interfacing transformer model provided in RSCAD's small time step component model library. In order for the solution of the two sub-networks (large and small time step) to be mathematically valid, a finite amount of leakage inductance must be included in this interfacing transformer model.

Since an interfacing transformer model with some minimum amount of leakage inductance must be used to span the two sub-networks of the real-time model, it is logical, wherever possible, to choose the point of interface between the large time step network solution and the small time step sub-network to correspond to a part of the plant where a transformer is actually present, and hence where such leakage inductance actually exists in the plant being modelled. Thus, with reference to the laboratory-scale study system being considered in this thesis (shown in Figure 4-1) a seemingly logical choice of point at which to divide the system model between large and small time step sub-networks would be the drive transformer, such that all plant upstream of Bus 2 would form part of the large time step network solution and all plant downstream from Bus 3 would be represented within the small time step sub-network, and the actual leakage inductance of the drive transformer could then be used to mathematically span the sub-networks.

However, as the results presented in Section 4.4 have demonstrated, in a study such as this the characteristics of the drive transformer need to be represented in detail using a particular special-purpose transformer model in RSCAD (the UMEC model) that is available only within the large time step modelling environment. In addition, at the time of this work the models that were available in the small time step library to implement general-purpose mathematical functions and to carry out dynamic control system modelling were not sufficient to allow the differential equation model of the dynamometer, presented in Section 4.6.2, to be included within the small-time step sub-network. As a result, in the final implementation of the real-time simulation model of the full laboratory-scale study system, the decomposition of the system model into a large time step network solution and a small time step sub-network was carried out as shown in the diagram of Figure 4-33.

Figure 4-33 shows that the mathematical models that were included within the small time step sub-network were the front-end converter and VC inverter power-electronic topologies, the DC-link capacitance and induction machine. An interface transformer model with a turns ratio of unity (not shown in Figure 4-33) was included in the small time step sub-network to span between the UMEC model of the drive reactor in the main network solution and the front-end converter model in the small time step sub-network. The value of leakage inductance included in this interface transformer was then deducted from the leakage inductance parameter of the UMEC model being used to represent the drive reactor. In this way, the mathematical requirements of the interfacing between small and large time step networks were satisfied whilst the total leakage reactance between Bus 3 and the drive's front-end converter within the simulation model remained equal to the value in the all-hardware implementation of the study system in the laboratory.

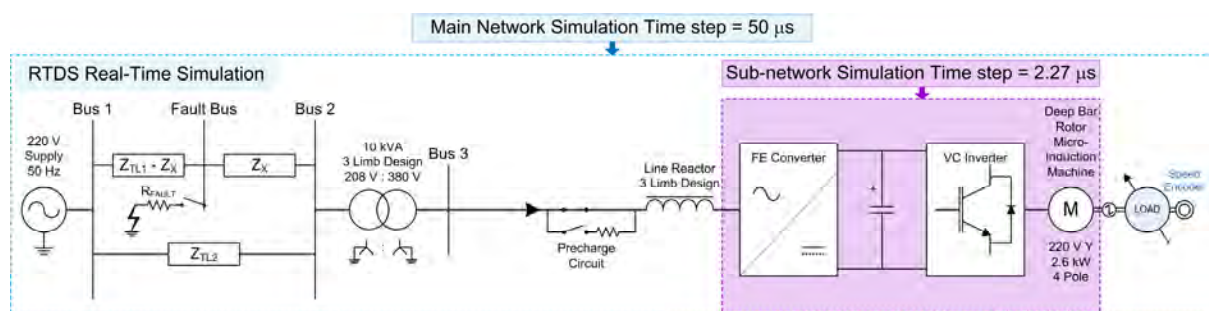


Figure 4-33: Schematic diagram showing final decomposition of the real-time model of the laboratory study system into large and small time step networks.

## 4.9 Summary

This chapter has described the development and parameterization of a real-time simulation model of all of the power-level plant elements within the laboratory-scale study system developed for this thesis. The real-time model was developed using the RSCAD simulation software suite, and built with the use of pre-defined elements that are provided in the RSCAD library of fundamental component models. Furthermore, as a part of the process of validating the real-time model of the power-level plant in the laboratory-scale study system, key sub-sections of the plant within the study system as a whole were tested under voltage sag conditions in the laboratory and their measured responses were compared against those of the parameterized real-time models to verify the correctness and accuracy of the models. The results of the model validation tests presented in this chapter provide confidence that the real-time models of these key sub-sections of plant in the laboratory-scale study system are able to accurately represent the actual characteristics of this plant under the intended range of test conditions.

This chapter has also briefly described the small time step modelling approach used to represent fast-switching power-electronic converters on an RTDS Technologies real-time simulator and has described the models used to represent the front-end converter and VC inverter modules of the industrial adjustable speed drive (ASD) hardware within the real-time simulation model of the power-level plant in the laboratory-scale study system.

These power-electronic converters within the ASD were the only elements of the plant within the laboratory-scale study system whose real-time models were not validated in this chapter by comparison against measured results. The reason for this is that these converter models require firing pulse inputs from the ASD controller hardware itself in order to operate under representative conditions and therefore their final validation is only possible once the real-time model of the plant in the laboratory-scale study system presented in this chapter is actually connected in a full, closed-loop arrangement with the hardware controller modules of the ASD. The validity of these power-electronic converter models will therefore be implicitly considered during the remaining chapters of this thesis when the measured performance of the full motion control system in the all-hardware implementation of the laboratory-scale study system is compared with the performance of the real-time model of this study system when connected hardware-in-the-loop (HIL) to the ASD controller modules of the motion control system.

The next chapter, Chapter 5, therefore begins by describing how the real-time simulation model of the power-level plant in the study system presented in this chapter was interfaced to the physical controllers of the ASD system in order to form the HIL simulation implementation of the study system. Chapter 5 then presents detailed comparisons of the results of the HIL real-time simulator testing approach against measured results from the all-hardware implementation of the study system for the particular case of an ASD with a diode-rectifier front end when subjected to faults in the upstream utility supply network.

# **Chapter 5: The Hardware-In-Loop Simulation Implementation Of The Study System And The Performance Of The Diode Rectifier Energised ASD Under Voltage Sag Conditions**

## **5.1 Introduction**

Chapter 1 has explained that in order to evaluate the hardware-in-loop (HIL) testing approach proposed in this thesis to study the dynamic performance of adjustable speed drives (ASDs), the measured performance of an ASD system in an all-hardware implementation of a laboratory-scale study system under a set of voltage disturbance conditions is to be compared against the performance of a hardware-in-loop simulation implementation of the same study system in which the power-level plant of the study system is modelled on a real-time digital simulator and the physical ASD controllers are connected hardware-in-loop with this real-time model of the power-level plant.

Chapter 3 introduced the actual study system that is to be used for this comparison and described its all-hardware implementation in a machines research laboratory. Furthermore, Chapter 3 also introduced a set of six fault conditions in the upstream supply network that were carefully chosen for the laboratory-scale system in order to allow the performance of the ASD in response to a representative range of voltage sags to be compared in the all-hardware and HIL simulation implementations of the system. Chapter 4 then described the development and parameterization of the real-time digital simulation model of the power-level plant within the laboratory-scale study system.

This chapter now begins by describing how this real-time model of the power-level plant was interfaced to the physical controllers of the ASD in order to form the hardware-in-loop simulation implementation of the study system in which the front-end converter in the ASD system could be configured to be either a diode rectifier or an active front end (AFE) converter. The chapter then presents the results of detailed performance tests carried out on the ASD system with a diode-rectifier front-end converter in response to the chosen set of upstream fault conditions, firstly by means of measurements on the full hardware implementation of the laboratory-scale study system, and then by means of the real-time simulation of the same study system when connected hardware-in-loop with the ASD's controllers. These results are used not only to demonstrate the performance of the ASD with this particular type of front-end converter technology in response to voltage sags, but also to evaluate the ability of the HIL testing approach itself to study the dynamic performance of such drives.

## **5.2 The Hardware-In-Loop Simulation Implementation of the Study System**

Figure 5-1 shows a schematic diagram of the hardware-in-loop real-time simulator implementation of the study system. The dotted blue box in Figure 5-1 illustrates, once again, that in the real-time simulator HIL implementation of the study system all of the power-level plant in the study system is represented using detailed mathematical models running in real time, and only the drive control modules from within the actual ASD equipment are represented using physical hardware. The dotted red box in Figure 5-1 illustrates that in this HIL implementation of the study system the electrical plant of the ASD system (converters and motor) is still under the control of the actual drive hardware and its internal algorithms, just as it is in the all-hardware implementation of the study system, with the firing signals to the individual power electronic devices within the real-time models of the converters being accepted as inputs from the drive controls, and all the necessary plant measurements required by the drive controls being output to them from the simulation as it runs in real-time.

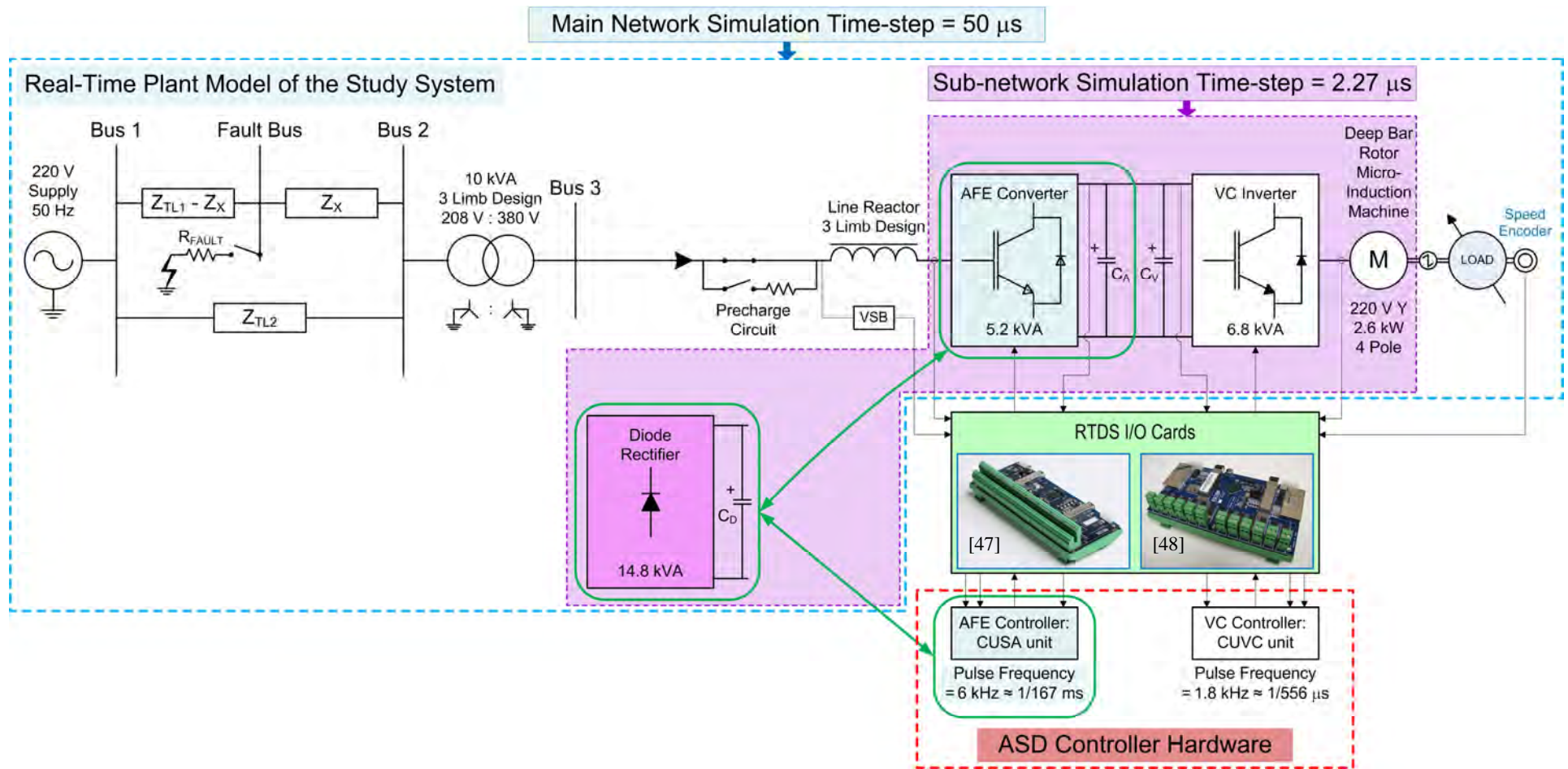


Figure 5-1: Schematic diagram of the HIL simulation implementation of the study system.

Figure 5-2 shows a photograph of the actual equipment used and the interconnections necessary in the HIL simulation implementation of the study system: the model of the study system plant was simulated in real-time on the RTDS simulator to the left of the picture, whilst the CUSA and CUVC hardware controllers within the ASD's AFE converter and VC inverter units (to the right of the picture) were interfaced in closed loop with the component models running in real time on the simulator via the RTDS input and output (I/O) cards in the centre ground.

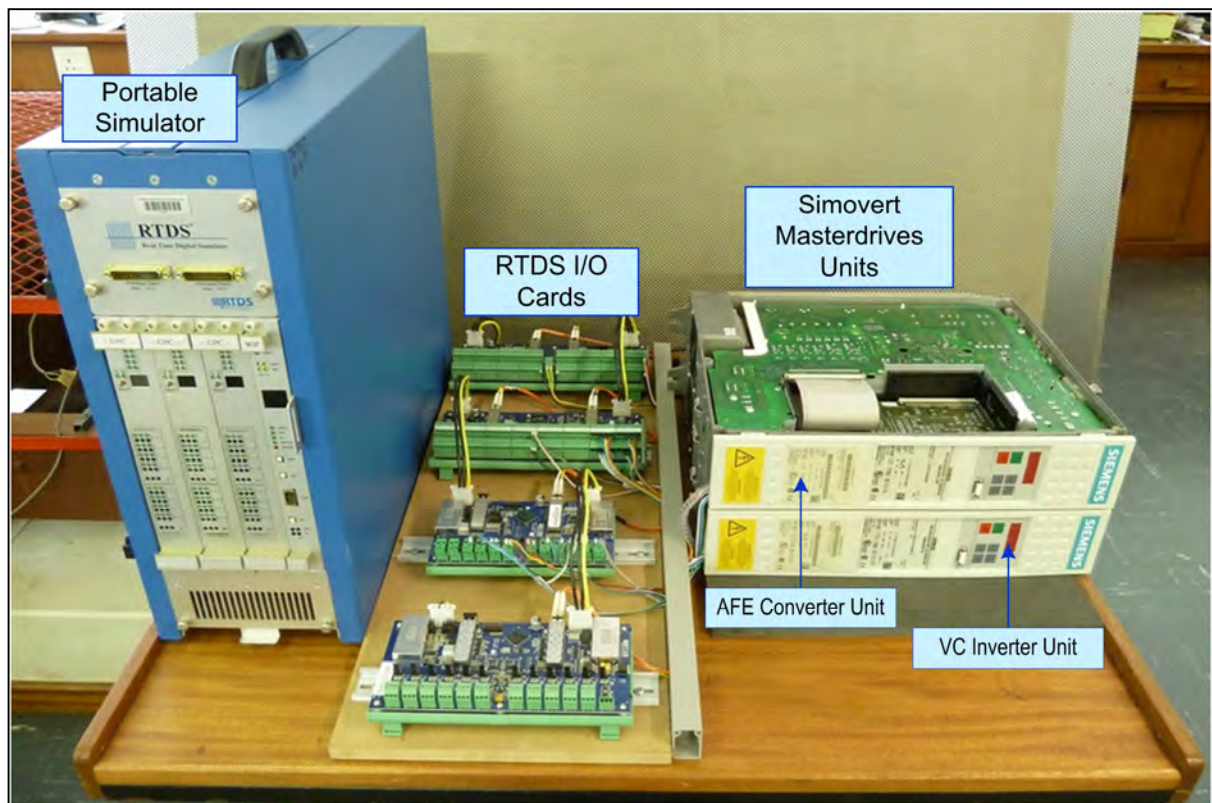


Figure 5-2: Photograph showing hardware-in-loop connection of the ASD system to the real-time simulator.

Figure 5-3 shows a close-up photograph of the connections of the input (current and voltage measurement) variables to the CUSA and CUVC hardware controllers from the real-time model of the plant, as well as the output (firing pulse signal) variables from the hardware controllers back to the real-time model of the plant in this hardware-in-loop testing approach. Figure 5-4 shows a close-up photograph of the analogue and digital I/O cards used to interface these ASD controller variables in the external hardware loop to the real-time simulation.

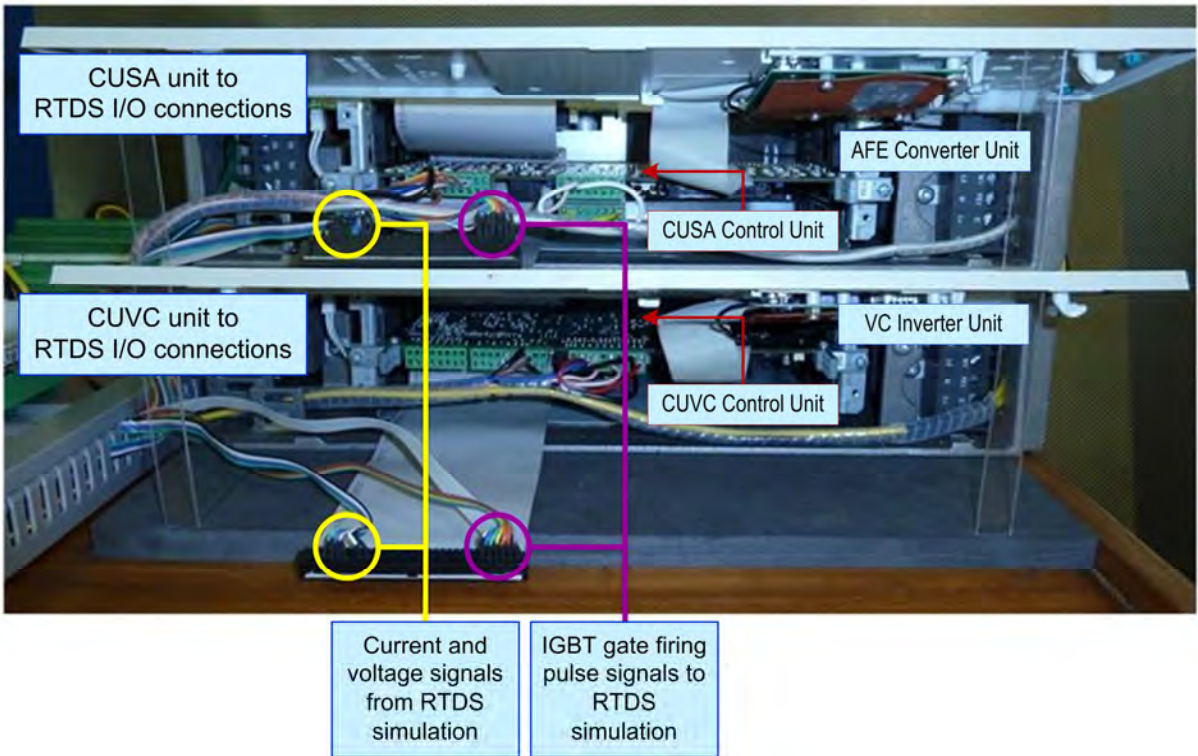


Figure 5-3: The I/O connections made within the ASD hardware to allow exchange of variables with the real-time simulator for hardware-in-loop testing.

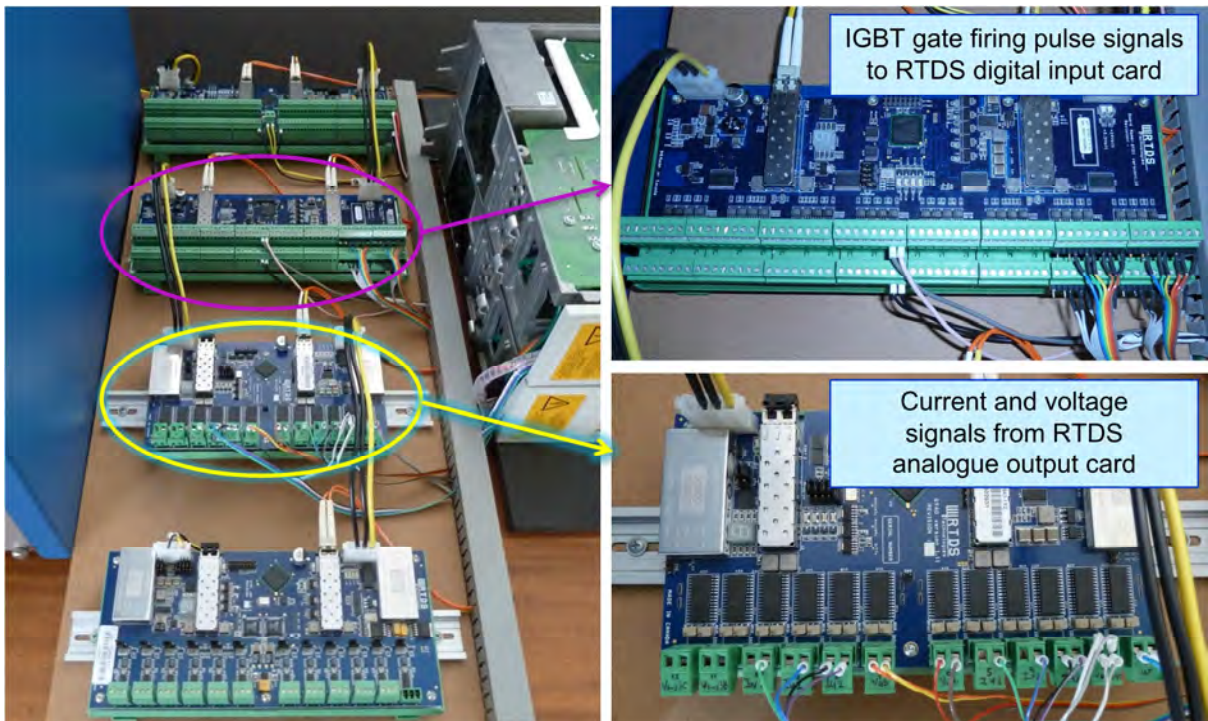


Figure 5-4: The I/O hardware used to interface the ASD's controls to the real-time simulator.

As shown in Figure 5-1, the actual variables that were sent to the CUSA controller hardware from the real-time simulation model in the HIL implementation of the study system were the three-phase voltages and currents at Bus 3, and the DC-link voltage, whilst the variables that were fed back into the real-time model from the CUSA controller comprised the firing pulse signals for each of the six IGBTs in the two-level, three-phase AFE converter. The actual variables that were sent to the CUVC controller hardware from the simulation model were the DC-link voltage, the three-phase currents supplied to the induction motor, and the shaft speed of the motor, whereas the variables that were fed back into the real-time model from the CUVC controller comprised the firing pulse signals for each of the six IGBTs in the two-level, three-phase VC inverter. The channels of the analogue output card used to pass these variables between the real-time model of the plant and the external ASD controller hardware were appropriately scaled to ensure that these variables appeared at signal-level within the ASD controllers with the same magnitudes as in the all-hardware implementation of the study system under the same operating conditions. Likewise, the digital input cards used to feed the two sets of firing pulses from the ASD controllers into the real-time models of the power-electronic converters in the study system were configured to accept the particular output voltage levels of these firing pulses on the ASD controller hardware.

The next section presents the results of detailed performance tests carried out on the ASD system for the particular case of a diode-rectifier front end in order to compare the results obtained from an all-hardware implementation of the study system with those obtained using the HIL simulation implementation of the study system.

### **5.3 Comparisons of the Results from the All-Hardware and HIL Simulation Implementations of the Study System Under Voltage Sag Conditions for the Case of the Diode Rectifier Energised ASD System**

#### **5.3.1 Introduction**

This section now considers the actual dynamic performance of the motion control system in the full laboratory-scale study system under voltage sag conditions for the particular case when a diode-rectifier unit was used as the converter technology feeding the front end of the drive as shown in Figure 5-5.

The operating conditions chosen for these tests on the laboratory-scale study system were discussed in Chapter 3 and are summarized again here for completeness. The ASD system was fed, via the upstream network, with its nominal input voltage of 380 V at Bus 3 and was configured to regulate the speed of the induction motor. In particular the ASD's closed-loop speed controller was set to maintain the speed of the induction motor at 157.1 rad/s (1500 rpm) while the dynamometer applied a torque of 8 Nm at its shaft (approximately 50 % of the rated load of the motor).

Whilst the ASD system was performing this motion control task it was then subjected to a range of different voltage sag conditions at its front end by applying each of the six pre-determined fault conditions in the upstream supply network of the study system, as described in Chapter 3. The details of these six fault conditions, and the associated sag types and nominal sag depths produced at Bus 3, are summarized again, for completeness, in Table 5-1.

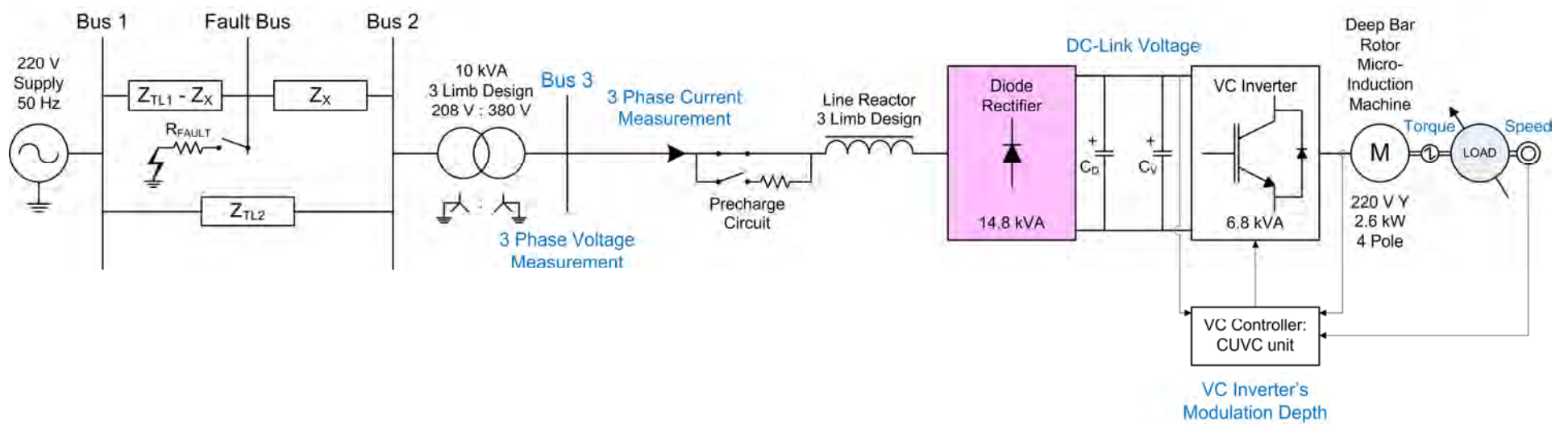


Figure 5-5: Schematic diagram of the laboratory-scale study system for the case in which the diode-rectifier unit was used to energise the machine-side inverter in the ASD system.

*Table 5-1: Sag characteristics and nominal sag depths at the Bus 3 voltage for the six particular fault conditions considered during experimental tests on the laboratory-scale study system.*

Fault Condition	Sagged Phase/s	Duration [ms]	Voltage Sag Depth [%]	Remaining Voltage During Fault [%]
(i)	A	200	35	65
(ii)	A	100	50	50
(iii)	A, B	100	35	65
(iv)	A, B	100	50	50
(v)	A, B, C	100	50	50
(vi)	A, B, C	100	70	30

These six fault conditions were applied first to the all-hardware implementation of the study system in the laboratory, and then to the hardware-in-loop real-time simulation implementation of the study system, with the same set of variables recorded from the study system in each case for comparison.

The specific variables that were recorded in each set of tests are highlighted in blue in the schematic diagram of the system in Figure 5-5. Within the power-level plant, the three-phase voltages and currents at the input to the front end of the ASD system at Bus 3 were recorded, as was the DC-link voltage, motor load torque and speed. In the case of the all-hardware implementation of the study system, these variables were obtained from measurements on the practical system in the laboratory, whereas in the case of the HIL simulation implementation, these variables were recorded within the simulation model of the power-level plant. Furthermore, in both implementations (all-hardware and HIL simulation) the VC inverter modulation depth commanded by the CUVC hardware controller during the tests was also recorded for comparison.

### 5.3.2 ASD Response to Single-Phase to Ground Faults

This subsection considers the performance of the ASD system with a diode-rectifier front end in response to the two different single-phase to ground faults at the Fault Bus in the upstream supply network that are shown in Table 5-1, namely Fault Conditions (i) and (ii).

Figure 5-6 (a) shows the AC currents and voltages from the front end (Bus 3) of the ASD before, during and after the particular phase A to ground fault at the upstream Fault Bus that results in a sag of nominal depth 35 % and duration 200 ms in the voltage of the faulted phase at the ASD front end (Fault Condition (i) in Table 5-1). The measured results from the application of the fault in the all-hardware implementation of the study system, as well as those obtained when the same fault was applied in the HIL simulation implementation of the study system, are each plotted on common axes in Figure 5-6 (a) to show how closely the two sets of test results agree with one another; the areas highlighted in pink show the period during which the fault was actually applied in both sets of test results.

The results in Figure 5-6 (a) show that under normal steady state conditions the currents drawn by the diode rectifier at the front end of the ASD, although balanced, are non-sinusoidal, which result in the harmonic distortion evident in the input voltages to the ASD under steady-state conditions. The results show that during the fault in phase A of the upstream power system network the currents drawn by the front end of the ASD not only become unbalanced, with a reduction in the amplitude of the current drawn by the ASD front end in the faulted phase, and an increase in the amplitudes of the currents drawn by the other two phases, but also that the level of harmonic distortion in the currents drawn by the ASD increases noticeably in all three phases during the fault. The results also show that, as would be expected during the fault, there is a sag in the input voltage to the ASD in the faulted phase, but that there are also noticeable, but less severe, sags in the input voltages to the ASD in the un-faulted phases and a noticeable increase in the harmonic distortion in these input voltages in all three phases.

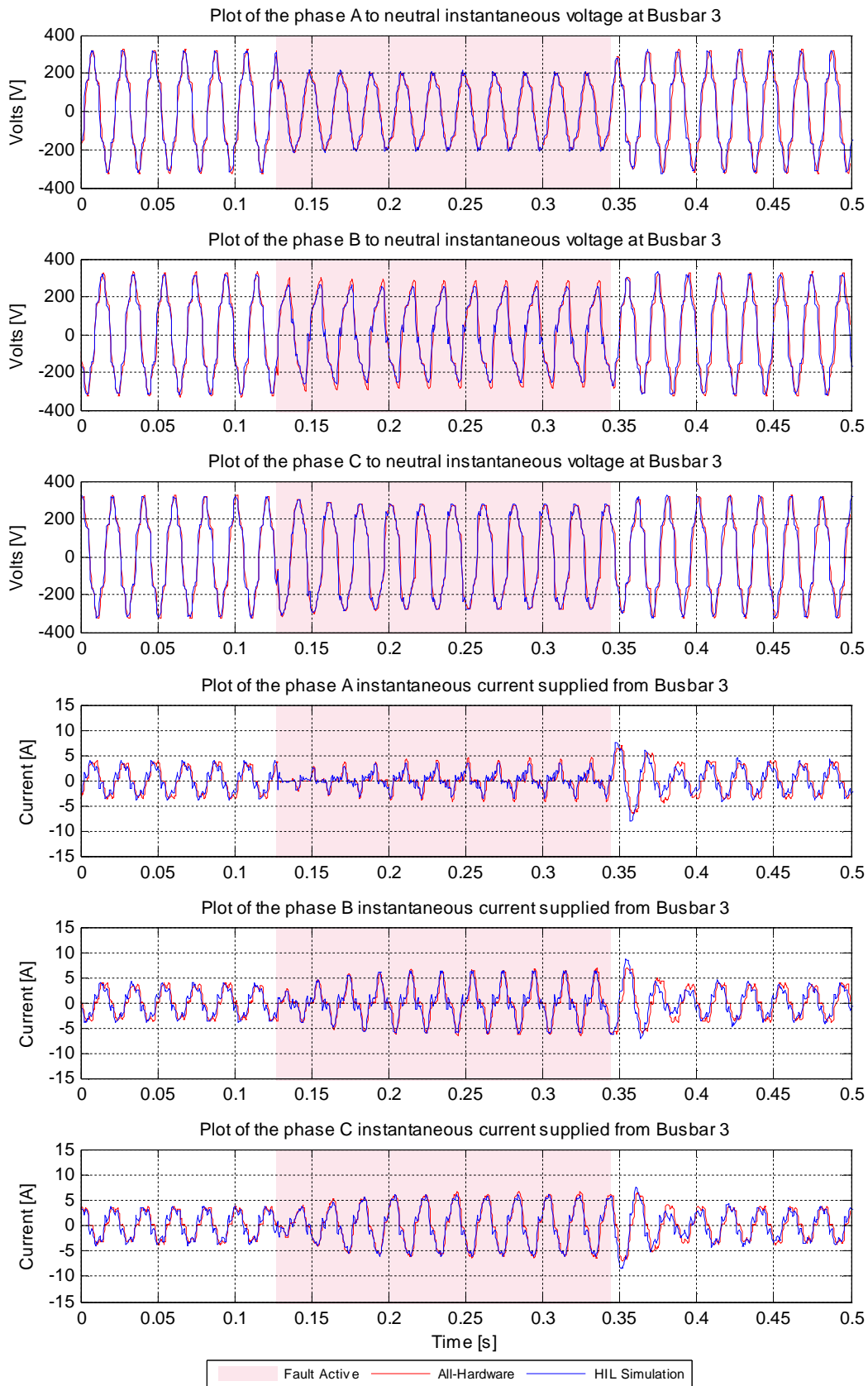


Figure 5-6 (a): Comparison of all-hardware versus HIL simulation implementations of study system — response of ASD system with diode-rectifier front end to phase A to ground fault causing sag of nominal depth 35 %, and duration 200 ms (Bus 3 variables).

Finally, the results in Figure 5-6 (a) show that there is excellent agreement between the behaviour of the currents and voltages at the front end of the ASD system measured in the all-hardware implementation of the laboratory-scale study system, and the currents and voltages obtained from the HIL simulation implementation of the same study system for this particular upstream fault test. The HIL simulation is able to closely replicate not only the amplitudes and harmonic characteristics of the voltages and currents at the ASD’s front end under faulted and un-faulted conditions in this test, but also the dynamic behaviour of these variables upon inception and removal of the fault.

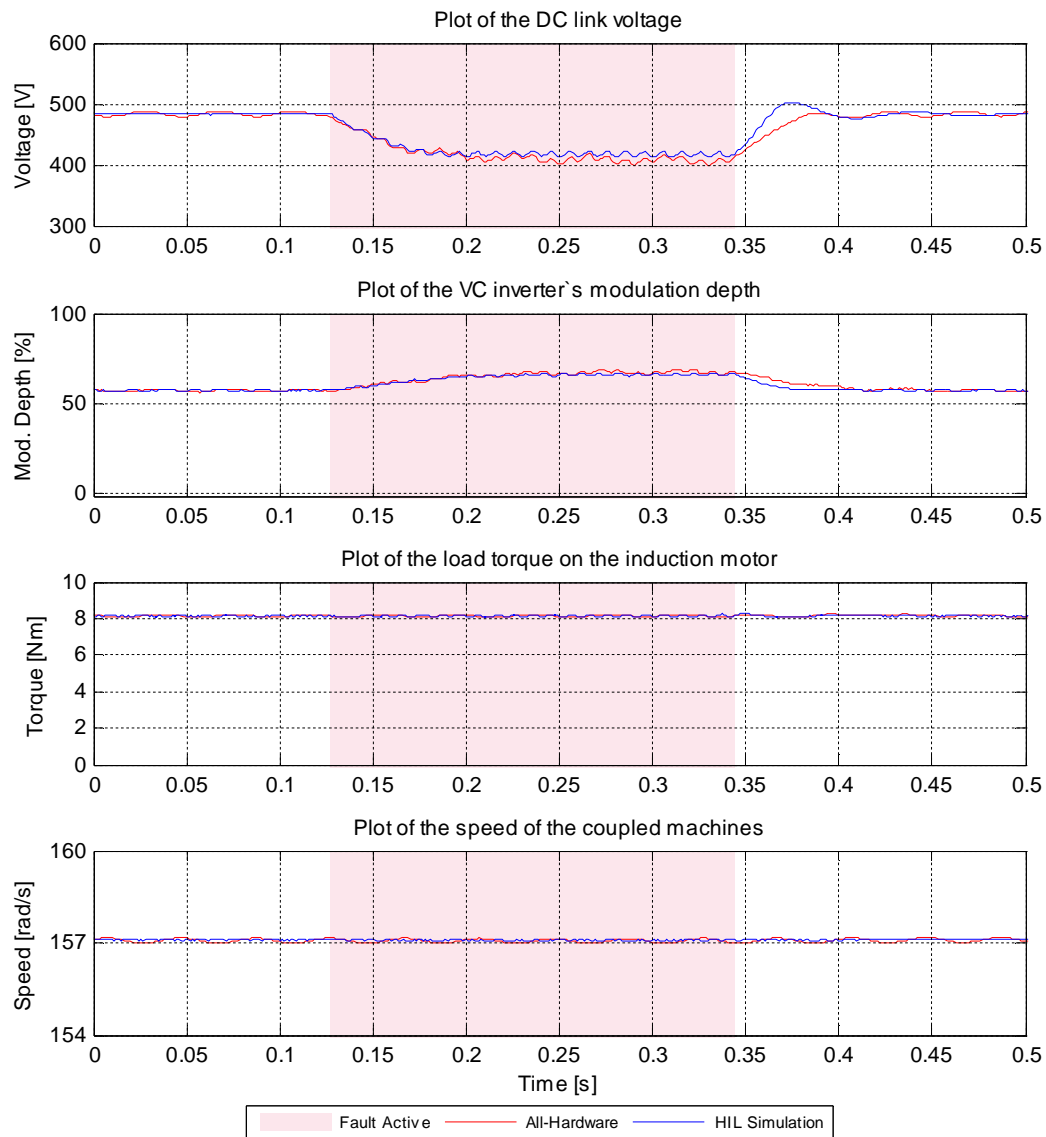


Figure 5-6 (b): Comparison of all-hardware versus HIL simulation implementations of study system — response of ASD system with diode-rectifier front end to phase A to ground fault causing sag of nominal depth 35 %, and duration 200ms (ASD system variables).

Figure 5-6 (b) now shows the response of the variables within the ASD system itself during the same single-phase to ground fault test shown in Figure 5-6 (a). Once again, the measured results from the

application of the fault test on the all-hardware implementation of the study system as well as those obtained from the same test on the HIL simulation implementation are each plotted on common axes in Figure 5-6 (b), with the areas highlighted in pink showing the period during which the fault was actually applied in each case.

The results in Figure 5-6 (b) show that immediately following the fault in the upstream network, the DC-link voltage begins to drop and continues to do so for approximately 50 ms until the capacitors in the DC link have discharged sufficient energy into the drive that the voltage across them reaches the reduced DC output voltage of the uncontrolled diode rectifier at the front end of the ASD associated with the sag condition in its AC input voltages. However the fact that the DC-link voltage then stays approximately constant for the remaining 150 ms of the fault indicates that the front-end converter is in fact able to meet the energy requirements of the drive, at least for this operating condition, throughout the disturbance, despite the sag in its input voltages.

The response of the VC inverter modulation depth in Figure 5-6 (b) shows, further, how the ASD controls react to the drop in DC-link voltage during the disturbance: the closed-loop speed control and field-oriented control of the induction machine that are implemented on the CUVC hardware within the ASD temporarily increase the modulation depth of the firing pulses to the VC inverter that supplies the induction motor in order to maintain the output torque and speed of the machine despite the reduction in the DC-link voltage at the input to the VC inverter. The measurements of the machine's torque and speed shown in Figure 5-6 (b) illustrate that not only is the ASD able to continue meeting the torque and speed requirements of the motion control task during the period of the sag in its input voltages, but also that there is negligible dynamic impact on these machine variables at the moments of inception and removal of the fault in the upstream network. These results also indicate that for a voltage sag of this particular type and depth at its front end the ASD system is able to satisfactorily ride through the voltage sag even with an uncontrolled diode rectifier at its front end, at least from the perspective of the behaviour of the internal drive variables.

Finally, the results in Figure 5-6 (b) show that there is very good agreement between the behaviour of the variables within the drive system itself that were measured in the all-hardware implementation of the laboratory-scale study system, and the corresponding variables obtained from the HIL simulation implementation of the study system for this particular upstream fault test. In particular, the HIL simulation is able to closely replicate the steady state and dynamic behaviour of the DC-link voltage and the VC inverter modulation depth control signal prior to, and during the upstream fault.

The dynamic behaviour of the DC-link voltage seen in Figure 5-6 (b) as it increases upon removal of the fault is slightly under-damped in the results obtained from the HIL simulation implementation of the study system when compared with the measured behaviour of this variable. However, this small difference appears to have a negligible impact on the predicted behaviour of all of the other variables within the simulation implementation of the system (both within the ASD and within the electrical supply system) which agree closely with those measured on the all-hardware implementation of the study system during the removal of the fault.

Figure 5-7 (a) now shows the AC currents and voltages from the front end of the ASD during the phase A to ground fault at the upstream Fault Bus that results in a sag of nominal depth 50 % and duration 100 ms in the voltage of the faulted phase at the ASD front end (Fault Condition (ii) in Table 5-1).

The impact of this single-phase fault on the electrical variables at the front end of the ASD seen in Figure 5-7 (a) is similar in nature to that seen in the previous single-phase fault study [Figure 5-6 (a)]: the currents drawn by the front end of the ASD become unbalanced as a result of the asymmetric fault in the upstream network, with a reduction in the amplitude of the current in the faulted phase and an increase in the amplitudes of the currents drawn by the other two phases. However, in the case of the particular fault test shown in Figure 5-7 (a) the impact in the faulted phase is more pronounced because of the greater sag in the input voltage in the faulted phase in this case: Figure 5-7 (a) shows that the front end of the ASD is unable to draw current at all from the faulted phase for the first part (approximately 50 ms) of the disturbance, and only a small amount of current during the remaining 50 ms of the disturbance. The initial inability of this phase of the diode rectifier to draw current is as a result of a sag in the input voltage of this phase to an amplitude below that needed to forward bias the diodes connected to that phase in the rectifier. (The fact that phase A of the front-end diode rectifier draws no current for the first half of the disturbance also results in the voltage in this phase being free from any harmonic distortion during the first part of its sag.)

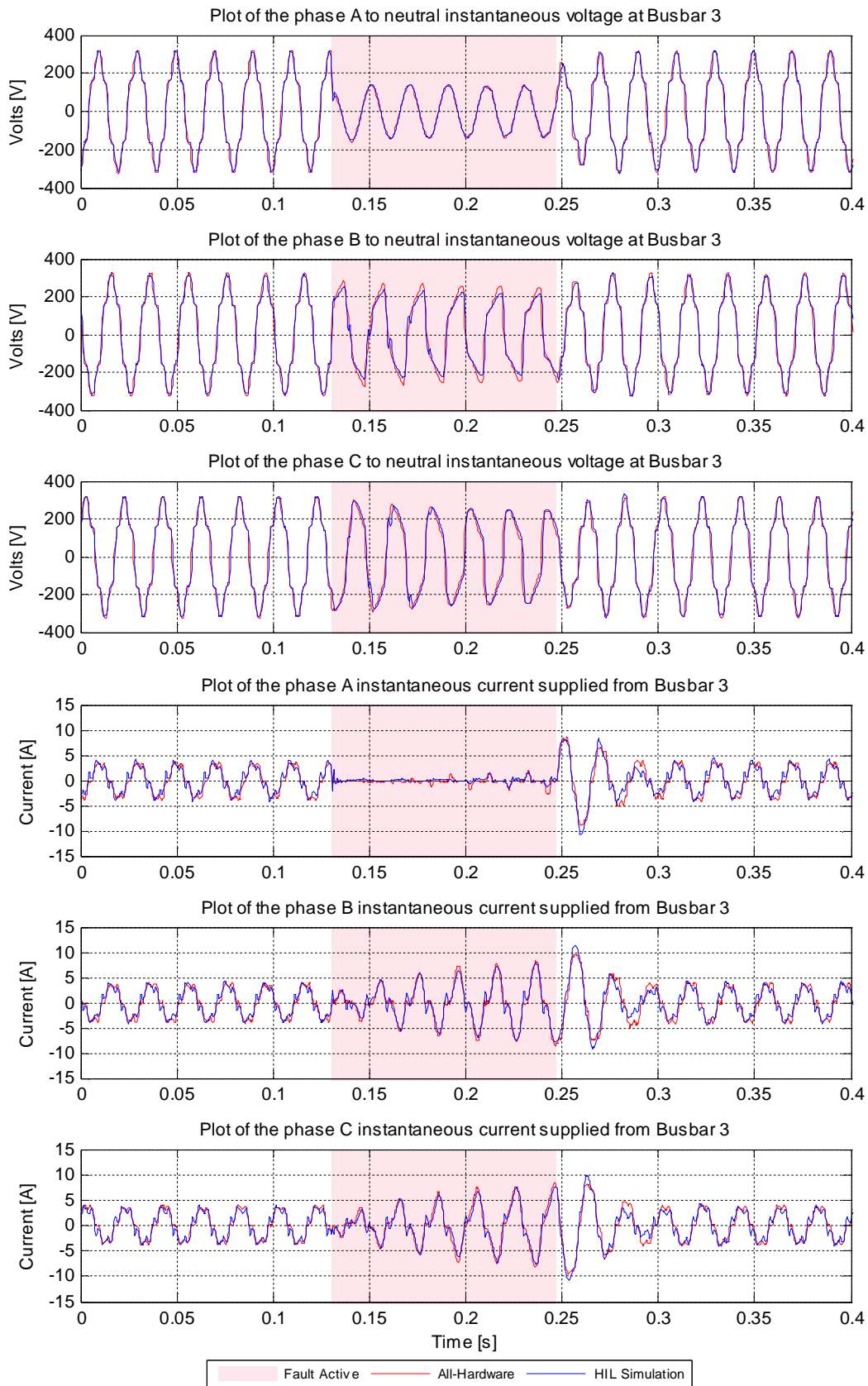


Figure 5-7 (a): Comparison of all-hardware versus HIL simulation implementations of study system — response of ASD system with diode-rectifier front end to phase A to ground fault causing sag of nominal depth 50 %, and duration 100 ms (Bus 3 variables).

Figure 5-7 (b) shows the response of the variables within the ASD system itself during the single-phase to ground fault test shown in Figure 5-7 (a). The results in Figure 5-7 (b) show that for this single-phase fault in the upstream network there is a more pronounced drop in the DC-link voltage than was the case in the previous single-phase fault test [cf. Figure 5-6 (b)] despite the shorter fault duration, because of the greater depth of sag in the input voltage to the ASD in the affected phase. Nevertheless the results indicate that the ASD controls are still able to temporarily increase the modulation depth of the firing pulses to the VC inverter feeding the motor so as to allow the drive to ride through the voltage sag with negligible impact on the torque and speed of the induction machine.

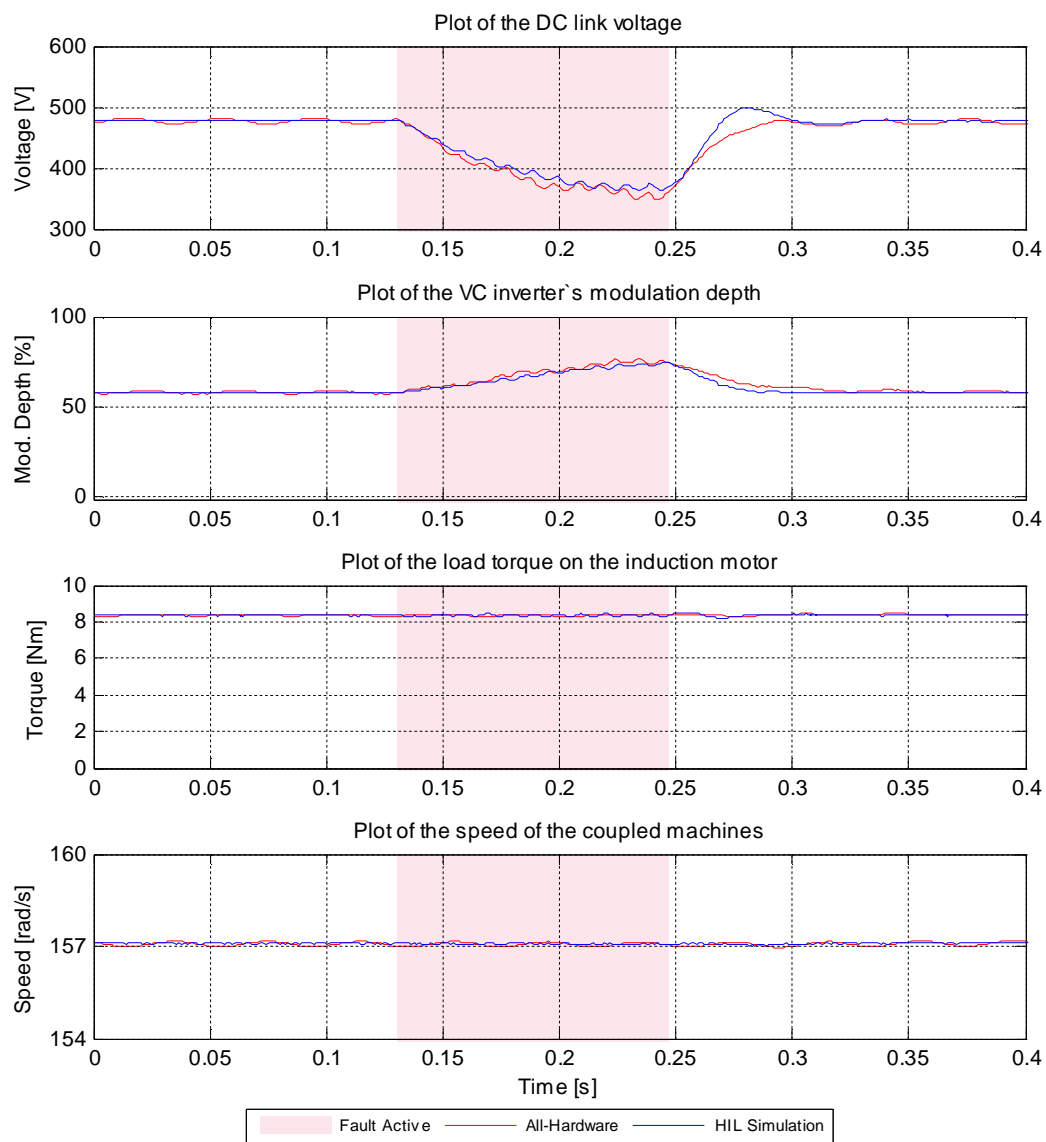


Figure 5-7 (b): Comparison of all-hardware versus HIL simulation implementations of study system — response of ASD system with diode-rectifier front end to phase A to ground fault causing sag of nominal depth 50 %, and duration 100 ms (ASD system variables).

Once again, the behaviour of the ASD system and its impact on the electrical variables in the power system during this fault test, as predicted using the HIL simulation implementation of the laboratory-scale study system, agrees closely with the measured behaviour of the all-hardware implementation of the study system.

### 5.3.3 ASD Response to Double-Phase to Ground Faults

This subsection considers the performance of the ASD system with a diode-rectifier front end in response to the two different double-phase to ground faults at the Fault Bus in the upstream supply network that are shown in Table 5-1, namely Fault Conditions (iii) and (iv).

Figure 5-8 (a) shows the AC currents and voltages from the front end of the ASD before, during and after the phase A to B to ground fault at the upstream Fault Bus that results in sags of nominal depth 35 % and duration 100 ms in the voltages of the faulted phases at the ASD front end (Fault Condition (iii) in Table 5-1).

The results in Figure 5-8 (a) show that during this fault in the upstream network, involving both phases A and B, the currents drawn by the front end of the ASD become unbalanced, with the amplitude of the current drawn by the ASD front end in the faulted B phase being smaller than both the amplitudes of the currents drawn by the A and C phases despite the A phase being involved in the upstream fault as well. Furthermore, the results show that the front end of the ASD is unable to draw current at all from the faulted B phase for the first quarter (25 ms) of the disturbance.

The results in Figure 5-8 (a) also show that, as would be expected during the fault, there are sags in the input voltages to the ASD front end, with similar depths, in the two faulted phases, but that there is also a significant sag in the input voltage to the ASD in the un-faulted phase with a depth comparable to that seen in the sags in the faulted phases. Therefore, the results indicate that the application of this particular asymmetric (phase A to B to ground) fault at the upstream Fault Bus actually creates a condition in which the input voltage at the front end of the ASD experiences a significant sag in all three phases.

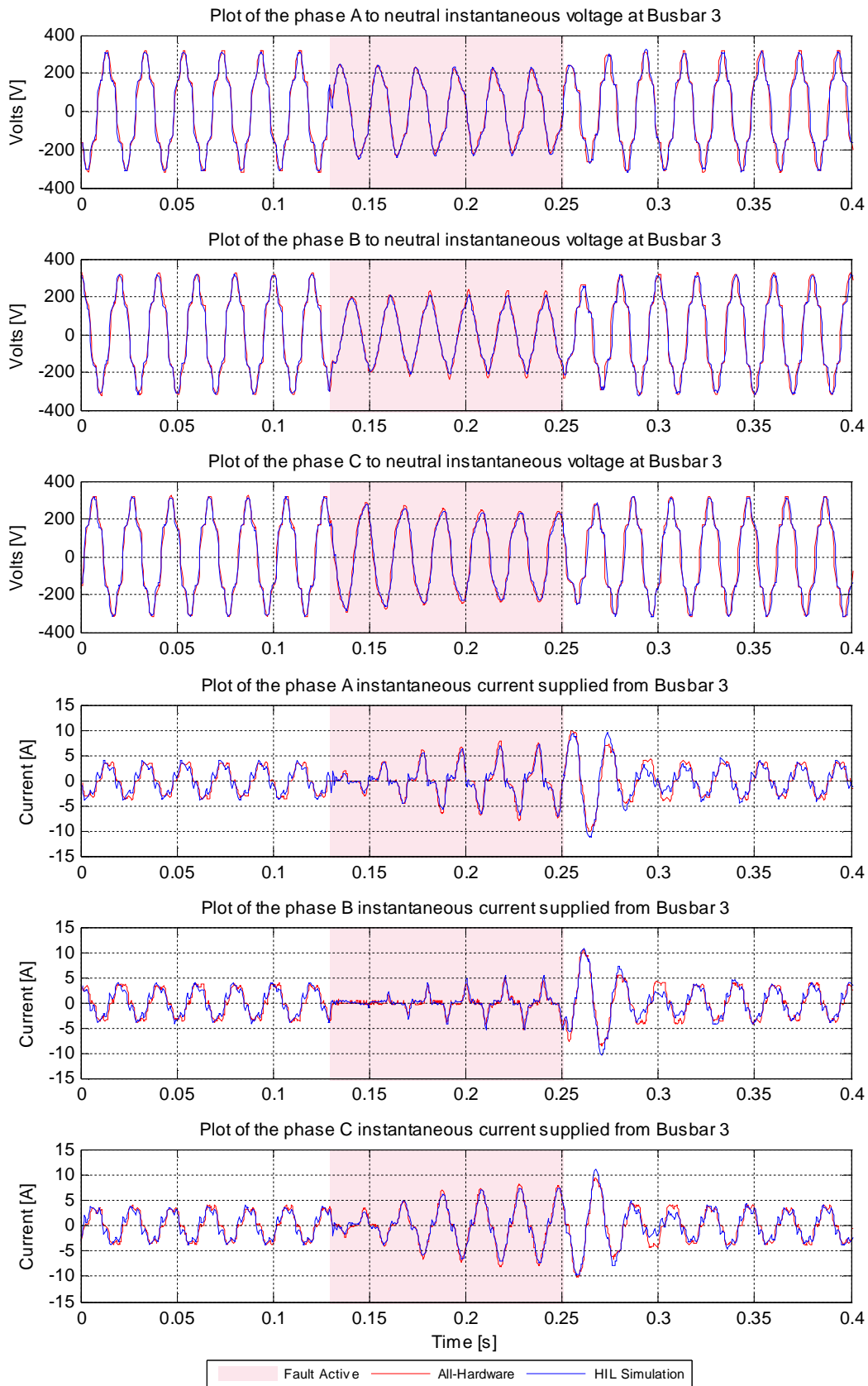


Figure 5-8 (a): Comparison of all-hardware versus HIL simulation implementations of study system — response of ASD system with diode-rectifier front end to phase A to B to ground fault causing sag of nominal depth 35 %, and duration 100 ms (Bus 3 variables).

Figure 5-8 (b) shows the response of the variables within the ASD system itself during the double-phase to ground fault test shown in Figure 5-8 (a). The results in Figure 5-8 (b) show that during the fault in the upstream network, the DC-link voltage decreases quite significantly as a result of the sags in all three phases of the input voltages at the front end of the ASD. However, the results indicate that despite the significant decrease in the DC-link voltage during the fault, the ASD controls are nevertheless still able to temporarily increase the modulation depth of the firing pulses to the VC inverter feeding the motor so as to allow the drive to ride through the voltage sag condition with negligible impact on the torque and speed of the induction machine.

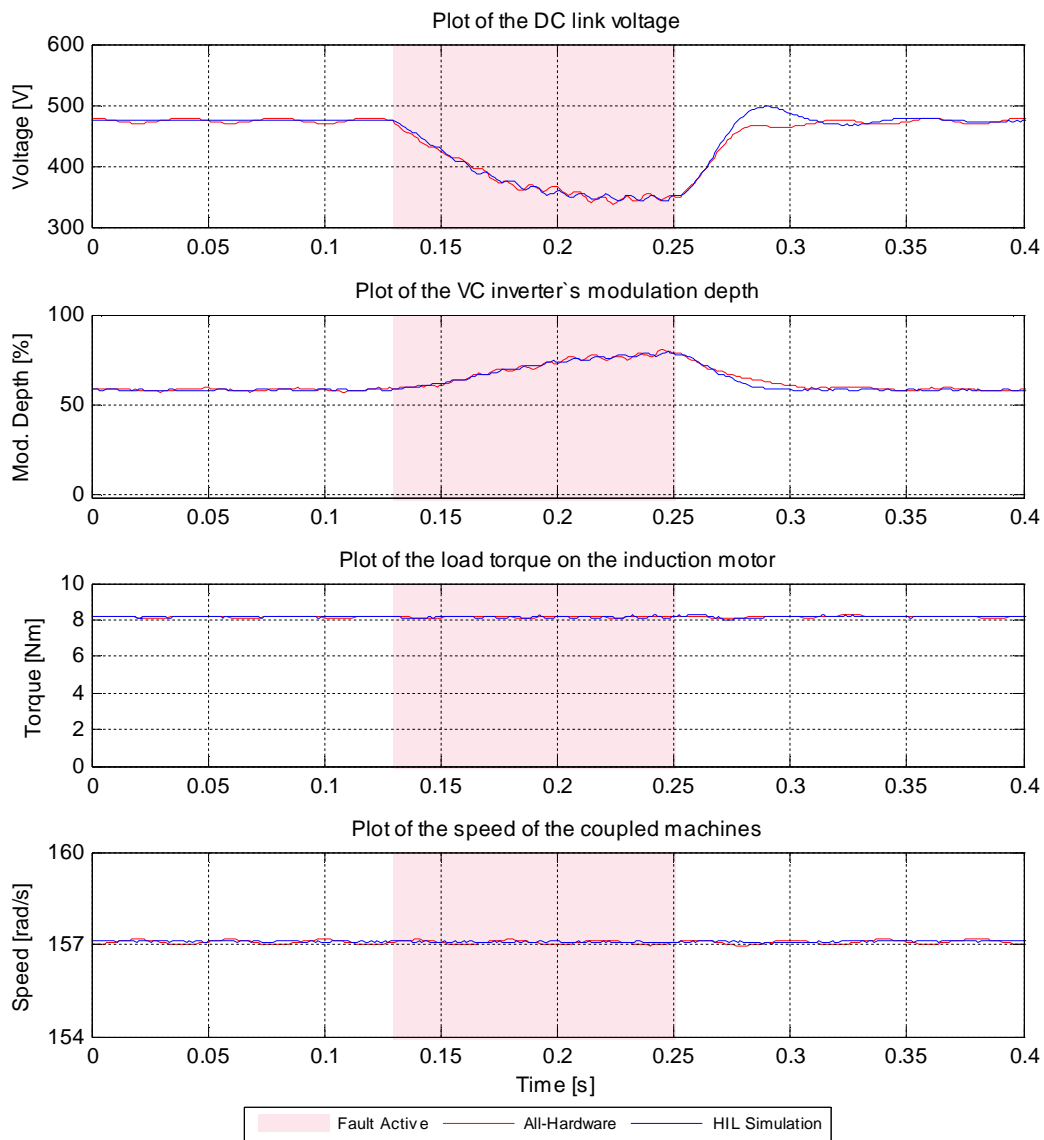


Figure 5-8 (b): Comparison of all-hardware versus HIL simulation implementations of study system — response of ASD system with diode-rectifier front end to phase A to B to ground fault causing sag of nominal depth 35 %, and duration 100 ms (ASD system variables).

Finally, the results in Figures 5-8 (a) and (b) show that the behaviour of the diode rectifier energised ASD system and its impact on the electrical variables in the power system during this fault, as predicted using the HIL simulation implementation of the laboratory-scale study system, agrees closely with the measured behaviour of the all-hardware implementation of the study system.

Figure 5-9 (a) now shows the AC currents and voltages from the front end of the ASD during the phase A to B to ground fault at the upstream Fault Bus that results in sags of nominal depth 50 % and duration 100 ms in the voltages of the faulted phases at the ASD front end (Fault Condition (iv) in Table 5-1).

The impact of this double-phase fault on the electrical variables at the front end of the ASD seen in Figure 5-9 (a) is similar in nature to that seen in the previous double-phase fault study [cf. Figure 5-8 (a)]: the currents drawn by the front end of the ASD become unbalanced during the asymmetric fault in the upstream network, with the amplitude of the current drawn by the faulted B phase being smaller than the amplitudes of the currents drawn by both the faulted A phase and unfaulted C phase. However, the impact on the currents in all three phases is more pronounced in the test shown in Figure 5-9 (a) because there is now a greater depth of sag in all three phases of the input voltages at the front end of the ASD in this case: Figure 5-9 (a) shows that the front end of the ASD is now unable to draw current from phases A and C for the first quarter (25 ms) of the disturbance, and it is also unable to draw current from the remaining phase for the first half (50 ms) of the disturbance.

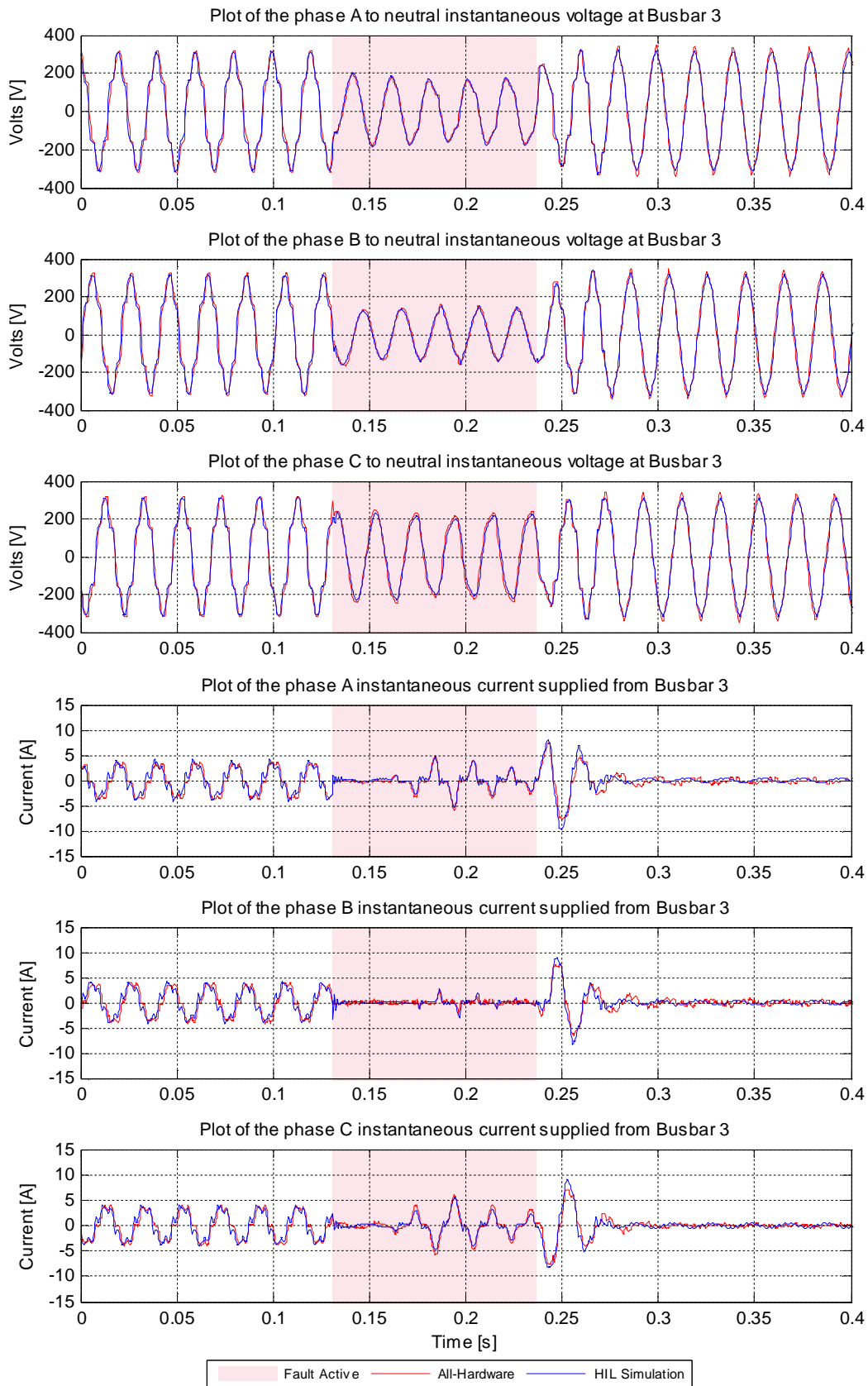


Figure 5-9 (a): Comparison of all-hardware versus HIL simulation implementations of study system — response of ASD system with diode-rectifier front end to phase A to B to ground fault causing sag of nominal depth 50 %, and duration 100 ms (Bus 3 variables).

Figure 5-9 (b) shows the response of the variables within the ASD system itself during the double-phase to ground fault test shown in Figure 5-9 (a).

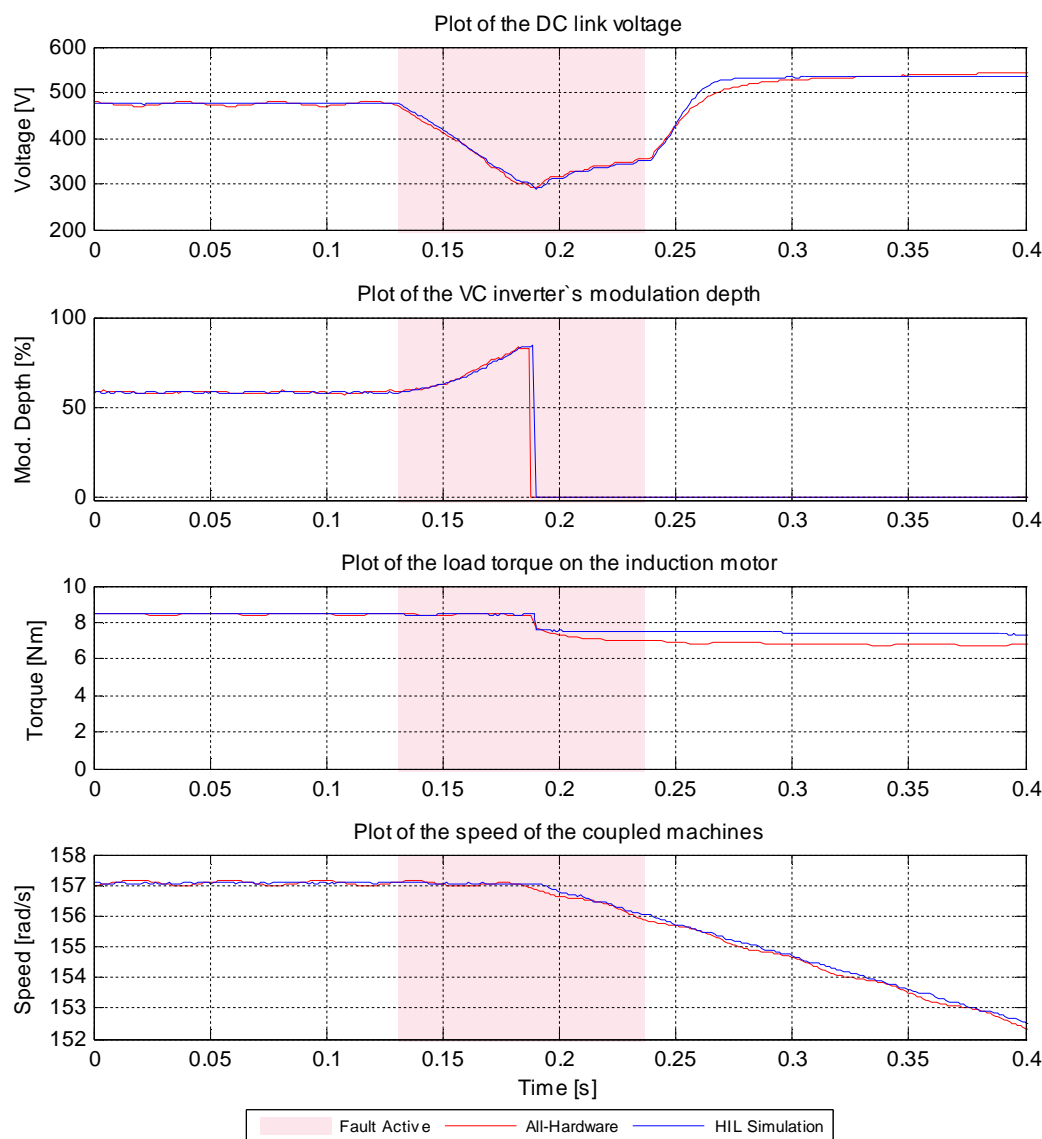


Figure 5-9 (b): Comparison of all-hardware versus HIL simulation implementations of study system — response of ASD system with diode-rectifier front end to phase A to B to ground fault causing sag of nominal depth 50 %, and duration 100 ms (ASD system variables).

The results in Figure 5-9 (b) show that immediately following the fault in the upstream network, the DC-link voltage begins to decrease as a result of the sag in the input voltages at the front end of the ASD and continues to do so for approximately 55 ms. The results show, once again, that the ASD controls react to the drop in the DC-link voltage by increasing the VC inverter modulation depth in an attempt to keep the output torque and speed of the machine constant. The results show that for the first 55 ms of the fault, the ASD controls are in fact able to keep the output torque and speed of the machine constant, despite the continuing drop in the DC-link voltage.

However, the results show that 55 ms after the onset of the fault the ASD tripped as a combined result of the modulation depth command being issued reaching a maximum pre-set value within the controller and of the DC-link voltage decreasing to a value below a pre-set threshold allowed by the controls. Thus, for this particular operating condition and upstream double-phase fault condition in the laboratory-scale study system, the ASD system equipped with a diode-rectifier front end is unable to successfully ride through the voltage sag condition.

The results in Figure 5-9 (b) show that, as would be expected, after the ASD trips, the speed of the induction motor and its coupled dynamometer begins to decrease, and the speed-dependent load torque exerted on the motor likewise decreases. The results also show that once the ASD has been tripped, the DC-link voltage begins to increase again, even prior to the removal of the fault since, in the absence of any energy demand on the DC link as a result of the drive being tripped, the energy input to the DC link at its front end is sufficient to charge the DC-link capacitors to some extent.

Finally, the results in Figures 5-9 (a) and (b) show that the behaviour of the ASD system and its impact on the electrical variables in the power system during this double-phase fault test, as predicted using the HIL simulation implementation of the laboratory-scale study system, agrees closely with the measured behaviour of the all-hardware implementation of the study system even for severe sag test conditions such as this in which the ASD system variables undergo large excursions and are driven into their control limits prior to the drive tripping out completely.

The results in Figure 5-9 (b) indicate that once the ASD system has tripped and the induction motor speed begins to decrease significantly after it has been disconnected from its AC supply, the simple dynamic model used to represent the load torque exerted by the dynamometer in the real-time simulation model of the laboratory-scale study system no longer agrees closely with the measured behaviour of the load torque's characteristics. Although it would be possible to refine the real-time simulator model of the dynamometer used in these studies to enable it to be more representative for larger excursions in speed, this was considered unnecessary since predicting the behaviour of the ASD system after failing to ride through a voltage sag condition, and while decelerating after tripping the induction motor, was not within the scope of this investigation.

### 5.3.4 ASD Response to Three-Phase to Ground Faults

This subsection now considers the performance of the ASD system with a diode-rectifier front end in response to the two different three-phase to ground faults at the Fault Bus in the upstream supply network that are shown in Table 5-1, namely Fault Conditions (v) and (vi).

Figure 5-10 (a) shows the AC currents and voltages from the front end of the ASD before, during and after the particular three-phase to ground fault at the upstream Fault Bus that results in sags of nominal depth 50 % and duration 100 ms in the voltages of all three phases at the ASD front end (Fault Condition (v) in Table 5-1). Figure 5-10 (b) shows the response of the variables within the ASD system itself during this three-phase fault condition.

The results in Figure 5-10 (a) confirm that the result of this upstream three-phase fault is a symmetrical sag in the input voltages at the front end of the ASD and that, furthermore, in the case of this particular three-phase fault the sag in these input voltages is sufficiently deep that the rectifier at the front end of the ASD is unable to draw current in all three phases for the entire duration of the fault and is therefore unable to supply energy to the DC-link capacitors during the fault. Figure 5-10 (b) shows that, as a result, the DC-link voltage decreases continuously following the onset of the fault because, whilst no energy is being supplied to the DC link from the ASD's front end during the fault, its VC inverter continues to supply the energy demanded by the motion control task at the expense of the charge stored in the DC-link capacitors.

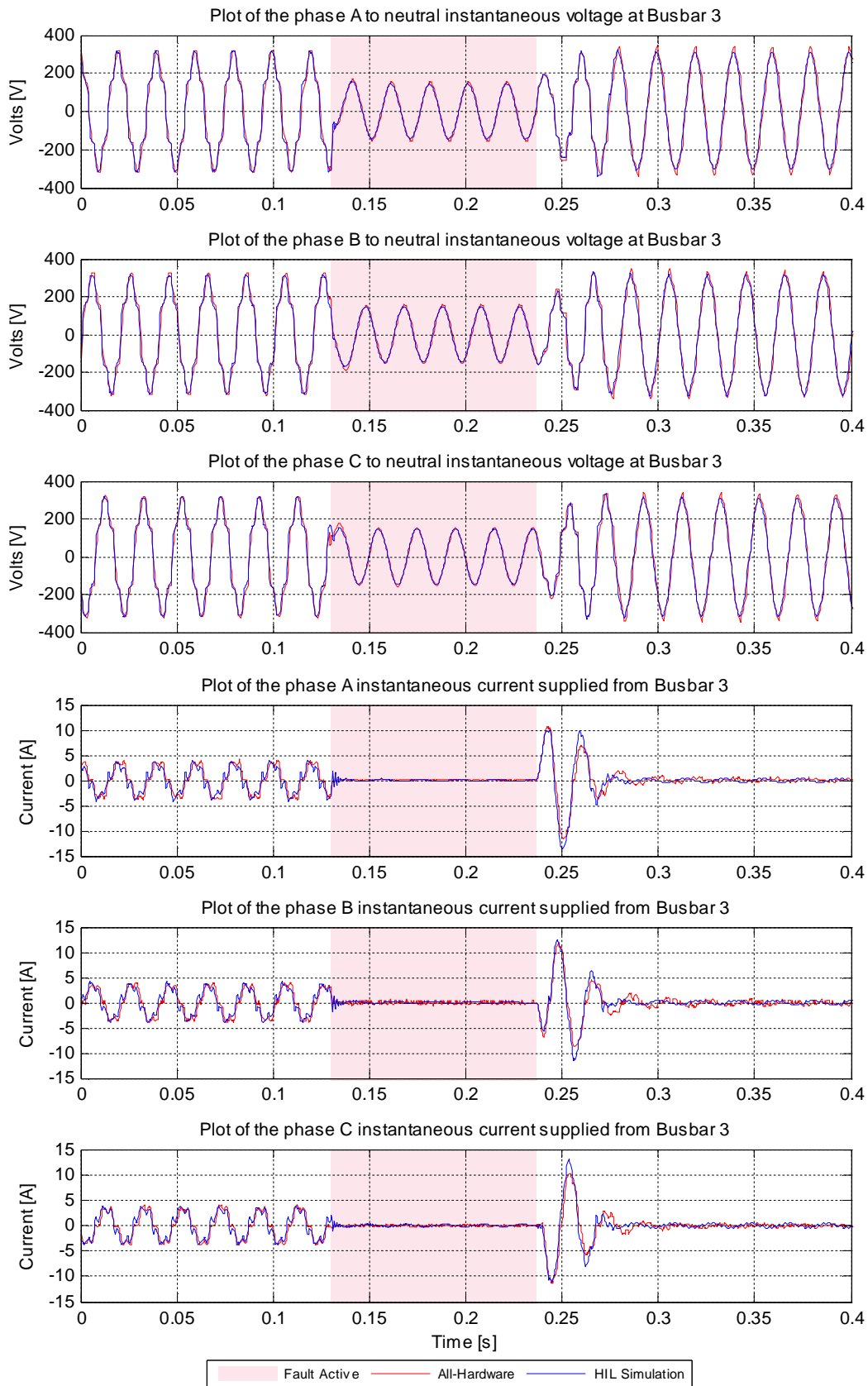


Figure 5-10 (a): Comparison of all-hardware versus HIL simulation implementations of study system — response of ASD system with diode-rectifier front end to phase A to B to C to ground fault causing sag of nominal depth 50 %, and duration 100 ms (Bus 3 variables).

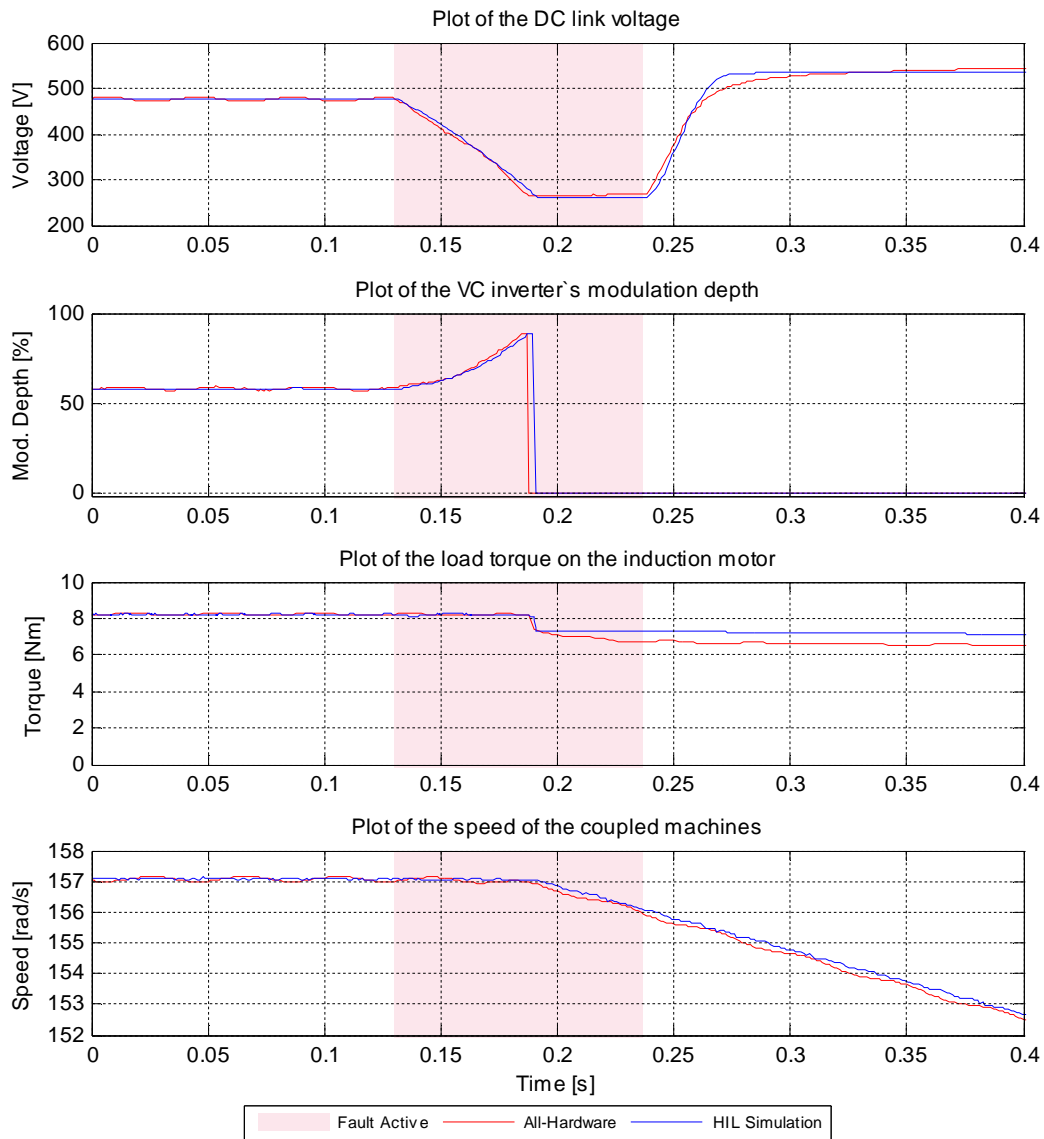


Figure 5-10 (b): Comparison of all-hardware versus HIL simulation implementations of study system — response of ASD system with diode-rectifier front end to phase A to B to C to ground fault causing sag of nominal depth 50 %, and duration 100 ms (ASD system variables).

Figure 5-10 (b) shows that the ASD controls initially react to the decreasing DC-link voltage by increasing the VC inverter modulation depth and that, until this modulation depth reaches the allowed limit this successfully keeps the output torque and speed of the machine constant despite the decreasing DC-link voltage. However, as the results in Figure 5-10 (b) demonstrate, after some time the drive trips as a combined result of the modulation depth command reaching the maximum allowable value and the DC-link voltage dropping below the minimum threshold allowed by the ASD controls. The results in Figure 5-10 also demonstrate that in this particular fault test, because the sag in all three input voltages to the ASD front end is sufficiently deep to prevent any current being drawn by the ASD's front-end rectifier at all during the fault, there is no recovery in the DC-link voltage in

the time between the drive tripping and the fault being removed as was the case in the previous fault test presented in Figure 5-9. In Figure 5-10, once the drive trips and no further energy is drawn from the DC-link capacitors, the DC-link voltage remains constant until the fault is removed and the input voltages to the ASD front end are again of sufficient magnitude to forward bias the front-end rectifier diodes and recharge the DC-link capacitors.

Finally, the results in Figures 5-10 (a) and (b) show that the behaviour of the ASD system and its impact on the electrical variables in the power system during this three-phase fault test, as predicted using the HIL simulation implementation of the laboratory-scale study system, agrees closely with the measured behaviour of the all-hardware implementation of the study system even though the ASD system variables, once again, are seen to undergo large excursions and are driven into their control limits prior to the drive tripping out completely in this case.

Figure 5-11 (a) now shows the AC currents and voltages from the front end of the ASD during the most severe three-phase to ground fault at the upstream Fault Bus, namely the fault that results in sags of nominal depth 70 % and duration 100 ms in the voltages of all three phases at the ASD front end (Fault Condition (vi) in Table 5-1). Figure 5-11 (b) shows the response of the variables within the ASD system itself during this three-phase fault condition.

The results in Figure 5-11 (a) show that, in terms of the depth of sag caused in the input voltages to the ASD's front end, this upstream three-phase fault is indeed more severe than that considered in the previous test [cf. Figure 5-10 (a)]. However, comparison of Figures 5-10 (a) and 5-11 (a) shows that the impact of both of these faults on the ability of the ASD's front-end rectifier to draw current is in fact the same, that is both of these upstream faults are sufficiently severe that the ASD is unable to draw current in all three phases for the entire duration of each fault, and is therefore completely unable to supply energy to its DC-link capacitors during each fault. Hence, since both of these faults have the same duration (100 ms) the impact on the ASD's performance would be expected to be the same in each case. Indeed, comparison of the results in Figure 5-11 (b) with those in Figure 5-10 (b) confirms this to be the case. Figure 5-11 (b) shows that immediately following the appearance of the fault, the DC-link voltage decreases continuously, and the VC inverter modulation depth increases continuously, both at the same rates as seen in the results of Figure 5-10 (b), until the drive trips, once again after the same duration of time following the fault onset in both cases.

Thus, the results of Figure 5-11 (taken together with those of Figure 5-10) show that in the case of symmetrical three-phase faults, and for the type of ASD front-end technology being considered in this chapter (uncontrolled diode rectifier) once a sag in the input voltages becomes sufficiently deep to prevent energy conversion by the front-end rectifier, the only characteristic of that sag that is then of interest with respect to the ride-through capability of the drive becomes the duration of the sag.

Finally, the results in Figures 5-11 (a) and (b) show that the behaviour of the ASD system and its impact on the electrical variables in the power system during this three-phase fault test, as predicted using the HIL simulation implementation of the laboratory-scale study system, agrees closely with the measured behaviour of the all-hardware implementation of the study system even though the ASD system variables, once again, are seen to undergo large excursions and are driven into their control limits prior to the drive tripping out completely in this case.

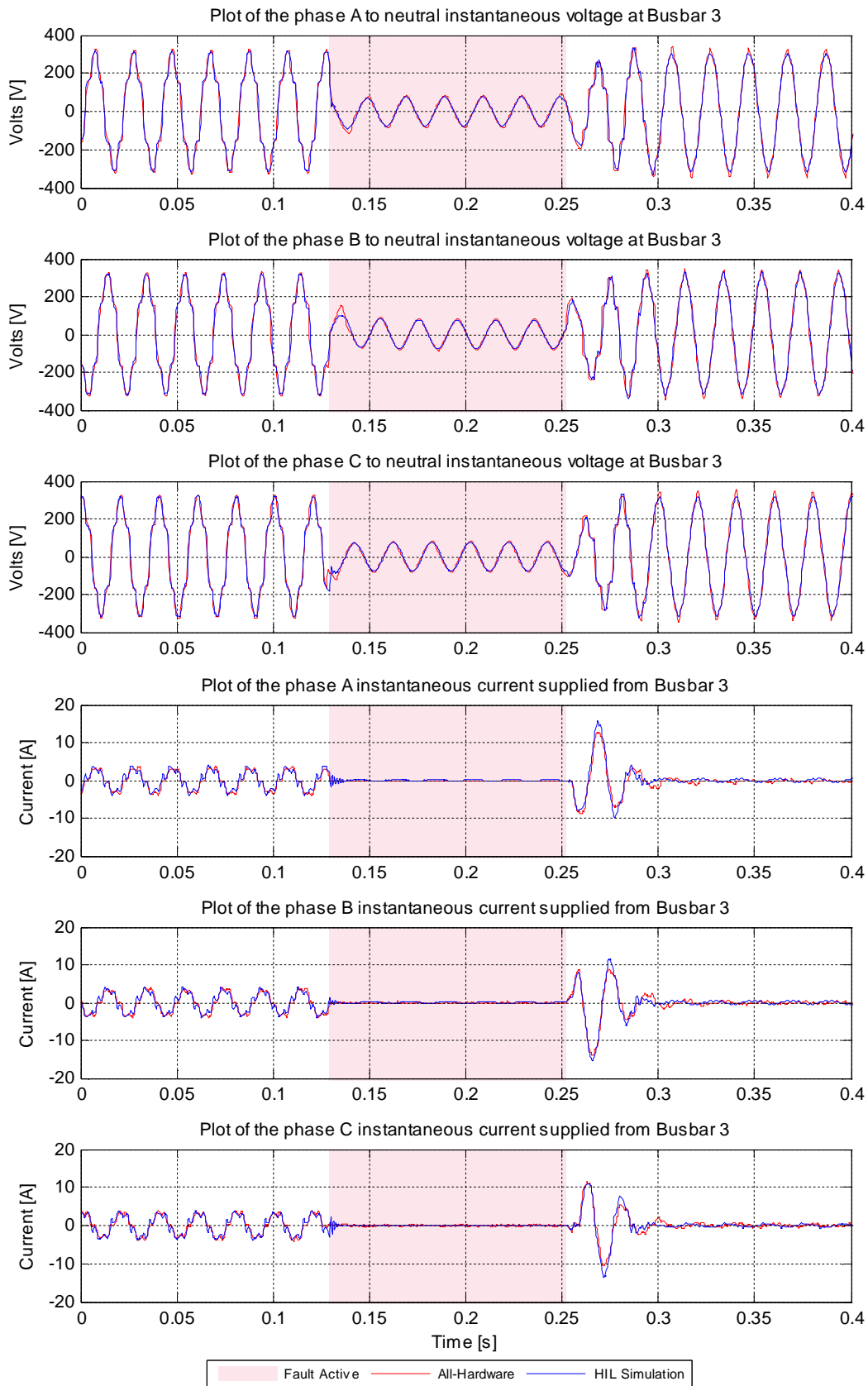


Figure 5-11 (a): Comparison of all-hardware versus HIL simulation implementations of study system — response of ASD system with diode-rectifier front end to phase A to B to C to ground fault causing sag of nominal depth 70 %, and duration 100 ms (Bus 3 variables).

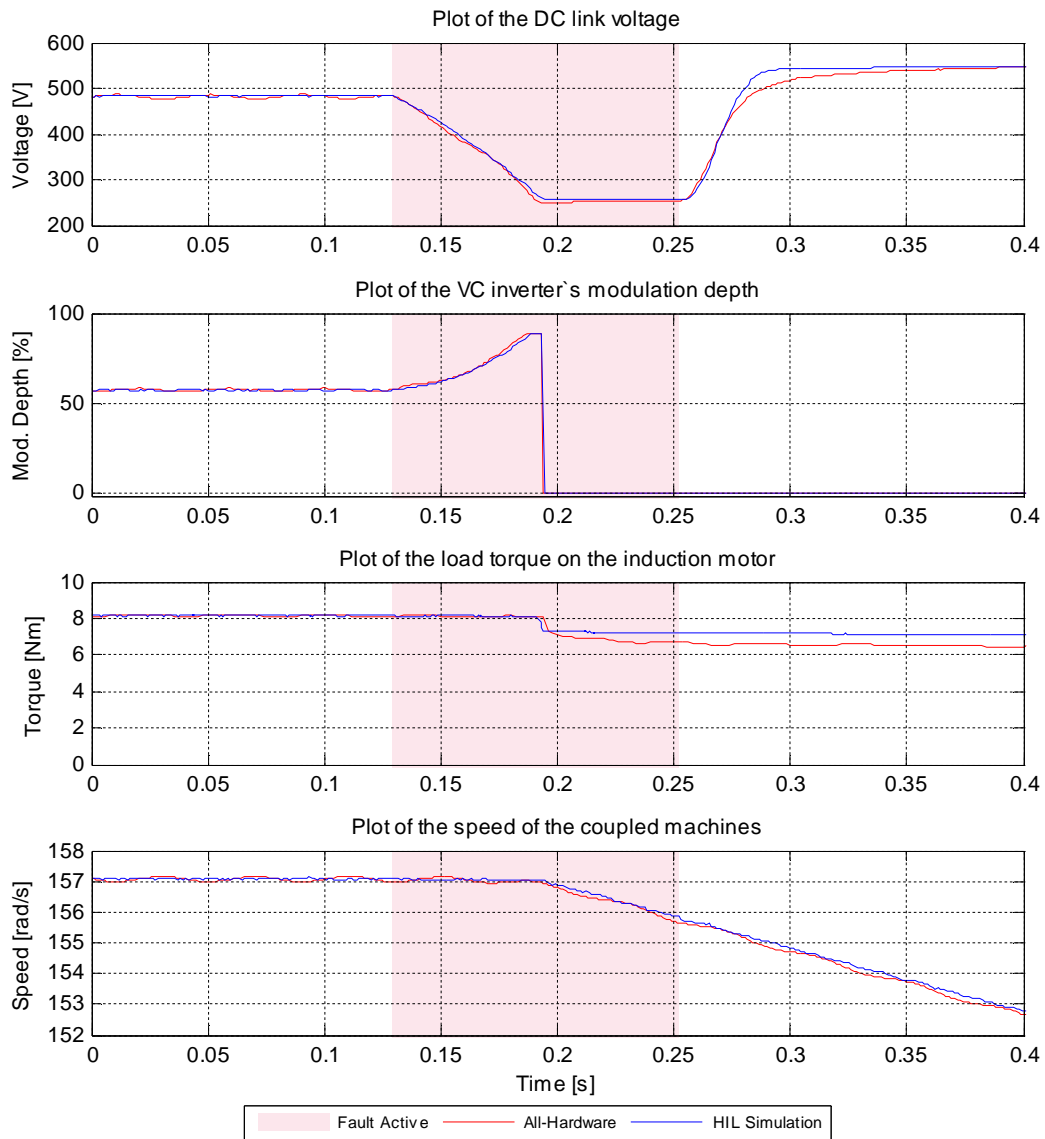


Figure 5-11 (b): Comparison of all-hardware versus HIL simulation implementations of study system — response of ASD system with diode-rectifier front end to phase A to B to C to ground fault causing sag of nominal depth 70 %, and duration 100 ms (ASD system variables).

### **5.3.5 Summary of the ASD's Response to Upstream Faults**

This section has presented the results of detailed measurements carried out on the all-hardware implementation of the laboratory-scale study system in order to test the dynamic performance of an ASD system with an uncontrolled diode-rectifier front end in response to a set of six pre-determined fault conditions (shown in Table 5-1) in the upstream supply network designed to cause a range of sag conditions at the input voltages to the ASD.

The results have shown that the diode-rectifier front-end ASD system was able to ride through the voltage sag conditions associated with Fault Conditions (i), (ii) and (iii) in Table 5-1. However, the results also showed that this ASD system was unable to ride through three of the more-severe voltage sag conditions, specifically those associated with Fault Conditions (iv), (v) and (vi) in Table 5-1: in each of these cases the ASD system tripped out in response to the sags caused by the upstream faults.

Furthermore, the close agreement between the measurements that were taken on the all-hardware implementation of the laboratory-scale study system and the results that were obtained from the HIL simulation implementation of the study system in response to the same six fault conditions in the upstream supply network provides confidence in the ability of the HIL real-time simulator testing approach to accurately predict the dynamic performance of ASD systems that are energised by uncontrolled diode-rectifier front-end converters in response to voltage sag conditions caused by upstream faults.

## 5.4 Summary

This chapter began by describing how the real-time simulation model of the power-level plant in the laboratory-scale study system was interfaced to the physical controllers of the industrial adjustable speed drive (ASD) system in order to form the hardware-in-loop (HIL) simulation implementation of the study system. The chapter thereafter considered the specific case in which the ASD in the laboratory-scale system was equipped with a diode-rectifier front-end converter and presented the results of detailed studies into the performance of this type of ASD in response to voltage sags caused by upstream faults in the laboratory-scale system. These results have not only documented the voltage-sag performance of this type of ASD technology by means of measurements carried out on a carefully-controlled and representative small-scale study system implemented in a research laboratory, but have also demonstrated the validity of the HIL real-time simulation approach to such testing. The close agreement between the results obtained from both implementations of the laboratory-scale study system (HIL simulation and all-hardware) has demonstrated that the HIL real-time simulator testing approach can accurately predict the dynamic performance of ASD systems equipped with diode-rectifier front-end converters in response to voltage sags caused by upstream faults.

The next chapter presents similarly-detailed comparisons between the results of the HIL real-time simulator testing approach and measurements carried out on the all-hardware implementation of the laboratory-scale study system for the particular case in which the ASD is equipped with an active front-end converter. Thereafter, the chapter presents the results of a further investigation, carried out solely using the HIL real-time simulator testing approach, in order to compare the influence of different ASD front-end converter technologies on the performance of the power system itself during upstream network faults.

## **Chapter 6: The Performance Of The AFE Converter Energised ASD System Under Voltage Sag Conditions**

### **6.1 Introduction**

Chapter 1 explained the procedure that has been developed in order to evaluate the hardware-in-loop (HIL) testing approach for studying the dynamic performance of adjustable speed drives (ASDs) being proposed in this thesis. The procedure involves comparison of the measured performance of a full, industrial ASD within an all-hardware implementation of a laboratory-scale study system in response to a set of upstream network faults against the performance of a hardware-in-loop simulation implementation of the same study system in which the power-level plant in the study system is modelled on a real-time digital simulator and the physical ASD controllers are connected hardware-in-loop with this real-time model of the power-level plant.

Chapter 3 introduced a small-scale study system that was specifically designed to allow all-hardware implementation within a machines research laboratory and HIL simulation implementation so that the aforementioned evaluation procedure could then be considered for the case of an industrial ASD equipped firstly with an uncontrolled diode-rectifier front-end converter and then with an active front end (AFE) converter. Chapter 5 then considered the particular case in which the ASD in the laboratory-scale study system was equipped with a diode-rectifier front-end converter and presented detailed comparisons between the results obtained from the all-hardware and HIL simulation implementations of the laboratory-scale study system during the voltage sag conditions created by the application of the upstream network faults. In accordance with the aforementioned procedure, these detailed comparisons were then used to evaluate the suitability of the HIL simulator testing approach for studying the dynamic performance of ASD systems equipped with diode-rectifier front-end converters.

This chapter now considers the particular case in which the ASD in the laboratory-scale study system is equipped with an AFE converter and presents detailed results obtained from both implementations of the laboratory-scale study system (all-hardware and HIL simulation) which demonstrate the dynamic performance of this category of industrial ASD system in response to voltage sag conditions. Once again, in accordance with the aforementioned procedure, the detailed results obtained from both implementations of the study system are compared in order to evaluate the HIL simulator testing approach for studying the dynamic performance of ASD systems equipped with AFE converters.

Thereafter, the chapter presents the results of a further investigation, carried out solely using the HIL simulator testing approach, in order to compare the influence of the two different ASD front-end converter technologies considered in the thesis on the performance of the power system itself during upstream network faults.

## **6.2 Comparisons of the Results from the All-Hardware and HIL Simulation Implementations of the Study System Under Voltage Sag Conditions for the Case of the Active Front End Converter Energised ASD System**

### **6.2.1 Introduction**

This section now considers the actual dynamic performance of the motion control system in the full laboratory-scale study system under voltage sag conditions for the particular case when an active front end unit was used as the converter technology feeding the front end of the drive as shown in Figure 6-1.

The operating conditions chosen for these tests on the laboratory-scale study system were discussed in Chapter 3 and are summarized again here for completeness. The ASD system was fed, via the upstream network, with its nominal input voltage of 380 V at Bus 3 and the ASD system controllers were configured to regulate the DC-link voltage supply to the machine-side inverter and the speed of the induction motor. In particular the ASD's closed-loop speed controller was set to maintain the speed of the induction motor at 157.1 rad/s (1500 rpm) while the dynamometer applied a torque of 8 Nm at its shaft (approximately 50 % of the rated load of the motor).

Whilst the ASD system was performing this motion control task it was then subjected to a range of different voltage sag conditions at its front end by applying each of the six pre-determined fault conditions in the upstream supply network of the study system, as described in Chapter 3. The details of these six fault conditions, and the associated sag types and nominal sag depths produced at Bus 3, are summarized again, for completeness, in Table 6-1.

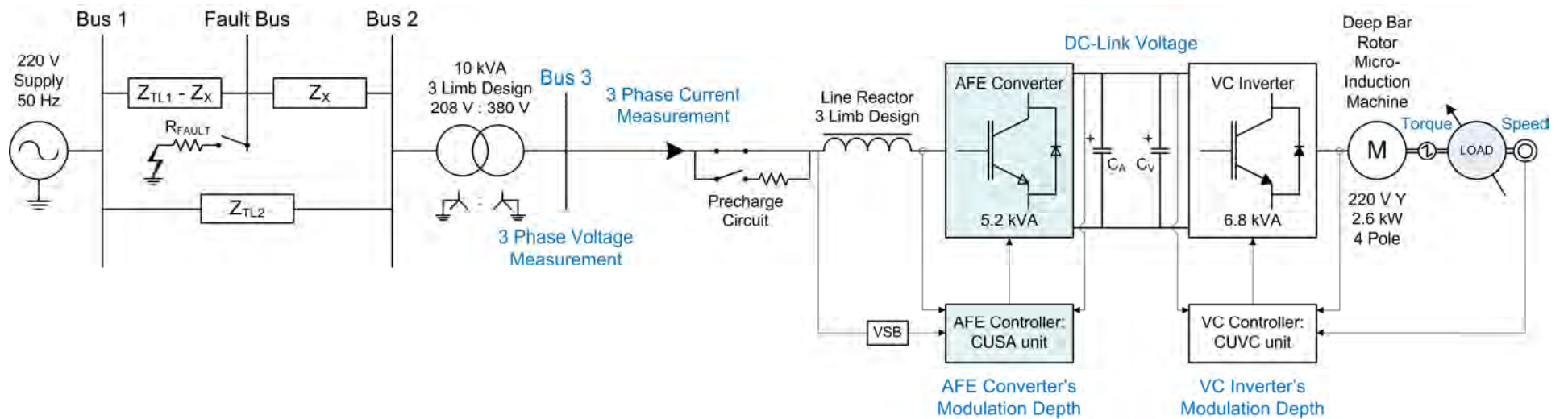


Figure 6-1: Schematic diagram of the laboratory-scale study system for the case in which the AFE converter unit was used to energise the machine-side inverter in the ASD system.

*Table 6-1: Sag characteristics and nominal sag depths at the Bus 3 voltage for the six particular fault conditions considered during experimental tests on the laboratory-scale study system.*

Fault Condition	Sagged Phase/s	Duration [ms]	Voltage Sag Depth [%]	Remaining Voltage During Fault [%]
(i)	A	200	35	65
(ii)	A	100	50	50
(iii)	A, B	100	35	65
(iv)	A, B	100	50	50
(v)	A, B, C	100	50	50
(vi)	A, B, C	100	70	30

These six fault conditions were applied first to the all-hardware implementation of the study system in the laboratory, and then to the hardware-in-loop real-time simulation implementation of the study system, with the same set of variables recorded from the study system in each case for comparison.

The specific variables that were recorded in each set of tests are highlighted in blue in the schematic diagram of the system in Figure 6-1. Within the power-level plant, the three-phase voltages and currents at the input to the front end of the ASD system at Bus 3 were recorded, as was the DC-link voltage, motor load torque and speed. In the case of the all-hardware implementation of the study system, these variables were obtained from measurements on the practical system in the laboratory, whereas in the case of the HIL simulation implementation, these variables were recorded within the simulation model of the power-level plant. Furthermore, in both implementations (all-hardware and HIL simulation) the values of the modulation depth commanded by both the AFE converter and the VC inverter hardware controllers (i.e. the CUSA and CUVC control units respectively) during the tests were also recorded for comparison.

## 6.2.2 AFE Converter Energised ASD Response to Single-Phase to Ground Faults

This subsection considers the performance of the ASD system with an active front end converter in response to the two different single-phase to ground faults at the Fault Bus in the upstream supply network that are shown in Table 6-1, namely Fault Conditions (i) and (ii).

Figure 6-2 (a) shows the AC currents and voltages from the front end (Bus 3) of the ASD before, during and after the particular phase A to ground fault at the upstream Fault Bus that results in a sag of nominal depth 35 % and duration 200 ms in the voltage of the faulted phase at the ASD front end (Fault Condition (i) in Table 6-1). The measured results from the application of the fault in the all-hardware implementation of the study system, as well as those obtained when the same fault was applied in the HIL simulation implementation of the study system, are each plotted on common axes in Figure 6-2 (a) to show how closely the two sets of test results agree with one another; the areas highlighted in pink show the period during which the fault was actually applied in both sets of test results.

The results in Figure 6-2 (a) show that under normal steady state conditions the AFE converter draws virtually sinusoidal currents at unity power factor because of the pre-commissioned settings programmed into the AFE controller (as described in Chapter 3, Section 3.4.3). As a result of the sinusoidal currents drawn by the AFE converter, Figure 6-2 (a) shows that the input voltages to the converter also appear to be free from any harmonic distortion during these steady-state conditions.

Figure 6-2 (a) shows that during the fault in phase A of the upstream power system network the currents drawn by the front end of the ASD become unbalanced, with the amplitude of the current drawn by the ASD front end in the faulted phase being smaller than the amplitudes of the currents drawn by the ASD in both of the un-faulted phases. Figure 6-2 (a) also shows that during this particular upstream fault, there are no significant changes in the amplitudes of the input voltages to the ASD front end in the un-faulted phases. In fact, a close inspection of Figure 6-2 (a) shows that the voltage at the input to the ASD front end in phase B actually increases slightly during the fault, whereas its phase C front-end voltage decreases slightly during the fault. A further close analysis of the current and voltage waveforms in Figure 6-2 (a) shows that this slight increase in the input voltage to phase B during the fault is as a result of the active front end converter drawing a current that leads the voltage in this phase during the fault, resulting in a degree of reactive power compensation in this phase during the fault as a result of the response of the AFE controls. However, as pointed out, the

magnitudes of the front-end voltage changes in the un-faulted phases (increasing in phase B and decreasing in phase C) are relatively small in both cases.

Finally, the results in Figure 6-2 (a) show that there is excellent agreement between the behaviour of the currents and voltages at the front end of the ASD system measured in the all-hardware implementation of the laboratory-scale study system, and the currents and voltages obtained from the HIL simulation implementation of the same study system for this particular upstream fault test. The HIL simulation is able to closely replicate not only the amplitudes of the voltages and currents at the ASD's front end under faulted and un-faulted conditions in this test, but also the dynamic behaviour of these variables upon inception and removal of the fault.

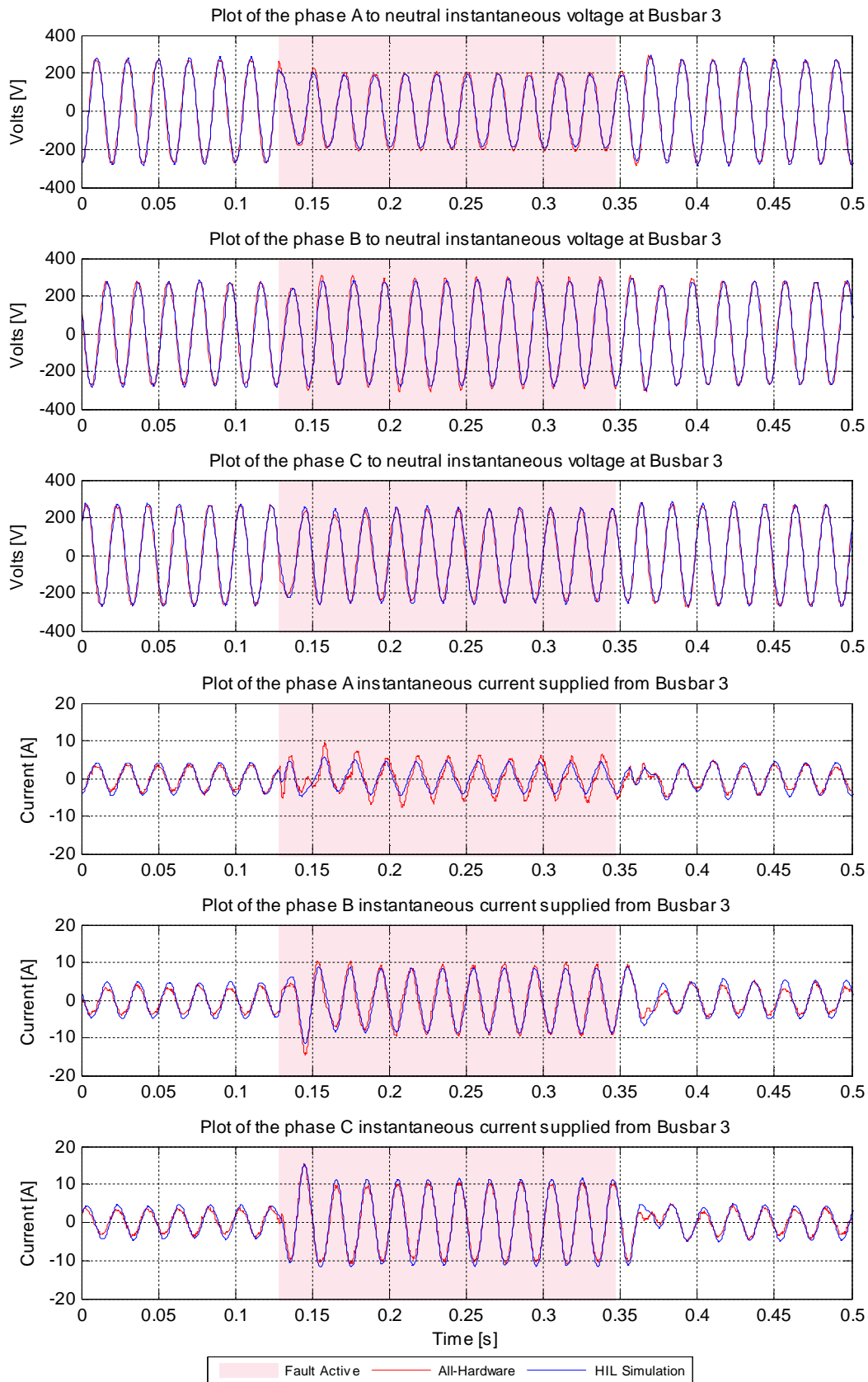


Figure 6-2 (a): Comparison of all-hardware versus HIL simulation implementations of study system — response of ASD system with active front end converter to phase A to ground fault causing sag of nominal depth 35 %, and duration 200 ms (Bus 3 variables).

Figure 6-2 (b) now shows the response of the variables within the ASD system itself during the same single-phase to ground fault test shown in Figure 6-2 (a).

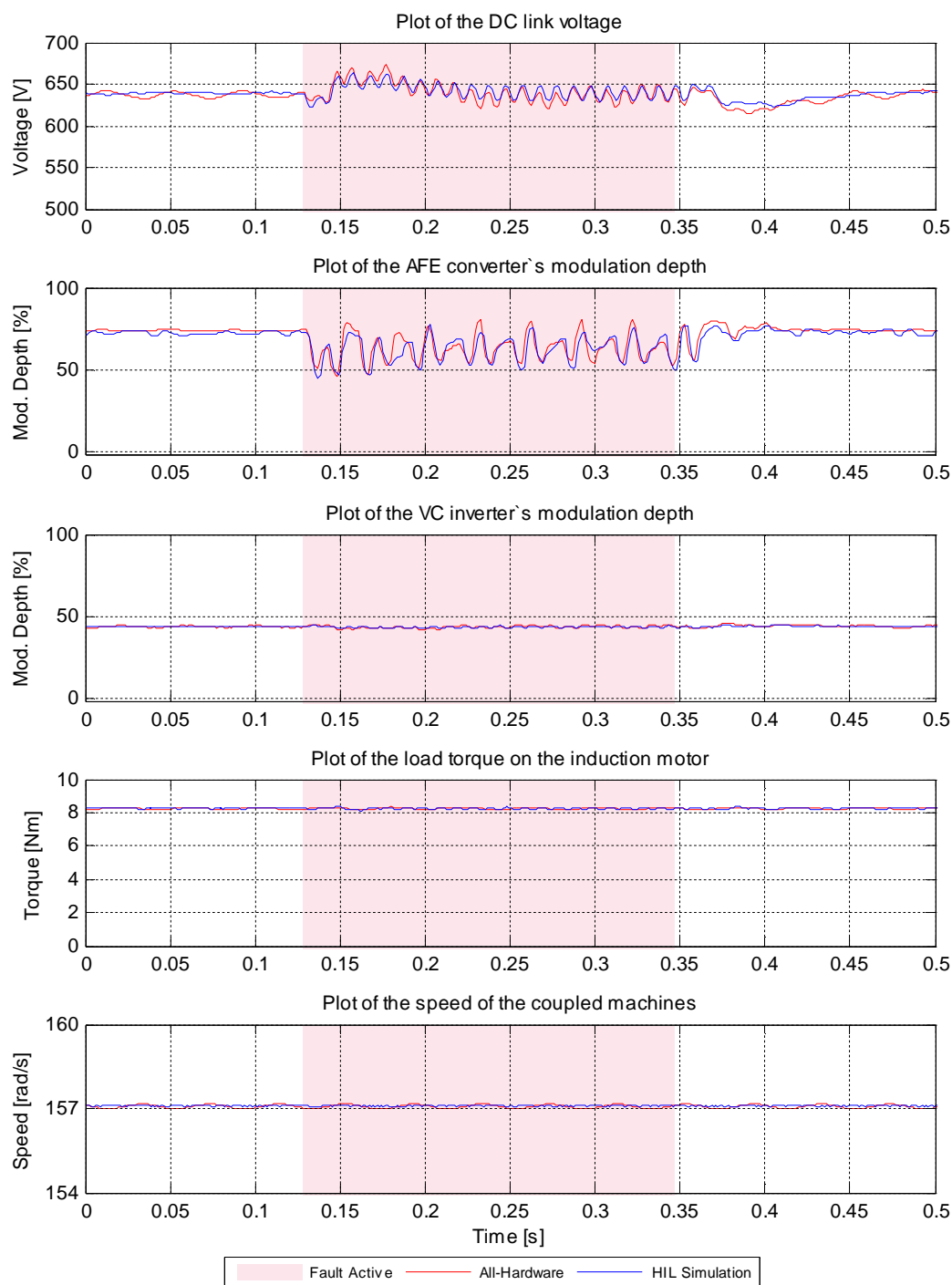


Figure 6-2 (b): Comparison of all-hardware versus HIL simulation implementations of study system — response of ASD system with active front end converter to phase A to ground fault causing sag of nominal depth 35 %, and duration 200 ms (ASD system variables).

Once again, the measured results from the application of the fault test on the all-hardware implementation of the study system as well as those obtained from the same test on the HIL

simulation implementation are each plotted on common axes in Figure 6-2 (b), with the areas highlighted in pink showing the period during which the fault was actually applied in each case.

The results in Figure 6-2 (b) show that at the onset of the fault in the upstream network, the DC-link voltage initially decreases as a result of the sag in the voltage at the input to the ASD's front end in the faulted phase. However, the results show that the DC-link voltage then quickly increases back above its pre-fault, steady-state operating value (within approximately 10 ms of the onset of the fault) before settling back down for the remainder of the fault to a level approximately equal to its pre-fault, steady-state value.

Chapter 3 explained that when configured to operate with an active front end converter module, the industrial ASD system considered in this thesis was commissioned in such a way as to maintain its DC-link voltage constant by controlling the three-phase currents at the AC terminals of the front-end converter, and that when the ASD is programmed to operate in this mode its CUSA unit controls both the DC-link voltage and the three-phase currents of the front-end converter in a closed-loop manner using a technique that is based on the field oriented control algorithm. The results in Figure 6-2 now illustrate how the CUSA controller maintains the DC-link voltage of the ASD system under voltage sag conditions by decreasing the modulation depth of the firing pulses sent to the AFE converter at the front end of the drive [Figure 6-2 (b)] which in turn causes the front-end converter to draw more current in all three phases during the fault [Figure 6-2 (a)]. The results in Figure 6-2 (b) confirm that throughout the period of the sag in the voltage at the input to the ASD's front end, the DC-link voltage magnitude is indeed maintained by the AFE controller and, as a result, the closed-loop speed control and field-oriented control of the induction machine that are implemented on the VC controller are able to maintain the desired output torque and speed of the machine during the front-end voltage sag without the need to command any significant change in the modulation depth of the firing pulses sent to the machine-side VC inverter.

Thus, the results in Figures 6-2 (a) and (b) demonstrate that the ability of the active front end converter's controller to maintain the DC-link voltage of the drive during a sag in the voltages at its AC inputs by adjusting its own modulation depth allows the ASD system to ride through this voltage sag in a manner that effectively decouples the machine-side inverter that feeds the motor and load from the impact of this sag in the AC input voltage appearing at the front end of the ASD.

The results in Figure 6-2 (b) show that once the upstream fault is removed, the AFE controller responds to the restoration of the Bus 3 voltages by increasing the modulation depth of the AFE

converter back to its pre-fault value; Figure 6-2 (a) shows that the AC currents drawn by the AFE converter then likewise return to their pre-fault steady-state values.

Finally, the results in Figure 6-2 (b) show that there is excellent agreement between the behaviour of the variables within the drive system itself that were measured in the all-hardware implementation of the laboratory-scale study system, and the corresponding variables obtained from the HIL simulation implementation of the study system for this single-phase fault test. In particular, the HIL simulation is able to closely replicate the steady state and dynamic behaviour of both the DC-link voltage and the AFE converter modulation depth control signal prior to, during and after the upstream fault.

Figure 6-3 (a) now shows the AC currents and voltages from the front end of the ASD during the phase A to ground fault at the upstream Fault Bus that results in a sag of nominal depth 50 % and duration 100 ms in the voltage of the faulted phase at the ASD front end (Fault Condition (ii) in Table 6-1). Figure 6-3 (b) shows the response of the variables within the ASD system itself during this single-phase fault condition.

The impact of this single-phase fault on the electrical variables at the front end of the ASD seen in Figure 6-3 (a) is similar in nature to that seen in the previous single-phase fault study [Figure 6-2 (a)]: in addition to the expected sag in the input voltage to the ASD in the faulted phase, the input voltage in one of the two un-faulted phases increases slightly whilst the input voltage in the other un-faulted phase once again sags; the currents drawn by the front end of the ASD become unbalanced during the sag, with the amplitude of the currents drawn by the ASD front end in the faulted phase being smaller than the amplitudes of the currents drawn by the ASD in both of the un-faulted phases. However, in the case of the particular single-phase fault test shown in Figure 6-3 (a) the impact on the sag in voltage in one of the un-faulted phases, and on the currents drawn by all three phases is more pronounced because of the greater sag in the input voltage in the faulted phase in this case. However, the response of the variables within the ASD system in Figure 6-3 (b) shows that despite these more-severe voltage sags at the input to the drive, the AFE controller is still able to maintain a near-constant DC-link voltage throughout the fault and, as a result, the ASD system is therefore able to ride through the voltage sags with very little adjustment required in the VC inverter's modulation depth and hence with negligible impact on the output torque and speed of the induction machine. However, comparison of the responses in Figures 6-2 and 6-3 shows that in the case of the more-severe single-phase fault condition (Figure 6-3), maintaining the DC-link voltage magnitude during the sag requires the AFE controller to command a greater reduction in the modulation depth signal sent to the front-end converter and hence for the ASD to draw larger amplitudes of unbalanced current from the faulted upstream network at its AC front end.

Finally, the results in Figures 6-3 (a) and (b) show that, once again, the behaviour of the ASD system and its impact on the electrical variables in the power system during this single-phase fault test, as predicted using the HIL simulation implementation of the laboratory-scale study system, agrees closely with the measured behaviour of the all-hardware implementation of the study system.

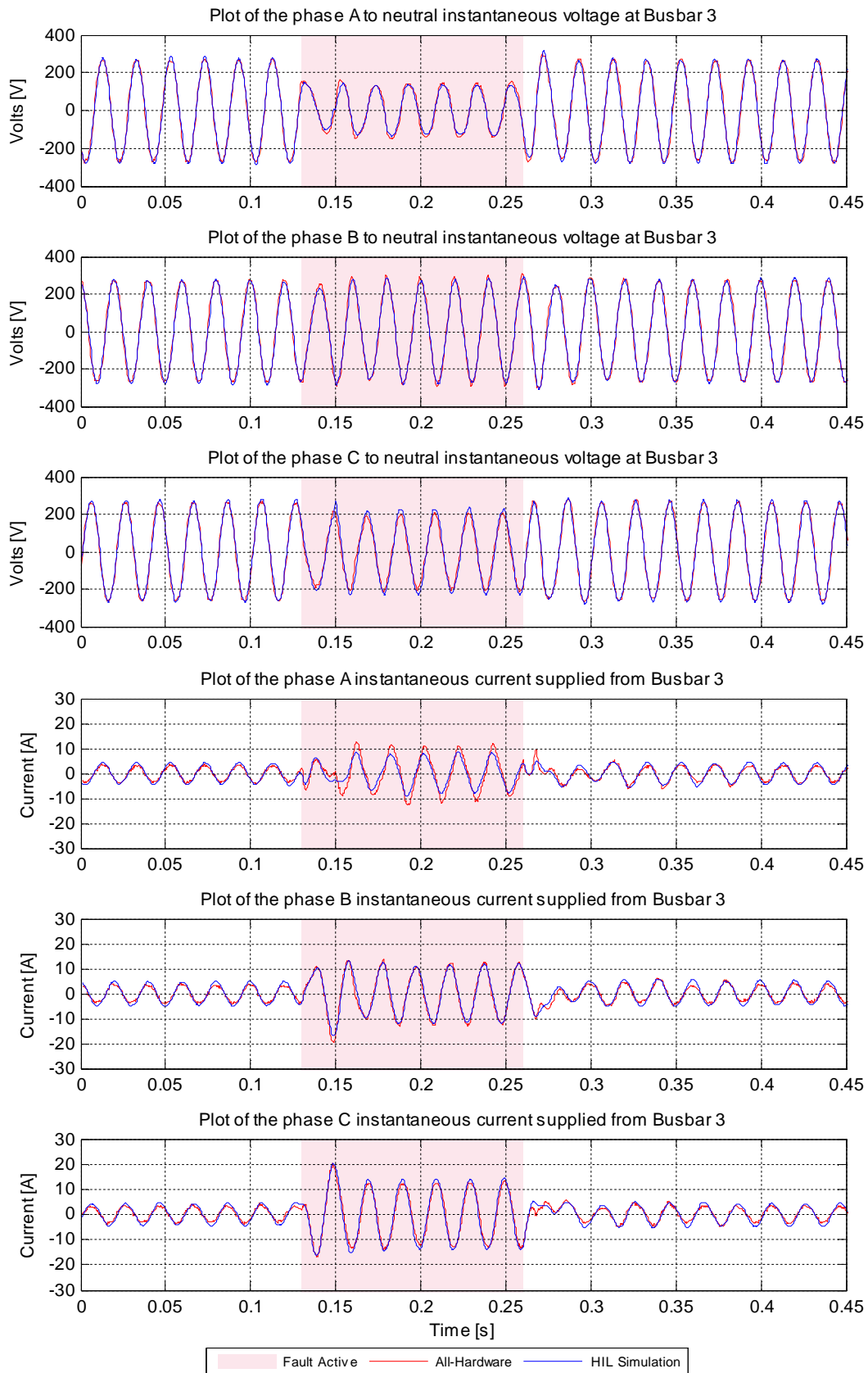


Figure 6-3 (a): Comparison of all-hardware versus HIL simulation implementations of study system — response of ASD system with active front end converter to phase A to ground fault causing sag of nominal depth 50 %, and duration 100 ms (Bus 3 variables).

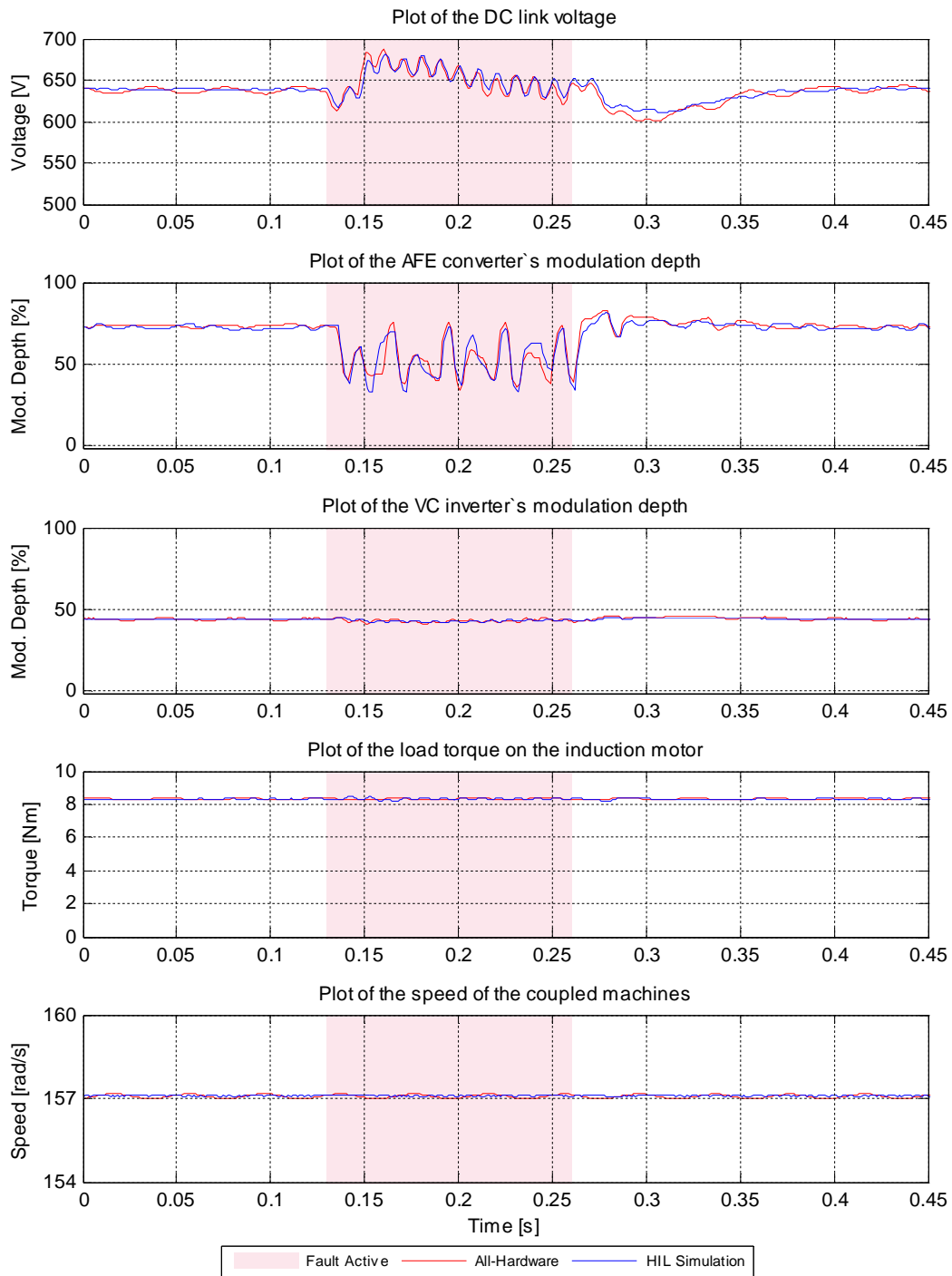


Figure 6-3 (b): Comparison of all-hardware versus HIL simulation implementations of study system — response of ASD system with active front end converter to phase A to ground fault causing sag of nominal depth 50 %, and duration 100 ms (ASD system variables).

### 6.2.3 AFE Converter Energised ASD Response to Double-Phase to Ground Faults

This subsection considers the performance of the ASD system with an active front end converter in response to the two different double-phase to ground faults at the Fault Bus in the upstream supply network that are shown in Table 6-1, namely Fault Conditions (iii) and (iv).

Figure 6-4 (a) shows the AC currents and voltages from the front end of the ASD before, during and after the phase A to B to ground fault at the upstream Fault Bus that results in sags of nominal depth 35 % and duration 100 ms in the voltages of the faulted phases at the ASD front end (Fault Condition (iii) in Table 6-1). Figure 6-4 (b) shows the response of the variables within the ASD system itself during this double-phase fault condition.

The results in Figure 6-4 (a) show that during this fault in the upstream network, involving both phases A and B, the currents drawn by the front end of the ASD become unbalanced, with the amplitude of the current drawn by the ASD front end in the faulted B phase being smaller than the amplitudes of the currents drawn by both the A and C phases, despite the A phase being involved in the upstream fault as well. The results in Figure 6-4 (a) also show that, as would be expected during the fault, there are sags in the input voltages to the ASD's front end, with similar sag depths in the two faulted phases; however, there is also a significant sag in the input voltage to the ASD in the un-faulted phase, with a depth comparable to that seen in the sags in the faulted phases. Therefore, the results indicate that the application of this particular double-phase asymmetric fault at the upstream Fault Bus actually creates a condition in which the input voltages at the front end of the ASD experience significant sags in all three phases.

The response of the variables within the ASD system in Figure 6-4 (b) shows that, nevertheless, during the period of the sags in the voltages at the input to the ASD's front end, the AFE controller is still able to maintain a near-constant DC-link voltage and, as a result, the ASD system is therefore able to ride through the voltage sag with very little adjustment required in the VC inverter's modulation depth and with negligible impact on the output torque and speed of the induction machine.

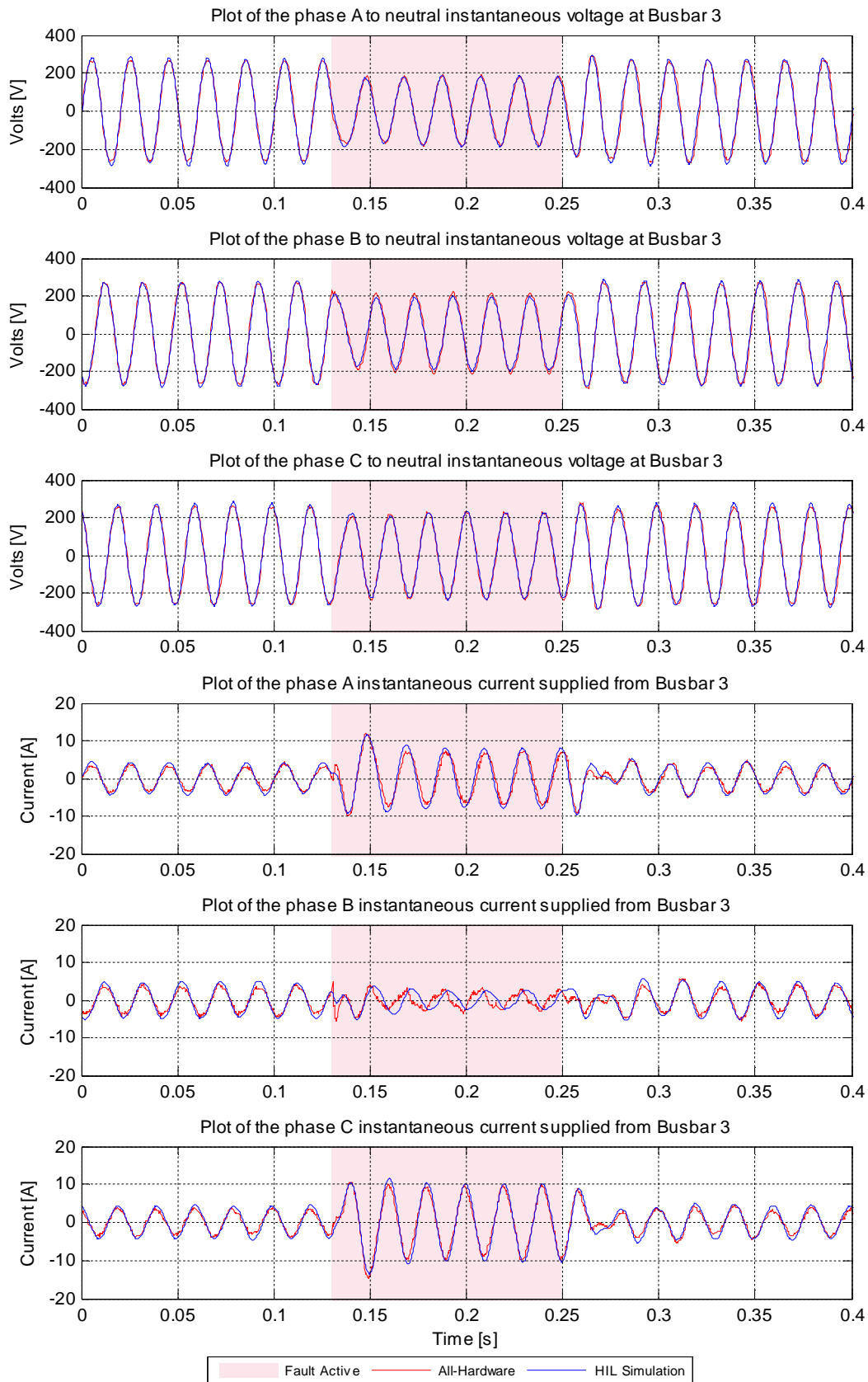


Figure 6-4 (a): Comparison of all-hardware versus HIL simulation implementations of study system — response of ASD system with active front end converter to phase A to B to ground fault causing sag of nominal depth 35 %, and duration 100 ms (Bus 3 variables).

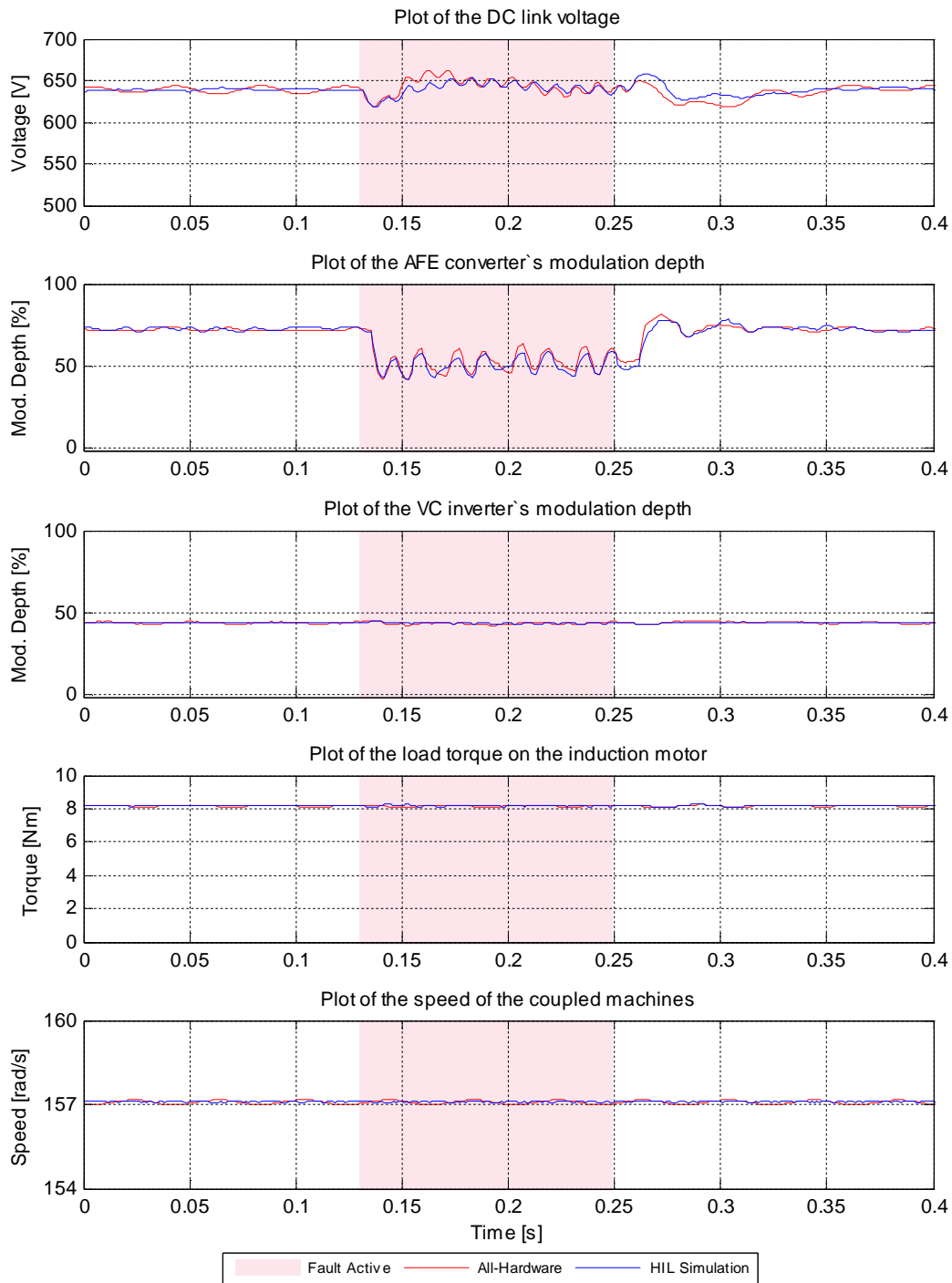


Figure 6-4 (b): Comparison of all-hardware versus HIL simulation implementations of study system — response of ASD system with active front end converter to phase A to B to ground fault causing sag of nominal depth 35 %, and duration 100 ms (ASD system variables).

Finally, the results in Figures 6-4 (a) and (b) show that the behaviour of the ASD system and its impact on the electrical variables in the power system during this double-phase fault test, as predicted using the HIL simulation implementation of the laboratory-scale study system, agrees closely with the measured behaviour of the all-hardware implementation of the study system, apart from a slight difference in the behaviour of the phase-B current drawn by the ASD at its front end during the fault.

Although both the measured phase-B current drawn by the ASD during the fault, and the phase-B current predicted by the HIL simulation study have similar amplitudes, the waveform of this phase-B current during the fault is somewhat distorted in the measured results in Figure 6-4 (a). However, this difference appears to have a negligible impact on the behaviour of all of the other system variables predicted by the HIL simulation implementation of the system (both within the ASD and within the electrical supply system), all of which agree closely with the behaviour of the same variables measured on the all-hardware implementation of the study system during the fault test.

Figure 6-5 (a) now shows the AC currents and voltages from the front end of the ASD during the phase A to B to ground fault at the upstream Fault Bus that results in sags of nominal depth 50 % and duration 100 ms in the voltages of the faulted phases at the ASD front end (Fault Condition (iv) in Table 6-1). Figure 6-5 (b) shows the response of the variables within the ASD system itself during this double-phase fault condition.

The results in Figure 6-5 (a) show that the impact of this particular double-phase fault on the input voltages to the ASD front end is more severe than was the case for the previous double-phase fault [cf. Figure 6-4 (a)]: in the case of this more-severe double-phase fault there is now not only a greater depth of sag in the ASD's input voltages in the faulted A and B phases, but also in the un-faulted C phase. However, the response of the variables within the ASD system in Figure 6-5 (b) shows that despite these more-severe voltage sags at the input to the drive, the AFE controller is still able to maintain a near-constant DC-link voltage throughout the fault and, as a result, the ASD system is therefore able to ride through the voltage sags with very little adjustment required in the VC inverter's modulation depth and hence with negligible impact on the output torque and speed of the induction machine. Comparison of the responses in Figures 6-4 and 6-5 shows that in the case of the more-severe double-phase fault condition (Figure 6-5) maintaining the DC-link voltage magnitude during the sag requires the AFE controller to command a greater reduction in the modulation depth signal sent to the front-end converter and hence for the ASD to draw larger amplitudes of unbalanced current from the faulted upstream network at its AC front end.

Finally, the results in Figures 6-5 (a) and (b) show that, once again, the behaviour of the ASD system and its impact on the electrical variables in the power system during this double-phase fault test, as predicted using the HIL simulation implementation of the laboratory-scale study system, agrees closely with the measured behaviour of the all-hardware implementation of the study system.

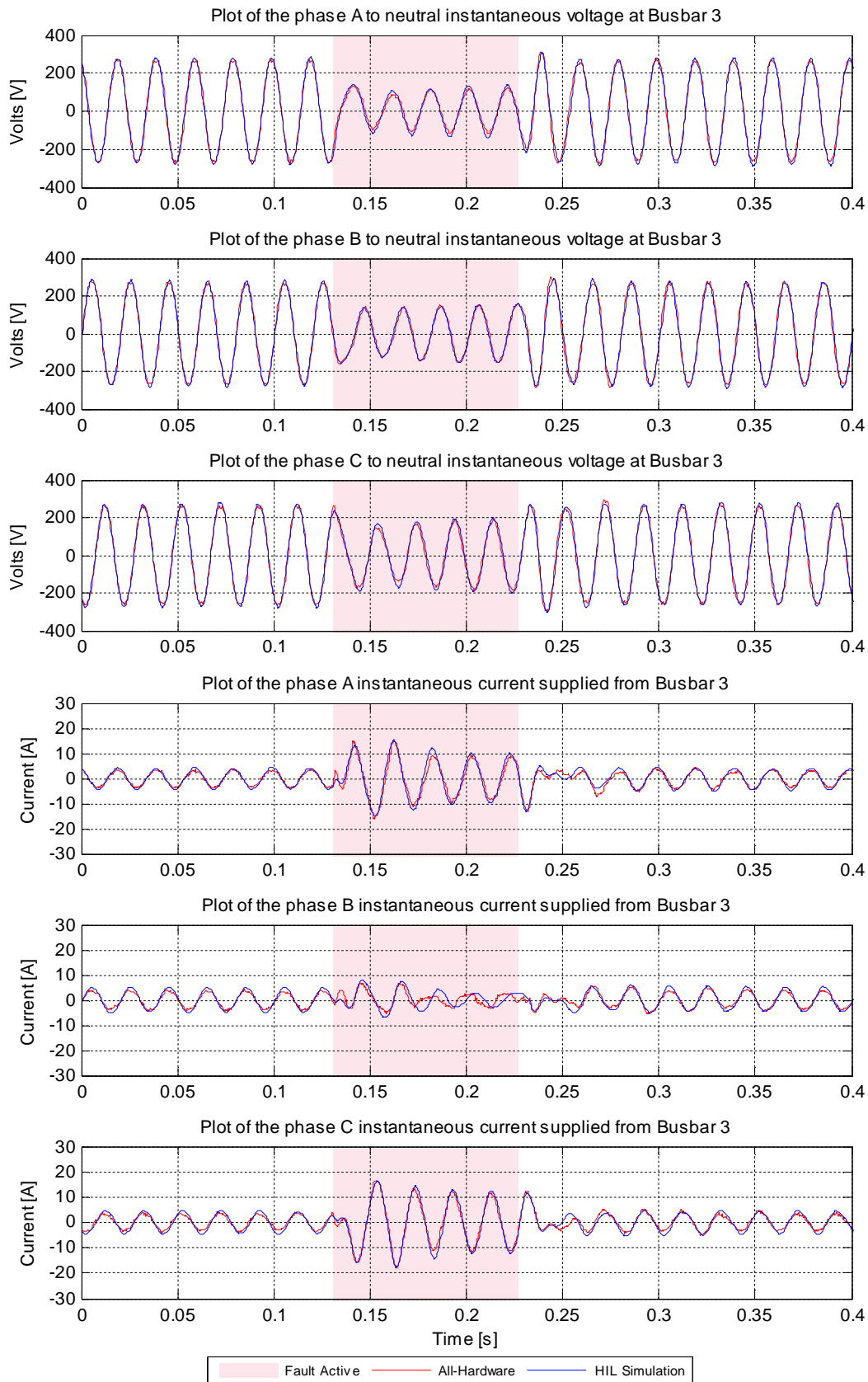


Figure 6-5 (a): Comparison of all-hardware versus HIL simulation implementations of study system — response of ASD system with active front end converter to phase A to B to ground fault causing sag of nominal depth 50 %, and duration 100 ms (Bus 3 variables).

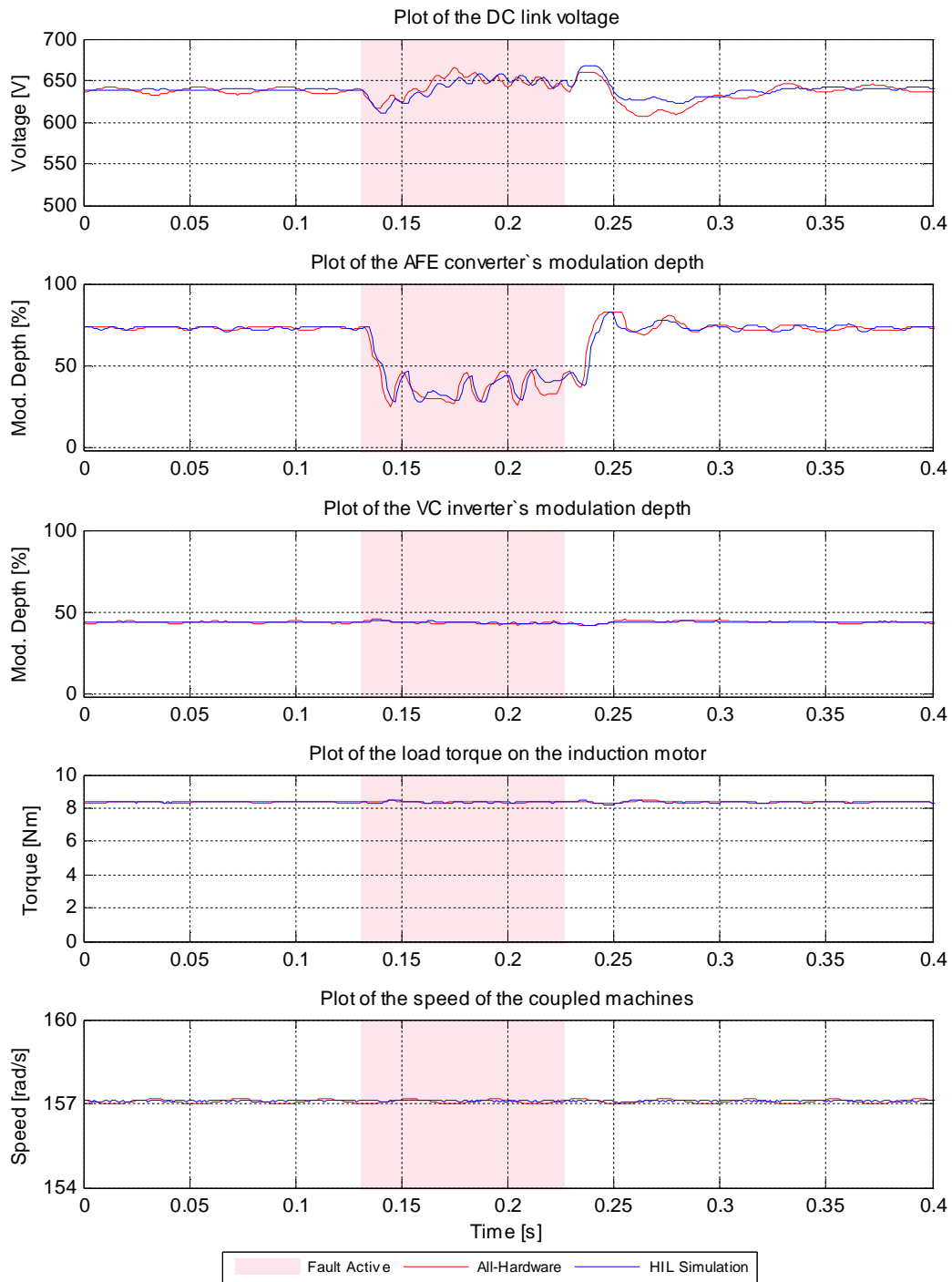


Figure 6-5 (b): Comparison of all-hardware versus HIL simulation implementations of study system — response of ASD system with active front end converter to phase A to B to ground fault causing sag of nominal depth 50 %, and duration 100 ms (ASD system variables).

#### **6.2.4 AFE Converter Energised ASD Response to Three-Phase to Ground Faults**

This subsection now considers the performance of the ASD system with an active front end converter in response to the two different three-phase to ground faults at the Fault Bus in the upstream supply network that are shown in Table 6-1, namely Fault Conditions (v) and (vi).

Figure 6-6 (a) shows the AC currents and voltages from the front end of the ASD before, during and after the particular three-phase to ground fault at the upstream Fault Bus that results in sags of nominal depth 50 % and duration 100 ms in the voltages of all three phases at the ASD front end (Fault Condition (v) in Table 6-1). Figure 6-6 (b) shows the response of the variables within the ASD system itself during this three-phase fault condition.

The results in Figure 6-6 (a) show that, as would be expected, the upstream three-phase fault causes a symmetrical sag in the input voltages at the front end of the ASD but that, for this particular three-phase sag condition, the AFE converter is still able to draw current in all three phases for the entire duration of the sag. The response of the variables within the ASD system in Figure 6-6 (b) shows that, consequently, throughout the period of this symmetrical voltage sag condition, the AFE controller is able to maintain a near-constant DC-link voltage and, as a result, the ASD system is therefore able to ride through the voltage sag condition with very little adjustment required in the VC inverter's modulation depth and with negligible impact on the output torque and speed of the induction machine.

Finally, the results in Figures 6-6 (a) and (b) show that the behaviour of the ASD system and its impact on the electrical variables in the power system during this three-phase fault test, as predicted using the HIL simulation implementation of the laboratory-scale study system, agrees closely with the measured behaviour of the all-hardware implementation of the study system.

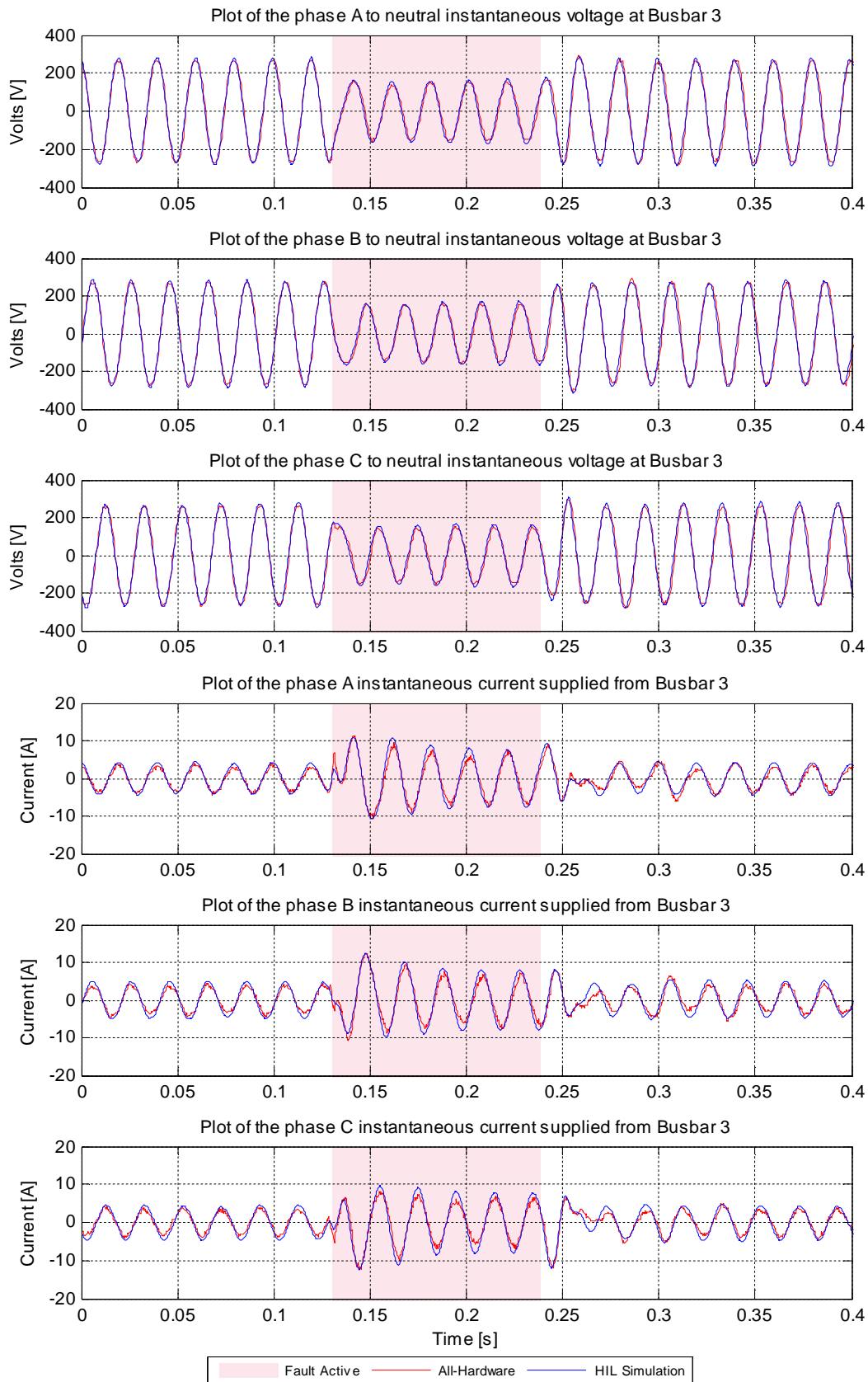


Figure 6-6 (a): Comparison of all-hardware versus HIL simulation implementations of study system — response of ASD system with active front end converter to phase A to B to C to ground fault causing sag of nominal depth 50 %, and duration 100 ms (Bus 3 variables).

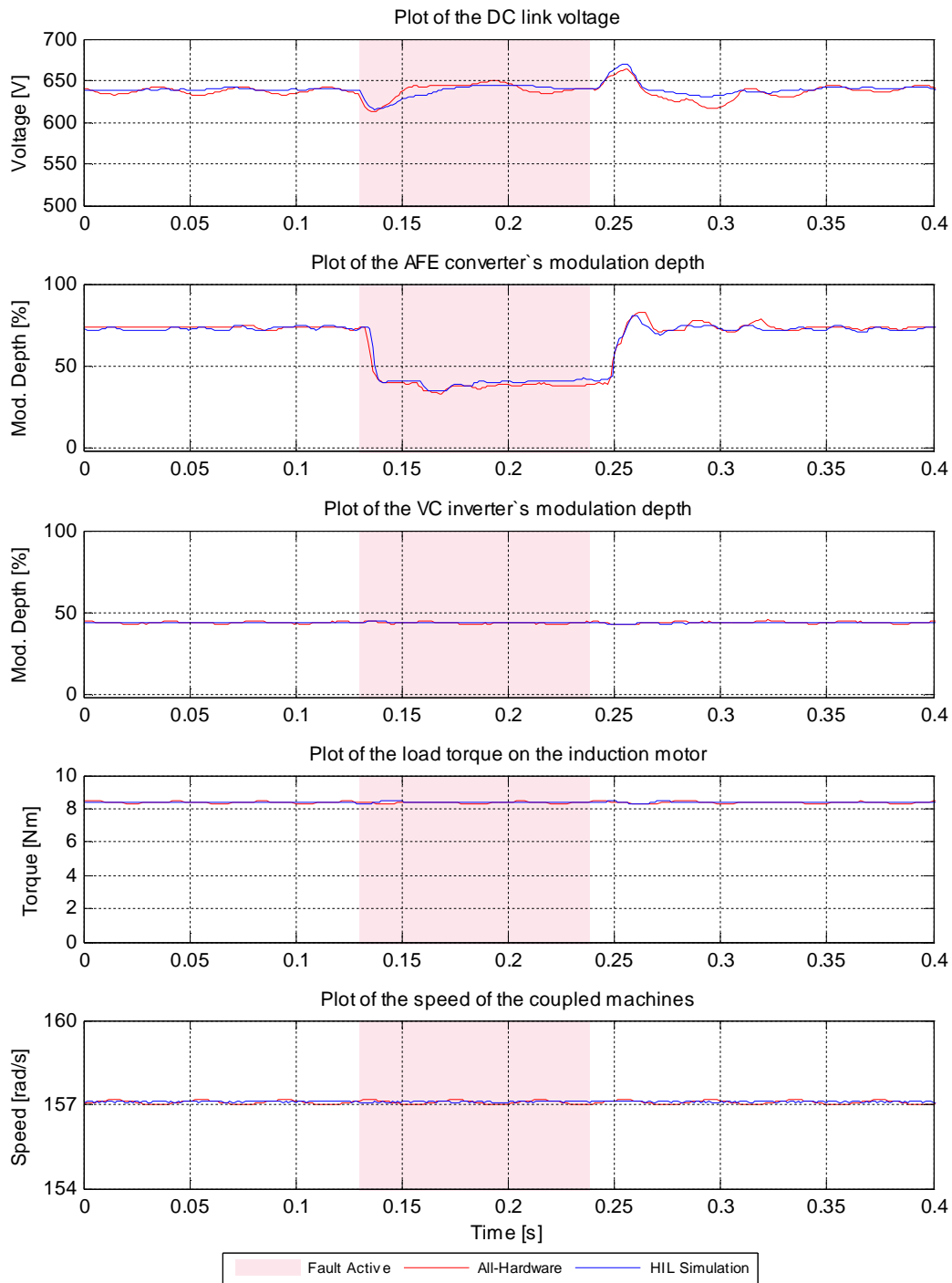


Figure 6-6 (b): Comparison of all-hardware versus HIL simulation implementations of study system — response of ASD system with active front end converter to phase A to B to C to ground fault causing sag of nominal depth 50 %, and duration 100 ms (ASD system variables).

Figure 6-7 (a) now shows the AC currents and voltages from the front end of the ASD during the most severe three-phase to ground fault considered at the upstream Fault Bus, namely the fault that results in sags of nominal depth 70 % and duration 100 ms in the voltages of all three phases at the ASD front end (Fault Condition (vi) in Table 6-1). Figure 6-7 (b) shows the response of the variables within the ASD system itself during this three-phase fault condition.

The results in Figure 6-7 (a) confirm that the impact of this particular three-phase fault on the input voltages to the ASD's front end is more severe than was the case for the previous three-phase fault [cf. Figure 6-6 (a)]. Furthermore, the results in Figure 6-7 (a) show that, as a result of this more-severe three-phase voltage sag in the ASD's input voltages, with the exception of a brief period of 15 ms duration immediately following the application of the upstream fault, the ASD is unable to draw current in any of the phases at its front end during the voltage sag condition. The results in Figure 6-7 (b) show that during this 15 ms period immediately following the onset of the upstream fault, there is a relatively-modest initial decrease in the DC-link voltage as a result of the symmetrical voltage sag condition at the input to the ASD's front end and that the AFE controller responds by decreasing the modulation depth of the firing pulses sent to the front-end converter, as seen in all previous cases, in an attempt to restore the DC-link voltage to its set-point magnitude. However, Figure 6-7 (b) shows that, unlike in the previous fault tests, in the case of this more-severe three-phase input voltage sag, the AFE controller continues to decrease the modulation depth of the firing pulses to the AFE converter all the way to zero which then results in all the IGBTs in the converter being turned off completely.

In the industrial ASD system used in these studies the AFE controller was commissioned to stop firing (turn off) all the IGBTs in the front-end converter when the amplitude of the voltage in each phase at the input to the converter drops below a minimum value that is pre-set within the AFE controls. Once the AFE controller stops firing the front-end converter's IGBTs, the mode of operation of the converter immediately changes from active front end control mode (i.e. closed-loop, three-phase AC current control and closed-loop DC-link voltage control) into uncontrolled diode rectifier mode. While the front-end converter is in uncontrolled diode rectifier mode, it follows that the AFE controller no longer regulates the DC-link voltage of the drive. Furthermore, the AFE controller will only change the mode of operation of the front-end converter back into active front end control mode if the voltages at the input to the converter have been restored and the ASD system has not already tripped the induction machine as a result of its response to the voltage sag conditions. However, if the ASD system is forced to trip the induction machine before the front-end converter's input voltages are

restored, the AFE controls then issue a command to trip the front-end converter and disconnect it (and hence the entire drive) from its three-phase supply.

Figure 6-7 shows that in the case of this particular upstream three-phase fault, the symmetrical sag in the input voltages to the drive is sufficiently deep that the AFE controls are forced to switch the front-end converter into uncontrolled diode rectifier mode 15 ms into the sag, and that the front-end converter is kept in this mode for the remainder of the sag (as evidenced by the AFE converter's modulation depth signal remaining at zero thereafter). Furthermore, the depth of the symmetrical sag in the input voltages in this case is such that, once in uncontrolled diode rectifier mode the front-end converter can no longer draw any current at its AC inputs to supply energy to the DC-link. Consequently, the energy being drawn from the DC link by the VC inverter to service the motion control task causes the DC-link voltage to start decreasing rapidly once the front-end converter is switched into uncontrolled diode rectifier mode.

Figure 6-7 (b) shows that the VC controller within the ASD responds to the decreasing DC-link voltage by increasing the modulation depth signal to the IGBTs in the machine-side VC inverter and that, while this modulation depth signal remains within the allowable limits set within the ASD's controls, this successfully keeps the output torque and speed of the machine constant despite the decreasing DC-link voltage. However, approximately 0.1 seconds into the sag the ASD controls trip the motor as a combined result of the VC inverter's modulation depth command reaching the maximum allowable value and the DC-link voltage dropping below the minimum threshold allowed by the drive controls.

Because the motor in the fault test in Figure 6-7 was tripped before the input voltages to the drive recovered to their pre-sag magnitudes, the AFE controls issued a signal to trip the front-end converter in order to disconnect it from the three-phase supply in accordance with the settings commissioned in the drive. However, as can be seen from the behaviour of the DC-link voltage in Figure 6-7 (b), the front-end converter of the ASD actually remained connected, and operating in uncontrolled diode rectifier mode, for the remainder of the test measurement period; the reason is that the main contactor that disconnects the front-end converter in the drive system has an inherent delay of 300 ms, so the disconnection of the drive from the three-phase supply actually only occurred after the end of the capturing period of the results shown in Figure 6-7 (at approximately  $t = 0.53$  seconds).

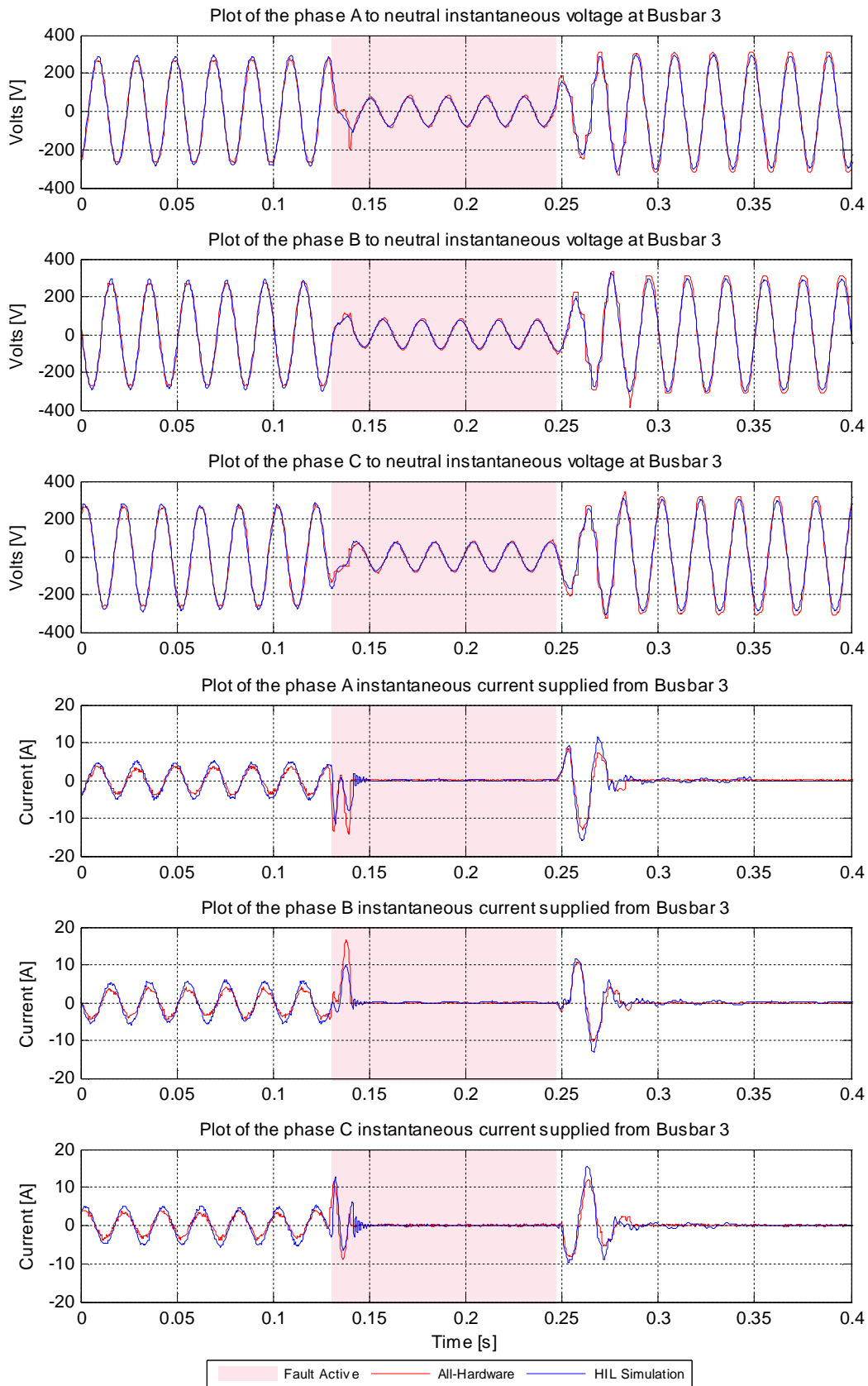


Figure 6-7 (a): Comparison of all-hardware versus HIL simulation implementations of study system — response of ASD system with active front end converter to phase A to B to C to ground fault causing sag of nominal depth 70 %, and duration 100 ms (Bus 3 variables).

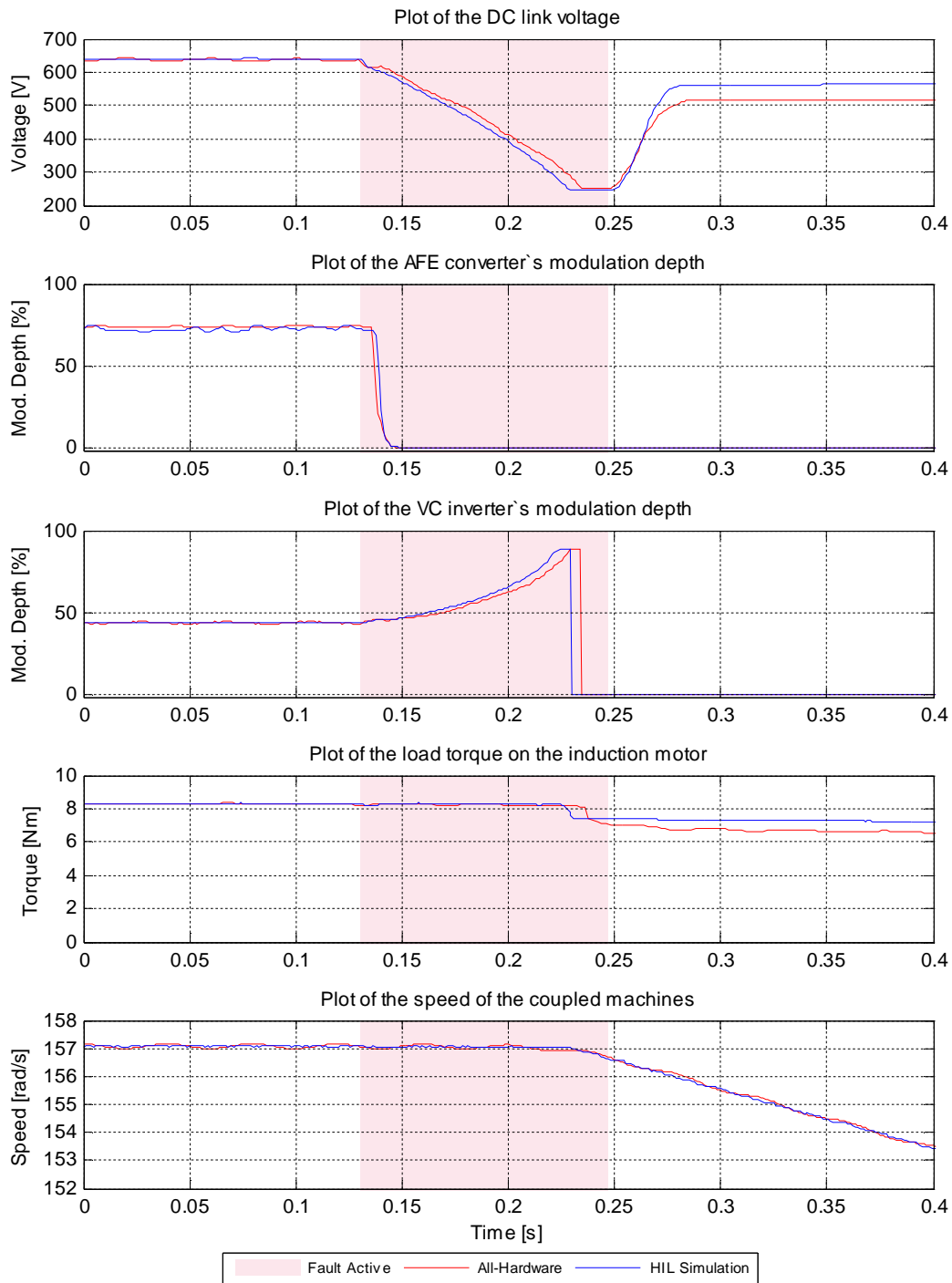


Figure 6-7 (b): Comparison of all-hardware versus HIL simulation implementations of study system — response of ASD system with active front end converter to phase A to B to C to ground fault causing sag of nominal depth 70 %, and duration 100 ms (ASD system variables).

Comparison of the results in Figure 6-7 with those in Figure 6-6 show that, whilst a drive equipped with active front-end controls can ride through a symmetrical sag in its input voltages of quite-significant depth, once the depth of such a sag becomes too great for the AFE controls to function the front-end converter has the same performance limitations as an uncontrolled rectifier front-end drive that were seen in the test results of Chapter 5, and the ride-through capability of the drive is then

determined by the duration of the sag. For example, it is evident from the results in Figure 6-7 that the ASD system under test here would have been able to ride through a symmetrical sag of the same depth, but shorter duration.

Finally, the results in Figures 6-7 (a) and (b) show that the behaviour of the AFE-type of ASD system and its impact on the electrical variables in the power system during this most severe three-phase fault test considered in the studies, as predicted using the HIL simulation implementation of the laboratory-scale study system, agrees closely with the measured behaviour of the all-hardware implementation of the study system even for severe sag test conditions such as this in which the ASD system variables undergo large excursions that force the drive firstly into scheduled operating mode changes, and then, finally into their control limits prior to the motor and active front end converter tripping completely.

### **6.2.5 Summary of the AFE Converter Energised ASD Response to Upstream Faults**

This section has presented the results of detailed measurements carried out on the all-hardware implementation of the laboratory-scale study system in order to test the dynamic performance of an ASD system with an active front end converter in response to a set of six pre-determined fault conditions (shown in Table 6-1) in the upstream supply network designed to cause a range of sag conditions at the input voltages to the ASD.

The results have shown that the AFE converter energised ASD system was able to ride through the voltage sag conditions associated with Fault Conditions (i) to (v) in Table 6-1. However, the results also showed that this ASD system was unable to ride through the most-severe voltage sag condition associated with Fault Condition (vi) in Table 6-1: in this case the voltage sag condition had not only a depth that was severe enough to stop the AFE converter unit from continuing to regulate the DC-link voltage, but also a duration that was sufficient to cause the ASD controllers to trip both the motor and AFE converter.

Furthermore, the close agreement between the measurements that were taken on the all-hardware implementation of the laboratory-scale study system and the results that were obtained from the HIL simulation implementation of the study system in response to the same six fault conditions in the upstream supply network provides confidence in the ability of the HIL real-time simulator testing approach to accurately predict the dynamic performance of ASD systems that are energised by active front end converters in response to voltage sag conditions caused by upstream faults, irrespective of whether or not the ASD system will, in practice, be able to successfully ride through the sag condition.

## 6.3 An Investigation into the Influence of Different ASD Front-End Converter Technologies on the Performance of a Power System Network During Network Faults

### 6.3.1 Introduction

The test results presented in both the previous section of this chapter and in Chapter 5 have demonstrated that the HIL real-time simulator testing approach can accurately predict the dynamic performance of ASD systems equipped with either active front end (AFE) or uncontrolled diode rectifier (UDR) based front-end converter technologies in response to voltage sags caused by upstream power system network faults. Having carefully established the validity and accuracy of the HIL approach to testing drives, this section now presents the results of a further investigation, carried out solely using the HIL real-time simulator testing approach, in order to compare the influence of different ASD front-end converter technologies on the performance of the power system itself during network faults.

In order to carry out this investigation, the same HIL simulation implementation of the laboratory-scale study system that was developed for the work presented thus far in the thesis was used to predict the influence that ASDs equipped with both AFE- and UDR-type front-end converter technologies have on a power system network using the procedure described below.

Firstly, the HIL simulation implementation of the laboratory-scale study system was set up for the particular case in which the ASD within the study system is equipped with an AFE converter as shown in the schematic diagram in Figure 6-8.

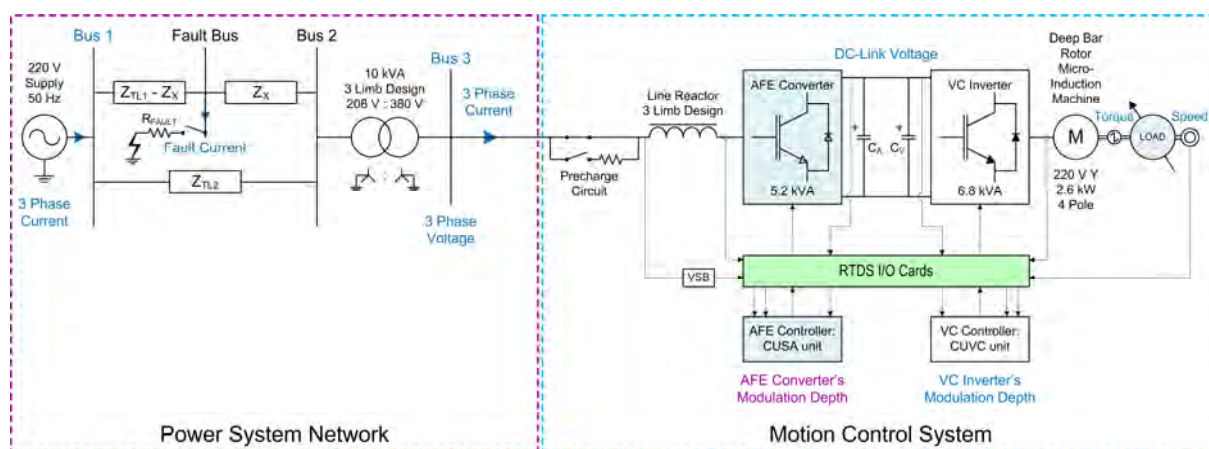


Figure 6-8: Schematic diagram of the HIL real-time simulation implementation of the laboratory-scale study system used to investigate the influence of an ASD equipped with active front end converter technology on a power system network during fault conditions.

The AFE-equipped ASD system shown in Figure 6-8 was then fed, via the upstream power system network, with its nominal voltage of 380 V at Bus 3 and the ASD system control hardware was configured to regulate the speed of the induction motor. In particular the ASD's closed-loop speed controller was set to maintain the speed of the motor at 157.1 rad/s (1500 rpm) while the dynamometer applied a torque of 8 Nm at its shaft (approximately 50 % of the rated load of the motor). These nominal operating conditions chosen for the ASD system in the remaining investigations are the same as those that have been used to carry out the previous investigations presented thus far in the thesis.

Whilst the ASD system was in operation and performing the aforementioned motion control task, a set of four pre-determined fault conditions, each of 100 ms duration, was then applied at the Fault Bus in the power system network (shown in Figure 6-8) by switching in a selected resistance value  $R_{FAULT}$  between the requisite phases and ground. During the application of each of the four fault conditions, the performance of the power system network and the response of the AFE-equipped ASD system were captured by simultaneously recording a set of variables from within the real-time simulation model of the study system and from within the ASD's controllers that were connected hardware-in-loop with this model.

Secondly, the HIL simulation implementation of the laboratory-scale study system was set up for the particular case in which the ASD within the study system is equipped with an uncontrolled diode rectifier (UDR) converter as shown in the schematic diagram in Figure 6-9.

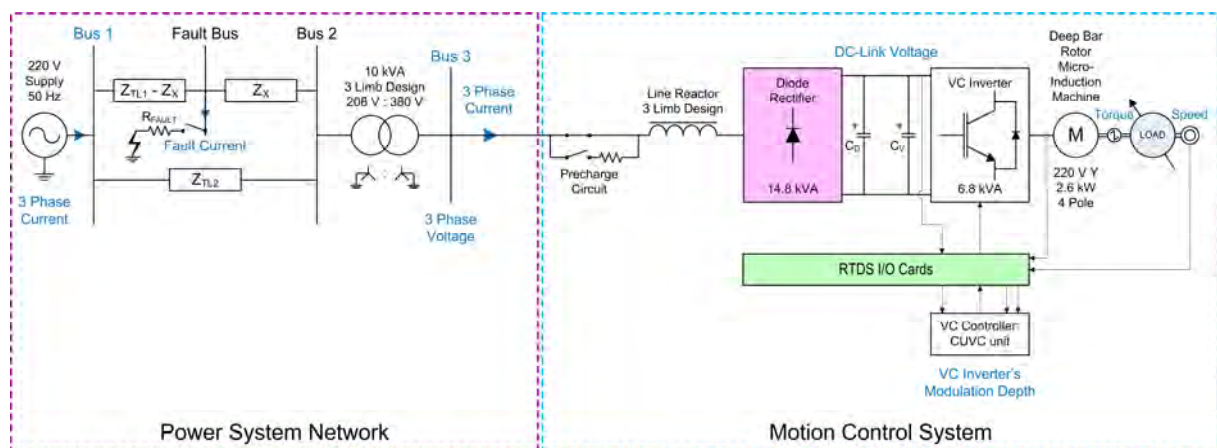


Figure 6-9: Schematic diagram of the HIL real-time simulation implementation of the laboratory-scale study system used to investigate the influence of an ASD equipped with uncontrolled diode rectifier front-end converter technology on a power system network during fault conditions.

The HIL simulation study system shown in Figure 6-9 differs from that shown in Figure 6-8 only in respect of the ASD front-end converter used; all of the other components in the system in Figure 6-9

and their characteristic parameters were kept identical to those used in the study system in Figure 6-8 during the comparative tests.

The UDR-equipped ASD system shown in Figure 6-9 was then fed, via the upstream power system network, with its nominal voltage of 380 V at Bus 3 and the ASD control hardware was configured in the same manner as for the AFE-equipped ASD system, such that the closed-loop speed controller would maintain the speed of the motor at 157.1 rad/s (1500 rpm) while the dynamometer applied a torque of 8 Nm at its shaft. Whilst the UDR-equipped ASD system was performing the motion control task the same set of four pre-determined fault conditions was then applied at the Fault Bus in the power system network. During the application of each of the four fault conditions, the performance of the power system network and the response of the UDR-equipped ASD system were once again captured by simultaneously recording the same set of variables as for the previous tests from within the real-time simulation model and from within the ASD's controllers that were connected hardware-in-loop with this model.

The sets of system variables recorded during these HIL simulation tests of the study system when feeding the AFE-equipped and UDR-equipped ASDs respectively, were then compared against each other in order to determine the influence of each type of ASD front-end converter technology on the upstream power system during network faults that cause sags in the voltages feeding the ASDs.

The specific details of the four fault conditions that were applied in the power system network during the HIL simulation tests of the two different drive front-end technologies are summarised in Table 6-2.

*Table 6-2: Details of the conditions applied at the Fault Bus in the study system during HIL simulation test comparisons of AFE-equipped and UDR-equipped ASD systems.*

Fault Condition	Type of Fault at Fault Bus [Phases to ground]	Duration [ms]	Value of Fault Resistance $R_{\text{FAULT}}$ [ $\Omega$ ]
(1)	A	100	1.0
(2)	A, B	100	3.5
(3)	A, B, C	100	3.2
(4)	A, B, C	100	0.5

The specific variables that were recorded for comparison during the HIL simulation tests of each type of drive front-end technology are highlighted in blue in the schematic diagrams of the respective drive

types shown in Figures 6-8 and 6-9. Within the power system network, the three-phase voltages and currents at the input to the front end of the ASD system at Bus 3 were recorded, as were the three-phase currents supplied to Bus 1 from the 220 V source and the fault currents flowing to ground at the Fault Bus. The variables that were recorded from within the real-time model of the ASD system plant included the DC-link voltage, the motor load torque and speed. The variables that were recorded from within the ASD's hardware controllers were the modulation depth command sent to the motor-side inverter from the CUVC unit (in the case of both types of drive system tested) and the modulation depth command sent to the front-end converter from the CUSA unit (only in the case of the drive system equipped with active front-end technology).

### **6.3.2 Performance of the Power System Network Feeding AFE- and UDR-Type Drives During Asymmetric Fault Conditions**

This subsection directly compares the performance of the power system network and the responses of the motion control system of the ASD when the ASD is equipped with both AFE- and UDR-type front-end technologies during the application of the two different asymmetric faults in the power system network that are shown in Table 6-2, namely Fault Conditions (1) and (2).

Figures 6-10 (a), (b) and (c) compare the performance of the laboratory-scale study system when feeding an ASD equipped with both types of front-end technology, before, during and after the application, for 100 ms, of the phase-A to ground fault of fault resistance  $1.0 \Omega$  at the Fault Bus (Fault Condition (1) in Table 6-2): Figure 6-10 (a) compares the AC currents and voltages at Bus 3 in the study system in each case; Figure 6-10 (b) compares the currents supplied by the source at Bus 1, and the fault currents in each case; Figure 6-10 (c) compares the variables within the ASD system in each case. The areas highlighted in pink in Figures 6-10 (a), (b), and (c) show the period during which the fault was actually applied in each case.

The results in Figure 6-10 (a) show that under normal steady-state conditions the UDR-equipped ASD system draws non-sinusoidal currents from the upstream power system network which result in the harmonic distortion evident in the Bus 3 voltages (the voltages supplying the front-end converter of the ASD). By comparison, the results also show that under normal steady-state conditions the AFE-equipped ASD system draws virtually sinusoidal currents from the upstream power system network and, as a result, the Bus 3 voltages supplying the front-end of this type of ASD appear to be virtually free from any harmonic distortion.

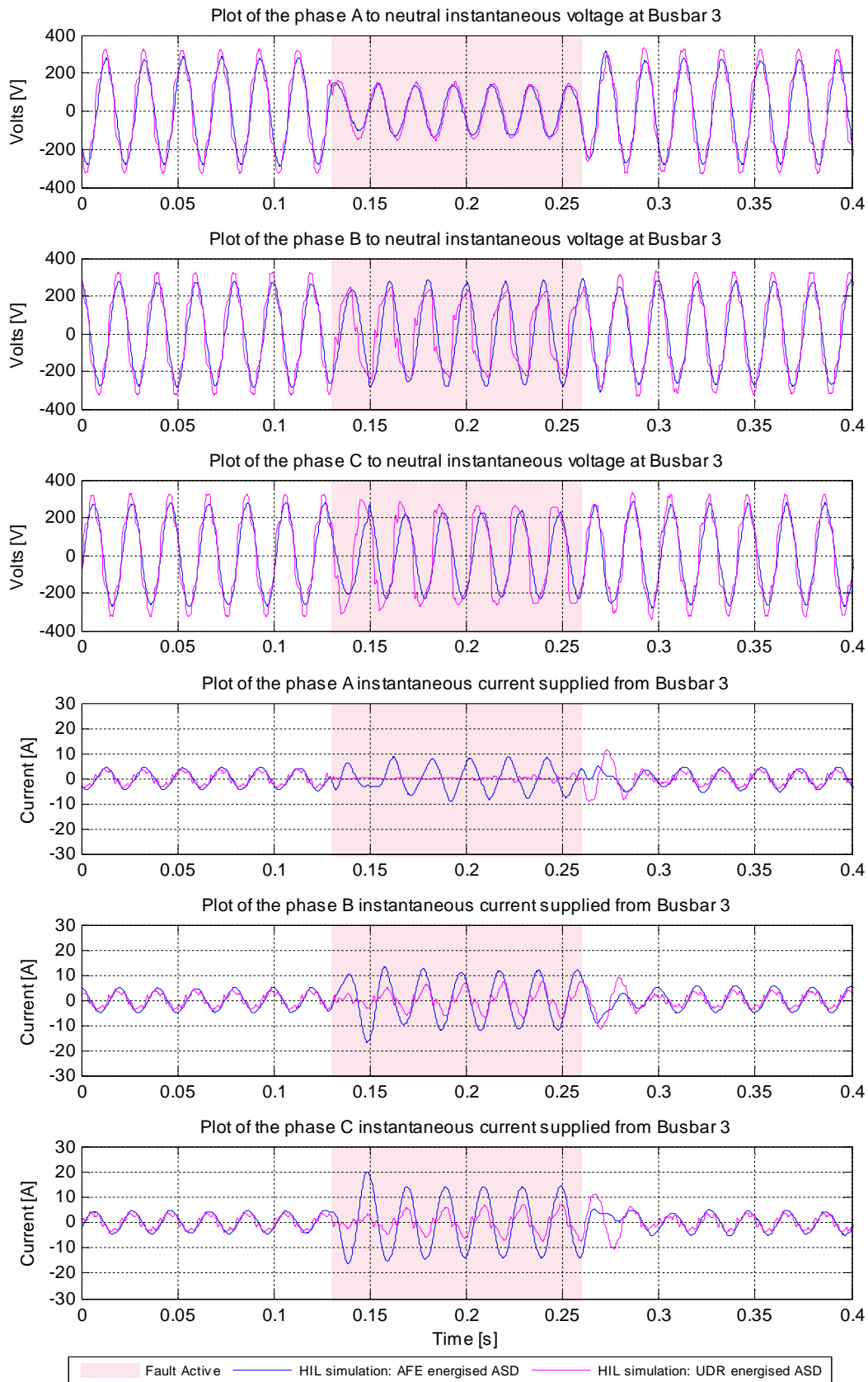


Figure 6-10 (a): Comparison of power system performance when feeding an ASD equipped with AFE- versus UDR-type front-end technologies — response to phase-A to ground fault with  $R_{FAULT} = 1.0 \Omega$  and duration 100 ms (Bus 3 variables).

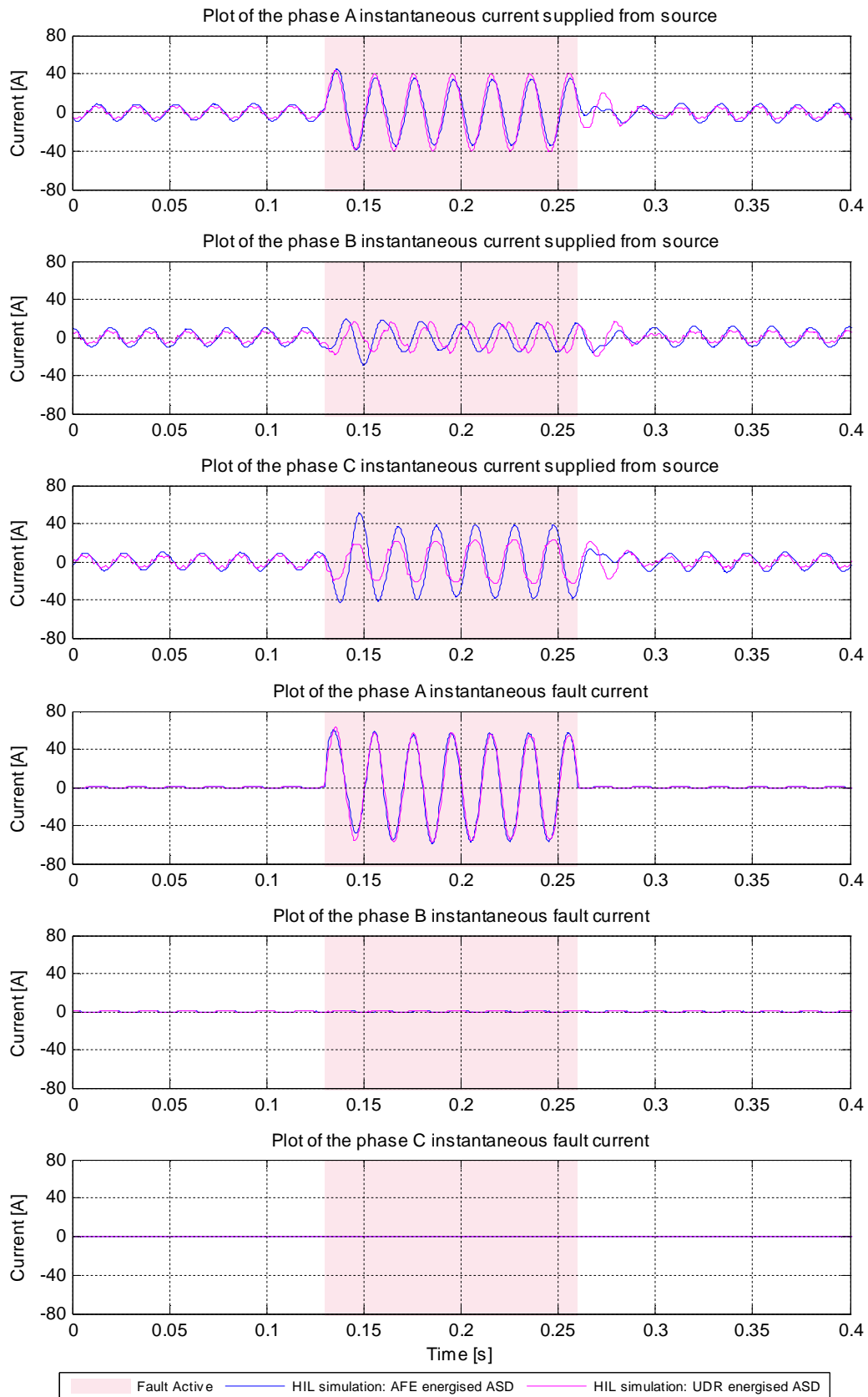


Figure 6-10 (b): Comparison of power system performance when feeding an ASD equipped with AFE- versus UDR-type front-end technologies — response to phase-A to ground fault with  $R_{FAULT} = 1.0 \Omega$  and duration 100 ms (220 V source currents and fault currents).

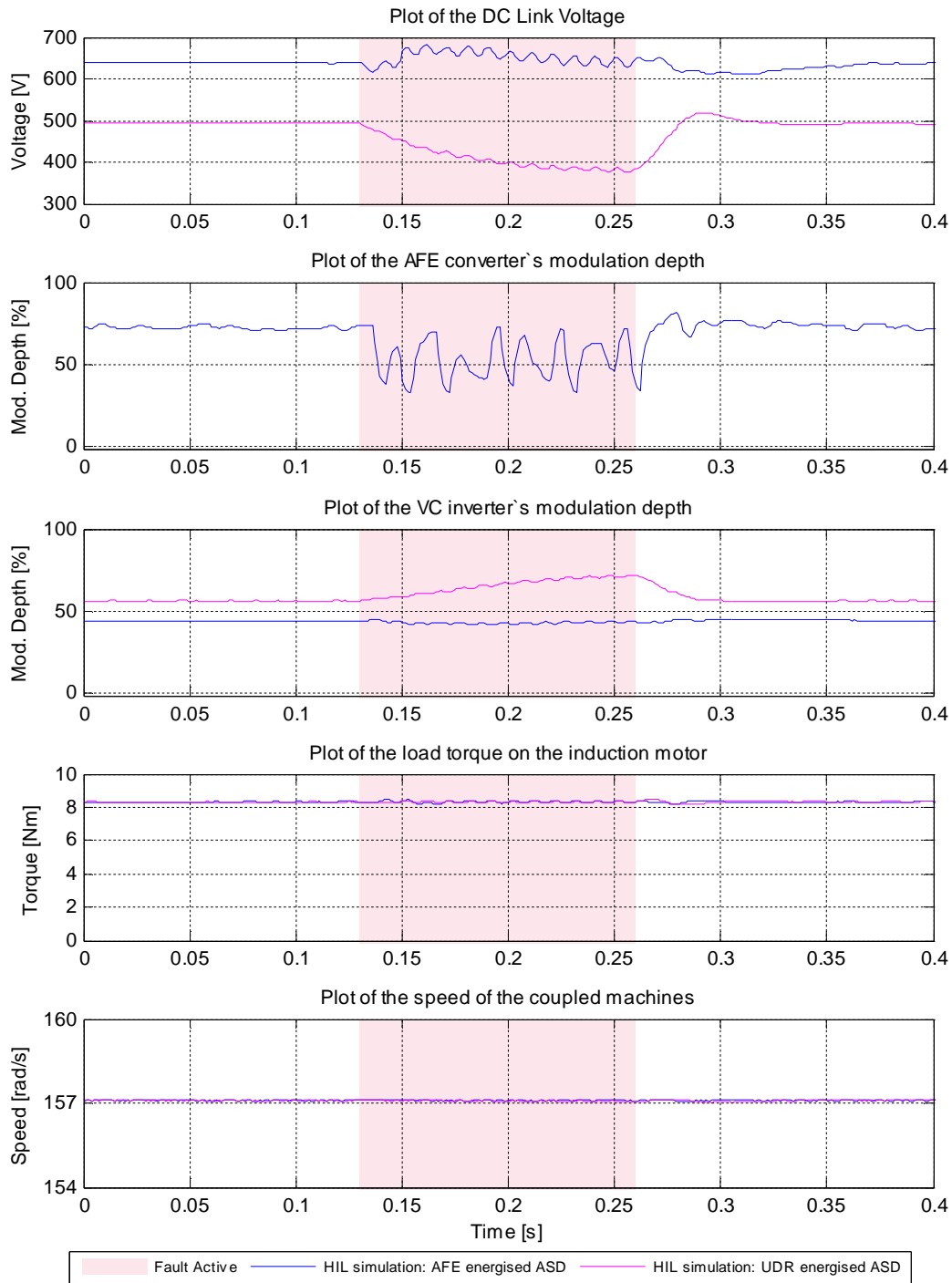


Figure 6-10 (c): Comparison of power system performance when feeding an ASD equipped with AFE-versus UDR-type front-end technologies — response to phase-A to ground fault with  $R_{FAULT} = 1.0 \Omega$ , and duration 100 ms (ASD system variables).

A comparison of the variables within the UDR- and AFE-equipped ASD systems themselves during the pre-fault period in Figure 6-10 (c) shows that when these two ASD systems operate under the same steady-state conditions and produce the same output torque and speed, the AFE-equipped ASD system is able to operate with a lower VC inverter modulation depth because the DC-link voltage that is output from the AFE converter is higher than that which is output from the UDR converter.

Returning to the performance of the power system, the results in Figure 6-10 (a) show that, as expected, the single-phase fault in the power system supply network causes sags in the voltages of all three phases at the inputs to the front-end converter of both types of ASD system, with the sag depth being greatest in the faulted phase in both cases. Furthermore, the results show that in the case of this particular single-phase fault, both types of ASD system experience very similar depths of voltage sag at their inputs in the faulted phase itself.

With respect to the influence of the AFE and UDR converters on the upstream power system network in the case of this particular fault, Figure 6-10 (a) shows that the UDR converter is unable to draw current at all from the faulted A phase for the first half (50 ms) of the fault and only a small amount of current during the second half of the fault; as a result, the Bus 3 voltage supply to the UDR converter in phase A appears to be virtually free from any harmonic distortion during the entire period of the fault. However, the results also show that during the upstream fault the UDR converter is able to draw large amounts of current from the un-faulted B and C phases, but that these currents are non-sinusoidal and therefore result in the significant harmonic distortion evident in the Bus 3 voltage supply to the UDR converter in phases B and C during the fault.

By comparison, Figure 6-10 (a) shows that during the fault the AFE converter is able to draw larger currents than the UDR converter from all three phases, with the largest current drawn from the un-faulted phase C. However, these larger currents drawn by the AFE converter are virtually sinusoidal in all three phases and, as a result, all three phases of the Bus 3 voltage supply to the AFE converter appear to be virtually free from any harmonic distortion during the fault.

The results in Figure 6-10 (a) show that even though the AFE converter draws a much larger current than the UDR converter in the faulted A phase, the depth of the sag in the input voltage to these two types of front-end converter in the faulted phase is virtually the same, at least for this single-phase fault. Hence the larger current drawn by the AFE converter in the faulted phase does not have a significant influence on the depth of the resulting input voltage sag during this particular fault.

The behaviour of the variables within the upstream power system network in Figure 6-10 (b) shows that during this phase-A to ground fault the amplitude of the phase-C current supplied by the source that feeds Busbar 1 is significantly larger when the ASD system being fed by the power system network has an AFE-type converter than is the case when the ASD system has a UDR-type converter. This larger current flowing in the un-faulted phase C of the upstream power system network is a direct

consequence of the large current drawn by the AFE type of converter from those phases at its inputs that are less impacted by an asymmetric voltage sag condition.

With respect to the performance of the drive systems themselves, the comparison of the results in Figure 6-10 (c) shows that during the upstream fault the AFE- and UDR-equipped ASD systems are both able to continue meeting the torque and speed requirements of the motion control task, but that each of these ASD systems responds to the fault differently according to its particular type of front-end converter technology. In the case of the UDR-equipped ASD system, Figure 6-10 (c) shows that during the upstream fault the DC-link voltage decreases as a result of the voltage sag condition at the front-end of the drive, and in response to this decreasing DC-link voltage the ASD controls temporarily increase the modulation depth of the firing pulses to the machine-side VC inverter so as to allow the ASD system to ride through the voltage sag condition with negligible impact on the output torque and speed of the induction machine.

By contrast, in the case of the AFE-equipped ASD system, Figure 6-10 (c) shows that during the upstream fault the DC-link voltage is kept relatively constant despite the voltage sag condition at the front end of the drive because of the AFE controller's action to appropriately adjust the modulation depth command sent to the front-end converter [Figure 6-10 (c)], and hence draw more current at the front-end of the drive in response to the voltage sag condition. Figure 6-10 (c) shows that as a result of being able to maintain a near-constant DC-link voltage during the fault, the AFE-equipped ASD system is therefore able to ride through the voltage sag condition not only with negligible impact on the output torque and speed of the induction machine, but also with very little adjustment required in the machine-side VC inverter's modulation depth.

Lastly, the results in Figure 6-10 (c) show that in the case of the AFE-equipped ASD system, the AFE controller responds to the restoration of the Bus 3 voltages upon removal of the upstream fault by increasing the modulation depth of the AFE converter to its pre-fault value. Figure 6-10 (a) shows that from this time onwards the currents drawn by the AFE converter quickly decrease back down to the pre-fault steady-state values required by the ASD system for it to meet the mechanical requirements of the motion control task. By comparison, in the case of the UDR-equipped ASD system, Figure 6-10 (a) shows that the ASD system initially experiences an inrush of currents at its front end upon restoration of the Bus 3 voltages. These inrush currents recharge the DC-link voltage to its pre-fault value in approximately 0.02 seconds [Figure 6-10 (c)] and, as a result, the ASD controls respond by decreasing the modulation depth of the machine-side VC inverter back to its pre-fault value [Figure 6-10 (c)]. Correspondingly, Figure 6-10 (a) shows that approximately 0.02 seconds after

the removal of the fault, when the DC-link voltage has been recharged, the currents drawn by the front-end converter of the UDR-type drive return to the steady-state values required by the ASD system for it to meet the mechanical requirements of the motion control task.

Figures 6-11 (a), (b) and (c) now compare the performance of the laboratory-scale system when feeding an ASD equipped with both types of front-end technology, before, during and after the application, for 100 ms, of the phase A to B to ground fault of fault resistance  $3.5 \Omega$  at the Fault Bus (Fault Condition (2) in Table 6-2): Figure 6-11 (a) compares the AC currents and voltages at Bus 3 in the study system in each case; Figure 6-11 (b) compares the currents supplied by the source at Bus 1, and the fault currents in each case; Figure 6-11 (c) compares the variables within the ASD system in each case. The areas highlighted in pink in Figures 6-11 (a), (b), and (c) show the period during which the fault was actually applied in each case.

The results in Figure 6-11 (a) show that in the case of both types of ASD system, during this upstream double-phase fault, the currents drawn by the front-end converters of the drives become unbalanced, with the amplitude of the current drawn in the faulted B phase being smaller than the amplitudes of the currents drawn by both the A and C phases, despite the A phase being involved in the upstream fault as well. The results in Figure 6-11 (a) also show that in the case of both types of ASD system, during the fault there are significant sags in the input voltages to the drives in both faulted phases (phases A and B), as well as a sag in the input voltage in the un-faulted phase (phase C). However Figure 6-11 (a) shows that, whilst the depth of the sag in the input voltages to both types of drive is similar in one of the faulted phases (phase B), in the other faulted phase (phase A) and in the un-faulted phase (phase C) the depth of the sag in the input voltages is noticeably greater in the case of the AFE-type drive. Figure 6-11 (a) shows that this is because the AFE converter draws significantly larger currents from Bus 3 during the fault in phases A and C than does the UDR converter.

The behaviour of the variables within the upstream power system network in Figure 6-11 (b) shows that during this phase A to B to ground fault, the amplitudes of the phase A and C currents supplied by the source that feeds Busbar 1 are significantly larger when the ASD system being fed by the power system network has an AFE-type converter than is the case when the ASD system has a UDR-type converter. These larger amplitudes of currents in both faulted and un-faulted phases of the upstream power system network are a direct consequence of the manner in which the front-end converter of the AFE-type of drive draws current in response to asymmetric sags in its input voltages.

The results in Figure 6-11 (b) also show that the current in one phase (phase A) of the fault branch itself is actually lower when the power system feeds the AFE-type drive. This lower phase-A fault current is a result of the greater sag depth in phase A of the Bus 3 voltage during the fault when the system feeds the AFE-type drive, as seen in Figure 6-11 (a). By contrast, Figure 6-11 (b) shows that the fault currents in phase B of the fault branch are similar in the case of both types of ASD system, and Figure 6-11 (a) confirms that the sags in the phase B voltages at Bus 3 are similar in the case of both types of drive.

With respect to the performance of the drive systems themselves, the comparison of the results in Figure 6-11 (c) shows that during the asymmetric voltage sag condition created by this upstream fault, both ASD systems are still able to continue meeting the torque and speed requirements of the motion control task. However, as in the case of the previous study, the results in Figure 6-11 (c) once again show that each type of ASD system rides through the voltage sag condition by responding in a different manner to the upstream fault, according to its particular type of front-end converter technology: the AFE converter unit responds to the voltage sag condition at its input by drawing more AC input current to maintain the DC-link voltage and, as a result, the machine-side VC inverter and its controller, the motor and load are all effectively decoupled from the impact of the sag; by contrast, the UDR converter unit cannot prevent the DC-link voltage from decreasing in the face of the voltage sag condition at its input, and the ASD controls are then required to respond to the impact of the sag on the DC-link voltage by increasing the modulation depth of the VC inverter.

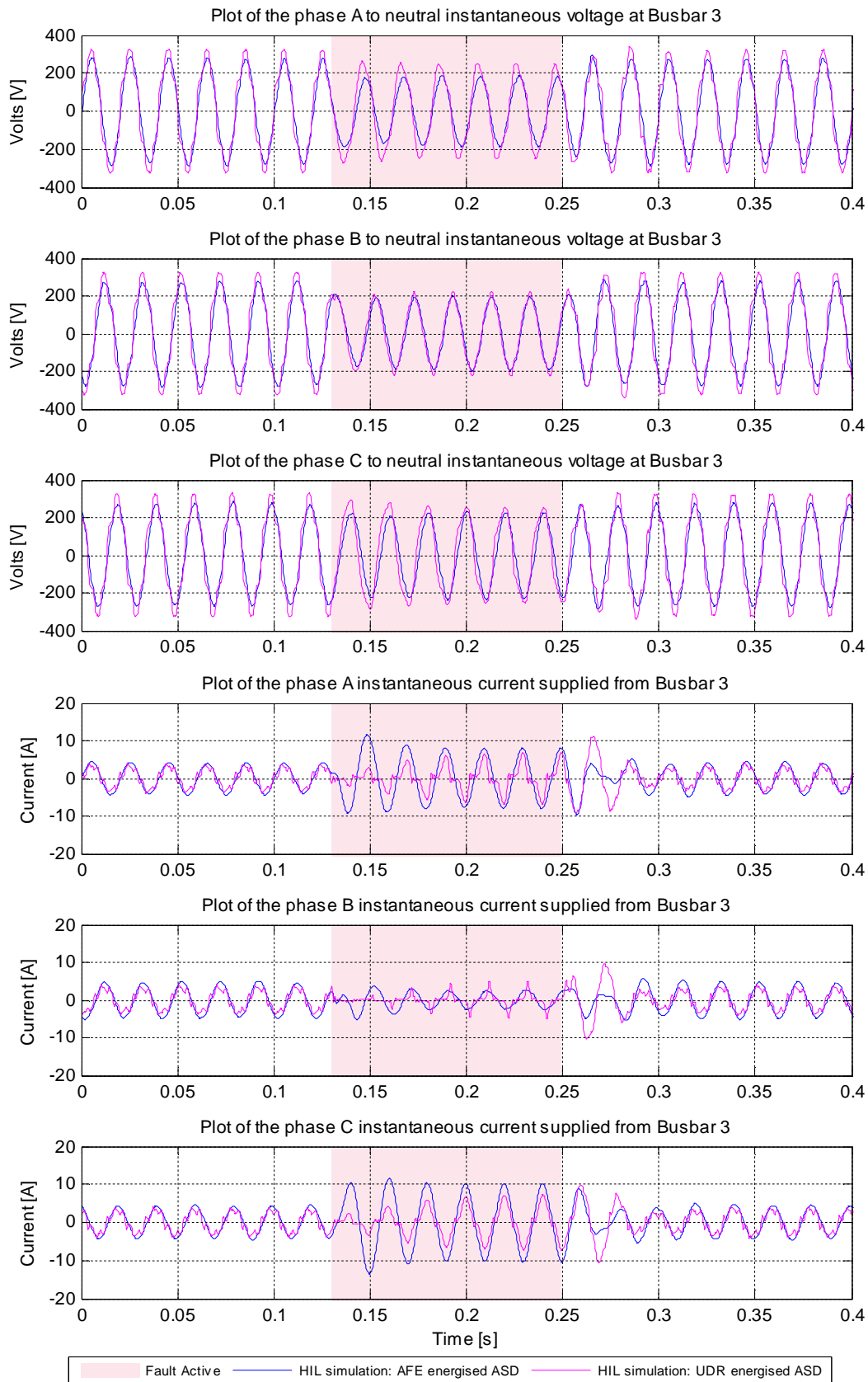


Figure 6-11 (a): Comparison of power system performance when feeding an ASD equipped with AFE- versus UDR-type front-end technologies — response to phase A to B to ground fault with  $R_{FAULT} = 3.5 \Omega$  and duration 100 ms (Bus 3 variables).

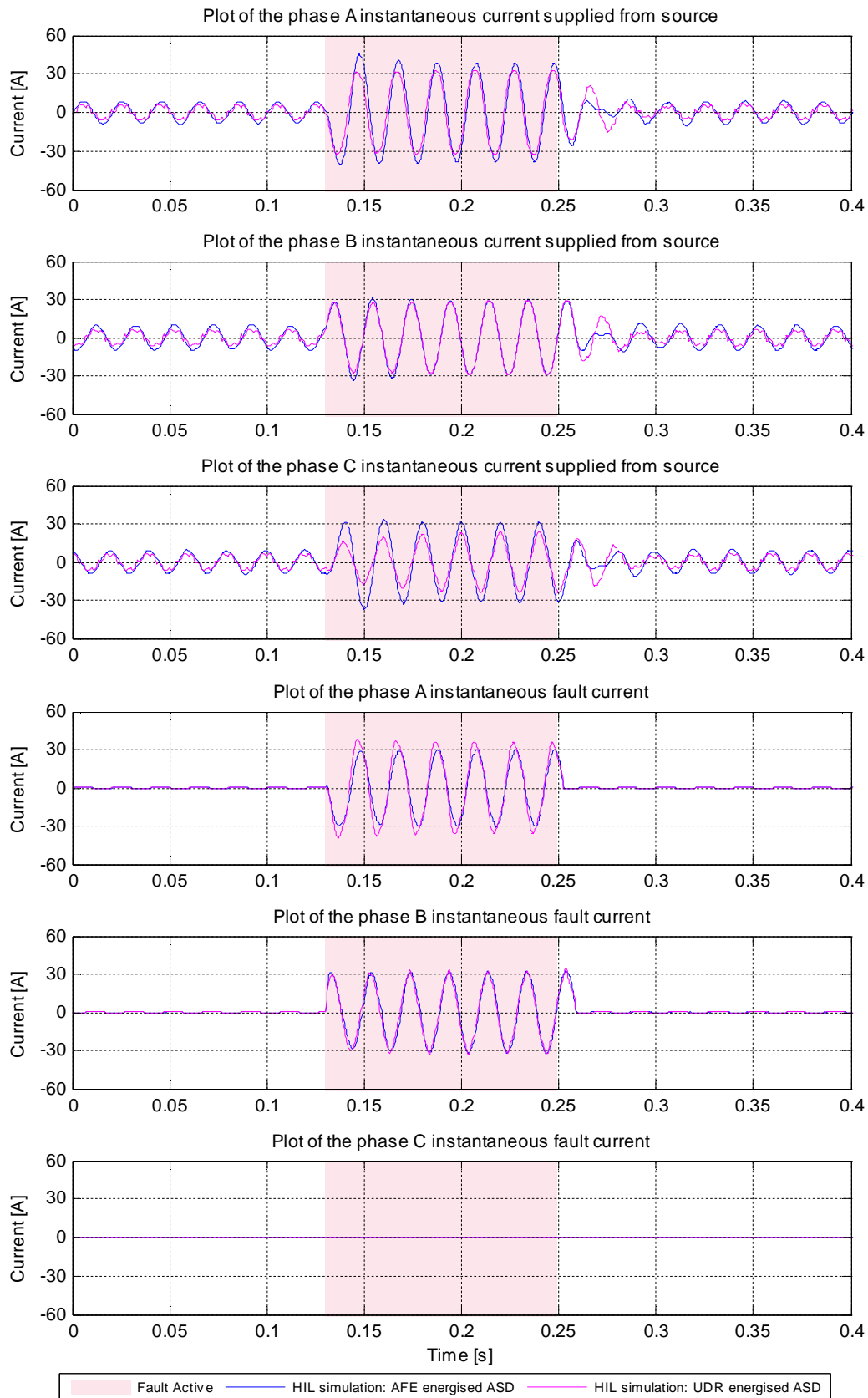


Figure 6-11 (b): Comparison of power system performance when feeding an ASD equipped with AFE- versus UDR-type front-end technologies — response to phase A to B to ground fault with  $R_{FAULT} = 3.5 \Omega$  and duration 100 ms (220 V source currents and fault currents).

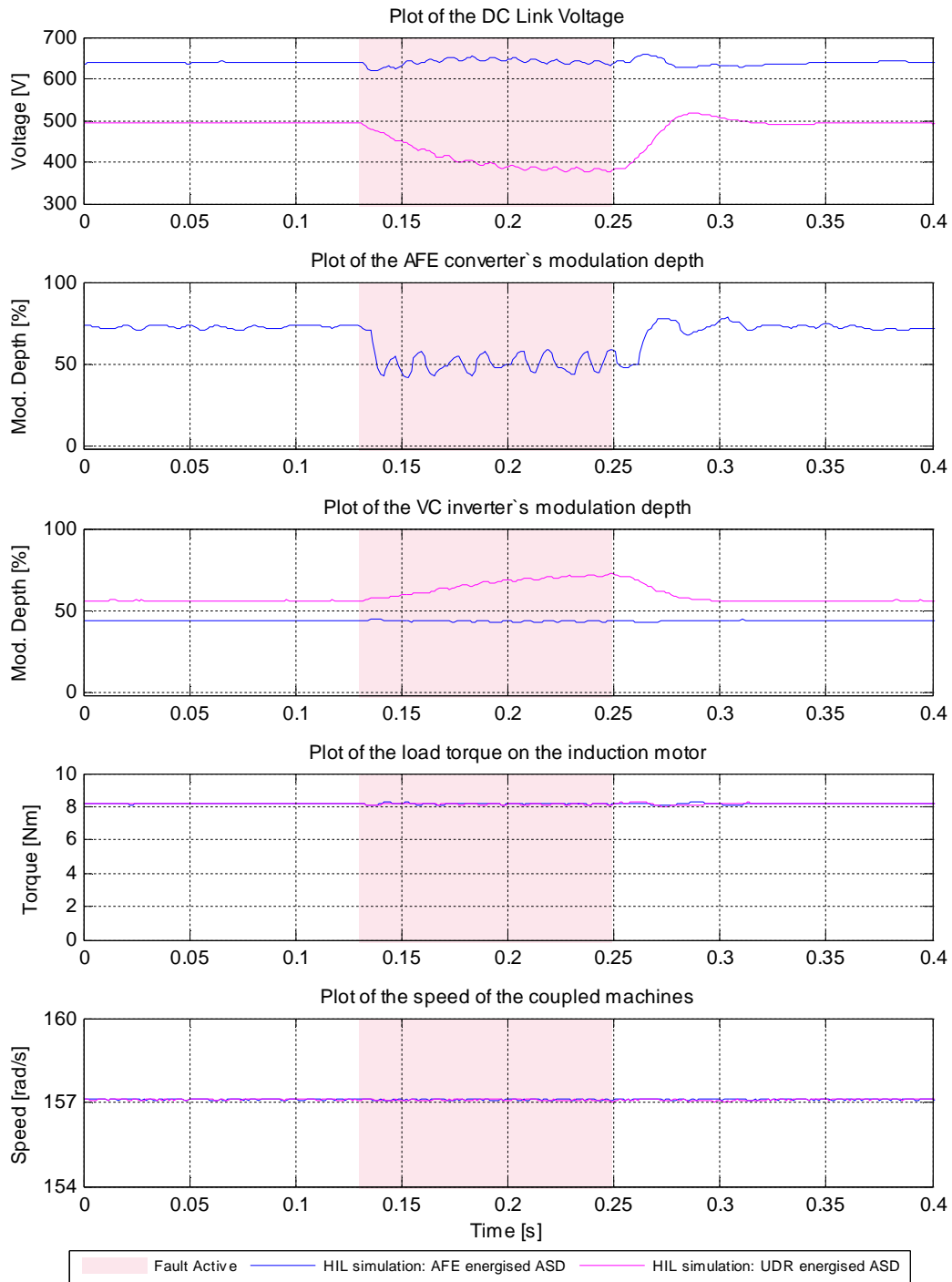


Figure 6-11 (c): Comparison of power system performance when feeding an ASD equipped with AFE-versus UDR-type front-end technologies — response to phase A to B to ground fault with  $R_{FAULT} = 3.5 \Omega$ , and duration 100 ms (ASD system variables).

### 6.3.3 Performance of the Power System Network Feeding AFE- and UDR-Type Drives During Symmetric Fault Conditions

This subsection now directly compares the performance of the power system network and the responses of the motion control system of the ASD when the ASD is equipped with both AFE- and UDR-type front-end technologies during the application of the two different symmetric faults in the power system network that are shown in Table 6-2, namely Fault Conditions (3) and (4).

Figures 6-12 (a), (b) and (c) compare the performance of the laboratory-scale study system when feeding an ASD equipped with both types of front-end technology, before, during and after the application, for 100 ms, of the phase A to B to C to ground fault of fault resistance  $3.2 \Omega$  at the Fault Bus (Fault Condition (3) in Table 6-2): Figure 6-12 (a) compares the AC currents and voltages at Bus 3 in the study system in each case; Figure 6-12 (b) compares the currents supplied by the source at Bus 1, and the fault currents in each case; Figure 6-12 (c) compares the variables within the ASD system in each case. The areas highlighted in pink in Figures 6-12 (a), (b), and (c) show the period during which the fault was actually applied in each case.

The results in Figure 6-12 (a) show that, as expected, a symmetrical three-phase fault in the power system supply network causes a symmetrical sag in the voltages of all three phases at the inputs to the front-end converter of both types of ASD system. However, the results show that the depth of this symmetrical sag in the input voltages to the ASD is significantly greater, for this particular three-phase fault condition, when the power system is feeding an ASD system with an AFE-type front-end converter. The results in Figure 6-12 (a) also show clearly why this is the case: the ASD system equipped with the AFE-type converter draws significantly larger currents during the upstream fault in the power system than is the case for the ASD system equipped with the UDR-type converter.

The results shown in Figure 6-12 (b) demonstrate a further consequence of the different responses of the two types of ASD front-end converter technology to the power system supplying the drives: the currents supplied by all three phases of the source that feeds Busbar 1 are significantly larger during the three-phase fault when the ASD system being fed by the power system has an AFE-type converter than is the case when the ASD system has a UDR-type converter. Figures 6-12 (a) and (b) thus illustrate that the improved voltage-sag ride through capability of AFE-type drives can come at the expense of creating both greater depths of voltage sag in the power system, and at the expense of drawing larger currents from the power system whilst it is in a faulted condition.

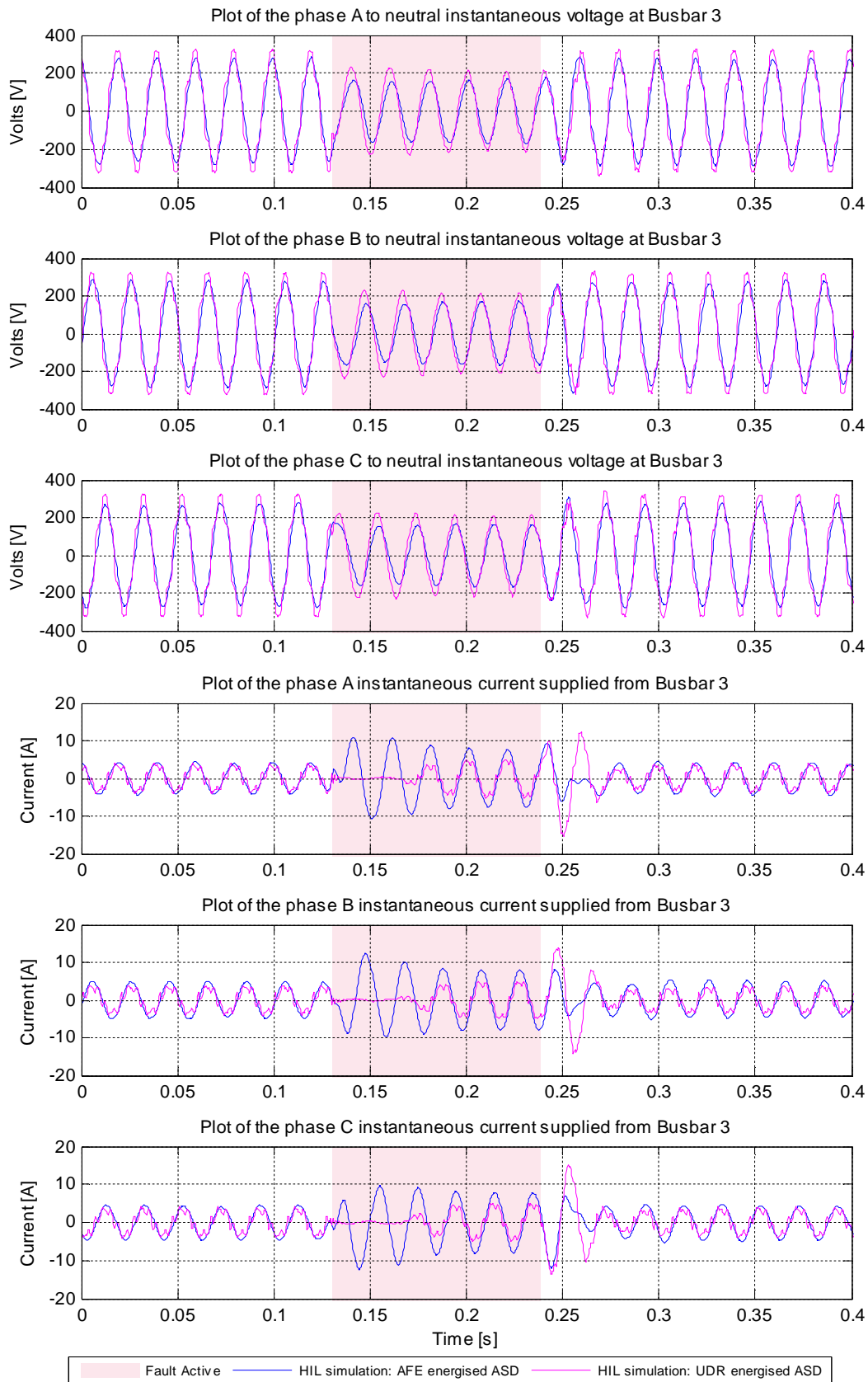


Figure 6-12 (a): Comparison of power system performance when feeding an ASD equipped with AFE- versus UDR-type front-end technologies — response to phase A to B to C to ground fault with  $R_{FAULT} = 3.2 \Omega$  and duration 100 ms (Bus 3 variables).

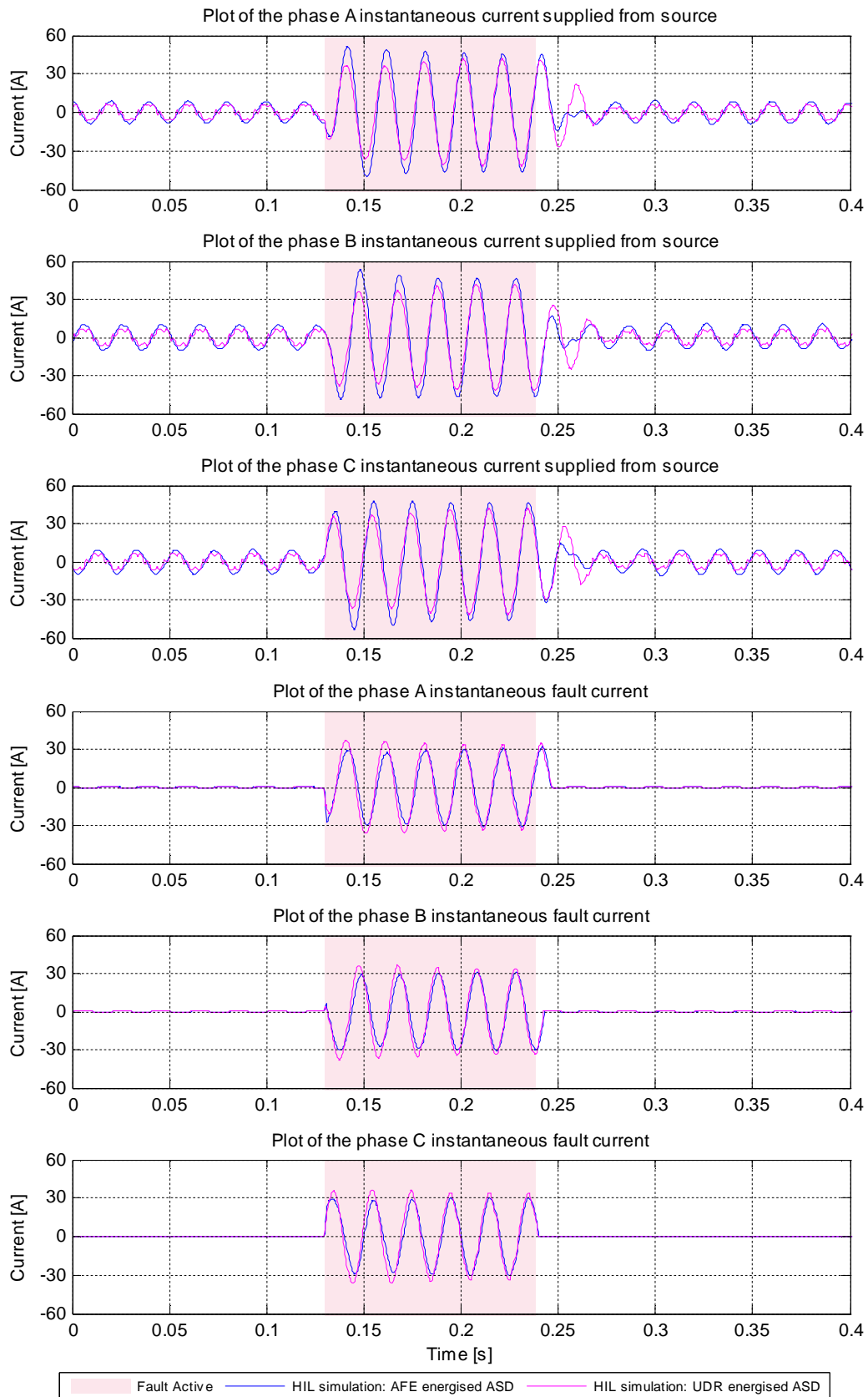


Figure 6-12 (b): Comparison of power system performance when feeding an ASD equipped with AFE- versus UDR-type front-end technologies — response to phase A to B to C to ground fault with  $R_{FAULT} = 3.2 \Omega$  and duration 100 ms (220 V source currents and fault currents).

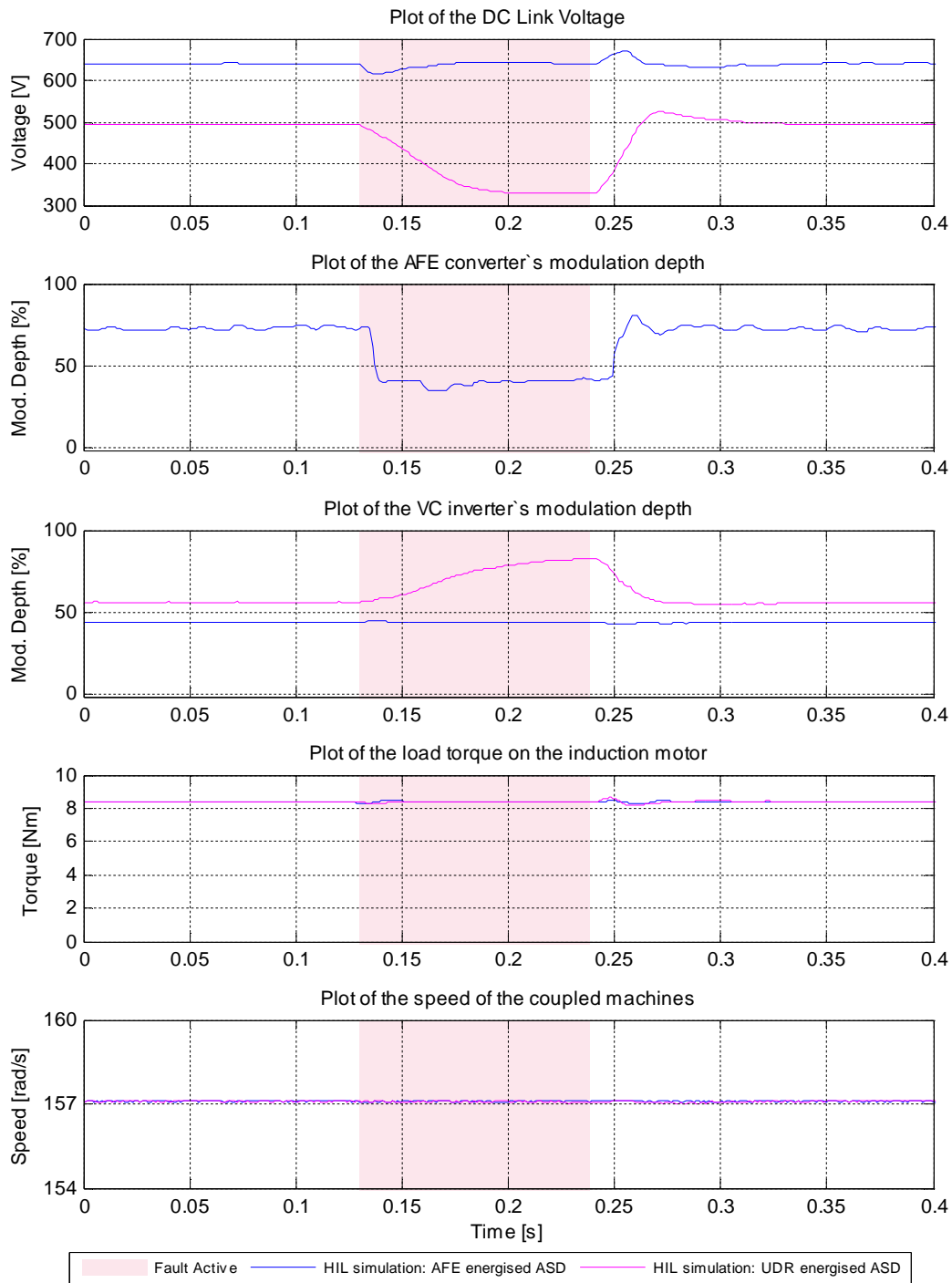


Figure 6-12 (c): Comparison of power system performance when feeding an ASD equipped with AFE-versus UDR-type front-end technologies — response to phase A to B to C to ground fault with  $R_{FAULT} = 3.2 \Omega$ , and duration 100 ms (ASD system variables).

With respect to the performance of the drive systems themselves, the comparison of the results in Figure 6-12 (c) confirms that during the symmetrical voltage sag condition created by this upstream fault, both ASD systems are still able to continue meeting the torque and speed requirements of the motion control task. However, once again the results show that each type of ASD system rides through the voltage sag condition by responding in a different manner to the upstream fault, according

to its particular type of front-end converter technology: for this particular three-phase sag the AFE converter unit is still able to decouple the machine-side VC inverter unit, motor and load from the impact of the sag by drawing more AC input current to maintain the DC-link voltage; by contrast, the UDR converter unit is unable to regulate the DC-link voltage in the face of the voltage sag condition and the ASD controls are thus required to respond to the drop in DC-link voltage by temporarily increasing the modulation depth of the VC inverter.

Figures 6-13 (a), (b) and (c) now compare the performance of the laboratory-scale system when feeding an ASD equipped with both types of front-end technology, before, during and after the application, for 100 ms, of the phase A to B to C to ground fault of fault resistance  $0.5 \Omega$  at the Fault Bus (Fault Condition (4) in Table 6-2): Figure 6-13 (a) compares the AC currents and voltages at Bus 3 in the study system in each case; Figure 6-13 (b) compares the currents supplied by the source at Bus 1, and the fault currents in each case; Figure 6-13 (c) compares the variables within the ASD system in each case. The areas highlighted in pink in Figures 6-13 (a), (b), and (c) show the period during which the fault was actually applied in each case.

From the results already seen in Chapter 5, and earlier in this chapter, a fault such as that now being considered in Fault Condition (4) in Table 6-2 is known to result in a symmetrical voltage sag condition at the inputs to the drive system that is severe enough, in terms of sag depth and duration, to cause an ASD system equipped with either an AFE-type or UDR-type converter to trip the machine within the drive. Furthermore, in the case of the AFE-equipped ASD system, this voltage sag condition is also known to be sufficiently severe that it forces the mode of operation of the AFE converter unit to change from active front end control mode to uncontrolled diode rectifier mode during the sag.

With respect to the performance of the drive systems themselves, the results in Figure 6-13 (c) confirm that the ASD system equipped with an AFE-type converter is, almost immediately after the onset of the sag condition, forced into uncontrolled diode rectifier mode (as evidenced by the modulation depth signal sent to the AFE converter being driven to zero almost immediately upon the commencement of the sag). Figure 6-13 (c) shows that once the drive equipped with an AFE-type converter goes into uncontrolled diode rectifier mode, its response becomes virtually the same as that of the ASD equipped only with a UDR-type converter. Figure 6-13 (c) shows that neither type of drive front-end technology can maintain the desired motor torque and speed in the face of the voltage sags created by this severe symmetrical fault in the upstream network and in both cases the drives trip.

The results show that the ASD system equipped with the AFE-type converter trips approximately 35 ms after the ASD system equipped with the UDR-type converter due to the higher pre-fault DC-link voltage.

With respect to the impact of the two types of ASD systems' responses on the power system, the results in Figures 6-13 (a) and (b) confirm that, because the ASD system equipped with the AFE-type converter is forced so quickly into uncontrolled diode rectifier mode in response to this fault condition, the impact of both types of drive technology on the power system variables is almost identical, barring the very brief period (approximately 15 ms) after the onset of the fault when the AFE-type converter can still draw currents at its AC inputs.

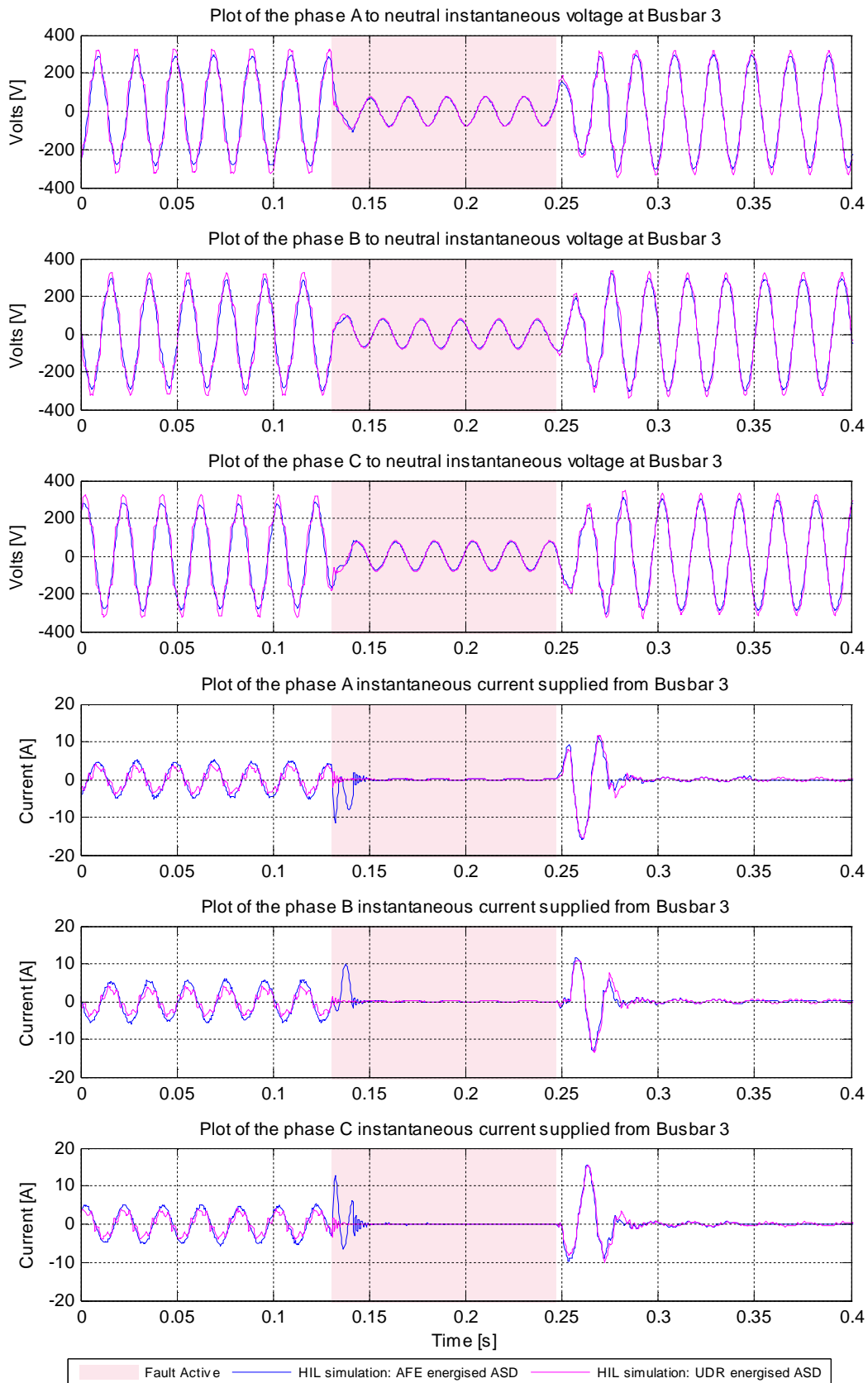


Figure 6-13 (a): Comparison of power system performance when feeding an ASD equipped with AFE- versus UDR-type front-end technologies — response to phase A to B to C to ground fault with  $R_{FAULT} = 0.5 \Omega$  and duration 100 ms (Bus 3 variables).

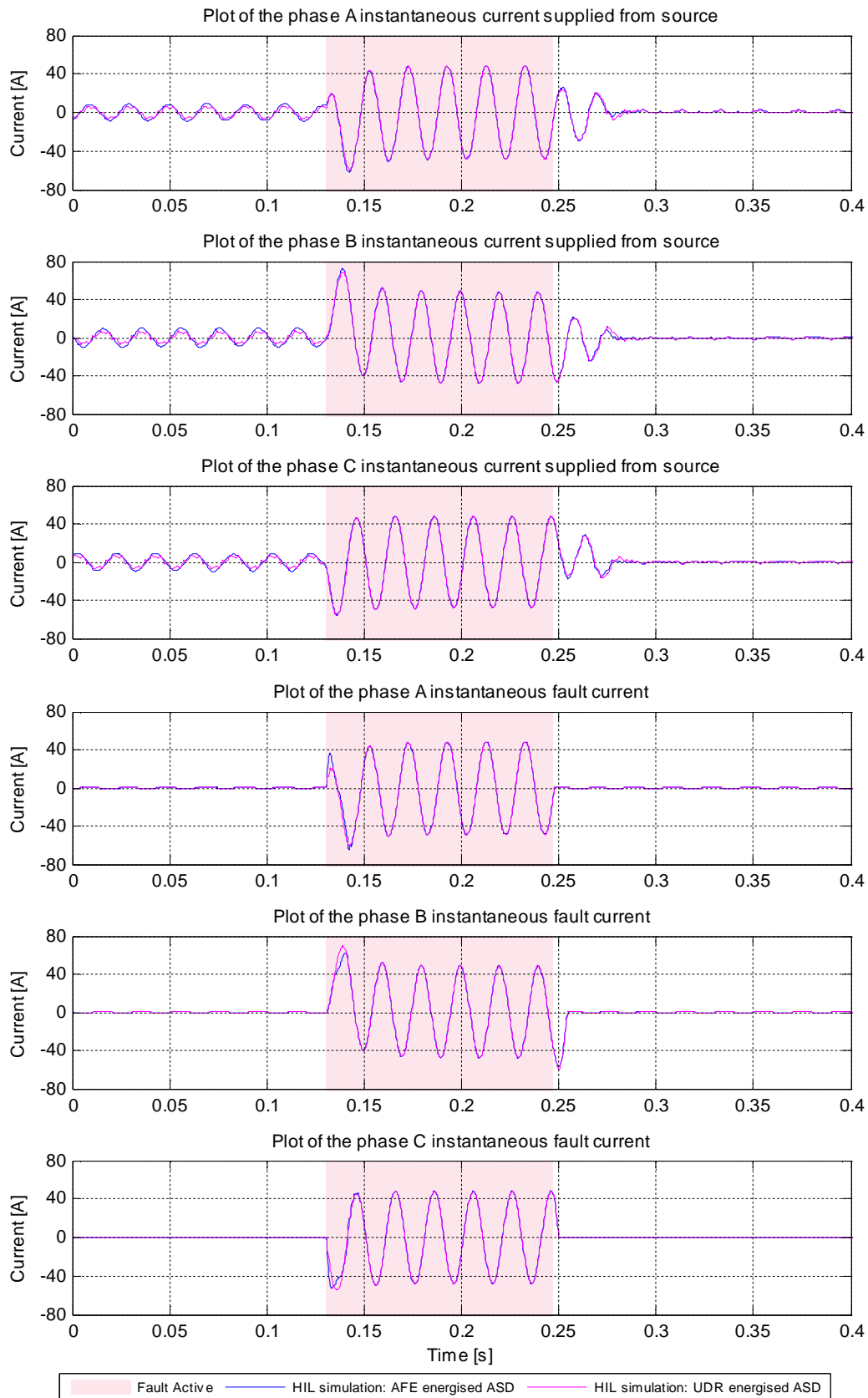


Figure 6-13 (b): Comparison of power system performance when feeding an ASD equipped with AFE- versus UDR-type front-end technologies — response to phase A to B to C to ground fault with  $R_{FAULT} = 0.5 \Omega$ , and duration 100 ms (220 V source currents and fault currents).

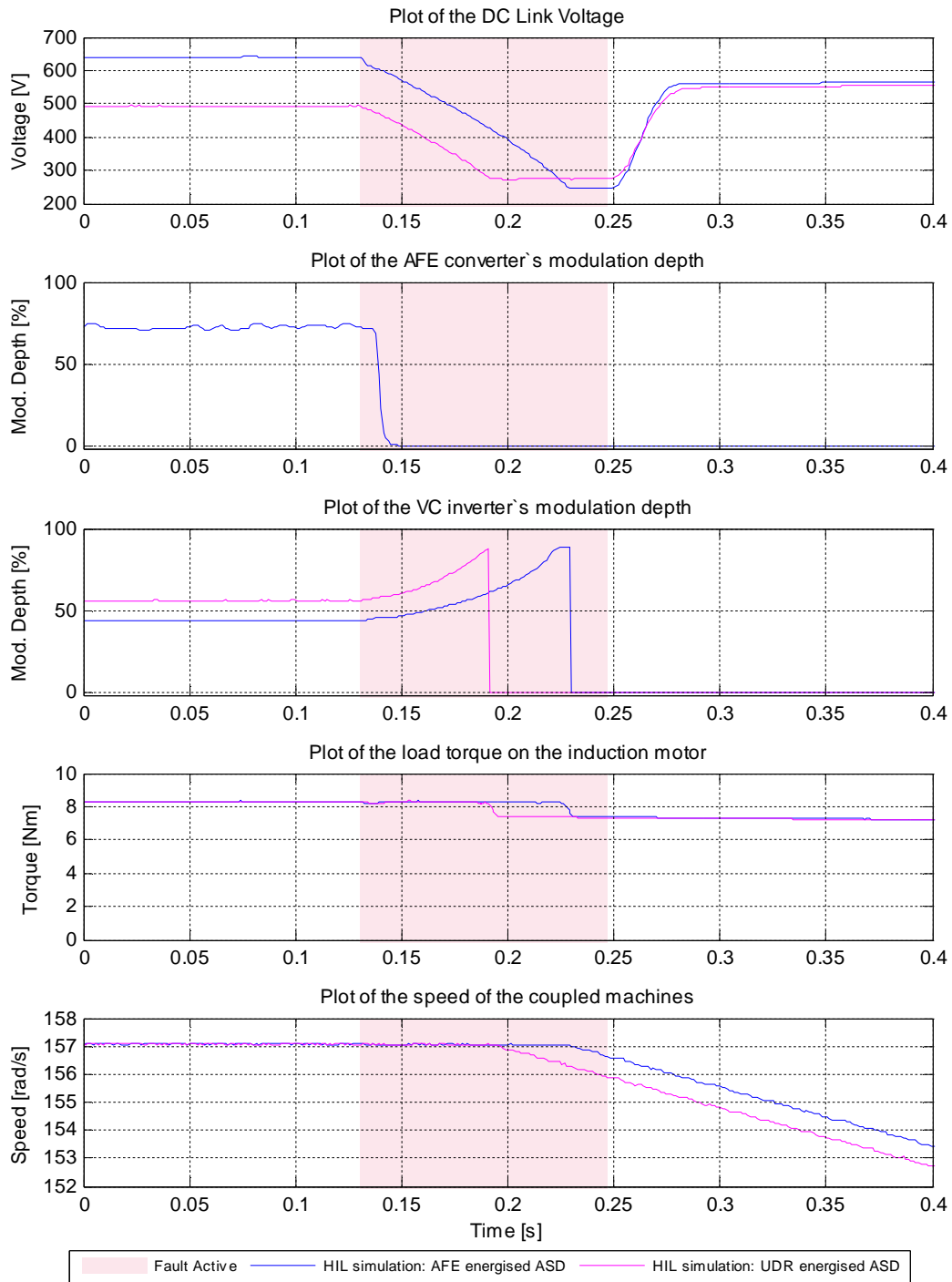


Figure 6-13 (c): Comparison of power system performance when feeding an ASD equipped with AFE- versus UDR-type front-end technologies — response to phase A to B to C to ground fault with  $R_{FAULT} = 0.5 \Omega$ , and duration 100 ms (ASD system variables).

#### **6.3.4 Summary of the Results of Tests into the Response of the Power System Network Feeding AFE- and UDR-Type Drives During Network Fault Conditions**

This section has presented the results of an investigation, carried out solely using the HIL real-time simulator testing approach in order to compare the influence of different ASD front-end converter technologies on the performance of the power system itself during the application of a set of four network fault conditions.

The comparative analyses shown in this section confirm that AFE- and UDR-equipped ASD systems respond differently to upstream fault conditions, and that these different drive technologies therefore not only have different influences on the power system network supplying them during voltage sag conditions, but their own motion control systems are influenced by such sags in different ways.

In the case of those fault conditions considered in these tests that were within the ride-through capabilities of the AFE-equipped ASD system (Fault Conditions (1), (2) and (3) in Table 6-2), the AFE controller was able to quickly detect the resulting voltage sag conditions and react by commanding the AFE converter to draw higher currents at its AC inputs in order to maintain the voltage level of the DC link within the drive system. These increased currents drawn by the AFE converter can in turn place further stress on the faulted power system network and hence give rise to greater depths of voltage sag appearing at the AC inputs to the AFE converter; however, despite the increased magnitude of these currents drawn by the AFE converter, they typically result in negligible harmonic distortion in the AFE converter's supply voltages during the fault.

By comparison, an ASD system equipped with a UDR front-end converter typically draws lower currents at its AC inputs under the same network fault conditions, placing less stress on the faulted power system network, and hence resulting in less-severe sags in the voltages at the AC inputs to the ASD system. However, despite the reduced magnitude of these currents drawn by the UDR converter during voltage sag conditions, these currents are non-sinusoidal and they can therefore result in significant levels of harmonic distortion being evident in the supply voltages to this type of ASD system during sag conditions.

With respect to the influence of the AFE- and UDR-converters on the performance of the motion control system itself during upstream fault conditions, the ability of an AFE converter to regulate the DC-link voltage during the resulting voltage sag conditions can, within the capability limits of the front-end converter, virtually decouple the machine-side inverter, machine and load in this type of motion control system from the impacts of the faults and, as a result, the motion control system is able

to ride through the faults in a manner that requires very little dynamic adjustment by the control hardware operating the machine. By comparison, a UDR converter is not able to prevent voltage sag conditions at the AC inputs to the ASD system from being reflected into its DC-link voltage and, as a result, the control hardware within the ASD responsible for the high-performance motion control tasks has to make significant dynamic changes in its control action in order to allow this type of motion control system to be able to ride through the faults.

## 6.4 Summary

The first half of this chapter considered the specific case in which the ASD in the laboratory-scale system was equipped with an active front end converter, and presented the results of detailed studies into the performance of this type of ASD in response to voltage sags caused by upstream faults in the laboratory-scale system. These results have not only documented the voltage-sag performance of this type of ASD technology by means of measurements carried out on a carefully controlled and representative small-scale study system implemented in a research laboratory, but have also demonstrated the validity of the HIL real-time simulation approach to such testing. The close agreement between the results obtained from both implementations of the laboratory-scale study system (HIL simulation and all-hardware) has demonstrated that the HIL real-time simulator testing approach can accurately predict the dynamic performance of ASD systems equipped with active front-end converters in response to voltage sags caused by upstream faults.

The detailed tests presented in Chapter 5 and in the first half of this chapter have thus served to carefully establish the validity and accuracy of the HIL real-time simulation approach to studying the performance of adjustable speed drives for the cases of both active, and non-active front-end converter technologies. Hence, in the second half of this chapter it was therefore possible to rely solely on this HIL real-time simulator testing approach in order to directly compare the influence of these two different types of front-end converter technologies on the performance of the power system itself during network faults that cause voltage sag conditions at the drive front-ends. The results of these comparative studies have shown not only how adjustable speed drives equipped with these different front-end converter technologies respond differently to a given set of upstream network faults, but also how they can interact differently with the power system network, and result in different levels of harmonic distortion, fault levels, and voltage sag depths within the power system itself in response to given upstream network faults. Furthermore, the results have also shown that the type of front-end converter technology used within an adjustable speed drive also influences the manner in which the control hardware responsible for the high-level motion control tasks within the drive system responds dynamically during the supply voltage sags caused by upstream faults.

## **Chapter 7: Conclusion**

### **7.1 Introduction**

Sophisticated motion control systems that are used to achieve high-performance applications in industry can potentially have a high level of interaction with upstream power system networks. A testing method to accurately predict the performance of these motion control systems and their interactions with upstream power system networks under dynamic conditions would be of immense benefit. Testing methods that have been used previously to study the dynamic performance of motion control systems have had some limitations. However, a hardware-in-loop (HIL) testing method, which is based on recent developments made in real-time simulator technology could address such limitations.

The aim of this thesis has been to evaluate the suitability and accuracy of this testing method in which the actual control hardware of a commercial adjustable speed drive (ASD) is connected in a hardware-in-loop arrangement with a real-time digital simulation model of the industrial drive plant under control and of the upstream power system network supplying the drive plant.

The evaluations in the thesis were carried out according to a structured procedure that involved comparison of the measured performance, under dynamic conditions, of an industrial ASD system in an all-hardware implementation of a specially-developed, laboratory-scale study system with the results obtained from the HIL testing method in which the power-level plant in the same laboratory-scale study system was modelled entirely on a real-time digital simulator, and the physical ASD controllers were connected hardware-in-loop with this real-time model of the power-level plant.

As an additional dimension to the research in the thesis, the abovementioned structured procedure was used to evaluate the HIL testing method as applied to two different types of ASD front-end converter technology that are currently used in industrial motion control systems, namely active front end (AFE) and uncontrolled diode rectifier (UDR) front-end converter technologies.

The main conclusions from each of the sections of the work presented in the thesis are summarised as follows under the relevant section headings.

## **7.2 An Introduction to Field Oriented Control**

As a theoretical foundation to the work presented in the thesis, the manner in which torque is produced in a squirrel cage induction machine was described. Thereafter, a signal flow representation of the two-axis dynamic model of this type of induction machine was presented. With the use of this two-axis model, the principles, and method of operation of the field oriented control algorithm were presented in order to demonstrate the sophisticated nature of this control algorithm, a proprietary implementation of which is used in the industrial ASD system whose performance was studied in this thesis.

## **7.3 The All-Hardware Laboratory-Scale Implementation of the Study System**

The topology of the laboratory-scale study system used as a benchmark for the comparisons in the thesis was outlined, and the practical details of key components that were used to implement both the motion control system and the power system supply network in the study system within a machines research laboratory were then described. Thereafter, the modes of operation and the procedures adopted for commissioning the drive controller hardware were discussed, both for the front-end converter and machine-side inverter units of the industrial ASD system. Finally, it was explained how the characteristics of the study system were carefully designed so as to allow a practical range of voltage sag conditions to be created in a controllable manner at the front end of the drive as a result of realistic upstream short-circuit faults applied in the supply network.

## **7.4 Development and Parameterization of the Real-Time Model for the HIL Simulation Implementation of the Study System**

The development and parameterization of a real-time simulation model of all of the power-level plant elements within the laboratory-scale study system was described. Thereafter, key sub-sections of the actual plant used to make up the study system were tested under voltage sag conditions in the laboratory and their measured responses were compared against those of the parameterized real-time models to verify the correctness and accuracy of the models. The results of these model validation tests showed that the real-time models of the key sub-sections of plant in the laboratory-scale study system were able to accurately represent the actual characteristics of this plant under the intended range of test conditions.

In particular, the results of the model verification tests of the three-limb type drive transformer showed that the influence of its inter-phase magnetic coupling effects on supply voltage sags can be

accurately represented by using a carefully-parameterized, unified magnetic equivalent circuit (UMEC) transformer model. With respect to the deep-bar rotor type of drive motor used in the laboratory-scale study system, the results of its model verification tests showed that the effects of its deep-bar rotor construction on its dynamic behaviour under voltage sag conditions can be accurately represented by using an appropriately-parameterized, double-cage rotor induction machine model; in the work presented in this thesis these double-cage rotor machine parameters were calculated by means of a parameter fitting algorithm that was developed by the author.

### **7.5 The HIL Simulation Implementation of the Study System and the Performance of the Diode Rectifier Energised ASD Under Voltage Sag Conditions**

A detailed description of how the real-time simulation model of the power-level plant in the laboratory-scale study system was interfaced to the physical controllers of the industrial ASD system to form the HIL simulation implementation of the study system was presented.

Thereafter, the particular case in which the ASD in the laboratory-scale study system was equipped with a UDR-type of front-end converter was considered, and detailed studies were presented to examine the performance of this type of ASD in response to voltage sags caused by upstream short-circuit faults in the laboratory-scale study system. As a consequence of the carefully-structured procedure adopted in the thesis to evaluate the HIL testing method, the results of these studies have not only documented the voltage-sag performance of this type of ASD technology by means of measurements carried out on the all-hardware implementation of the laboratory-scale study system, but they have also demonstrated the validity of the HIL real-time simulation approach for such testing. The close agreement between the results obtained from both implementations of the laboratory-scale study system (all-hardware and HIL simulation) has demonstrated that the HIL real-time simulation testing approach can accurately predict the dynamic performance of ASD systems equipped with diode-rectifier front-end converters in response to voltage sags caused by upstream faults.

## **7.6 The Performance of the AFE Converter Energised ASD System Under Voltage Sag Conditions**

The particular case in which the ASD in the laboratory-scale study system was equipped with an active front end converter was then considered, and detailed studies were presented to examine the performance of this type of ASD in response to voltage sags caused by upstream short-circuit faults in the laboratory-scale study system.

Once again, as a consequence of the structured procedure adopted to evaluate the HIL testing approach, the results of these studies have not only documented the voltage-sag performance of this type of ASD technology by means of measurements carried out on the all-hardware implementation of the laboratory-scale study system, but they have also demonstrated the validity of the HIL real-time simulation approach for such testing. The close agreement between the results obtained from both implementations of the laboratory-scale study system has demonstrated that the HIL real-time simulator testing approach can accurately predict the dynamic performance of ASD systems equipped with active front-end converters in response to voltage sags caused by upstream faults.

Since the validity and accuracy of the HIL real-time simulation approach for studying the performance of adjustable speed drives had been carefully established for the cases of both active and non-active front-end converter technologies, it was therefore possible to rely solely on this HIL testing approach in order to directly compare the influence of these two different types of front-end converter technologies on the performance of the power system itself during network faults that cause voltage sag conditions at the front ends of such drives. The results of these comparative studies have shown not only how ASDs equipped with these different front-end converter technologies respond differently to a given set of upstream network faults, but also how they can interact very differently with the power system network during such disturbances. Furthermore, the results have also shown that the type of front-end converter technology used within an ASD also influences the manner in which the control hardware responsible for the high-level motion control tasks within the drive system responds dynamically during the supply voltage sags caused by upstream faults.

## **7.7 Concluding Comments**

The work in this thesis has served to establish the validity and accuracy of the HIL real-time simulation testing approach to studying the dynamic performance of ASD systems for the cases of both active and non-active front-end converter technologies.

This HIL real-time simulation testing approach has the advantage of allowing the inclusion of far more detailed representations of the plant in the motion control system and power supply system, as well as the inclusion of representations of neighbouring plant fed off busbars in the vicinity of the drive, than would be possible in a laboratory-scale all-hardware test. Therefore, the HIL approach to testing ASDs has potential applications in future for studying the impact of power quality issues on various types of drive system equipment (which can have intricate power-electronic converter / inverter topologies) in much larger-scale representations of the utility supply network. With a detailed representation of a utility supply network, the possibility opens up for simultaneous HIL testing to be carried out on ASD system controls and utility protection systems, using the same real-time simulation model, so that the interaction and coordination of power system and ASD system protection and control functions can be studied in a detailed and representative manner.

## **7.8 Suggestions for Further Work**

Many further research studies could be carried out using the HIL real-time simulation implementation of the laboratory-scale study system developed in this thesis by considering different permutations and options in:

- the real-time model of the power system network and of the drive plant under control;

- the real-time simulation environment to represent different ASD operating conditions, power quality issues and fault scenarios;

- the control settings and modes of operation selected within the industrial ASD motor control and front-end converter control hardware.

Examples of some further investigations that could be carried out with the use of the HIL simulation implementation of the study system by making a few changes in the real-time model, real-time simulation environment, and ASD control hardware include:

- a study into the performance of an ASD system and its influence on an upstream power system network under conditions of supply over-voltages or severe supply harmonics;

a comparative investigation into the influence of different induction motor control algorithms (for example: scalar control, field oriented control, and sensor-less vector control) on the performance of an ASD system under supply voltage sag conditions;

an investigation into the influence of an ASD system on the performance of a power system network during upstream faults for a case in which the ASD system's front-end converter is operated to actively provide a level of reactive power support for the power system.

## Appendix A: Real-Time Simulation Model Of The Power-Level Plant In The Laboratory-Scale Study System Used For HIL Tests

This section shows the real-time simulation model representation of the power-level plant in the laboratory-scale study system that was interfaced to the physical controllers of the industrial ASD system to make up the HIL simulation implementation of the study system. Figure A-1 shows that this real-time simulation model is divided into four parts: the power system network; the ASD pre-charge circuit and line reactor; the ASD frequency converter and motor; the dynamometer load. The detailed representations of each of these four parts of the real-time model in RSCAD's DRAFT programme are shown in Figures A-2 to A-5.

Real-Time Model of Power-Level Plant in Lab-Scale Study System

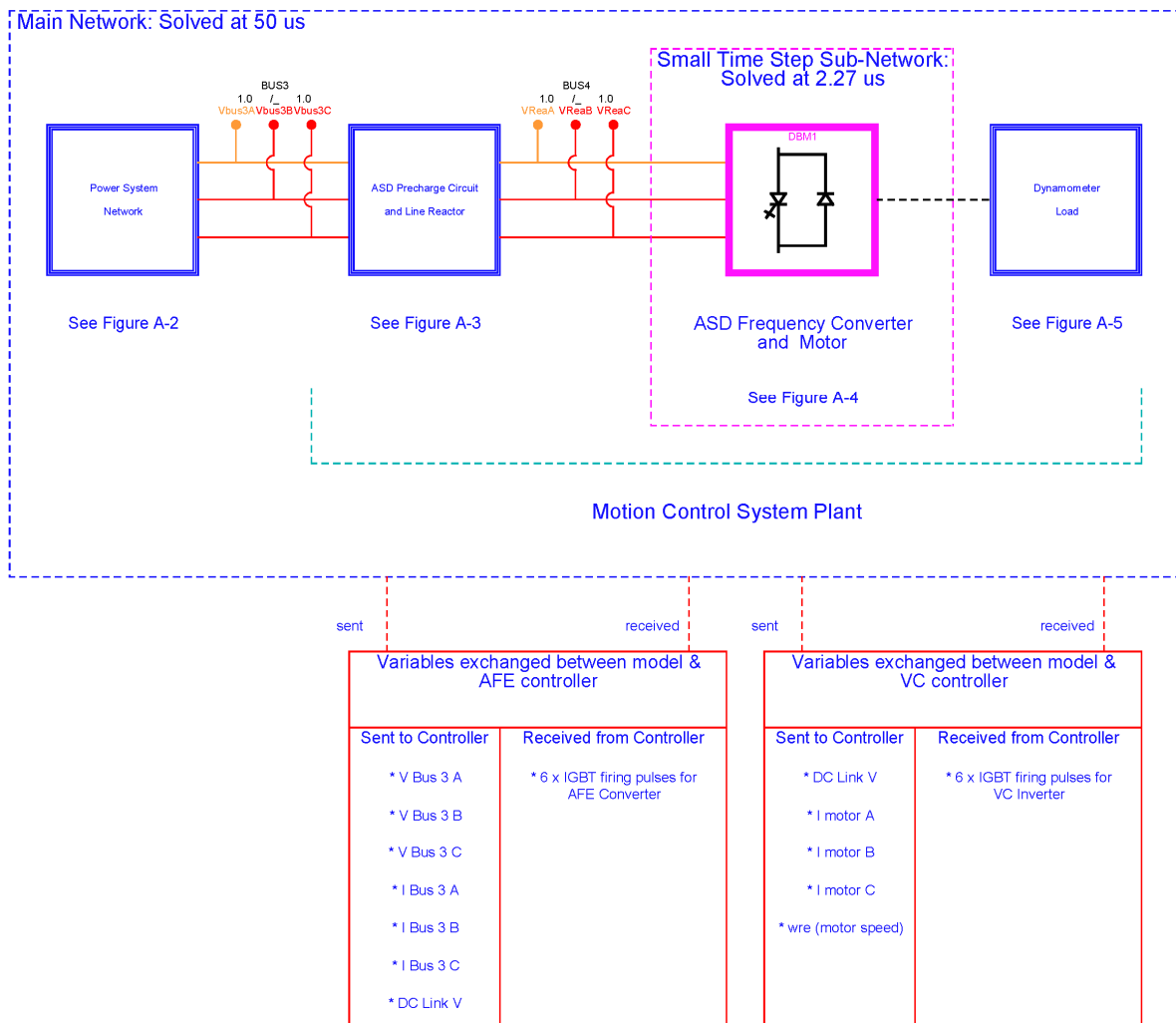


Figure A-1: Real-time model representation of the power-level plant in the laboratory-scale study system that was interfaced hardware-in-loop to the physical controllers of the industrial ASD system. The variables that were exchanged between the controllers and the model during testing are also shown.

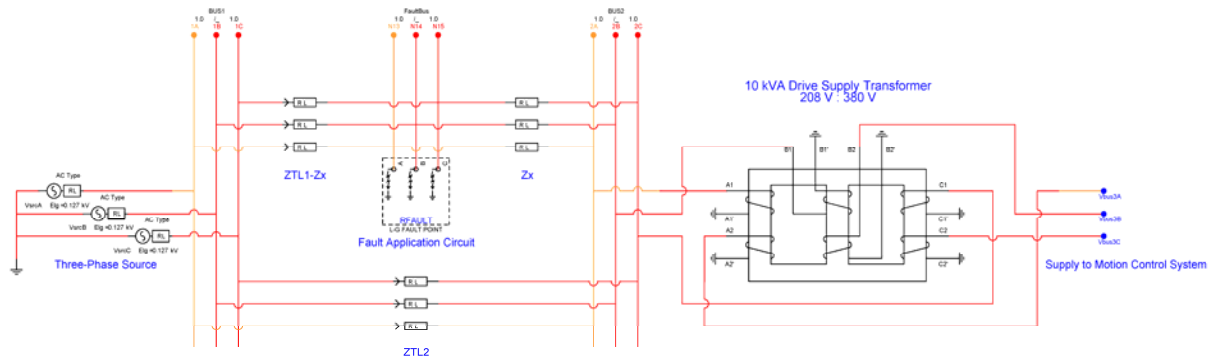


Figure A-2: Detailed real-time model representation of the power system network in the laboratory-scale study system.

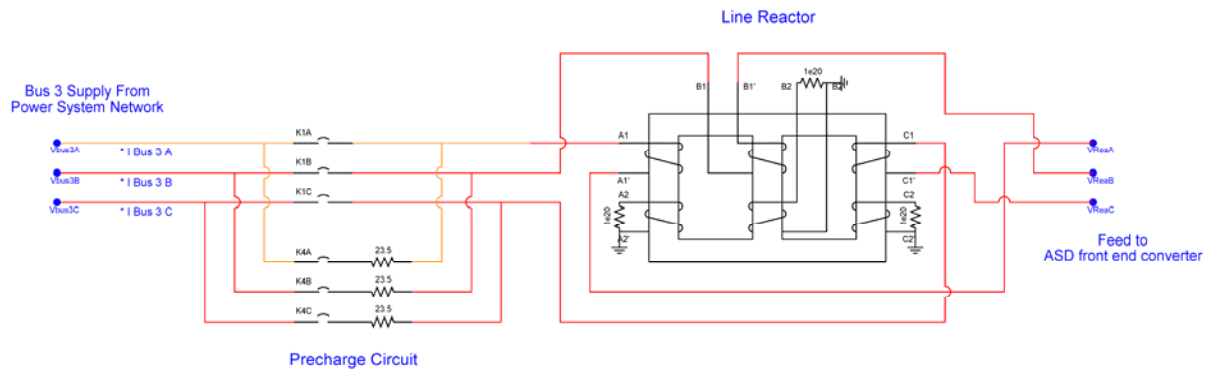


Figure A-3: Detailed real-time model representation of the ASD pre-charge circuit and line reactor in the laboratory-scale study system.

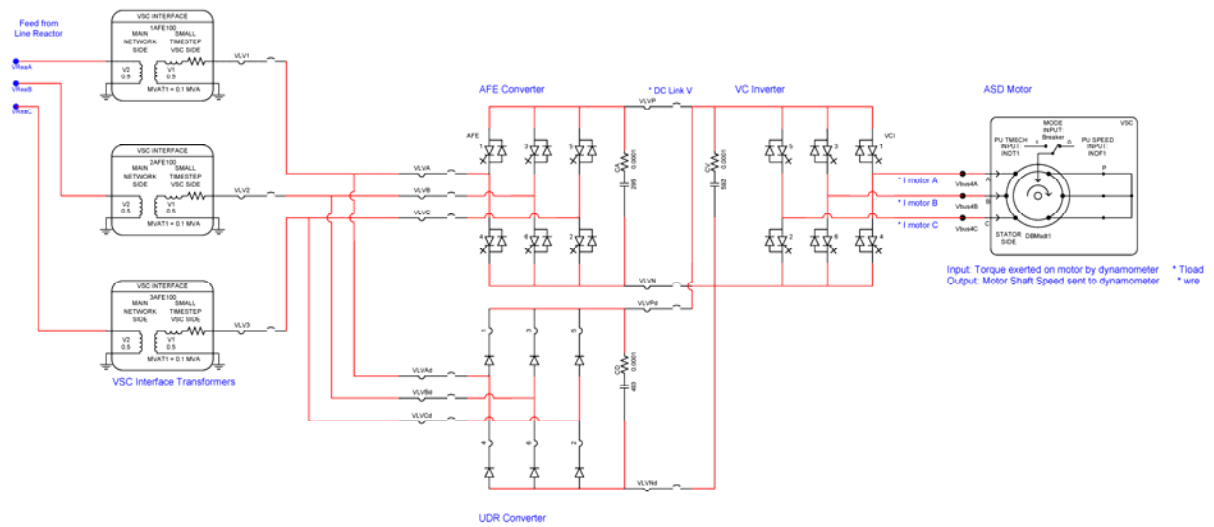


Figure A-4: Detailed real-time model representation of the ASD frequency converter and motor in the laboratory-scale study system.

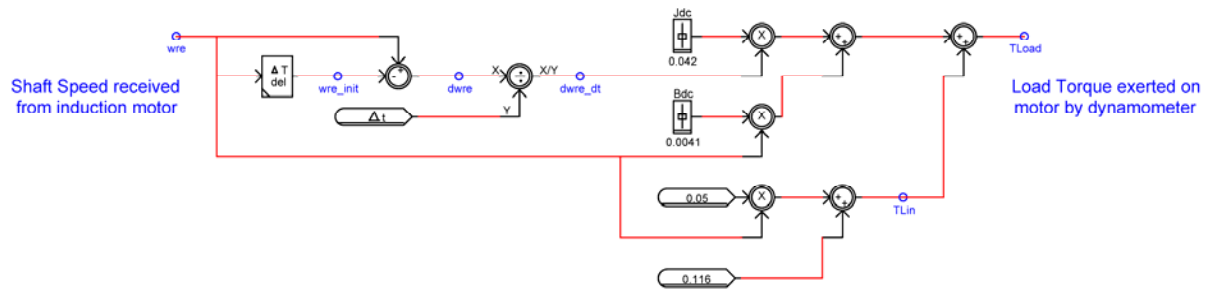


Figure A-5: Detailed real-time model representation of the dynamometer load in the laboratory-scale study system.

## References

1. Leonhard W: "Controlled AC Drives, a Successful Transition from Ideas to Industrial Practice", *Control Engineering Practice*, Vol. 4, No. 7, pp. 897-908, 1996.
2. Leonhard W: "Adjustable-Speed AC Drives", *Proceedings of the IEEE*, Vol. 76, No. 4, pp. 455-471, April 1988.
3. Kazmierkowski M P, Franquelo L G, Rodriguez J, Perez M A, Leon J I: "High-Performance Motor Drives", *IEEE Industrial Electronics Magazine*, Vol. 5, No. 3, pp. 6-26, September 2011.
4. Kohlmeier Helmut, Niermeyer Olaf, and Schroder Dierk F: "Highly Dynamic Four-Quadrant AC Motor Drive with Improved Power Factor and On-Line Optimized Pulse Pattern with PROMC", *IEEE Transactions on Industry Applications*, Vol. IA-23, No. 6, pp. 1001-1009, November/December 1987.
5. Hasse K: "Zum dynamischen Verhalten der Asynchronmaschine bei Betrieb mit variabler Standerfrequenz und Standerspannung", *ETZ-A* 89, pp. 387-391, 1968.
6. Blaschke F: "The Principle of Field Orientation as Applied to the New Transvector Closed-Loop Control System for Rotating Field Machines", *Siemens Review*, Vol. 34, pp. 217-220, May 1972.
7. Takahashi I and Ohmori Y: "High-Performance Direct Torque Control of an Induction Motor", *IEEE Transactions on Industry Applications*, Vol. 25, No. 2, pp. 257-264, March/April 1989.
8. Wiechmann Eduardo P, Ziogas Phoivas D, and Stefanović Victor R: "A Novel Bilateral Power Conversion Scheme for Variable Frequency Static Power Supplies", *IEEE Transactions on Industry Applications*, Vol. IA-21, No. 5, pp. 1226-1233, September 1985.
9. *IEEE Standard 519-1992, IEEE Recommended Practices and Requirements for Harmonics Control in Electric Power Systems*, 1992.
10. *NRS 048-2:2003, Electricity Supply — Quality of Supply, Part 2: Voltage characteristics, compatibility levels, limits and assessment methods*, Second Edition, 2003.
11. "SIMOVERT® MASTERDRIVES, Active Front End (AFE), AFE Rectifier / Regenerative Feedback Unit, Compact Type A to D, AC – DC, Operating Instructions", Order No: 6SE7087-6KD80, Edition AC, Copyright © Siemens AG, 2001.
12. "SIMOVERT® MASTERDRIVES, Vector Control, 0.55 kW to 2300 kW, Catalog DA 65.10, 2003/2004", Order No: E86060-K5165-A101-A3-7600, Copyright © Siemens AG, 2003.
13. Ooi B T, Dixon J W, Kulkarni A B, and Nishimoto M: "An Integrated AC Drive System Using a Controlled-Current PWM Rectifier/Inverter Link", *IEEE Transactions on Power Electronics*, Vol. 3, No. 1, pp. 64-71, January 1988.
14. Keus A K, Abrahams R, van Coller J M, and Koch R G: "Analysis of Voltage Dip (Sag) Testing Results of a 15 kW PWM Adjustable Speed Drive," *IEEE International Electric Machines Drives Conference*, Seattle, WA, May 9-12, 1999.
15. Duran-Gomez J L, Enjeti P N and Byeong Ok Woo: "Effect of Voltage Sags on Adjustable-Speed Drives: A Critical Evaluation and an Approach to Improve Performance", *IEEE Transactions on Industry Applications*, Vol. 35, No. 6, pp. 1440-1449, November/December 1999.
16. Matheson E, Von Jouanne A and Wallace A: "A Remotely Operated Power Quality Test Platform Based on a 120 kVA Fully Programmable Three-Phase Source", *IEEE Industry*

- Applications Conference 2001, Thirty-Sixth IAS Annual Meeting, Chicago, IL, USA, Vol. 2, pp. 1188-1195, September 30-October 4, 2001.*
17. Djokić S Ž, Stockman K, Milanović J V, Desmet J J M, and Belmans R: “Sensitivity of AC Adjustable Speed Drives to Voltage Sags and Short Interruptions”, *IEEE Transactions on Power Delivery*, Vol. 20, No. 1, pp. 494 – 505, January 2005.
  18. *SEMI F42-0600, Test Method for Semiconductor Processing Equipment Voltage Sag Immunity*, 2000.
  19. *BS EN 61000-4-11, Electromagnetic Compatibility (EMC), Part 4: Testing and Measurement Techniques, Section 11: Voltage Dips, Short Interruptions and Voltage Variations Immunity Tests*, 1994.
  20. *IEC 1800-3: Adjustable Speed Electrical Power Drive Systems, Part 3: EMC Product Standard Including Specific Test Methods*, 1996.
  21. Pedra J, Córcoles F and Suelves F J: “Effects of Balanced and Unbalanced Voltage Sags on VSI-Fed Adjustable-Speed Drives”, *IEEE Transactions on Power Delivery*, Vol. 20, No. 1, pp. 224-233, January 2005.
  22. Bollen M H J and Zhang L D: “Analysis of Voltage Tolerance of AC Adjustable-Speed Drives for Three-Phase Balanced and Unbalanced Sags”, *IEEE Transactions on Industry Applications*, Vol. 36, No. 3, pp. 904-910, May/June 2000.
  23. Liu Y, Steurer M and Ribeiro P: “A Novel Approach to Power Quality Assessment: Real Time Hardware-In-The-Loop Test Bed”, *IEEE Transactions on Power Delivery*, Vol. 20, No. 2, pp. 1200-1201, April 2005.
  24. Seung Tae Cha, Qiuwei Wu, Nielsen A H, Østergaard J and Park In Kwon: “Real-Time Hardware-In-The-Loop (HIL) Testing for Power Electronics Controllers”, *Asia-Pacific Power and Energy Engineering Conference (APPEEC) 2012*, Shanghai, China, pp. 1-6, 27-29 March 2012.
  25. Steurer M, Edrington C S, Sloderbeck M, Wei Ren and Langston J: “A Megawatt-Scale Power Hardware-In-The-Loop Simulation Setup for Motor Drives”, *IEEE Transactions on Industrial Electronics*, Vol. 57, No. 4, pp. 1254-1260, April 2010.
  26. Wei Ren, Steurer M and Baldwin T L: “Improve the Stability and the Accuracy of Power Hardware-In-The-Loop Simulation by Selecting Appropriate Interface Algorithms”, *IEEE Transactions on Industry Applications*, Vol. 44, No. 4, pp. 1286-1294, July/August 2008.
  27. Lehfuss F, Lauss G, Kotsampopoulos P, Hatziargyriou N, Crolla P and Roscoe A: “Comparison of Multiple Power Amplification Types for Power Hardware-In-The-Loop Applications”, *IEEE Workshop on Complexity in Engineering (COMPENG 2012)*, Aachen, Germany, pp. 1-6, 11-13 June 2012.
  28. Schurig O R: “A Miniature AC Transmission System for the Practical Solution of Network and Transmission-System Problems”, *Transactions of the American Institute of Electrical Engineers*, Vol. XLII, pp. 831-840, January 1923.
  29. Hazen H L, Schurig O R and Gardner M F: “The MIT Network Analyzer Design and Application to Power System Problems”, *Transactions of the American Institute of Electrical Engineers*, Vol. 49, No. 3, pp. 1102-1113, July 1930.
  30. Hudson J E, Hunter E M and Wilson D D: “EHV-DC Simulator”, *IEEE Transactions on Power Apparatus and Systems*, Vol. PAS-85, No. 11, pp. 1101-1107, November 1966.

31. Croft W H, Hartley R H, Linden R L and Wilson D D: "Switching-Surge and Dynamic Voltage Study of Arizona Public Service Company's Proposed 345-kV Transmission System Utilizing Miniature Analyzer Techniques", *Transactions of the American Institute of Electrical Engineers on Power Apparatus and Systems, Part III*, Vol. 81, No. 3, pp. 302-311, August 1962.
32. Jakominich D, Krebs R, Retzmann D and Kumar A: "Real Time Digital Power System Simulator Design Considerations and Relay Performance Evaluation", *IEEE Transactions on Power Delivery*, Vol. 14, No. 3, pp. 773-781, July 1999.
33. Dommel H W: "Digital Computer Solution of Electromagnetic Transients in Single- and Multiphase Networks", *IEEE Transactions on Power Apparatus and Systems*, Vol. PAS-88, No. 4, pp. 388-399, April 1969.
34. Nayak O, Irwin G and Neufeld A: "GUI Enhances Electromagnetic Transients Simulation Tools", *IEEE Computer Applications in Power*, Vol. 8, No. 1, pp. 17-22, January 1995.
35. Woodford D A, Gole A M and Menzies RW: "Digital Simulation of DC Links and AC Machines", *IEEE Transactions on Power Apparatus and Systems*, Vol. PAS-102, No. 6, pp. 1616-1623, June 1983.
36. Woodford D A: "Validation of Digital Simulation of DC Links", *IEEE Transactions on Power Apparatus and Systems*, Vol. PAS-104, No. 9, pp. 2588-2595, September 1985.
37. Kuffel R, Giesbrecht J, Maguire T, Wierckx R P and McLaren P: "RTDS - A Fully Digital Power System Simulator Operating in Real Time", *First International Conference on Digital Power System Simulators, ICDS 1995*, College Station, Texas, U.S.A., pp. 19-25, 5-7 April 1995.
38. McLaren P G, Kuffel R, Wierckx R, Giesbrecht J and Arendt L: "A Real Time Digital Simulator for Testing Relays", *IEEE Transactions on Power Delivery*, Vol. 7, No. 1, pp. 207-213, January 1992.
39. Badelt T, Claus M, Friedrich B, Retzmann D, Boshoff S, Davel P, Forsyth P and Maguire T.L.: "Advanced SVC Testing using a Real Time Digital Simulator", *International Conference on Digital Power System Simulators, ICDS 1997*, Montreal, Canada, pp. 265-270, May 1997.
40. Duchon H, Lagerkvist M, Kuffel R and Wierckx R: "HVDC Simulation and Control Testing using a Real Time Digital Simulator (RTDS)", *First International Conference on Digital Power System Simulators, ICDS 1995*, College Station, Texas, U.S.A., pp. 213-218, 5-7 April 1995.
41. Bergmann K, Braun K, Kuhn G, Retzmann D, Baran L, Pereira F, Forsyth P and Maguire T.L.: "Advanced Fully Digital TCSC Real-Time Simulation in Comparison with Computer Studies and On-Site Testing", *International Conference on Digital Power System Simulators, ICDS 1999*, Vasteras, Sweden, paper number 35, May 1999.
42. Forsyth P and Kuffel R: "Utility Applications of a RTDS<sup>®</sup> Simulator", *8<sup>th</sup> International Power Engineering Conference, IPEC 2007*, Singapore, pp. 112-117, 3-6 December 2007.
43. Forsyth P, Maguire T and Kuffel, R: "Real Time Digital Simulation for Control and Protection System Testing", *IEEE 35th Annual Power Electronics Specialists Conference 2004, PESC 04*, Aachen, Germany, Vol. 1, pp. 329-335, 20-25 June 2004.
44. McLaren P G, Kuffel R, Giesbrecht J, Keerthipala W, Castro A, Fedirchuk D, Innes S, Mustaphi K and Sletten K: "On Site Relay Transient Testing for a Series Compensation Upgrade", *IEEE Transactions on Power Delivery*, Vol. 9, No. 3, pp. 1308-1315, July 1994.
45. Kuffel R, McLaren P, Yalla M and Wang X: "Testing of the Beckwith Electric M-0430 Multifunction Protection Relay using a Real-Time Digital Simulator (RTDS)", *First*

- International Conference on Digital Power System Simulators, ICDS 1995*, College Station, Texas, U.S.A., pp. 49-54, 5-7 April 1995.
46. Rigby B S: “Closed-Loop Testing of an Overcurrent Relay Using a Real-Time Digital Simulator”, *IEEE AFRICON 2004*, Gaborone, Botswana, Vol. 2, pp. 783-788, 15-17 September 2004.
  47. “RTDS™ Manuals, Hardware Manual, GTDI Digital Input Card”, Filename: “HDWR-CH10-GTDI-rev00.pdf”, Cover Page, rev 00, January 2009.
  48. “RTDS™ Manuals, Hardware Manual, GTA0 Analogue Output Card”, Filename: “HDWR-CH7-GTA0-rev00.pdf”, Cover Page, rev 00, January 2009.
  49. “RTDS™ Manuals, Hardware Manual, Cubicle & Power”, Filename: “HDWR-CH1-Cubicle-rev00.pdf”, pp 1.6, rev 00, January 2009.
  50. Hui S Y R, Christopoulos C: “A Discrete Approach to the Modeling of Power Electronic Switching Networks”, *IEEE Transactions on Power Electronics*, Vol. 5, No. 4, pp. 398-403, October 1990.
  51. Maguire T, Forsyth P and Kuffel R: “Small Time-Step ( $< 2\mu\text{Sec}$ ) VSC Machine Drives for the Real Time Digital Simulator”, *8th International Conference on Modeling and Simulation of Electrical Machines, Convertors and Systems, Electromacs 2005*, Hammamet, Tunisia, April 17 – 20, 2005.
  52. Palhad C and Rigby B S: “A Laboratory Test System to Evaluate the Performance of Adjustable-Speed Drives Under Fault Conditions”, *Southern African Universities Power Engineering Conference, SAUPEC 2011*, Cape Town, South Africa, 13-15 July 2011.
  53. Palhad C and Rigby B S: “Real-Time Simulation and Laboratory Measurements of a System to Study Fault Tolerance of Adjustable Speed Drives”, *IEEE AFRICON 2011*, Livingstone, Zambia, pp. 1-6, 13-15 September 2011.
  54. Palhad C and Rigby B S: “An Investigation Into the Use of Hardware-In-Loop Testing Techniques for Assessing the Performance of Adjustable Speed Drives in Response to Power Quality Events”, *Protection, Automation and Control World Conference 2013*, Dublin, Ireland, 24-27 June 2013.
  55. Palhad C and Rigby B S: “Hardware-In-Loop Test to Assess the Performance of Adjustable Speed Drives in Response to Power Quality Events”, *Protection, Automation and Control World Africa Conference 2013*, Cape Town, South Africa, 30 July - 2 August 2013.
  56. Leonhard W: “Field-Orientation for Controlling AC-Machines – Principle and Application”, *3<sup>rd</sup> International Conference on Power Electronics and Variable-Speed Drives*, London, England, pp. 277-282, 13-15 July 1988.
  57. Leonhard W: “AC Drives with Macroelectronic Power Supply and Microelectronic Control, Flexible Sources of Controlled Mechanical Energy”, *IEEE International Symposium on Industrial Electronics, ISIE '95*, Athens, Greece, 1995.
  58. “Siemens, Low-Voltage Motors, 1LA5/6/7/9, 1LP7/9, 1PP6/7/9, 1MA6/7, 1MF6/7, 1MJ6, 1LE1, Operating Instructions”, Order No: 5 610 00000 02 000, Copyright © Siemens AG, 10/2008.
  59. Vas P, *Electrical Machines and Drives, A Space-Vector Theory Approach*, Clarendon Press, Oxford, Oxford University Press, New York, 1992.
  60. Diana G and Harley R G: “An Aid for Teaching Field Oriented Control Applied to Induction Machines”, *IEEE Transactions on Power Systems*, Vol. 4, No. 3, pp. 1258-1262, August 1989.

61. “SIMOVERT<sup>®</sup> MASTERDRIVES, Vector Control, Wechselrichter (DC-AC) Bauform Kompakt, Inverter (DC-AC) Compact Type”, Order No: 6SE7087-6KD60, Edition: AG, Copyright © Siemens AG, 2008.
62. “SIMOVERT<sup>®</sup> MASTERDRIVES, Compendium Vector Control”, Order No: 6SE7087-6QX60 (Version AG), Edition: AI, Copyright © Siemens AG, 2006.
63. “International Rectifier, Three Phase Bridge, MT Series Power Modules”, Bulletin I2771, rev. E 04/03.
64. “DriveMonitor<sup>®</sup>”, Version 5.04, Copyright © 1995-2009 Siemens AG, All Rights Reserved.
65. “RSCAD”, Version 3.001, Copyright RTDS<sup>™</sup> Technologies Incorporated.
66. Enright W, Watson N and Nayak O: “Three-Phase Five-Limb Unified Magnetic Equivalent Circuit Transformer Models for PSCAD V3”, *International Conference on Power System Transients, IPST '99*, Budapest, Hungary, pp. 462-467, 20-24 June 1999.
67. “RTDS<sup>™</sup> Manuals, VSC Small Time-Step Modeling”, Filename: “smalldt.pdf”, pp 1.6, October 2006.

